



UNIVERSITÄT  
DES  
SAARLANDES

# Cryopreservation of complex three-dimensional cell systems

Dissertation  
zur Erlangung des Grades  
der Doktorin der Naturwissenschaften  
der Naturwissenschaftlichen-Technischen Fakultät  
der Universität des Saarlandes

von  
Saskia Altmaier

Saarbrücken, 2024

Tag des Kolloquiums: 21.05.2025  
Dekan: Prof. Dr.-Ing. Dirk Bähre  
Berichterstatter: Prof. Dr. Heiko Zimmermann  
Prof. Dr. Franziska Lautenschläger  
Akad. Mitarbeiter: Dr. Jens Neunzig  
Vorsitz: Prof. Dr. Marc Schneider

---

Table of contents

Table of contents	I
List of abbreviations	III
Zusammenfassung	V
Abstract	VI
1 Introduction	1
2 Theoretical background	7
2.1 Progress and potential of multicellular 3D systems . . . . .	7
2.1.1 Advancements and perspectives of pluripotent stem cells in vitro . . . . .	7
2.1.2 Emerging research fields using iPSCs-derived human cell models . . . . .	9
2.1.3 Progress of 3D cell culture technologies . . . . .	10
2.1.4 Generation methods of 3D cell models . . . . .	11
2.1.5 Organoids as preclinical 3D cell models . . . . .	13
2.2 Biobanking of biological samples by cryopreservation . . . . .	15
2.2.1 Slow-rate freezing with crystallisation . . . . .	15
2.2.2 Ice-free vitrification without crystallisation . . . . .	18
2.2.3 Properties and applications of cryoprotectants . . . . .	20
2.2.4 Cryopreservation of complex 3D cell systems . . . . .	21
3 Materials and Methods	25
3.1 Cell culture . . . . .	25
3.1.1 Cultivation of human induced pluripotent stem cells . . . . .	25
3.1.2 Differentiation and cultivation of hiPSCs-derived neural stem cells . . . . .	26
3.1.3 Differentiation and cultivation of hiPSCs-derived hepatocyte-like cells . . . . .	26
3.2 Generation of three-dimensional cell culture systems . . . . .	28
3.2.1 Static cultivation in ULA plates . . . . .	28
3.2.2 Dynamic cultivation and differentiation in the CERO 3D bioreactor . . . . .	29
3.3 Cryopreservation . . . . .	29
3.3.1 Slow-rate freezing of single cells . . . . .	29
3.3.2 Slow-rate freezing of 3D cell systems . . . . .	30
3.3.3 Thawing of 2D and 3D cell samples in cryovials and ULA plates . . . . .	30
3.3.4 Vitrification with a Twist and warming of 3D cell systems . . . . .	31
3.3.5 Analysis of different cryopreservation media . . . . .	31
3.4 Diffusion analysis by Raman micro-spectroscopy and two-photon excitation microscopy . . . . .	32
3.5 Metabolic and structural analysis . . . . .	34
3.5.1 Viability analysis . . . . .	34
3.5.2 Analysis of hepatic marker expression by Nano-Glo Luciferase Assay . . . . .	36
3.5.3 Clearing and immunocytochemistry (ICC) of spheroids . . . . .	36

---

3.5.4	Ultrastructure analysis of spheroids by scanning electron microscopy (SEM)	38
3.5.5	Gene expression analysis with real-time quantitative polymerase chain reaction (RT-qPCR)	39
3.5.6	Protein expression analysis with flow cytometry (FC)	41
3.6	Data and image processing	42
4	Results	43
4.1	Comparative investigations on cryopreservation effects on metabolic properties in precursor organoids of defined volumes	43
4.1.1	Differentiation and 3D generation techniques of NSC spheroids	43
4.1.2	Effects of cryopreservation media diffusion in NSC spheroids	44
4.1.3	Cryo-induced metabolic effects in NSC spheroids of defined volumes	50
4.2	Comparative investigations on cryopreservation effects on metabolic properties in organoids from distinct germ layers and with different maturity	57
4.2.1	3D differentiation and upscaling of hepatic organoids	58
4.2.2	Cryo-induced metabolic effects in hepatic organoids of different maturity	59
4.3	Comparative investigations on cryopreservation effects on structural and functional properties in precursor organoids	64
4.3.1	Crystallisation effects on cell structure and adhesion in NSC spheroids	64
4.3.2	Vitrification effects on cell structure and metabolism in NSC spheroids	70
4.4	Comparative investigations on the diffusion kinetics of cryoprotective agents in different 3D cell systems	72
4.4.1	Diffusion kinetics of DMSO in organoids using Raman micro-spectroscopy	74
4.4.2	Cryo-induced metabolic and adhesion effects with adapted CPA incubation	75
5	Discussion	81
6	Conclusion and Outlook	111
7	References	113
8	Appendix	143

## List of abbreviations

AFP	antifreeze proteine
ALD	alcoholic liver disease
a.t.	after thawing
ATR	attenuated total reflection
a.w.	after warming
Blebb	(S)-4'-nitro-Blebbistatin
BMP4	Bone Morphogenetic Protein 4
BSA	Bovine Serum Albumin Fraction V
Ca	calcium
cDNA	complementary DNA
CLD	chronic liver disease
clsm	confocal laser scanning microscope
cm	centimetre
Conc.	concentration
CPA	cryoprotective agent
d	day(s)
DMSO	dimethyl sulfoxide
dNTPs	deoxyribonucleoside triphosphate
DNA	deoxyribonucleic acid
DPBS(-/-)	Dulbecco's phosphate buffered saline w/o $\text{Ca}^{2+}$ and $\text{Mg}^{2+}$
EB	embryoid body
EtB	ethidium bromide
e.g.	for example
EG	ethylene glycol
ECM	extracellular matrix
FACS	fluorescence-activated cell sorting
FC	flow cytometry
FDA	fluorescein diacetate
FGF2	fibroblast growth factor
FTIR	Fourier transform infrared
GAiT	Global Alliance for iPSC Therapies
h	hour(s)
HMDS	hexamethyldisilazane
hESC	human embryonic stem cell
hiPSC	human induced pluripotent stem cell
HLC	hepatocyte-like cell
HP	hepatocyte progenitor

ICC	immunocytochemistry
IIF	intracellular ice formation
INA	ice-nucleating agent
IRI	ice recrystallisation inhibitor
ITS	insulin-transferrin-selenium
KOSR	KnockOut Serum
LAA	L-Ascorbic acid
LN <sub>2</sub>	liquid nitrogen
max.	maximum
min	minute(s)
ml	millilitres
mM	millimolar
mRNA	messenger ribonucleic acid
NAFLD	non-alcoholic fatty liver disease
NEAA	non-essential amino acids solution
nfc	non-frozen control
NSC	neural stem cell
OPS	open pulled straw
Pa·s	unit of viscosity [Pascal-seconds]
PHH	primary human hepatocyte
PLL	Poly-L-Lysin
PMA	purmorphamine
PO	Poloxamer 188
RT-qPCR	quantitative reverse transcription polymerase chain reaction
RNA	ribonucleic acid
ROCK	Rho-associated protein kinase
ROS	reactive oxygen species
rpm	revolutions per minute
RQ	relative quantification
RT	room temperature
s	second(s)
SEM	scanning electron microscopy
TNF	tumour necrosis factor
UV	ultraviolet
ULA	ultra-low attachment
VEGF	vascular endothelial growth factor
w/o	without
x g	relative centrifugal force

## Zusammenfassung

Humane dreidimensionale (3D) Zellmodelle bieten die einzigartige Möglichkeit, die zelluläre Architektur und Physiologie menschlicher Organe nachzubilden. In der biomedizinischen Forschung sind sie von immer größerer Bedeutung, um humane Entwicklungsprozesse, Krankheiten und therapeutische Wirkstoffe zu untersuchen. Aus diesem Grund steigt die Nachfrage nach 3D-Zellmodellen, wobei ihre umfassende Nutzung durch das Fehlen geeigneter Langzeitkonservierungsstrategien eingeschränkt ist. Diese Arbeit befasst sich daher mit der Kryokonservierung von 3D Zellmodellen, um das Wissen über Kryo-Effekte in multizellulären Systemen zu erweitern. Dazu wurden die Auswirkungen verschiedener Kryoparameter auf Stammzell-basierte Sphäroide und Organoide mit unterschiedlichen Eigenschaften untersucht. Mittels Standard-Kryoverfahren wurden hierbei signifikante strukturelle Veränderungen nachgewiesen. Bei schonender Kultivierung nach dem Auftauen blieben jedoch Vitalität, Proliferation, Genexpression und Differenzierungspotential der Zellen erhalten. Dynamische Zellkultur oder eisfreie Kryokonservierung konnten dies weiter verbessern. Darüber hinaus wurde eine spektroskopische Analysemethode mittels Raman-Mikrospektroskopie zur Quantifizierung von Diffusionskinetiken diverser Moleküle eingeführt und etabliert. Diese Technik ermöglicht die Vorhersage modellspezifischer Perfusionszeiten verschiedener Substanzen, wie u.a. Kryoprotektiva, um Kryoverfahren für 3D-Zellmodelle zu standardisieren.

## Abstract

Human three-dimensional (3D) cell models provide the unique possibility to imitate the cellular architecture and physiology of human organs. They have become crucial in biomedical research in studying human developmental processes, diseases and therapeutic compounds. With their increasing importance, the demand for ready-to-use 3D cell models has risen. However, the lack of adequate long-term preservation strategies restricts their comprehensive use. Hence, this thesis focuses on the cryopreservation of 3D cell models to expand the knowledge about cryo-induced effects in multicellular systems. This work investigated the impact of different cryopreservation parameters on the cellular network and physiology of stem cell-derived spheroids and organoids with different properties. These 3D cell models showed significant structural changes after standard freezing. However, with gentle handling, cell viability, proliferation, genetic status and differentiation potential were maintained after thawing. These results could be further improved by dynamic recovery approaches or ice-free cryopreservation. Furthermore, a spectroscopic analysis method using Raman micro-spectroscopy to quantify the diffusion kinetics of various molecules was introduced and established. This technique enables the prediction of model-specific perfusion times of different compounds, such as cryoprotectants, in order to characterise and standardise cryopreservation procedures for 3D cell models.

## 1 Introduction

Various cell model systems, including cell lines and animal models, provide advanced insights into disease mechanisms, pathogenesis and preclinical drug screenings (J. Kim et al. 2020). However, a significant drawback is the limited transfer and extrapolation of model-based results to human in vivo conditions. Cell signalling pathways, biochemical and metabolic processes or drug targets are often specific to complex cellular interactions in human physiology. In animal models, many processes are altered, and human two-dimensional (2D) cell models can only represent simple single or partial biochemical pathways. These models may be sufficient for the prediction of physiological processes; however, precisely modelling an entire physiological human tissue or organ with essential interactions of diverse cell types is limited (Duval et al. 2017, Huch et al. 2017). Several studies have shown altered cell characteristics on proliferation (Chitcholtan et al. 2013), differentiation (Mabry et al. 2016) and gene expression (Pineda et al. 2013) in 2D cultures compared to the corresponding 3D tissue models. Thus, the demand for physiological, more relevant human in vitro model systems is increasing. In this context, the introduction of three-dimensional (3D) cell culture methods (Barcellos-Hoff et al. 1989, Petersen et al. 1992) and the pioneering development of human induced pluripotent stem cells (hiPSCs) by K. Takahashi and Yamanaka 2006 are key technologies for modern biotechnology. The self-assembly and pluripotent properties of iPSCs are essential for differentiating specific interconnecting cell types. The processes are triggered by directive signalling by the extracellular matrix (ECM), the cultivation medium and, once the cell network is formed, by the cell types themselves. Together with 3D cell culture techniques, stem cells enable the development and growth of human-derived tissues and organ-like structures in vitro, allowing the recapitulation of metabolic pathways and the functions of entire organs. At the beginning of the development, cells start to adhere and aggregate, forming simple, multicellular 3D models called spheroids. Spheroids represent only single or partial tissue components consisting of one cell type. With increasing maturation induced by external signals and internal developmental processes, more complex 3D systems with several cell types, so-called organoids, were formed (Takebe and Wells 2019, Gunti et al. 2021). They represent a human-physiological relevant basic model system for fundamental biomedical research to improve the understanding of cell type-specific 3D architecture, compositions of ECM and the interactions of organ-like cell structures. Based on this, they offer the possibility to recapitulate human developmental processes during organogenesis and study disease progressions in different stages. With patient-derived iPSC organoids, disease patterns can be analysed directly from individuals, as well as potential therapeutic compounds. Finally, new drug discovery strategies and future personalised therapies can be developed (Doss and Sachinidis 2019, Sharma et al. 2020). Hence, human stem cell-derived spheroids and organoids represent an innovative, groundbreaking tool that influences biomedical research and patient-based therapy with a lasting impact.

In recent years, the use of stem cell-derived 3D brain organoid models has emerged concerning neurodegenerative disease research. In the past decades, the prevalence of neurodegenerative

diseases has steadily increased worldwide (Hansson 2021). The most common neurodegenerative disorders are dementia and Parkinson’s disease, with together about 60 million people currently affected worldwide. By 2050, the number of patients with dementia is expected to rise to at least 130 million people worldwide (Martin et al. 2015). Hence, society is globally confronted with the growing economic impact of neurodegenerative diseases, with annual treatment costs of about 350 billion euros in Europe (BMBF 2023) and over 650 billion dollars in the U.S. (Thorpe et al. 2021). The common feature of neurodegenerative diseases is the progressive degeneration of the neural system that is not curable yet. The primary difficulty in diagnosis is the complex, heterogeneous pathogenesis and diverse range of symptoms leading to 20-30% misdiagnosed patients (Bradford et al. 2009, Beach et al. 2012). Insufficient clinical diagnostic accuracy impedes the identification of efficient, individualised therapies. Current knowledge of neurodegenerative disorders mainly relies on postmortem examination, models from conventional cell lines or primary cell cultures and animal models (Raslan and Kee 2013). However, the transfer and extrapolation of 2D cell culture and animal models to human physiology in vivo are limited due to the lack of the recapitulation of integrative cell communication of several specific cell types, such as neurons and glial cells (Duval et al. 2017). Thus, the development of hiPSCs-derived 3D cell models to study neurodegenerative diseases is on the rise. Brain organoids can resemble different parts of human brain structures and serve as models for disease-relevant pathology. A significant advantage of 3D brain organoids is the superior connectivity of the neurons compared to 2D cell culture systems, which increases the complexity of the neuronal network, closely resembling that of human brains (Smits and Schwamborn 2020). For instance, brain organoids derived from iPSCs by Alzheimer’s patients have been used to recapitulate the pathogenesis and understand the development of characteristic biomarkers, like the amyloid- $\beta$  agglomerations to cortical extracellular plaques and the hyperphosphorylation of tau proteins. Based on this, Raja et al. 2016 could identify  $\beta$ - and  $\gamma$ -secretase inhibitors to mitigate amyloid- $\beta$  and tau alterations. Hence, patient-based organoid models improve preclinical personalised drug screening (Bubnys and Tsai 2022). These studies provided new insights into associated genetic risk factors in Alzheimer’s patients like the E4 allele of the gene *APOE4* (Lin et al. 2018). A wide range of current differentiation protocols and applications to model and understand Alzheimer’s disease pathogenesis via human brain organoids are described by Cerneckis et al. 2023. Similarly, McComish et al. 2022 published recent advances such as the higher neuronal connectivity and the production of neuromelanin in human midbrain organoids compared to 2D cell cultures to investigate pathogenesis in Parkinson’s disease and to improve therapies.

Another emerging field for applying iPSC-derived 3D cell systems is the research on chronic liver diseases (CLD). The most common CLDs are viral hepatitis, alcoholic liver disease (ALD), and non-alcoholic fatty liver disease (NAFLD), causing over two million deaths annually worldwide (Hirode et al. 2020, Blaszkiewicz and Duncan 2022). CLDs are currently the fourth leading cause of death among patients between 45 to 65 years. With the ageing population, the economic burden is increasing, with an annual total expenditure of over 32 billion dollars only in

the U.S. (Asrani et al. 2013, Devarbhavi et al. 2023). CLDs generally encompass a diverse range of diseases with many complex etiologies that are not completely understood. Hence, there is a need for in vitro cell models to improve the understanding of disease mechanisms and diagnostics, leading to the development of effective therapies. Since the availability and long-term cultivation of primary hepatocytes is limited, immortalised human liver cell lines and rodent models have classically been used for studying CLDs (Liu et al. 2013, Nagarajan et al. 2019). However, altered metabolic differences in both models led to the generation of hepatocyte-like cells (HLCs) derived from iPSCs. HLCs can be expanded and maintain human physiological functions during in vitro cultivation, providing significant advantages for modelling liver diseases and drug screenings (Song et al. 2009). In recent years, various liver disease models based on iPSCs have been developed (Blaszkiwicz and Duncan 2022). In particular, 3D models, like HLC organoids, demonstrate higher expression of CYP family genes and a lower expression of fetal hepatocyte markers than 2D cell models, indicating a higher maturation level. These advancements improve the modelling of hepatic structures to simulate disease symptoms, like for CLDs or other diseases such as malaria or hepatitis B (Ng et al. 2015, Nie et al. 2018). Thus, virus pathophysiologies can be investigated to seek new antimalarial drugs or treatments for hepatitis B. In another example, hiPSCs-derived hepatic organoids could be used to show the same altered structures and gene expressions after exposure to high concentrations of fatty acids as in patients with NAFLD (Ramli et al. 2020).

Nevertheless, organoid technology is still a young research field with some limitations. One drawback compared to animal models is the remaining challenge to differentiate and induce all relevant cell types in a single brain or liver cell model (J. Kim et al. 2020, Tricot et al. 2022, Cerneckis et al. 2023). Moreover, the lack of vascularisation protocols causes internal metabolic stress, such as hypoxia and nutrient deficiency. Non-vascularisation impairs the maturation of specific cytoarchitectures. Thus, organoids can only resemble certain parts of brain and liver cell structures and functions (Bhaduri et al. 2020, Kim et al. 2023). Another limiting factor is the time and cost-intensive generation of complex brain and liver organoids. For instance, reprogramming patient-derived fibroblasts into hiPSCs takes three to four weeks, and the differentiation of cerebral or midbrain organoids subsequently takes five to six weeks. Further maturation steps to develop highly complex, interconnected, multicellular networks can vary from 200 days to one year (Mayhew and Singhania 2022). In addition, the time frame for application and downstream experiments is short compared to the generation times, which leads to the generation of multiple batches. The resulting high batch-to-batch variability affects the reproducibility of experiments and delays high-throughput therapeutic screenings in patient-based organoids (Cerneckis et al. 2023). However, due to the broad range of applications, the importance of hiPSCs-derived organoids is steadily increasing. This currently leads to a high demand for ready-to-use organoid models in biomedical research. For high-throughput drug screenings, avoiding complex and time-consuming 3D cell culture procedures would be beneficial. Hence, establishing suitable cryopreservation routines for organoids is a crucial technology to enable robust stock-keeping and accelerate a ready-to-use supply. Compared to

on-demand production, indefinite storage of large organoid batches with standardised quality controls would also reduce batch variability, which may improve experimental reproducibility. So far, mainly cryopreservation protocols for different single cell types in suspension have been established, including both cryopreservation regimes, the slow-rate freezing with crystallisation and the ice-free vitrification without crystallisation (Meneghel et al. 2020). Successful slow-rate freezing protocols for single cells depend on applying optimal cooling rates influenced by various cell type-specific characteristics, like the intracellular osmotic active water volume or membrane permeability. With the optimal freezing and thawing rates and the support of cryoprotective agents (CPAs), cells can survive despite extracellular ice crystals due to balanced dehydration and concentration of intracellular molecules (Mazur et al. 1972). Unlike single cells in suspension, organoids consist of a heterogeneous cell composition with different cell types and specific properties, like different osmotic active water volumes or cell junctions. Additionally, cells in the periphery have higher dynamic water volumes, whereas inner cells are more compressed due to proliferation- and metabolic-induced stress (McEvoy et al. 2020). Different intracellular water volumes lead to the emergence of different cell layers with their respective optimal cooling and thawing rates depending on the cellular volumes. However, implementing optimal temperature rates for each cell layer poses specific difficulties. Cells in the periphery are constantly exposed to the temperature minima and maxima for extended periods compared to the inner cells, leading to a higher temperature gradient throughout the organoid during freezing and thawing. Moreover, the CPA-induced protection of core cells is impaired due to limited internal diffusion and the lack of vascularisation (Taylor et al. 2019). The inhomogeneous penetration of CPAs and thermal gradients leads to high osmotic stress in inner cell layers during cryopreservation and thawing. Related cryo injury mechanisms, like unbalanced dehydration, extra- and intracellular ice-crystal formation or CPA toxicity in outer cells, can cause cell shrinking, disruptions and even apoptosis. These effects endanger the viability and structural integrity of the organoid, which is directly associated with organotypic functions (Taylor et al. 2004).

For this reason, new, innovative approaches for efficient and standardised cryopreservation protocols are required to preserve multicellular models while reducing cryo injury mechanisms (Tsai et al. 2018). Therefore, an essential prerequisite is to understand these cryo-induced harmful effects. The aim is to maintain the 3D cytoarchitecture with characteristic morphologies, cellular interactions and functionalities after thawing. Establishing a next-generation living biobank with high-quality 3D cell models is an essential and forward-looking key technology for biomedical research. In recent years, the first steps of cryopreservation and biobanking of human tissues and organoids have been taken (Taylor et al. 2019). In particular, the cryopreservation of human ovarian tissue to preserve fertility in women has been further developed. Rivas Leonel et al. 2019 provide an overview of successful, approved slow-rate freezing protocols for ovarian tissue worldwide. In addition, vitrification protocols are currently being developed as an alternative ice-free cryopreservation method for tissues and cell aggregates (Shi et al. 2018, Arav 2022, Behl et al. 2023). Biological samples were transformed into a glass-like state via ultra-fast cooling rates and increased intracellular solutes with CPAs (Fahy et al. 1984). Similar to the slow

freezing method, the homogeneous supply of CPAs and applying uniform optimal cooling rates through many cell layers are still challenging in vitrification. Besides human primary tissues, innovative cryopreservation strategies are also being investigated for spheroids and organoids. This ranges from the testing of different medium and CPA compositions to new bioengineering approaches, like isochoric or perfusion bioreactor-based cryopreservation (Wendt et al. 2003, Rubinsky 2015). However, despite these promising cryopreservation concepts, there are still technical hurdles to overcome in optimised heat and CPA transfer to meet the high demand and essential quality requirements for robust biobanking of complex 3D cell systems. Regarding this, there is a lack of fundamental studies with basic quality controls and application-oriented functionality assays in 3D cell systems to understand cryo-induced damaging processes and implement optimised cryopreservation and warming workflows.

This work provides new insights into cryo injury mechanisms and CPA diffusion modelling in early neural stem cell (NSC) and hepatocyte progenitor (HP) spheroids as well as HLC organoids, all derived from hiPSCs (Fig. 1). NSC and HP spheroids serve as single-cell-type precursor models of either matured brain or liver organoids that arise during the differentiation. HLC organoids are more mature and serve as heterogeneous, multicellular liver models. The aim is to elucidate the underlying factors of cryo-related damaging effects in different cryopreservation approaches, including slow-rate freezing and vitrification. In this context, the impact of various parameters, such as cell type specificity, different diameters and degrees of maturation, are investigated. This includes cell type characteristic quality and functionality controls to validate the batches before freezing and after thawing (Fig. 1). Moreover, the radial diffusion of the CPA dimethyl sulfoxide (DMSO) is analysed via Raman micro-spectroscopy to model optimal, cell type-specific and diameter-dependent DMSO incubation times in respective 3D cell models. The advanced knowledge from this work expands the basic understanding of spheroid and organoid cryopreservation and provides a basis for improving the efficiency of cryopreservation protocols.

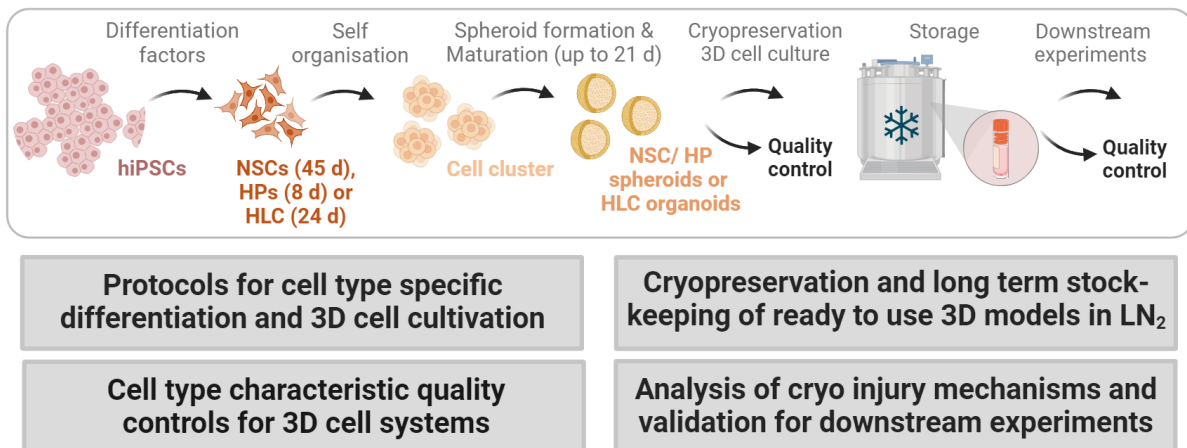


Figure 1: **Concept and objective of present thesis.** Workflow of cryopreservation and validation of cryo injury mechanisms in NSC/HP spheroids and HLC organoids to gain new insights into cryo-induced processes in biomedically relevant hiPSC-derived 3D cell models to implement efficient cryo protocols. Created with biorender.

## 2 Theoretical background

### 2.1 Progress and potential of multicellular 3D systems

Over the last 30 years, many studies have shown the lack of representative 3D cell models to fill the gap between 2D cell cultures and animal models (Jensen and Teng 2020). The organisation and complexity of cells cultured *in vitro* in 2D formats are simplified compared to cell type-specific properties *in vivo*. This includes the inaccurate representation of characteristics like cell type-specific morphology, metabolism, cell structures, signalling pathways or responses to stimuli, which limits disease modelling and the development of new therapies. Concerning these limitations in 2D cell models, animal models better reflect characteristic *in vivo* conditions. However, the transferability to human physiology is limited (Duval et al. 2017), and animal trials are ethically discussed and legally restricted. Hence, cell models cultured in 3D patterns to form tissue- or organ-like structures define the next step towards modelling cell networks as described in section 2.1.5. In particular, the development of spheroids and organoids derived from human stem cells represents an innovative, human-based 3D model system for biomedical research. The pluripotent and self-assembly properties of iPSCs are crucial for generating specific interconnected cell types (Brassard and Lutolf 2019). In addition, their fast and robust availability is beneficial over most human primary cells. In the following, the recent advancements and current applications of stem cell-derived 3D cell technologies are described in detail.

#### 2.1.1 Advancements and perspectives of pluripotent stem cells *in vitro*

Human bodies consist of approx.  $2 \times 10^{13}$  cells and at least 200 different cell types with very different morphological characteristics and functions (Regev et al. 2017). All these human cell types arise from a fertilised zygote as a totipotent initial cell. Totipotent cells can differentiate into any cell or tissue, and develop into a complete organism. In humans, the unicellular zygote develops into early embryos that remain totipotent only in the blastomere stage until the 8-cell stage (Condic 2014). These cells can form extraembryonic tissue and thus independent organisms in an appropriate environment, like the human uterus. They become "human pluripotent embryonic stem cells" (hESCs) in the blastocyst stage and possess the ability to differentiate into cell types of all three germ layers (mesoderm, endoderm and ectoderm). Cells at this stage can no longer form extraembryonic tissue or develop an individual organism (Reubinoff et al. 2000). They have a great potential for self-renewal due to their high telomerase activity, which theoretically allows unlimited propagation. ESCs develop into adult stem cells (AdSCs) depending on developmental fate. These cells are multipotent and can be found in the adult body, e.g. in bone marrow, adipose tissue or umbilical cord tissue. They can only transform into different cell types of one germ layer. Their function is to repair or regenerate injured or damaged tissue (Watt and Hogan 2000). In particular, multipotent hematopoietic stem cells (HSCs) have been investigated for about 50 years (Barnes and Loutit 1967). The isolation of

HSCs from various sources, e.g. from bone marrow, and their use in cell therapy have been extensively researched and standardised (Bujko et al. 2019, Casado-Díaz 2022). Further differentiated cells that are more specialised are called oligopotent or unipotent. Oligopotent cells can give rise to multiple cell types, while unipotent cells can only differentiate into a specific cell type, such as lymphoid stem cells. They only differentiate into a few different cell types or the same cell type within the same tissue type (Bujko et al. 2019).

In 1998, the first embryonic stem cells were successfully isolated from human blastocysts and cultured in vitro (Thomson et al. 1998). The cultivation of ESCs provides the potential to specifically generate any type of somatic cells, such as neuronal cells or hepatocytes. The discovery of hESCs was a milestone in biomedical stem cell research and provided novel model systems to understand human developmental and disease-related processes better. Thus, hESCs have been a valuable and promising cell source for cell therapy in degenerative diseases, such as Parkinson's or Alzheimer's disease (Doss et al. 2004, Cyranoski 2018). However, allogenic transplants of hESCs, i.e. transplants from another individual, can lead to immune reactions and cell rejection, which causes a lifelong dependence on immunosuppressants for the patients (Almeida et al. 2013). In addition, the isolation of hESCs and ESC-based clinical trials are subject to stringent ethically controversial discussions and legal restrictions in Germany (see paragraph 6 of the *Stammzellgesetzes*, StZG) (Aach et al. 2017). For this reason, the discovery of "human induced pluripotent stem cells" by Takahashi and Yamanaka in 2006 was a groundbreaking progress for stem cell research. They enabled a successful reprogramming of completely differentiated adult somatic cells, such as fibroblasts or T lymphocytes, by viral transduction of specific transcription factors (c-Myc, Klf4, Oct3/4 and Sox2) (Takahashi and Yamanaka 2006, Takahashi et al. 2007). The induced ectopic expression of reprogramming factors activates specifically regulated network pathways to reprogram somatic cells into iPSCs. These cells exhibit similar morphology, gene expression, epigenetic profile, telomerase activity and pluripotency to ESCs (Doss and Sachinidis 2019). Only one year later, three independent groups confirmed the iPSCs generation from different human fibroblasts (Park et al. 2024). Meanwhile, various combinations of transcription factors have been tested to derive iPSCs (Poetsch et al. 2022, Park et al. 2024). For example, besides the described Yamanaka transcription factors, Thomson's factors (Nanog, Lin28, Oct3/4 and Sox2) can be used for reprogramming somatic cells (Liao et al. 2008). Furthermore, different inducing non-viral methods, like transfection via episomal vectors, mini-circle DNA vectors or piggyBag transposons, but also via DNA-free methods with recombinant proteins or synthetic mRNAs, are developed since viruses can lead to genome changes and activation of tumour genes (Doss and Sachinidis 2019, Giallongo et al. 2021, Scesa et al. 2021).

In biomedical research, the application potential of iPSCs is constantly expanding (Kobold et al. 2023), as they represent a promising alternative to human primary cells with limited availability. Besides the use of hiPSCs in biomedical research, like in developmental biology, they were used as starting material for personalised cell therapies in clinical trials. The main advantages are the possibility of individualised reprogramming of hiPSCs directly from the cell material of

the patient and the targeted differentiation for the treatment of diseases (Jalil et al. 2021). In addition, individual disease markers can be analysed with patient-derived hiPSCs. However, the generation of patient- or disease-specific hiPSCs is still very complex and time-consuming and causes high costs (Nießing et al. 2021). Thus, the demand for already reprogrammed hiPSC lines and hiPSC-derived differentiated (disease) cell lines is steadily increasing. Hence, iPSC biobanks are currently in development to enable a robust stock-keeping and supply of standardised iPSCs with high quality and tested pluripotency (Huang et al. 2019). For example, the “European Bank for induced pluripotent Stem Cells” (EBiSC) was established in 2014 and contains more than 800 cell lines, including 45 different disease lines. Furthermore, to enable a fast supply of patient-matching hiPSCs, precisely characterised, allogeneic hiPSCs from each Human Leukocyte Antigen (HLA) should be reprogrammed and stored in stem cell banks. This concept is currently being established worldwide as part of the Global Alliance for iPSC Therapy (GAIiT) (Sullivan et al. 2020). However, it is still difficult to achieve complete coverage with cells of all HLA types from a genetically inhomogeneous population (Rham and Villard 2014).

### 2.1.2 Emerging research fields using iPSCs-derived human cell models

In principle, hiPSCs offer a potentially less ethically and legally contentious, unlimited source of cells for biomedical research. With their self-renewal properties *in vitro*, hiPSCs provide the opportunity to derive donor-based, healthy cell lines without allogeneic reactions for clinical studies. It has become possible to develop personalised hiPSC-based therapeutic approaches in regenerative medicine. For instance, first clinical trials have shown a successful implantation of hiPSCs-derived dopaminergic neurons into the brain of a patient with Parkinson’s disease (Takahashi et al. 2019). Besides the use of hiPSCs in cell therapies, patient-specific hiPSCs-derived disease cell models have also been studied to get new insights into cellular disease mechanisms and the discovery of relevant biomarkers (Z. Wang et al. 2017, Lau et al. 2019). The *in vitro* modelling of diseases using iPSCs requires the development of specific differentiation protocols for each cell type that should be standardised, efficient and reproducible. For instance, Reinhardt et al. 2013 published a robust protocol to differentiate neural precursor cells (NPCs) derived from iPSCs of healthy people and patients with mutational Parkinson’s disease to model neural cell subtypes. In this protocol, iPSCs differentiate into ectodermal cells via embryoid bodies. Therefore, the neural induction medium contains the small molecules dorsomorphin and SB43152 to inhibit BMP and TGF $\beta$  signalling pathways. The use of CHIR 99021 turns on the canonical WNT signalling pathway, and purmorphamine stimulates the SHH pathway. All factors induce the formation of epithelial cells with neural progenitor characteristics, including the expression of SOX1, SOX2, Nestin and PAX6. After attachment to plates, EBs form neural rosettes from which neural stem cells can arise (Bell et al. 2019). Alternatively, the cells can also be differentiated by using monolayer-based protocols (Chandrasekaran et al. 2017). Multipotent NSCs exhibit self-renewal and unlimited proliferation potential. Matura-

tion during passages leads to the formation of NPCs (Shi et al. 2012, 2017). Compared to NSCs, the proliferation of NPCs is limited, and they cannot self-renew. Further cultivation in a specific maturation medium can induce the differentiation into different neural cell types, such as neurons, astrocytes and oligodendrocytes. Hence, these cells provide a suitable model for investigating patient-based neurodegenerative or other neural diseases.

Another emerging research field is the *in vitro* generation of hepatocyte-like cells using hiPSCs to assess hepatotoxicity and thus improve high-throughput drug screenings (Blaszkiwicz and Duncan 2022). Due to their ability of self-renewal and unlimited proliferation capacity of hiPSCs, derived HLCs represent a suitable alternative to the limited available primary human hepatocytes. Rezania et al. 2014, Carpentier et al. 2016 and Pettinato et al. 2016 published a combination of different protocols to enhance the maturation of HLCs via definitive endoderm and hepatocyte progenitor stages. These protocols rely on the stimulation of signalling pathways with hepatic-specific transcription factors, like Wnt3a, activin A, fibroblast growth factor-basic, bone morphogenetic protein 4, hepatocyte growth factor and oncostatin M (Du et al. 2018). Such advancements in HLC differentiation improve the high-throughput assessment of the hepatotoxicity of drugs and enable the modelling of human liver diseases like CLDs (Nie et al. 2018, Ramli et al. 2020).

These two examples of the differentiation of NSCs and HLCs illustrate the great potential and need for developing hiPSCs-derived cell models. However, accurately simulating a complete physiological human tissue or organ, including crucial interactions among various cell types, remains challenging (Duval et al. 2017). Thus, there is an increasing need for human tissue models based on hiPSCs, providing an even more robust platform for disease modelling and therapy discovery. In this context, the implementation of 3D cell culture methods (Barcellos-Hoff et al. 1989, Petersen et al. 1992) defines a critical technology in modern biotechnology to mimic human physiology in tissue models.

### 2.1.3 Progress of 3D cell culture technologies

Under specific cultivation conditions, stem cells, like ESCs or iPSCs, have the ability to self-organise and form defined organ-like microstructures with a size of up to several millimetres (Koo et al. 2019). The development of new 3D cell culture techniques signifies the next step for biological model systems and bridges the gap between 2D *in vitro* cell systems and *in vivo* animal models. Prospectively, 3D cell models are expected to effectively replace and reduce the use of animal models. The main characteristics of 3D cell models are schematically represented in Fig. 2 (modified and extended according to Costa et al. 2016). The formation of 3D cell systems is based on the processes of self-assembly and differentiation of the cells. Due to the different expression of cell adhesion molecules, each cell type sorts itself into its domain. At the same time, the differentiation of the cells is influenced by spatial restrictions and/or their division orientation (Lancaster and Knoblich 2014). Different system-intrinsic mechanisms, including the bistability of regulatory networks and asymmetric cell division, affect

the cell arrangements in cell shape, morphology, localisation and movement (Ferrell 2012, Sasai 2013). The development of organ-like 3D structures is influenced by the culture environment, endogenous signalling and exogenous simulations, like the addition of specific growth factors or the presentation of ECM patterns on a carrier matrix. In the last decade, various 3D cell culture protocols with different cell sources and translational applications were published (Lancaster and Knoblich 2014, Rossi et al. 2018). The first step of 3D cell culture is the induction of cell aggregation. These so-called spheroids are multicellular 3D structures which are formed due to cell self-aggregation, e.g. via cell-cell adhesion induced by integrin binding to ECM and intercellular E-Cadherin connections (Fig. 2 C) (Lin et al. 2006). This process is affected by their culture conditions, including the influence of nutrients, oxygen and growth factors, as well as the support of scaffolds with or without ECM (Bates et al. 2000). Spheroids resemble a simple 3D organisation with heterogeneous cell proliferation and low complexity. Depending on the cell type, cells can aggregate and form initial spheroids within 24 hours. Cell sources may include cell lines, primary cells, stem cells, tumour cells or tissue cells (Gunti et al. 2021). Spheroids often serve as a single-cell-type model system for systematic pre-studies. In contrast, organoids imitate the physiological morphology and functions of organs at a higher maturation level (Fig. 2 E & F) (Clevers 2016). These structures are more complex and are formed due to self-organisation and internal developmental processes based on physical and chemical stimulation. The cell sources can be stem cells, like ESCs, AdSCs, iPSCs, tumour cells or tissue cells. With the support of ECM interactions and the specific composition of growth factors, cells differentiate into multiple cell types and form an organ-like 3D structure with specific functions (Fig. 2 A). Organoids can have long-term viability and must be cultured and matured for weeks up to months (J. Kim et al. 2020, Gunti et al. 2021). Further insights into the timeline of progress of organoid technologies and a comparison of different organoid definitions are given in Simian and Bissell 2017.

#### 2.1.4 Generation methods of 3D cell models

In the last decade, various bioengineering approaches were developed to generate different types of spheroids and organoids in vitro. These methods can be divided into static and dynamic 3D cell culture techniques (Penfornis et al. 2017, Huang et al. 2022). As a static approach, ultra-low cell attachment (ULA) surfaces force intercellular interactions while reducing adhesion to the culture plate (Weiswald et al. 2015). The polystyrene surface of these plates can be covalently bonded to a hydrophilic hydrogel, enabling 3D cell culturing. ULA plates offer high reproducibility in a standardised microplate format (ANSI-Standard) but only in low throughput. Another static method is the hanging drop technique. Suspended cells in medium aggregate in a hanging droplet due to gravitational forces and the lack of adhesion surfaces. The advantage is high cost-efficiency; however, standardised handling in high-throughput is limited. Automated hanging drop techniques by robots can improve reproducibility and increase throughput (Tung et al. 2011). Microfluidic devices and organoid-on-a-chip models represent

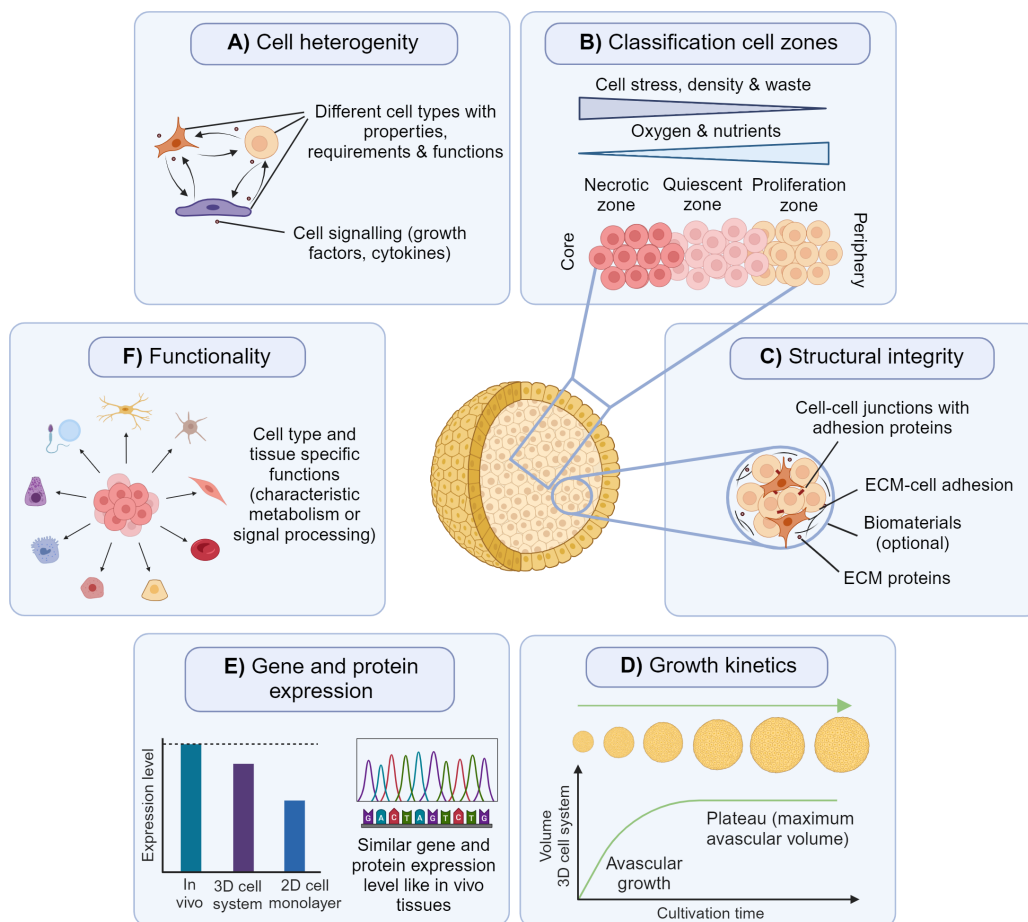


Figure 2: **Schematic overview of main characteristics of 3D cell cultures.** (A) Cell heterogeneity due to different cell types in organoids, (B) organisation of cell zones from core to periphery, (C) 3D structural integrity by cell-cell or artificial scaffold-cell connections, (D) avascular growth kinetics, (E) similar gene and protein expression level and (F) functions like in vivo, especially in organoids. Figure modified and extended according to Costa et al. 2016 and created with biorender.

dynamic 3D cell culture techniques (Huang et al. 2022). These methods are based on cell agglomeration in specially designed microchambers controlled by continuous medium perfusion. Although the experimental effort due to the design of microfluidics is increased, the adaptability and reproducibility are high (Wu et al. 2008, Huang et al. 2022). In suspension-based 3D culture, suspended cells in a medium rotate in spinning or rotating flasks of bioreactors. They agglomerate by spontaneous collision and low attachment to the flask surface (Lei et al. 2014). The impeller-free suspension-based bioreactor and incubator from OLS, called CERO 3D, is specially designed for dynamic 3D cell culture (Kwok et al. 2022). The advantages are improved throughput, viability and maturation during long-term cultivation due to low shear forces while reducing the running costs. These factors enhance the production of 3D cell models from single cells. For example, the yield of beating cardiac spheroids derived from hiPSCs could be increased

to 98% using a dynamic, optimised CERO 3D protocol (Kwok et al. 2022). Besides non-scaffold-based 3D technologies, the integration of 3D scaffolds can additionally improve the generation of multicellular systems by mimicking the characteristics of the respective microenvironment of tissues or organs. Different scaffold properties, such as stiffness, porosity, chemical charging or artificial ECM presentation, can affect the 3D cell culture. The biomaterials range from natural origin, like gelatin or alginate, with the advantage of being biocompatible and biodegradable, to synthetic materials, like synthetic polymers or ceramic with increased stability (Ekaputra et al. 2011, Walters and Stegemann 2014, Baino et al. 2015, Marchini and Gelain 2022).

### 2.1.5 Organoids as preclinical 3D cell models

Multicellular 3D systems are currently regarded as emerging technologies with increasing potential to revolutionise biomedical research, diagnostics and therapies. Compared to 2D cell cultures, these advanced models more accurately resemble the physical morphology and functions of human tissues and organs, enhancing their translatability to human physiology. In particular, organoids derived from hiPSCs provide enormous potential in basic biomedical research (Jensen and Teng 2020). This includes modelling developmental biology processes, understanding signalling pathways, inter- and intracellular mechanisms, and stem cell homeostasis (Fig. 3). Besides understanding fundamental human biological processes, patient-derived organoids can be used for individual disease modelling. Organoids from affected patients with genetic disposition, e.g. cancer or mono- and multigenetic disorders, improve the understanding of individual disease patterns by means of pathogenic, genomic, proteomic, and metabolomic analysis (J. Kim et al. 2020). Based on individual disease modelling, personalised treatments, like cell and drug therapies, as well as genetic and tissue engineering approaches, can be developed (Fig. 3) (Friedman et al. 2015). Moreover, these models not only reduce the need for animal trials but also offer improved relevance to human studies. Nevertheless, as a very young field of research, the development of innovative organoid technologies and patient-based therapies is still ongoing and faces many challenges. One major limitation is still the lack of reproducible organoid generation protocols and quality controls (Spence et al. 2011, LeSavage et al. 2022). Heterogeneous organoid development leads to complications in study design and data analyses. In addition, standard quality controls regarding metabolic assays, single-cell flow cytometry, RNA sequencing or optical analysis techniques are often established for 2D cell culture. New characterisation methods for 3D cell models are currently being developed (Louey et al. 2021, Maharjan et al. 2024). Another significant limitation is the insufficient nutrient content within the organoids, resulting from a deficiency of vascularisation to adequately supply inner cells with nutrients through capillaries, as occurs *in vivo*. Inner cells of non-vascularised spheroids and organoids are affected by metabolic cell stress caused by insufficient diffusion of nutrients, hypoxia stress and limited cell waste removal. This is further promoted by internal solid stress caused by proliferation-driven intercellular pulling forces. Thus, spheroids and organoids consist of a proliferating outer zone, a quiescent middle zone and a necrotic inner core (Fig. 2 B

& D) (Chaicharoenudomrung et al. 2019). Depending on the cultivation format, the cell type and density, the formation of a necrotic core occurs in a radial distance of 100-200  $\mu\text{m}$  from the periphery (Jain et al. 2005, Markou et al. 2020, LaMontagne et al. 2022). Recent studies present vascularised-like tissues with artificial channels generated by sacrificial moulds, laser ablation or bioprinting to form blood vessels using endothelial cells (Wang et al. 2014, Zhu et al. 2017, Mansour et al. 2018). Alternatively, endothelial cells can be integrated during organoid formation to build a microvascular network (Pham et al. 2018). Current investigations towards the next generation of vascularised organoids deal with incorporating specific cells typically arising in another germ layer, like blood and lymphatic vessels, nerves, stromal and immune cells (Strobel et al. 2022, Li et al. 2023). The lack of efficient and reproducible protocols for the induction of these cells is still a main factor limiting the full maturation of organoids.

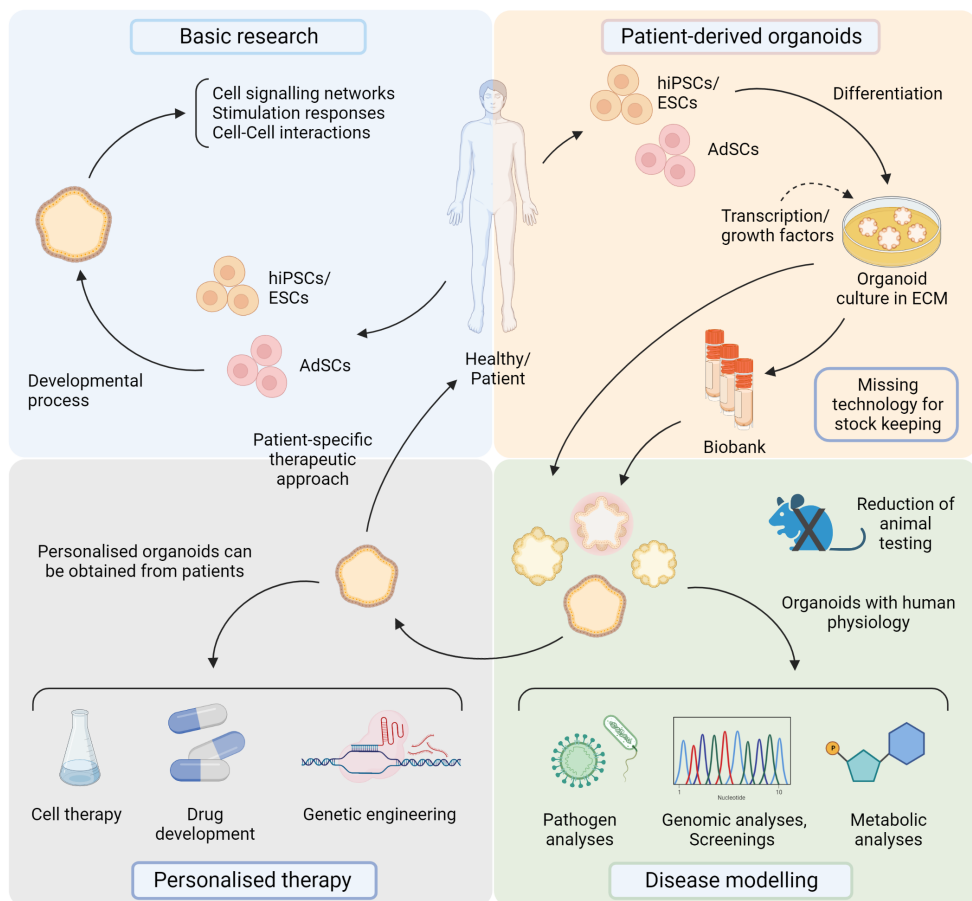


Figure 3: **Overview of potential applications of stem cell-derived organoids.** Firstly, 3D cell culture technologies can be used for basic research to understand developmental processes. Secondly, patient-derived organoids can be created using stem cells. Thirdly, they facilitate individual disease modelling, and fourthly, they enhance personalised therapy. Figure modified from J. Kim et al. 2020 and created with biorender.

An essential prerequisite for the on-demand availability of human stem cells or derived 3D cell systems in biotechnical research and medical applications is stable long-term storage in

sufficient quantities. So far, cryopreservation is the only possibility to preserve living biological samples for a prolonged period at ultralow (cryogenic) temperatures (Li and Ma 2012, Whaley et al. 2021). The following chapter 2.2 describes the current state-of-the-art and challenges of cryopreservation.

## 2.2 Biobanking of biological samples by cryopreservation

As early as the 17th and 18th centuries, Robert Boyle and Lazzaro Spallanzani investigated the essential role of low and cryogenic temperature for living organisms in biology (Boyle 1683, Whaley et al. 2021). Only in the 1950s and 1960s, with the work of James Lovelock, Alan Parks and Peter Mazur, "Cryobiology" was defined as a modern biological discipline (Lovelock 1953b, Mazur 1963, Parkes 1964). Lovelock's discovery of osmotic cell stress during cryopreservation in the 1950s laid the foundation for Mazur's characterisation of intracellular freezing (Mazur 1963) and the "Two-factor hypothesis" (Mazur 1984), as described further in chapter 2.2.1. Due to the improved understanding of cryo-mechanisms in the last decades (Al-Hasani et al. 1987, Chesné and Guillouzo 1988), the demand for application-oriented cryopreservation protocols for biological research and medical applications is increasing. Thus, the establishment and dynamic development of biobanks of stem cells is crucial for scientific researchers as they depend on guaranteed access to reliable and safe cell resources (Meneghel et al. 2020). Well-established cryopreservation techniques allow the implementation of stable and reliable biobanking. A biobank is a professional storage of biological samples, usually under cryogenic conditions, also providing epidemiological, medical and general source data (Paskal et al. 2018). Long-term storage is possible since no more thermally driven or chemical reactions occur under cryogenic conditions below the glass transition temperature of water at approx. 136 K (Capaccioli and Ngai 2011). Water is usually in crystalline form with a viscosity of  $> 10^{12}$  Pa·s, hence diffusion is negligible (Mazur 1984). Biochemical reactions are slowed down or even completely stopped. Subcellular components and details of the ultrastructure can be preserved for a long time without any change. However, exposing unprotected cells to subzero temperatures is generally lethal. The challenge is preserving cellular structures and maintaining their vitality and functionality during freezing and thawing while preventing damage or at least keeping it to a minimum (Mazur et al. 1972). In this context, two essential cryopreservation methods have evolved: conventional, slow freezing with crystallisation, and fast cooling without crystallisation, called vitrification.

### 2.2.1 Slow-rate freezing with crystallisation

Cryo-induced cell damage and, thus, lower survival rates are, in particular, based on the behaviour of water under cryogenic conditions. From a temperature below 0 °C, the equilibrium freezing point, pure water can exist simultaneously in solid and liquid aggregation forms. At decreasing temperatures, during the super-cooling, hydrogen bonds are rearranged to the thermodynamic, more favourable form of an energetically increased crystal lattice, resulting in

first ice crystals and a short-term rise in temperature. The transition from liquid water to ice crystals during the nucleation phase is an exothermic process that causes a measurable latent heat release (Morris and Acton 2013). In contrast to heterogeneous nucleation, homogeneous nucleation results in the formation of an ice nucleus without any nucleating agents, such as salt or saccharides (Wypych 2021). Nucleation occurs by a spontaneous accumulation of water molecules. Pure water only crystallises at about  $-39\text{ }^{\circ}\text{C}$ , whereas heterogeneous nucleation can already occur at about  $-2\text{ }^{\circ}\text{C}$  (Mullen and Critser 2007a). By comparison to heterogeneous nucleation, homogeneous nucleation is a very rare natural event.

Thus, during the slow-rate freezing of cells, heterogeneous nucleation of extracellular water occurs, which leads to an increased osmolarity of the residual liquid. The resulting osmotic gradient across the cell membrane forces the cells to dehydrate and balance the chemical potential. Lovelock 1953b described this effect as the so-called "solution effect". Up to a certain level, the increasing concentration of intracellular solutes is beneficial, as it reduces the probability of intracellular ice formation (IIF) (Morris and Acton 2013, Murray and Gibson 2022). However, if the applied cooling rate is too slow, cells dehydrate excessively, and the concentration of solutes increases up to lethal levels (Fig. 4). Another damaging mechanism is that the continued growth of extracellular ice crystals leads to extremely high solute concentrations in the residual water channels between ice crystals, causing osmotic shock and mechanical stress to trapped cells (Murray and Gibson 2022). The resulting membrane ruptures may cause an excessive outflow of intracellular material. On the other hand, cooling down too fast leads to a fast osmotically driven water efflux across the cell membrane and, thus to an inadequate dehydration status of the cells. This increases the likelihood of harmful IIF and osmotic-induced mechanical cell membrane or cytoskeleton damage (Fig. 4). The formation mechanisms of intracellular ice are still discussed. According to current hypotheses, the seeding of intracellular ice is induced by extracellular ice through aqueous pores or osmotic-induced damages in the cell membrane. Another theory assumes that the undercooling catalyses the intracellular ice via extracellular ice across the cell membrane called surface-catalysed nucleation or via intracellular particles called volume-catalysed nucleation (Toner et al. 1990, Lin et al. 2023). Overall, the optimal cooling rate to find the balance between dehydration and no IIF is directly linked to optimal survival rates, as described by the "Two-factor hypothesis" by Mazur et al. 1972. Cell type-specific factors influencing the optimal cooling rate are membrane permeability, volume-to-surface-area ratio and intracellular solute concentration (Mazur 1963). These cell type-specific parameters are often fixed and cannot or should not be changed. Thus, the optimal cooling rate must be determined for each cell type. On the other hand, the properties of the medium, the concentration of chemical additives, cooling and thawing rates, as well as cryo storage time, temperature, and cryo vessels are adaptable factors influencing the cryopreservation success (see section 2.2.3). All these cryo-variables affect the cryopreservation stress factors (Fig. 4), such as ice crystal formation and osmotic stress. These factors cause various cellular effects, like mechanical, biochemical and epigenetic stress, up to the loss of functionality and integrity, leading to apoptosis and cell death (Fig. 5).

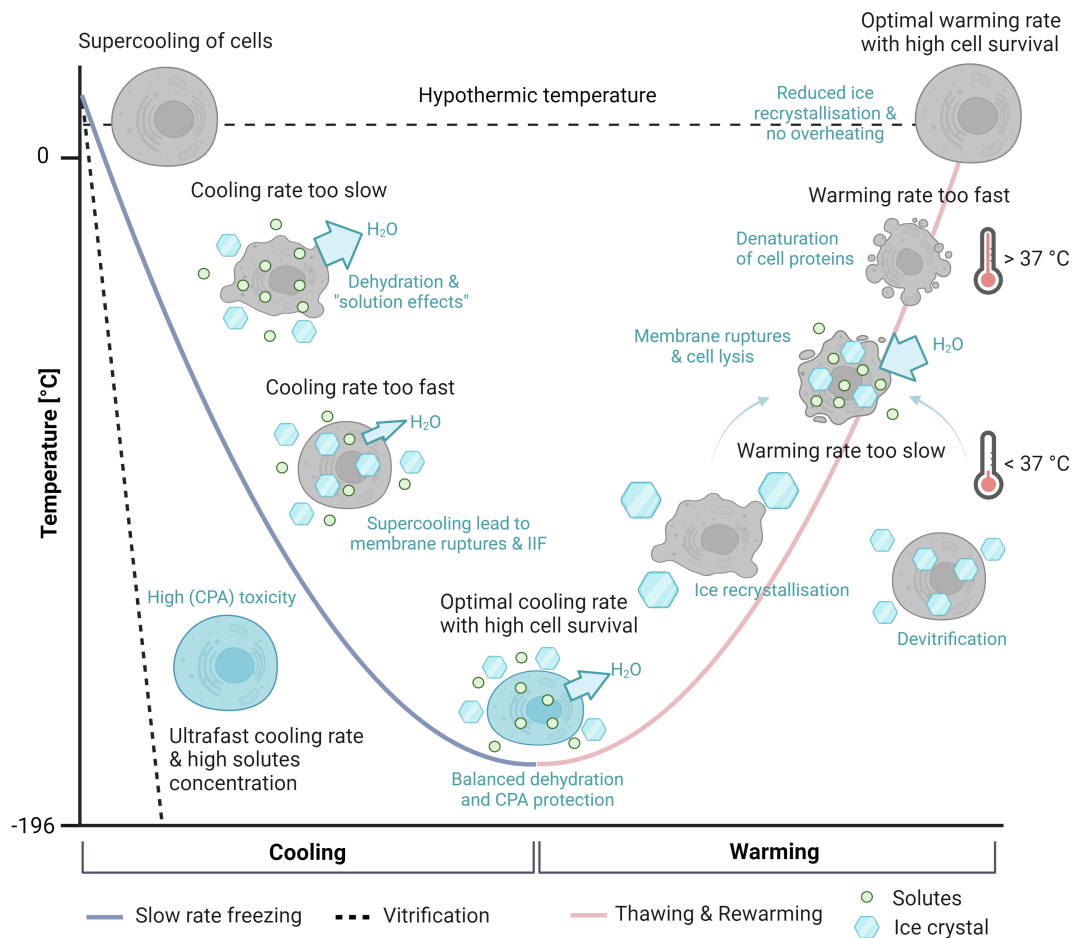


Figure 4: **Cryo injury mechanisms during cryopreservation.** According to the “Two-factor hypothesis” by Mazur et al. 1972, the optimal cooling rate is cell-type specific, resulting in a high cell survival rate after slow-rate freezing and depends on a balanced dehydration and the protection of CPAs while avoiding CPA cytotoxicity and IIF. Ultra-fast cooling rates and high concentrations of CPA can enable vitrification. Depending on the warming rate, ice recrystallisation or devitrification can occur, leading to cell lysis and mechanical stress. Optimised cooling and warming rates, as well as adapted CPA addition, should mitigate these stress factors. Figure modified from Murray and Gibson 2022 and created with biorender.

After cryopreservation, the warming of biological samples back to physiological temperatures poses a further challenge. The exposure of hypotonic aqueous buffer solution to dehydrated cells during thawing leads to a backward adjustment of the osmotic balance. The rapid water influx across the cell membrane may cause membrane damage, excessive swelling and even post-hypertonic cell lysis. Ice recrystallisation can occur by Ostwald ripening migration mechanisms. It describes the rearrangement and growth of small ice crystals into large ice crystals driven by a thermodynamic process to reduce free energy with larger ice crystals (Alley et al. 1986, Budke et al. 2009, Ampaw et al. 2021). This uncontrolled ice growth is a critical process during thawing since it increases osmotic and mechanical stress. Hence, many cryopreservation protocols include

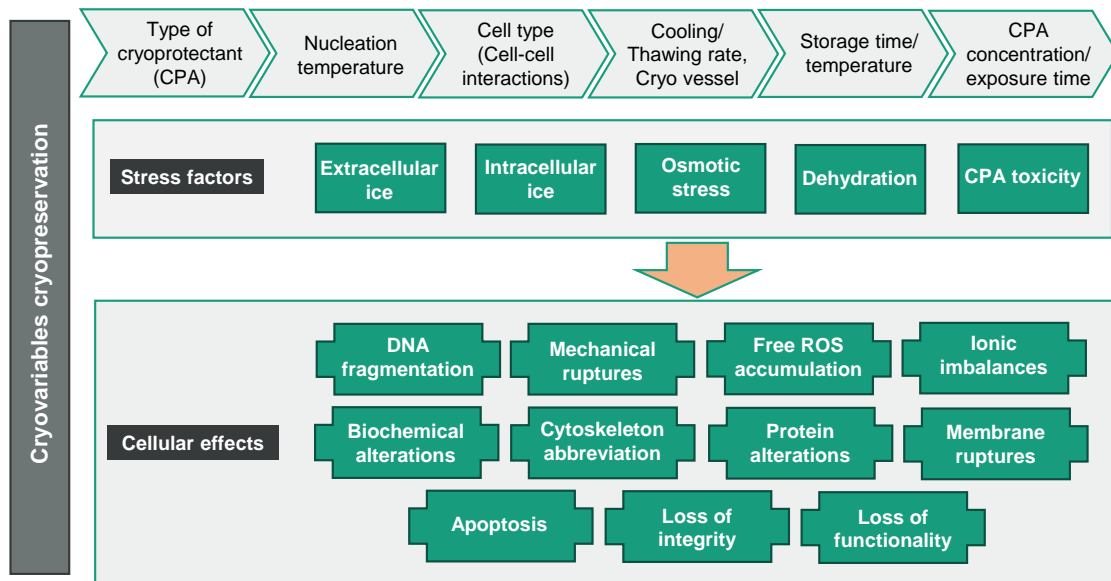


Figure 5: **Cryovariables influence cellular effects after cryopreservation.** Depending on suboptimal cryo-variables, various stress factors occur, such as ice crystal formation and osmotic stress. These stress factors lead to harmful cellular effects up to cell death. Figure modified from Chatterjee et al. 2017.

the usage of ice-binding proteins to inhibit ice recrystallisation (see section 2.2.3). In addition, the samples are thawed as quickly as possible to avoid long recrystallisation times while at the same time eliminating the risk of denaturation due to excessively high temperatures. The gold standard for thawing slowly frozen cells in cryotubes is incubating them for about 2 min at 37 °C in a water bath or heating device (Ha et al. 2005).

## 2.2.2 Ice-free vitrification without crystallisation

Vitrification, an ice-free cryopreservation regime, is the transformation of a substance into a non-crystalline, amorphous solid material (glass) by increasing its viscosity. This stable, glass-like state with a density of  $10^{13}$  Pa·s is achieved via ultra-fast cooling rates of up to several 10,000 °C/min (Mazur 1984). The biological sample is cooled very fast to the temperature range below the glass transition temperature ( $T_g$ ) so that harmful crystallisation is avoided (Fig. 6). Ultra-fast cooling rates can be achieved using cooling agents such as liquid nitrogen ( $LN_2$ ) with a temperature of -196 °C. Additionally, to achieve the fastest possible cooling and thus a genuinely glass-like state, the glass transition temperature must be increased by a higher concentration (up to 9 M) of the solutes with so-called cryoprotectants (CPA). CPAs lower the heterogeneous nucleation temperature ( $T_h$ ) and increase the glass transition temperature ( $T_g$ ) by increasing the viscosity (Fahy et al. 1984). Below a relative solute concentration of 45%, vitrification is not possible since  $T_h$  is higher than  $T_g$  (Phase I in Fig. 6). In phase II, the nucleation and glass transition temperature difference is marginal enough to allow vitrification. However, the sample is not thermodynamically stable (Mullen and Critser 2007b), and cell-

damaging nucleation is unavoidable. Stable vitrification is only possible in phases III and IV with high solute concentrations above 58% and feasible cooling rates (Fig. 6) (Vajta et al. 1998, Reubinoff et al. 2001). Suitable cooling rates are strongly dependent on the volume and thermal conductivity of the sample as well as on the heat capacity of the cryo vessel. Using the so-called "Open Pulled Straw" (OPS) method for vitrification, cooling rates of more than 20,000 °C/min can be achieved by direct contact with LN<sub>2</sub>. This is only possible with a tiny droplet of cells that is sucked into a narrow tube via capillary forces (Vajta et al. 1998). Other techniques include vitrification in a flexipet denuding pipette (Liebermann et al. 2002), micro drops (Papis et al. 2000), small nylon coils or meshes (Kurokawa et al. 1996, Matsumoto et al. 2001) and cryo loops (Oberstein et al. 2001, Liebermann et al. 2002).

Compared to slow-rate freezing, where the main challenge is to determine cell-type-specific cooling rates, the hurdle of vitrification is to ensure homogeneous and rapid cooling while minimising CPA cytotoxicity (see section 2.2.3). General disadvantages are the standardisation of the process, more complex handling, especially for higher volumes and the risk of contamination in the event of direct contact with LN<sub>2</sub> (Kuleshova and Lopata 2002).

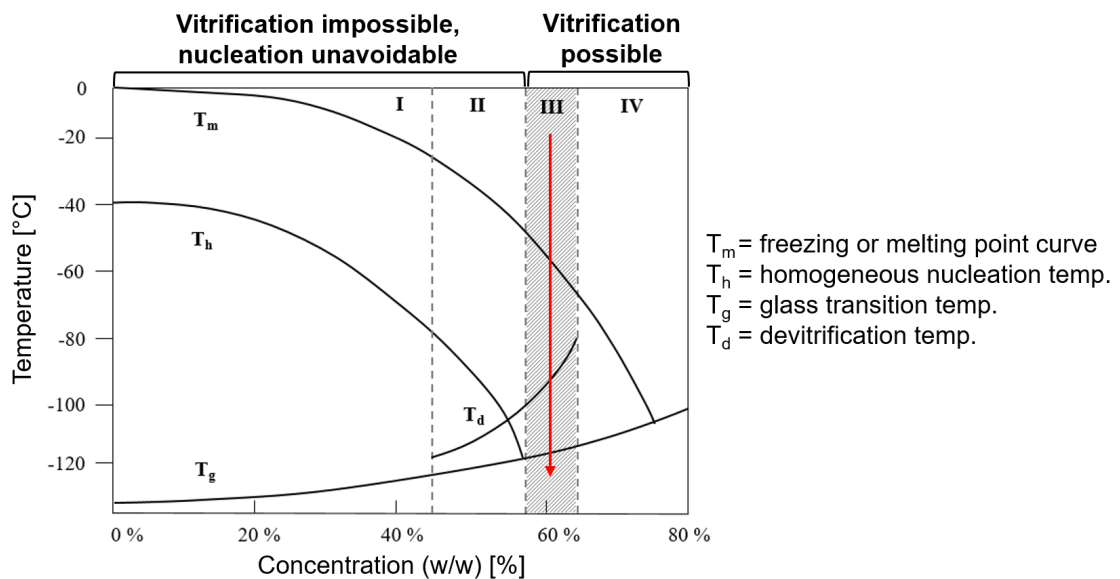


Figure 6: **Phase diagram of an aqueous solution at cryogenic temperatures.** The status of aqueous solution in different phases (I-IV) depends on the temperature [°C] and the concentration (w/w) [%] of the solution. The phases are dependent on the melting temperature ( $T_m$ ), homogeneous nucleation temperature ( $T_h$ ) and glass transition temperature ( $T_g$ ) as well as devitrification ( $T_d$ ). Figure modified from Fahy et al. 1984.

Nonetheless, vitrification can demonstrate beneficial effects across various cell types compared to slow-rate freezing. For instance, Nagy et al. 2020 postulated vitrification as a more efficient and safer approach for the cryopreservation of human oocytes. Additionally, ice-free vitrification is also a promising approach for heterogeneous samples containing different cell types with varying optimal cooling rates for slow-rate freezing or for samples with adherent or interconnected cells that rely on essential ECM connections to other cells or artificial scaffolds. Since the formation of

ice crystals and the associated osmotic imbalance is avoided, cell dehydration and shrinkage are absent so that optimal cooling rates are irrelevant, and the cellular connection remains adherent during vitrification (Beier et al. 2013). Osmotic-induced cryo injury effects are reduced, and adherent cells maintain their morphology and functionality efficiently. Hence, vitrification is routinely used to preserve multicellular embryos and small tissues (Nagy et al. 2020). First cryopreservation successes by vitrification were achieved with mouse embryos by Rall and Fahy 1985. Since the 1990s, human embryos have been successfully vitrified, and in 1998, the first human twins were born from vitrified embryos (Mukaida et al. 1998).

In the context of vitrification, "(re)warming" is the accurate term, whereas "thawing" describes the melting of ice. During the warming of vitrified samples, the risk of devitrification is high when the temperature rises above the glass transition temperature (Fig. 6). This implies that harmful ice nucleation and subsequent recrystallisation can occur when the devitrification temperature ( $T_d$ ) is reached during warming (Fahy and Wowk 2021). To cross the critical nucleation temperature very fast and high warming rates are required. Fahy and Rall 2007 showed that the critical cooling rate for either glycerol, propylene glycol or ethylene glycol increases from about 10 °C/min to 100 °C/min when concentration decreases from 50 % to 40 % (w/w), while the critical warming rate avoiding devitrification increases exponentially from about  $10^2$ - $10^3$  to  $10^5$ - $10^7$  °C/min with same decreasing concentrations. However, overheating of biological samples must be avoided, like for the thawing of slowly frozen samples. Furthermore, cells must be protected from rapid water influx during warming with an aqueous buffer, causing post-hypertonic cell lysis and membrane ruptures. To slowly equalise the high osmotic gradients due to high amounts of CPA, the cells are warmed with pre-warmed sucrose solutions of decreasing concentration (Beier et al. 2011).

### 2.2.3 Properties and applications of cryoprotectants

The application of CPAs can mitigate damaging cryo injuries and enable feasible cooling rates for vitrification. CPAs are any auxiliary substance which protects cells exposed to cryogenic temperatures and whose application results in a higher cell survival rate after warming. These substances were first discovered in various organisms in cold habitats, like plants, fungi, insects or polar fishes and other vertebrates. Naturally derived CPAs, like sugars, antifreeze proteins and glycopeptides (AF(G)P), ice recrystallisation inhibitors (IRIs), as well as ice nucleating agents (INA), provide protective properties to prevent lethal ice-induced cryo injuries (Elliott et al. 2007). AF(G)Ps cover the surface of ice crystals and thus kinetically inhibit the growth of thermodynamically preferred large ice crystals (Kristiansen and Zachariassen 2005). This "thermal hysteresis" was detected in antarctic fish at temperatures down to -2 °C (DeVries 1983) or freeze-tolerant plants (Griffith et al. 2005). The exact interaction between AFPs and the ice crystal surface has not yet been sufficiently clarified. Investigations with AFPs from the spruce budworm *Chorisonneura fumiferana* show that the proteins bind indirectly to the prism ice surface to inhibit ice propagation (Kuiper et al. 2015). As an antagonistic substance, INAs cause

targeted ice formation, promoting dehydration and reducing the likelihood of IIF development. Cold-tolerant insects, amphibians and marine molluscs use this strategy for hibernation by adjusting their supercooling temperature to allow selective ice formation at higher sub-zero temperatures (Zachariassen and Kristiansen 2000, K. B. Storey and J. M. Storey 2013). In 1949, Polge et al. first discovered the beneficial application of glycerol to preserve spermatozoa at ultra-low cryogenic temperatures. One decade later, Lovelock observed the protective properties of neutral substances, like glycerol (Lovelock 1953) and hydrogen bonding molecules as dimethyl sulfoxide (DMSO) during cryopreservation of red blood cells (Lovelock and Bishop 1959). In 1969, Karow et al. listed a wide range of CPAs and classified them into small molecular weight (membrane permeable) and high molecular weight (membrane impermeable). Permeable CPAs provide unspecific, colligative effects causing a reduction of electrolyte concentration during the freezing process. Water molecules are replaced, reducing ice crystal formation and harmful osmotic gradients (Lovelock 1954). The most popular examples of permeable CPAs are DMSO, ethylene glycol (EG) and glycerol. Representative impermeable CPAs are disaccharides, like trehalose and sucrose or polysaccharides, like hydroxyethyl starch. These CPAs stabilise the cell membrane during hypertonic extracellular ice crystal formation by binding with the polar head groups of phospholipids (Clegg et al. 1982, Rudolph and Crowe 1985). In addition, the increase of extracellular osmolarity causes beneficial cell dehydration.

The use of CPAs is a crucial prerequisite for successful cryopreservation of living biological samples. However, the application of some permeable CPAs, like DMSO and EG, is limited due to their cytotoxicity at room temperature. In particular, during vitrification, the loading and removal of highly concentrated CPAs can cause high cytotoxicity levels and osmotic stress. The cytotoxic effects have been shown in several studies (Nguyen et al. 2020, Awan et al. 2020, Gallardo-Villagrán et al. 2022). For instance, studies with cardiac microtissues demonstrate significant miRNA and epigenetic alterations induced by low concentrations of DMSO (Verheijen et al. 2019). Despite cytotoxic effects, DMSO is widely used in many standard cryopreservation protocols due to its high efficiency. However, these broad cytotoxic impacts on human cells restrict the clinical use of DMSO. Non-toxic alternatives are currently being researched for safer application in clinical treatments.

#### 2.2.4 Cryopreservation of complex 3D cell systems

The impact of 3D cell cultures derived from hiPSCs that mimic organ-like physiology continuously increases in biomedical research and even medical applications. Spheroids and organoids provide unique opportunities for diverse applications, such as diagnostics, drug development, disease modelling and tissue engineering (J. Kim et al. 2020). Since the on-demand generation of these cell systems is often complex, time-consuming and not reproducible, the unmet need for ready-to-use samples is increasing. Further, the time frame for application is short compared to the generation time. Facing these challenges, an efficient cryopreservation routine for 3D cell cultures would enable both a stock-keeping and fast ready-to-use supply (Taylor et

al. 2019). However, efficient cryopreservation protocols are mainly available for cell types that tolerate dissociation into single cells in suspension (Meneghel et al. 2020). The translation of these protocols for the long-term preservation of 3D systems at cryogenic temperatures is still challenging. So far, only short-term preservation of tissues and organs is achieved by hypothermic storage at temperatures just above the freezing point. For example, under hypothermic conditions, lung tissue can be preserved for 24-36 hours using cold static preservation and up to 3 days with cycling normothermic ex vivo lung perfusion (Ali et al. 2022). Significant challenges for the multicellular systems are to withstand inhomogeneous cooling and heat transfer and non-uniform mass penetration of CPAs or other additives during cryopreservation (J. G. Baust and J. M. Baust 2007, Fuller and Lee 2007, Guibert et al. 2011). Heterogeneous cell composition in 3D cell systems, such as cell densities, types and morphology, affect the osmotic and thermal conditions. This diversity of cell types and properties within the heterogeneous 3D structure, as discussed in section 2.1.3, leads to varying optimal cooling and warming rates for different cells (May and J. G. Baust 1988, Karlsson and Toner 1996, Acker 2007). However, the determination and regulation of optimum temperature rates in heterogeneous 3D cell systems is challenging. The non-uniform cooling and heat transfer from the periphery to the core cells creates areas within the 3D cell system that, according to Mazur's Two-factor hypothesis, do not achieve optimal cooling and warming rates (Fig. 7). Moreover, the diffusion kinetics of CPAs or other supportive additives, like antioxidants, are influenced by cell types, membrane composition, the kind of CPA, compactness, shape, and size of the cell structure, etc. This leads to an inhomogeneous supply of CPAs and additives throughout the system with limited protection of inner cells and high cytotoxicity in the periphery (Fig. 7). Inhomogeneous CPA penetration, together with heterogeneous dehydration status and excessive extra- and intracellular ice crystallisation, damages essential cell-cell and cell-matrix interactions. This endangers the structural integrity of the whole system, which is crucial for the maintenance of structures and functionality (Taylor and Pegg 1983, Acker et al. 1999, Armitage and Juss 2003, Higgins and Karlsson 2013, Bandzerewicz and Gadomska-Gajadhur 2022).

Innovative concepts for the cryogenic storage of large sample volumes are currently being investigated to reduce limiting thermal and CPA gradients. This includes promising bioengineering approaches, such as isochoric cryopreservation, to restrict ice growth with increased pressure (Szobota and Rubinsky 2006, Rubinsky 2015, Lyu et al. 2017) or the application of non-Newtonian and rheomagnetic CPA solutions to reduce shear stress by viscosity changes during CPA loading and unloading (Hartnett and Kostic 1989, Puschmann et al. 2014). Other concepts are directional freezing (Arav and Natan 2012, Maffei et al. 2014) or stepped vitrification (Corral et al. 2018), where the temperature is gradually lowered while the CPA concentrations are increased. Thus, CPA-induced cytotoxic effects can be reduced at lower temperatures in both techniques. In particular, directional freezing is characterised by high reproducibility, facilitated by the controlled regulation of crystallisation speed, and is associated with higher survival rates compared to non-directional slow freezing techniques (Arav 2022).

Another optimisation approach for the cryopreservation of large sample volumes includes per-

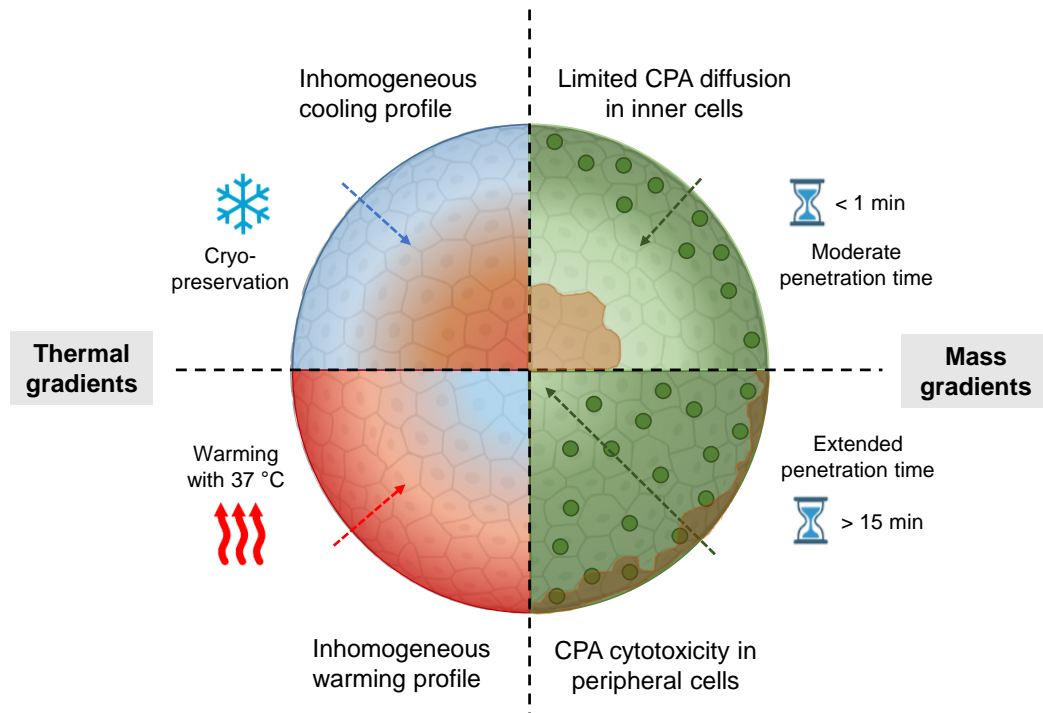


Figure 7: **Inhomogeneous thermal and mass transfer during cryopreservation of 3D cell systems.** Thermal gradients during freezing or vitrification and warming, as well as CPA gradients during loading and unloading, are major limitations for the cryopreservation of multicellular 3D systems.

fusion bioreactor-based cryopreservation (Wendt et al. 2003). In this context, the bioreactor was used to perfuse 3D cell systems with CPAs under a continuous flow, ensuring saturation (Petrenko et al. 2017). After the thawing of the samples, the bioreactor was subsequently utilised for the effective removal of the CPAs from the 3D tissues by constant agitation. Petrenko et al. 2017 have shown a significant increase in viability of cryopreserved mesenchymal stromal cell-based tissue after perfusion and removal of CPAs under perfused flow compared to conventional freezing methods. This optimal CPA penetration and saturation in 3D cell systems are being investigated by staining (Dolezalova et al. 2021) or Fourier transform infrared spectroscopy (Han et al. 2019). This extends the knowledge about CPA diffusion kinetics for 3D cell constructs.

Regarding the warming of tissues or 3D cell models, uniform and rapid rates of warming are essential to minimise thermal-mechanical stress, prevent cracking, and reduce uncontrolled ice recrystallisation. This is crucial for the warming of both slow-rate frozen and vitrified 3D samples. New methods, such as nanowarming with inductive heating of the samples by magnetic nanoparticles (Etheridge and Bischof 2013, Vogel et al. 2024) or laser warming with infrared laser energy, optimises the warming process in 3D cell systems and thus minimises the formation of damaging ice crystals (Daly et al. 2018). For example, scalable nanowarming was employed

by Manuchehrabadi et al. 2017 to achieve uniform warming rates exceeding 130 °C/min in large-scale porcine aortic heart valve leaflet tissues after vitrification. This approach demonstrated improved viability compared to conventionally slow-warmed samples while maintaining unchanged biomechanical properties of the tissue. In another example, Gao et al. 2022 have investigated nanowarming techniques using a vitrified rat heart model. Samples without nanowarming showed signs of cracking, whereas nanowarmed hearts had similar tissue integrity and morphology to controls, along with the retained electrical activity.

These new strategies of tissue cryopreservation and warming are primarily being investigated in the context of reproductive and regenerative medicine. For instance, the cryopreservation of human ovarian tissues is applied worldwide to ensure patients' fertility. The most frequently used cryopreservation method for human ovarian tissue is currently slow-rate freezing, which is optimised by fertility preservation groups in different countries (Rivas Leonel et al. 2019). However, vitrification with OPS or similar methods (see section 2.2.2) has become more popular in recent years as a suitable cryopreservation method for small tissues. So far, slow-rate freezing and ultra-fast vitrification require small sample volumes with a maximum biopsy size of 1-10 mm<sup>2</sup> and 1-2 mm thickness for successful ovarian tissue preservation (Diaz et al. 2022). Although larger tissue pieces would facilitate cutting and handling, cryopreserved tissue fragments larger than 2 mm that were slowly frozen according to the protocol of Lucci et al. 2004 showed abnormal follicular morphology (Ferreira et al. 2010). This is an exclusion criterion for the transplantation of these samples and larger tissues need further (enzymatic) dissections before cryopreservation. Nevertheless, these tissue dimensions are relatively large for cryopreservation. The application aims to restore fertility by maintaining the functionality of the ovaries in the tissue and not necessarily the exact intercellular integrity (Agca 2000). However, while in other tissues, such as the brain, the maintenance of the exact structural cell composition is crucial for their functionality, this is not required for ovarian tissue biopsies (Agca 2000). Hence, the transfer of the cryopreservation protocols of maximum-size ovarian tissue to other 3D cell systems is limited.

In summary, cryopreservation and biobanking of human primary tissues, like ovarian tissue and stem cell-derived spheroids or organoids, like brain or liver organoids, have become increasingly popular in recent years (Ma et al. 2010, Reichman et al. 2017, Corral et al. 2018, Diaz et al. 2022). However, despite the new and promising concepts of cryopreservation and warming of 3D cell systems, technical challenges remain in optimising homogeneous thermal and CPA transfer to meet the stringent demands and quality requirements for robust biobanking of complex 3D cell systems. Currently, there is a scarcity of foundational studies incorporating basic quality controls and application-oriented functionality assays in 3D cell systems to comprehend cryo-induced damage processes and develop optimised cryopreservation and warming protocols.

### 3 Materials and Methods

#### 3.1 Cell culture

Cell culture procedures were performed under aseptic conditions in microbiological safety cabinets. Each cell line was tested negative for mycoplasma. The sterility of devices, consumables, and reagents was either achieved by filtration, autoclaving, or disinfection using 80% ethanol or guaranteed by the manufacturer. Standard laboratory equipment and consumables are presumed, and respective manufacturers are not noted.

##### 3.1.1 Cultivation of human induced pluripotent stem cells

Two hiPSC lines were used (Tab. 1). They were cultured in 6 cm Petri dishes (Fisher Scientific, Schwerte, Germany) coated with 9  $\mu\text{g}/\text{cm}^2$  hESC qualified Matrigel (Corning, Kaiserslautern, Germany) in mTeSR (STEMCELL Technologies, Cologne, Germany) at 37 °C and 5% CO<sub>2</sub>. The medium was changed daily during the week, and cells were passaged in clumps and regrown until a confluence of max. 80% was reached (approx. 5-8 d). Before weekends, 5 ml of fresh medium was added instead of the usual 4 ml used during the week. Cell detachment for passaging was done with 0.5 mM EDTA (Fisher Scientific, Schwerte, Germany) in Dulbecco's phosphate buffered saline w/o Ca<sup>2+</sup> and Mg<sup>2+</sup> (DPBS(-/-)) (Fisher Scientific, Schwerte, Germany). After 5 min incubation at 37 °C and 5% CO<sub>2</sub>, EDTA was aspirated, leaving a thin film. After a further 5 min incubation, the clumps were detached by firmly tapping the dish and rinsing with culture medium. The cells were seeded in new Matrigel-coated plates at an appropriate cell density (1:3 to 1:20), depending on estimated cell number, confluence and expected proliferation. Cells were counted, and viability was determined based on membrane integrity using the NucleoCounter NC-200 (Chemometec, Kaiserslautern, Germany) according to the manufacturer's instructions. The threshold for cell viability used in the experiments was set at over 90%. The cell viability was calculated as follows:

$$Viability [\%] = \frac{viable\ cell\ number}{total\ cell\ number} \cdot 100$$

Table 1: List of hiPSC lines used.

hPSCreg Name	Deviation	Source	hPSCreg Link
BIONi010-C-64	human fibroblast	Bioneer	<a href="https://hpscereg.eu/cell-line/BIONi010-C-64">https://hpscereg.eu/cell-line/BIONi010-C-64</a>
UKKi011-A	human fibroblast	EBiSC	<a href="https://hpscereg.eu/cell-line/UKKi011-A">https://hpscereg.eu/cell-line/UKKi011-A</a>

### 3.1.2 Differentiation and cultivation of hiPSCs-derived neural stem cells

The neural differentiation of hiPSCs into neural stem cells (NSCs) via embryoid body (EB) formation is based on the protocol from Reinhardt et al. 2013. Briefly, hiPSCs were incubated in pre-warmed collagenase IV (Fisher Scientific, Schwerte, Germany) for 20 min at 37 °C and 5% CO<sub>2</sub>. Collagenase IV was removed, and cells were washed twice with DMEM/F12 GlutaMAX (Fisher Scientific, Schwerte, Germany). After discarding the supernatant, hiPSCs were mechanically detached into 5 ml EB 1 medium (Tab. 2) using a cell scraper. Cells were transferred into an ultra-low attachment 6-well plate (Corning, Kaiserslautern, Germany) and cultured for 2 d. On day 3, 2/3 of EB 1 medium was exchanged by 5 ml EB 2 medium (Tab. 2) and cells were cultured for 2 d. The same procedure was done for EB 3 medium (Tab. 2) on day 5. EBs were broken into smaller pieces using a 1 ml pipette, and 10-15 EBs were seeded in one well of a 12-well plate, pre-coated with 9 µg/cm<sup>2</sup> Matrigel. The EBs attached to the plate and were cultured in 1 ml NSC medium (Tab. 2). After 3 d, the attached and spread EBs were dissociated by adding 500 µl pre-warmed Accutase (Fisher Scientific, Schwerte, Germany) for 5 min at 37 °C and 5% CO<sub>2</sub>. The reaction was stopped with 1.5 ml DMEM/F12 GlutaMAX. Dissociated EB cells were centrifuged at 300 x g for 3 min, and the supernatant was discarded. The cells were split with a ratio of 1:5 into early NSCs (single cells) and were seeded in a new Matrigel-coated 12- or 6-well plate. NSCs were cultured in 500 µl or 1 ml NSC medium, respectively, with 10 µM Y-27632 (Biomol, Hamburg, Germany). The medium was changed every 2-3 d, and cells were passaged every 5-7 d, equivalent to the previously described EB splitting. To obtain a pure NSC culture, NSCs had to reach at least passage 5 (Reinhardt et al. 2013). The maturation status was verified by morphology assessment and flow cytometry (see section 3.5.6). Cell proliferation was reduced between passages 22 and 25, and cells beyond passage 25 were not utilised further.

### 3.1.3 Differentiation and cultivation of hiPSCs-derived hepatocyte-like cells

Altmaier et al. 2022 published a combination of different protocols to enhance the maturation of hepatocyte-like cells (HLCs) via definitive endoderm and hepatocyte progenitor (HP) stages based on studies from Rezanian et al. 2014, Carpentier et al. 2016 and Pettinato et al. 2016 (Fig. 8). Briefly, BIONi010-C-64 cells (Tab. 1) were seeded at a density of 5x10<sup>4</sup> cells/cm<sup>2</sup> on 9 µg/cm<sup>2</sup> Matrigel-coated plates, as previously described in 3.1.1. The cells were incubated in mTeSR with 1:100 Revitacell (Fisher Scientific, Schwerte, Germany) for one day. Then, the medium was changed to stage 1 (S1) medium (Tab. 3) to induce definitive endoderm (DE) differentiation for 4 d (modified according to Rezanian et al. 2014). For the second differentiation stage towards HP, modified according to Carpentier et al. 2016, DE cells were detached with TrypLE Express (Fisher Scientific, Schwerte, Germany), resuspended in 20% KnockOut Serum Replacement (KOSR) (Fisher Scientific, Schwerte, Germany) in DPBS (-/-) with 10 µM Y-27632 (Biomol, Hamburg, Germany). A cell density of 5x10<sup>5</sup> cells/cm<sup>2</sup> were seeded on LN521 (BioLamina, Sundbyberg, Sweden) coated wells and cultured in stage 2 (S2) medium (Tab.

3) for 6 d. The medium was changed every 2-3 d. On day 10, the third stage of hepatocyte maturation started by changing the medium to stage 3 (S3) medium (Tab. 3) including 0.25 mg/ml hESC qualified Matrigel (modified according to Pettinato et al. 2016). From days 17-24, 10  $\mu$ M hydrocortisone (Absource, Munich, Germany) and 1x cholesterol lipid concentrate (Fisher Scientific, Schwerte, Germany) were added to the S3 medium.

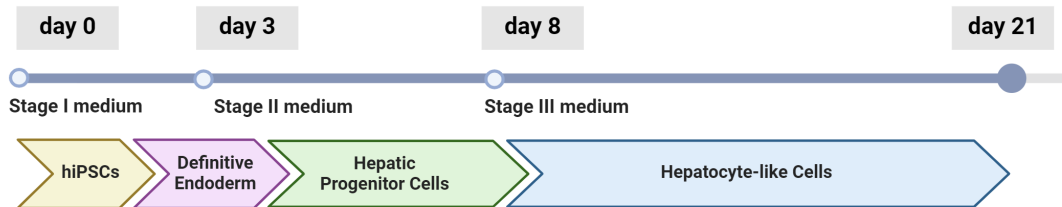


Figure 8: Differentiation from hiPSCs to HLCs. Figure modified from Kwok et al. 2022.

Table 2: Neural differentiation media for generating hiPSCs-derived NSCs.

Medium	Component	Conc.	Manufacturer
<b>Basic medium N2B27</b>	DMEM/F12 (-/-)	50%	Fisher Scientific, Schwerte, GER
	Neurobasal medium	50%	Fisher Scientific, Schwerte, GER
	N2 Supplement	0.5%	Fisher Scientific, Schwerte, GER
	B27 Supplement	1%	Fisher Scientific, Schwerte, GER
	Pen/Strep/Glu	1%	Fisher Scientific, Schwerte, GER
<b>EB 1 medium (Day 0-2)</b>	mTeSR	-	STEMCELL Tech., Cologne, GER
	SB-431542	10 $\mu$ M	Bio-Techne, Wiesbaden, GER
	LDN 193189	0.3 $\mu$ M	Bio-Techne, Wiesbaden, GER
	CHIR 99021	3 $\mu$ M	Bio-Techne, Wiesbaden, GER
	Purmorphamine (PMA)	0.6 $\mu$ M	Bio-Techne, Wiesbaden, GER
<b>EB 2 medium (Day 2-4)</b>	N2B27 medium	-	Fisher Scientific, Schwerte, GER
	SB-431542	10 $\mu$ M	Bio-Techne, Wiesbaden, GER
	LDN 193189	0.3 $\mu$ M	Bio-Techne, Wiesbaden, GER
	CHIR 99021	3 $\mu$ M	Bio-Techne, Wiesbaden, GER
	PMA	0.6 $\mu$ M	Bio-Techne, Wiesbaden, GER
<b>EB 3 medium (Day 4-6)</b>	N2B27 medium	-	Fisher Scientific, Schwerte, GER
	CHIR 99021	3 $\mu$ M	Bio-Techne, Wiesbaden, GER
	PMA	0.6 $\mu$ M	Bio-Techne, Wiesbaden, GER
	L-Ascorbic acid (LAA)	150 $\mu$ M	Fisher Scientific, Schwerte, GER
<b>NSC medium (Day 6-10)</b>	N2B27 medium	-	Fisher Scientific, Schwerte, GER
	CHIR 99021	3 $\mu$ M	Bio-Techne, Wiesbaden, GER
	PMA	0.6 $\mu$ M	Bio-Techne, Wiesbaden, GER
	LAA	225 $\mu$ M	Fisher Scientific, Schwerte, GER

Table 3: Hepatocyte differentiation media for generating hiPSCs-derived HLCs.

Medium	Component	Conc.	Manufacturer
<b>S1 medium</b> (Day 0-3)	MCDB131	-	Fisher Scientific, Schwerte, GER
	BSA	0.5%	Fisher Scientific, Schwerte, GER
	NaHCO <sub>3</sub>	1.5 g/l	Fisher Scientific, Schwerte, GER
	Glucose	10 mM	Fisher Scientific, Schwerte, GER
	GlutaMAX	1%	Fisher Scientific, Schwerte, GER
	Pen/Strep	0.1%	Fisher Scientific, Schwerte, GER
	Activin A	100 ng/ml	Fisher Scientific, Schwerte, GER
	CHIR 99021	3 $\mu$ M	Bio-Techne, Wiesbaden, GER
<b>S2 medium</b> (Day 4-9)	DMEM/F12 (-/-)	-	Fisher Scientific, Schwerte, GER
	KOSR	10%	Fisher Scientific, Schwerte, GER
	GlutaMAX	1%	Fisher Scientific, Schwerte, GER
	NEAA	1%	Fisher Scientific, Schwerte, GER
	Pen/Strep	1%	Fisher Scientific, Schwerte, GER
	DMSO	1%	Fisher Scientific, Schwerte, GER
<b>S3 medium</b> (Day 10-24)	William's E Medium w/o phenol red	-	Fisher Scientific, Schwerte, GER
	Dexamethasone	0.5 $\mu$ M	Fisher Scientific, Schwerte, GER
	Recombinant Human Hepa. Growth Factor	50 ng/ml	Fisher Scientific, Schwerte, GER
	Recombinant Human Oncostatin M	30 ng/ml	Fisher Scientific, Schwerte, GER

## 3.2 Generation of three-dimensional cell culture systems

### 3.2.1 Static cultivation in ULA plates

To generate spheroids or organoids in a static approach, 96-well plates with round bottoms and ULA surfaces (Corning, Kaiserslautern, Germany) were used (Fig. 9 A). The covalently bound hydrogel minimises cell attachment, protein absorption, enzyme, and cellular activation. This method was used for the generation of NSC spheroids of defined and homogeneous size. NSCs were detached and counted as previously described in 3.1.2. Different cell numbers were seeded into the ULA wells to generate spheroids with different, defined diameters in the same cultivation time. With the initial seeding numbers of 2,500, 7,000 or 12,000 NSCs per 60  $\mu$ l NSC medium in one ULA well, the spheroids formed diameters of about 300, 450 or 600  $\mu$ m after 5 d incubation at 37 °C and 5% CO<sub>2</sub>. For Raman micro-spectroscopy studies (see section 3.4), NSC spheroids with initial seeding cell numbers of 2,500 and 12,000 were cultivated for 3, 7 and 14 d. Three-quarters of the medium was changed every 2-3 d by carefully pipetting without touching the spheroids. For morphological analysis, the NSC spheroids were assumed to be

spherical, and their mean area ( $A = \pi \cdot r^2$ ) and volumes ( $V = \frac{4}{3} \cdot \pi \cdot r^3$ ) were determined by the areas measured with microscopic images and NIS Elements AR (Nikon, Düsseldorf, Germany).

### 3.2.2 Dynamic cultivation and differentiation in the CERO 3D bioreactor

With the dynamic approach using the CERO 3D Incubator & Bioreactor (OLS, Bremen, Germany), a large number of spheroids or organoids can be generated in a single CERO 3D tube (Fig. 9 A). Cells were detached and counted to create NSC spheroids as previously described in 3.1.2. CERO 3D tubes were inoculated with  $7.5 \times 10^6$  cells per 10 ml medium and were incubated in a CERO 3D bioreactor at 37 °C and 5% CO<sub>2</sub>. The cultivation program was adjusted to a rotation speed of 60 rpm, a rotation period of 2 s and a rotation pause of 0 s. Three-quarters of the medium was changed every 2-3 d after the spheroids had completely sedimented for 1-2 min. For hepatocyte 3D differentiation and cultivation, the same program was used with  $8 \times 10^6$  BIONi010-C-64 cells per 20 ml medium. The 3D differentiation was adapted from the 2D process as described in 3.1.3. For the first differentiation stage towards DE cells, the S1 medium was modified, using KnockOut-DMEM, 1% Pen/Strep/Glu and 0.1% ITS (all Fisher Scientific, Schwerte, Germany). Additional factors were 10 µM Y-27632 (Biomol, Hamburg, Germany), 10 ng/ml Activin A, 10 ng/ml FGF2 (both Fisher Scientific, Schwerte, Germany), 1 µM CHIR 99021, 1 ng/ml BMP4 and 0.3% methylcellulose (all Bio-Techne, Wiesbaden, Germany). S1 medium for day 2 and 3 were w/o Y-27632 and CHIR 99021. The composition of S2 and S3 medium was the same as previously described in 3.1.3 for the 2D differentiation (Tab. 3) but with 0.3% methylcellulose. For morphological analysis, the areas of hepatic spheroids and organoids were determined with microscopic images using the object area measurement in NIS Elements AR (Nikon, Düsseldorf, Germany).

## 3.3 Cryopreservation

### 3.3.1 Slow-rate freezing of single cells

Single cells (hiPSCs, NSCs or HLCs) were detached and counted according to cell type-specific protocols as described in 3.1.1, 3.1.2 or 3.1.3. A cell number of  $1-2 \times 10^6$  cells was centrifuged for 3 min at 300 x g in a 15 ml tube, and the supernatant was discarded. The cell pellet was gently resuspended in 4 °C precooled 1 ml CryoStor CS10 (STEMCELL Technologies, Cologne, GER) or an alternative cryopreservation medium (see section 3.3.5). The suspension was transferred into a 2 ml cryovial (Greiner, Frickenhausen, Germany). Immediately afterwards, the cryovials were placed either in the freezing container Cool Cell LX (bioCision, Mill Valley, USA) or into a controlled-rate freezer VIA Freeze Uno (Cytiva, Freiburg, Germany). The samples were cooled by storing the Cool Cell LX in a -80 °C freezer with an approx. cooling rate of -1 °C/min. In VIA Freeze Uno, the cooling program was adjusted to an initial equilibration time of 5 min at 4 °C and a following constant cooling rate of -1 °C/min until -80 °C. The next day, cryovials from both devices were stored in the LN<sub>2</sub> tank below -140 °C.

### 3.3.2 Slow-rate freezing of 3D cell systems

About 3000 NSC spheroids from each 10 ml cell culture medium in the CERO 3D tube were collected and sedimented in one cryovial without centrifugation after a cultivation time of 5 d. The supernatant was discarded, and spheroids were incubated in 1 ml 4 °C precooled cryopreservation medium (see section 3.3.5). The cryovials were slow-rate frozen with -1 °C/min in the VIA Freeze Uno up to -80 °C after an equilibration time of 5 min at 4 °C. The samples were subsequently stored in the LN<sub>2</sub> tank below -140 °C. Regarding the hepatic organoids, about 5000-7000 organoids generated in 20 ml cell culture medium in the CERO 3D bioreactor were collected at differentiation day 8 (HPs) and at the final differentiation day 21 (HLCs) and sedimented in one cryovial each. After discarding the supernatant, the organoids were resuspended in 1.5 ml precooled CryoStor CS10 and cryopreserved with the same protocol as the NSC spheroids.

For slow-rate freezing of NSC spheroids in the ULA plate, the medium of each well was gently discarded and changed by 30 µl 4 °C precooled cryopreservation media (see section 3.3.5). Then, the samples were cryopreserved with a cooling rate of -1 °C/min with the VIA Freeze Uno following the same protocol as for the cryovials (Fig. 9 B). The NSC spheroids, generated with different initial seeding cell numbers, were frozen after a cultivation time of 3, 5, 7 or 14 d in ULA plates.

### 3.3.3 Thawing of 2D and 3D cell samples in cryovials and ULA plates

Cryovials with frozen cell suspension were quickly transferred from the LN<sub>2</sub> tank into a 37 °C pre-warmed water bath. The vials were carefully moved to ensure uniform heating without touching the lid with water to avoid the risk of contamination (Fig. 9 C). The thawed cell suspension was pipetted carefully into 10 ml pre-warmed medium, depending on the respective cell type as described in 3.1. After centrifugation with 300 x g for 3 min, cells were seeded and treated with the appropriate passage protocol. The medium was always changed after 24 h. The thawing process of 3D cell samples frozen in cryovials was the same. However, spheroids and organoids were not centrifuged, very carefully treated and slowly transferred into a CERO 3D tube with 10-20 ml fresh pre-warmed cell culture medium using a 1 ml pipette with wide bore tips. Subsequently, the 3D cell systems were cultivated in the CERO 3D bioreactor, and the medium was changed every 2-3 d.

ULA 96-well plates with frozen NSC spheroids were quickly transferred from the LN<sub>2</sub> tank on a 37 °C heating pad under a microbiological safety cabinet. About 200 µl of the respective pre-warmed medium was quickly added to each well using a 96-well format pipetting device, a Vacuu-Pette (Fisher Scientific, Schwerte, Germany) (Fig. 9 C). The ULA plate and the heating pad were incubated for 5 min at 37 °C and 5% CO<sub>2</sub>. After complete thawing, the medium was quickly and carefully discarded using a 200 µl pipette without touching the samples. Then, 80 µl fresh medium was gently added to each well, and the plate was placed in the incubator. The medium was carefully changed after 24 h. NSC spheroids were further cultivated in ULA

plates and the medium was changed every 2-3 d. The compound testing with NSC spheroids was performed by adding 10  $\mu$ M of ROCK inhibitor (Chroman 1 or Y-27632, both Biomol, Hamburg, Germany) or 1% Poloxamer 188 (Fisher Scientific, Schwerte, Germany) to the fresh medium for 24 h after thawing (a.t.). For (S)-4'-nitro-Blebbistatin (Biomol, Hamburg, Germany) testing, spheroids were incubated for 30 min in 10  $\mu$ M compound solution before freezing.

Quality controls were performed respectively for NSC and hepatic 3D cell models, which were generated in ULA plates or a CERO 3D bioreactor, before freezing and at 0 h, 24 h, 3 d and 7 d a.t. (see section 3.5). HP spheroids were additionally analysed 14 d a.t.

### 3.3.4 Vitrification with a Twist and warming of 3D cell systems

To achieve ice-free vitrification of spheroids, the Twist approach for adherent cell layers was modified according to Beier et al. 2013. Briefly, NSC spheroids were generated as described in 3.2 and about 50-100 spheroids were transferred in one Twist dish. Twist dishes were made of two  $\mu$ -dishes 35 mm high (ibidi, Gräfelfing, Germany). The cultivation surface of the first dish was discarded, and the plastic rim was affixed to the bottom of the other intact dish using commercially available two-component epoxy glue. This two-compartment device enables the sterile cultivation of cells in the intact dish and the application of liquid nitrogen in the other dish without contamination risks (Fig. 9 B). The medium of the spheroids in the dish was carefully discarded with a 200  $\mu$ l pipette without touching the floating spheroids. Then, 1 ml of chilled vitrification solution VS1 (Tab. 4), containing 80% cell culture medium, 10% DMSO and 10% EG, was added for different incubation times (1-15 min). The VS1 solution was exchanged by 1 ml of chilled vitrification solutions VS2 (Tab. 4), containing 30% cell culture medium, 30% 1 M sucrose, 20% DMSO and 20% EG for 20-30 s. The medium was removed, the dish was closed, and the device was "twisted". The other dish was filled with LN<sub>2</sub>, and the whole device was immediately transferred into a transport vessel filled with LN<sub>2</sub> to avoid fast evaporation and warming. The spheroids were stored in LN<sub>2</sub> tank below -140 °C.

For warming, the device was "twisted" back, and 4 ml of pre-warmed warming solution W1 consisting of 80% cell culture medium and 20% 1 M sucrose was added directly to the spheroids for 1 min. W1 was exchanged by 1 ml of warming solution W2 consisting of 90% cell culture medium and 10% 1 M sucrose. After 5 min incubation, W2 was discarded, and 2 ml cell culture medium was added. Either single spheroids were collected and transferred into single ULA wells in 60  $\mu$ l medium, or all spheroids were transferred in a CERO 3D tube with 20 ml medium. The following 3D cell culture was performed as described in 3.2.1 and 3.2.2.

### 3.3.5 Analysis of different cryopreservation media

NSC spheroids of different diameters (300-600  $\mu$ m) that had been cultured for 5 days were exposed for 5, 15 and 30 min to cryopreservation media with different CPA compositions and analysed regarding morphology, volume regulation, cell viability (see section 3.5.1) and gene as well as protein expressions (see section 3.5.3, 3.5.5 and 3.5.6). Tab. 4 shows the list of applied

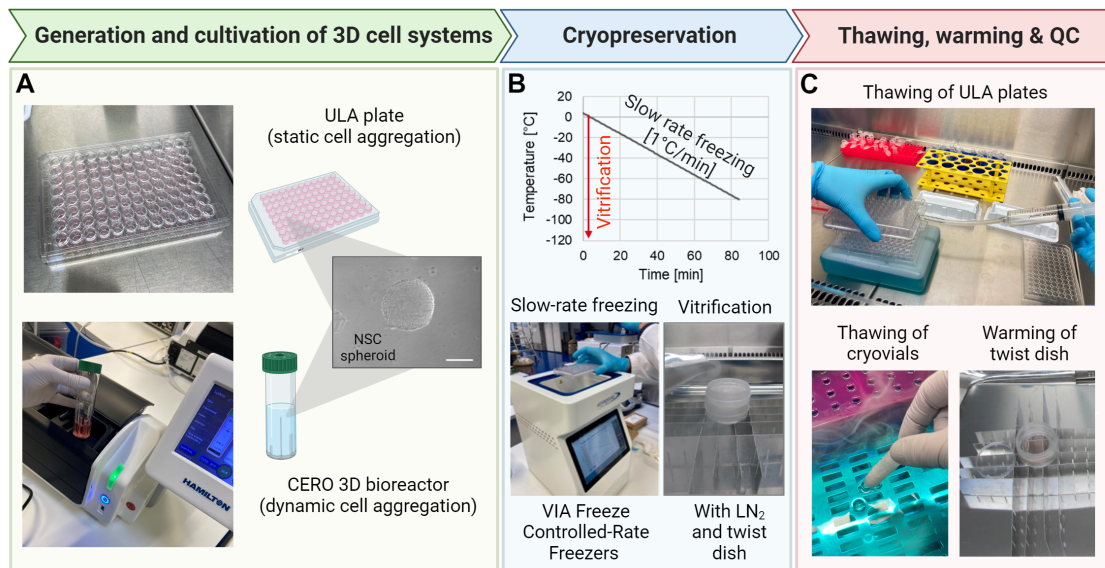


Figure 9: Overview of the workflow of (A) the generation and cultivation, (B) cryopreservation and (C) thawing or warming of 3D cell systems.

cryopreservation media.

Volume changes of NSC spheroids after cryopreservation media incubation were analysed by microscopic evaluation. Spheroids were cultured for 5 d at 37 °C and 5% CO<sub>2</sub> in a ULA 96-well plate. After 5 d, the NSC medium was removed carefully, and along with 20 µl fresh medium, the spheroids were transferred into a new 96-well ULA plate. Then, 80 µl of cryopreservation media with higher CPA concentrations was added to achieve the desired final concentrations (Tab. 4) with a 1:5 mixture. NSC spheroids were incubated for 30 min at room temperature and microscopic recordings were taken every 5 min. The images were analysed using NIS Elements AR (Nikon, Düsseldorf, Germany) to determine the area of the spheroids at each point in time (see section 3.6).

### 3.4 Diffusion analysis by Raman micro-spectroscopy and two-photon excitation microscopy

The temporal progression of DMSO penetration into the centre of an NSC spheroid was measured by confocal Raman micro-spectroscopy according to the protocol from Altmaier et al. 2024. Briefly, spheroids were immobilised to a glass slide with Poly-L-Lysin (PLL) (Fisher Scientific, Schwerte, Germany) to keep spheroids stationary and stable during medium exchange and data acquisition. Therefore, 15 µl drops of 20% PLL in DPBS (-/-) were incubated for 30 min at 37 °C and 5% CO<sub>2</sub>. Subsequently, the solution was discarded, and the slide was left to air dry at room temperature. The spheroids were placed on the dry PLL-spots with 15 µl medium and attached to the surface during the incubation for 4 h at 37 °C and 5% CO<sub>2</sub> (Fig. 10 A). Then, spheroids were carefully washed three times with DPBS (-/-). A Nikon Plan Apo 20x/0.75 objective was used for focus illumination and Raman scatter collection. The immobilised spheroid was focused in the centre of the cross-section (r- and z-adjustment) in

Table 4: List of cryopreservation media used for cryopreservation of NSC spheroids.

Cryopreservation medium	Concentrations	Manufacturer
Dimethyl sulfoxide (DMSO)	2%, 5%, 10%, 20% (v/v)	Merck, Darmstadt, GER
Ethylene glycol (EG)	10%, 20% (v/v)	Merck, Darmstadt, GER
Glycerol	10%, 20% (v/v)	Merck, Darmstadt, GER
Trehalose	0.3 M (w/v)	Merck, Darmstadt, GER
Sucrose	0.3 M (w/v)	Merck, Darmstadt, GER
CryoStor CS10	100%	STEMCELL Tech., Cologne, GER
HypoThermosol FRS	100%	STEMCELL Tech., Cologne, GER
Vitrification solution 1 (VS1)	80% cell culture medium + 10% DMSO + 10% EG (v/v)	Fisher Scientific, Schw- erte & Merck, Darmstadt, GER
Vitrification solution 2 (VS2)	30% cell culture medium + 20% DMSO + 20% EG + 30% 1 M sucrose (w/v)	Fisher Scientific, Schw- erte & Merck, Darmstadt, GER

15  $\mu\text{l}$  DPBS (-/-) drop (Fig. 10 B). Since the DMSO band spectrally coincides with analogous oscillations of other CH-containing compounds of biological samples, DMSO was bioorthogonally labelled with deuterium atoms to shift the major vibration band (C-H stretching vibration) from 2900 to 2160  $\text{cm}^{-1}$  (C-D stretching vibration). After positioning of the spheroid, 15  $\mu\text{l}$  of 20% DMSO-d6 (AppliChem GmbH, Darmstadt, Germany) in DPBS (-/-) were added to achieve a concentration  $c_0$  of 10% DMSO. The acquisition was started after  $t_0 = 20\text{-}30$  s, and a sequence of 600 Raman spectra with 1 s exposure time was recorded. Data was processed using the OriginPro 2020 software (OriginLab Corp., Northampton, USA). Further details about the course of the recorded Raman spectra can be found in section 4.4.1.

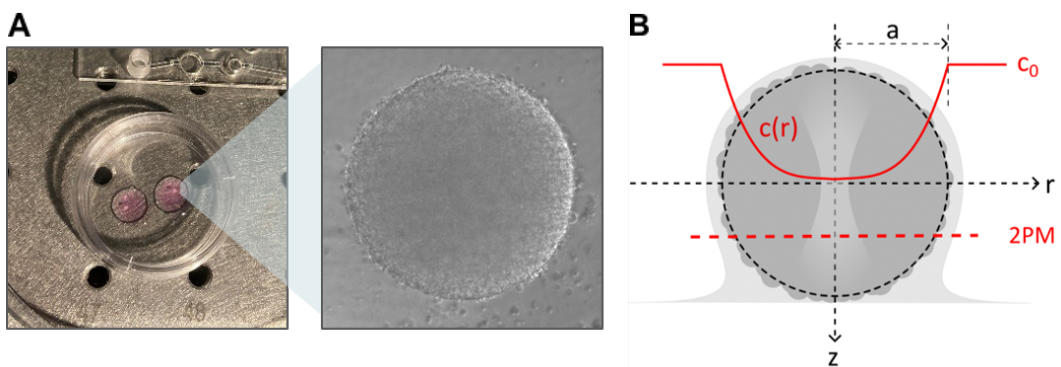


Figure 10: **Diffusion analysis in NSC spheroids.** (A) Immobilised NSC spheroid on a glass slide in a 15  $\mu\text{l}$  medium drop. (B) Schematic spheroid shows focus settings for confocal Raman micro-spectroscopy to analyse the time-dependent increase in DMSO-d6 concentration  $c(r)$ . DMSO-d6 concentration  $c_0$  is assumed to be 10 % in the medium drop. The dotted line (2 PM) represents the focus plane of two-photon excitation microscopy. Figure modified from Altmaier et al. 2024.

For two-photon excitation microscopy, NSC spheroids were incubated with 100 mM rhodamine B (Merck, Darmstadt, Germany) for 24 h to stain membrane structures and with NucBlue™ Live ReadyProbes™ Reagent (Hoechst 33342) (Fisher Scientific, Schwerte, Germany) for 5 h at 37 °C and 5% CO<sub>2</sub> to observe cell nuclei. Intercellular spaces were visualised by indicating with 10 mM non-permeable fluorescein (Fisher Scientific, Schwerte, Germany) for 1 h. Excitation was recorded 50 µm below the spheroid surface (Fig. 10 B) using a Miltenyi Trimscope Matrix operated at an excitation wavelength of 780 nm (Miltenyi, Bergisch Gladbach, Germany).

### 3.5 Metabolic and structural analysis

#### 3.5.1 Viability analysis

##### **Fluorescein diacetate (FDA) and ethidium bromide (EtB) cell viability staining**

The FDA and EtB stainings were used to investigate the metabolic activity and membrane integrity of cells. Active esterases convert membrane permeable FDA (Fisher Scientific, Schwerte, Germany) in viable cells into polar fluorescein with green fluorescence. Red EtB (Fisher Scientific, Schwerte, Germany) is non-permeable and intercalates with the DNA of dead cells with defective membranes. The staining solution consists of 5 ml DMEM/F12, 8 µl FDA (stock solution of 5 mg/ml in acetone (Merck, Darmstadt, Germany) and 50 µl EtB (stock solution of 1 mg/ml in deionised water). The solution was freshly prepared and used within 20 min. The solution was mixed 1:1 with cell suspension medium in the dark to stain the samples. After 4 min of incubation at room temperature, fluorescence was detected by the fluorescence microscope evos FL (Fisher Scientific, Schwerte, Germany) using the FITC and Texas Red filter.

##### **Cell viability analysis in 2D by CellTiter-Glo Luminescent Cell Viability Assay**

The CellTiter-Glo Luminescent Cell Viability Assay (Promega, Mannheim, Germany) is designed to determine the number of viable cells in 2D based on the quantification of the ATP that is present in viable, metabolically active cells. The assay was used according to the manufacturer's instructions. Briefly, 10 ml of CellTiter-Glo Buffer was transferred to CellTiter-Glo Substrate to generate a dye reagent. Then, 100 µl of reagent was mixed with 100 µl of medium-containing cells in a white 96-well plate (Corning, Kaiserslautern, Germany). The plate was shaken for 2 min to induce cell lysis and incubated at room temperature for 10 min without shaking. Luminescence was recorded with an integration time of 1,000 ms in a microplate reader Infinite F200 (Tecan, Männedorf Switzerland).

##### **Cell viability analysis in 3D by CellTiter-Glo 3D Cell Viability Assay**

The CellTiter-Glo 3D Cell Viability Assay (Promega, Mannheim, Germany) enables the determination of the number of viable cells in 3D cell cultures based on the amount of ATP that is present in metabolic active cells. ATP is quantified using a luciferase enzyme that generates a luminescence signal proportional to the amount of ATP present, indicating the number of viable cells. The viability assay was used according to the manufacturer's instructions. Briefly,

3-10 spheroids were collected three times in 100  $\mu$ l medium and transferred in a single well of a white 96-well plate. A volume of 100  $\mu$ l CellTiter-Glo 3D Reagent was added, and the mixture was agitated vigorously for 5 min to induce cell lysis. After incubation for 25 min at room temperature on a horizontal shaker with gentle shaking, the luminescence was recorded with an integration time of 1,000 ms in a microplate reader Infinite F200 (Tecan, Männedorf Switzerland).

### Quantification of apoptotic cells in spheroids by Caspase-Glo 3/7 3D assay

The Caspase-Glo 3/7 3D Assay (Promega, Mannheim, Germany) was used to measure caspase-3 and -7 activities in apoptotic cells of 3D cell cultures. The Caspase-Glo 3/7 3D Reagent consists of a luminogenic caspase-3/7 substrate. Followed by caspase cleavage, this substrate produces a luminescence signal generated by a luciferase enzyme that is proportional to the amount of caspase activity present. The assay was applied according to the manufacturer's instructions. Briefly, 3 spheroids were collected three times in 100  $\mu$ l medium and transferred in a single well of a white 96-well plate (Corning, Kaiserslautern, Germany). The Caspase-Glo 3/7 3D Substrate and Caspase-Glo 3/7 3D Buffer were mixed, and 100  $\mu$ l were added to the samples. After resuspension, the plate was incubated for 30 min at room temperature on a horizontal shaker with gentle shaking. Luminescence was recorded with an integration time of 1,000 ms in a microplate reader Infinite F200 (Tecan, Männedorf Switzerland).

### Detection of cell viability by Apoptosis/Necrosis Assay Kit

Using the Apoptosis/Necrosis Assay Kit (Abcam, Berlin, Germany), apoptotic, necrotic and viable cells were detected in a triple staining. The kit was applied according to the manufacturer's instructions. Briefly, 10-20 NSC spheroids were incubated in 96-well plates and washed with 100  $\mu$ l Assay Buffer by gently pipetting. The samples were resuspended with the staining mix, consisting of 200  $\mu$ l Assay Buffer, 2  $\mu$ l Apopxin Green, 1  $\mu$ l 7-AAD and 1  $\mu$ l CytoCalcein violet 450 (Tab. 5). After 30-60 min incubation, the samples were washed twice with 100  $\mu$ l Assay Buffer and resuspended in 200  $\mu$ l Assay Buffer. The samples were analysed with fluorescence microscope evos FL or confocal laser scanning microscopy, Leica TCS SP8 (Leica Microsystems, Wetzlar, Germany).

Table 5: Staining reagents of Apoptosis/Necrosis Assay Kit.

Dye	Cell stage	Channel	Ex/Em
Apopxin Green	Apoptotic cells	Green	490/525 nm
7-AAD	Necrotic cells, Apoptotic cells at late stage	Red	550/650 nm
CytoCalcein violet 450	Viable cells	Blue	405/450 nm

### 3.5.2 Analysis of hepatic marker expression by Nano-Glo Luciferase Assay

The hepatocyte-specific reporter hiPSCs line BIONi010-C-64 (Tab. 1) contains a Nanoluciferase gene downstream of the hepatic gene *CYP3A4* that was established by using CRISPR-Cas9 technology. This reporter line enables an easy readout of hepatocyte maturation with the luminescence-based Nano-Glo Luciferase Assay (Promega, Mannheim, Germany). In the presence of Nanoluciferase, which is secreted by hepatocyte reporters with high expression of *CYP3A4*, the Nano-Glo Luciferase Reagent generates an ATP-independent luminescence signal. The assay was performed according to the manufacturer's instructions. Briefly, the Nano-Glo Luciferase Assay Substrate and the Assay Buffer were mixed 1:50, and this reagent was mixed 1:1 with the sample volume. To normalise the *CYP3A4* activity against the number of viable cells, the CellTiter-Glo Luminescent Cell Viability Assay was applied after the Nano-Glo Luciferase Assay (see section 3.5.1). The Nano-Glo Luciferase Assay was incubated for 3 min before measuring luminescence with an integration time of 1,000 ms in a microplate reader Infinite F200 (Tecan, Männedorf Switzerland). Since this assay is incompatible with 3D samples, hepatic organoids were first cultured on a pre-coated Matrigel plate for 24 h to form a monolayer structure.

### 3.5.3 Clearing and immunocytochemistry (ICC) of spheroids

ICC was used to detect specific proteins in 3D cell systems via antibody staining. For standard ICC, samples were fixed in BD Cytifix Fixation Buffer (BD Biosciences, Heidelberg, Germany) at 4 °C overnight. Samples were washed three times with DPBS (-/-) and permeabilised for 1 h with a filtrated permeabilisation buffer consisting of 0.2% Triton X-100 (Merck, Darmstadt, Germany) in DPBS (-/-). Then, samples were blocked for 1 h at room temperature in filtered blocking buffer, consisting of DPBS (-/-), 10 mg/ml BSA (Merck, Darmstadt, Germany) and 0.2% Tween80 (Merck, Darmstadt, Germany). To stain the samples, the primary antibody was diluted with blocking buffer according to the manufacturer's protocol (Tab. 6). Then, 300 µl solution was added, and samples were incubated overnight at 4 °C on a microplate shaker. After washing three times with blocking buffer for 10 min, the secondary antibody was prepared in blocking buffer as recommended by the manufacturer (Tab. 7). The samples were incubated on a microplate shaker with 300 µl secondary antibody solution for 1 h at room temperature in the dark. The 3D cell systems were washed with blocking buffer for 5 min and resuspended in blocking solution with 2 drops/ml of NucBlue Fixed Cell ReadyProbes Reagent (DAPI) (Fisher Scientific, Schwerte, Germany) for nucleus staining. F-actin was stained by adding 2 drops/ml of ActinGreen 488 ReadyProbes phalloidin reagent (Fisher Scientific, Schwerte, Germany). To improve the visualisation in 3D systems, the clearing and ICC protocols published in Maselink et al. 2019 were modified and adjusted to NSC spheroids. Briefly, 50-100 NSC spheroids were collected in a glass round bottom tube and washed with 1 ml DPBS (-/-). Every following step was carried out on a microplate shaker. After 4 h fixation with 1 ml BD Cytifix Fixation Buffer at room temperature, spheroids were washed for 2 d with 1 ml PBSTxDB, consisting

of DPBS (-/-) with 20% DMSO, 2% Triton-X-100 and 50 mg/ml BSA. Then, spheroids were incubated for 5 d with a primary antibody solution in PBSTxDB at room temperature in the dark (Tab. 6). Afterwards, they were washed twice with 2 ml PBSTxDB for 1 min and twice with 1 ml PBSTxDB for 24 h. Then, spheroids were incubated for 5 d with a secondary antibody solution in PBSTxDB at room temperature (Tab. 7). After washing with 1 ml PBSTxDB for 24 h, 2 drops/ml of NucBlue Fixed Cell ReadyProbes Reagent (DAPI) (Fisher Scientific, Schwerte, Germany) were added to the next washing step with PBSTxDB for 24 h. Then, the samples were again fixed with BD Cytofix Fixation Buffer at 4 °C for 24 h. For subsequent dehydration, spheroids were washed with 30% 1-Propanol (Merck, Darmstadt, Germany) and incubated for 2 h each at 4 °C with 30%, 50%, 70% and twice with 100% 1-Propanol. The 1-Propanol was discarded and completely evaporated. Subsequently, spheroids were cleared by incubation in ethyl cinnamate (Merck, Darmstadt, Germany) until they appeared transparent. All samples were analysed with a confocal laser scanning microscope, Leica TCS SP8 (Leica Microsystems, Wetzlar, Germany).

Table 6: Primary antibodies for ICC.

<b>Primary antibody for NSC spheroids</b>	<b>Dilution</b>	<b>Manufacturer</b>
Mouse anti-human E-cadherin (#13-1700)	1:500	Fisher Scientific, Schwerte, GER
Mouse anti-human N-cadherin (#MA1-91128)	1:500	Fisher Scientific, Schwerte, GER
Mouse anti-human Nestin (#MA1-110)	7.5 µg/ml	Fisher Scientific, Schwerte, GER
Rabbit anti-human Ki-67 (#27309-1-AP)	15 µg/ml	Proteintech, Planegg-Martinsried, GER
<b>Primary antibody for hepatic organoids</b>	<b>Dilution</b>	<b>Manufacturer</b>
Mouse anti-human Hepatocyte nuclear factor 4 $\alpha$ (HNF4A) (#SC374229)	1:500	Santa Cruz, Heidelberg, GER
Mouse anti-human Cytochrome P450 3A4 (CYP3A4) (#MA517064)	1:500	Fisher Scientific, Schwerte, GER
Rabbit anti-human $\alpha$ -fetoprotein (AFP) (#ab3980)	1:500	Abcam, Berlin, GER
Rabbit anti-human Albumin (ALB) (#ab2406)	1:500	Abcam, Berlin, GER
Mouse anti-human Cytokeratin 18 (CK18) (#ab233915)	1:500	Abcam, Berlin, GER
Rabbit anti-human $\alpha$ 1 anti-Trypsin (A1AT) (#ab207303)	1:500	Abcam, Berlin, GER

Table 7: Secondary antibodies for ICC.

Secondary antibody	Dilution	Manufacturer
Goat anti-Rabbit Secondary Antibody, AF 488	10 µg/ml	Fisher Scientific, Schwerte, GER
Goat anti-Mouse Secondary Antibody, AF 488	10 µg/ml	Fisher Scientific, Schwerte, GER
Goat anti-Rabbit Secondary Antibody, AF 647	10 µg/ml	Fisher Scientific, Schwerte, GER
Goat anti-Mouse Secondary Antibody, AF 647	10 µg/ml	Fisher Scientific, Schwerte, GER

#### 3.5.4 Ultrastructure analysis of spheroids by scanning electron microscopy (SEM)

The preparation of spheroids for SEM was modified according to the protocol published in Kat-sen et al. 1998. At least 10 spheroids were transferred into 12-Well Millicell cell culture inserts (Merck, Darmstadt, Germany) and were washed with DPBS (-/-). Cell culture inserts were dipped into fresh 12-wells for each medium change with the appropriate solutions. Spheroids were fixed overnight at 4 °C with filtrated fixation solution, containing 0.1 M sodium cacodylate buffer and 1.8% glutaraldehyde (both Merck, Darmstadt, Germany) in distilled water, set to 300-359 mOsm and pH of 7.2-7.4. For post-fixation, samples were removed from the fixation solution and washed three times with filtered 0.15 M sodium cacodylate buffer. Next, samples were incubated in 2% osmium tetroxide (Merck, Darmstadt, Germany) diluted in 0.3 M sodium cacodylate buffer for 1 h at room temperature. From now on, plates were protected with aluminium foil. After washing the samples five times with distilled water, they were incubated with 1% tannic acid (Merck, Darmstadt, Germany) in distilled water for 1 h at room temperature. Samples were washed five times with distilled water and transferred into 1% uranyl acetate (Ted Pella, USA) in distilled water for 20-30 min at room temperature. After washing with distilled water, samples were dehydrated with increased series of ethanol solutions (w/w): 10%, 30%, 50%, 60%, 70%, 80%, 90%, 96% and 100%. Spheroids were incubated for 5 min in each concentration except for 10 min in 100% ethanol. For drying, samples were first placed in 50% hexamethyldisilazane (HMDS) (Merck, Darmstadt, Germany) in ethanol (v/v) and then twice in 100% HMDS for 10 min. HMDS was evaporated overnight at room temperature under a laboratory hood. Dry spheroids were carefully poured into a petri dish and collected to the sticky carbon tabs on the probe plates by dipping. Next, the samples were sputtered with 50 nm gold with sputter UNIVEX 450 (Leybold, Cologne, Germany) and analysed with the scanning electron microscope EVO MA 10 (Zeiss, Oberkochen, Germany) according to the manufacturer's instructions.

### 3.5.5 Gene expression analysis with real-time quantitative polymerase chain reaction (RT-qPCR)

RT-qPCR is used to detect, characterise and quantify gene expression levels of cells. The sample RNA was isolated, transcribed into complementary DNA (cDNA) by reverse transcription, and amplified. First, about  $5 \times 10^5$  dissociated cells were resuspended in 300  $\mu$ l RLT Lysis buffer from the RNeasy Micro Kit (Quiagen, Hilden, Germany) for enzymatic cell lysis. NSC spheroids were dissociated by incubating them in pre-warmed Accutase (Fisher Scientific, Schwerte, Germany) at 37 °C and 5% CO<sub>2</sub> for 5 minutes, followed by mechanical dissociation using pipetting. Hepatic organoids were dissociated with the Embryoid Body Dissociation Kit (Miltenyi, Bergisch Gladbach, Germany) according to the manufacturer's instructions. The samples were stored at -80 °C. After slow thawing on ice, the sample was vortexed for 30-60 s to homogenise the lysate and support the RNA release. Every following step was done on ice, and the centrifugation was performed at 4 °C. The sample was mixed with 350  $\mu$ l 70% ethanol and transferred into RNeasy MinElute Spin Columns. After centrifugation at 20,000 x g for 30 s, the flow through was discarded, and 350  $\mu$ l RW1 buffer was added. Next, the column was centrifuged at 20,000 x g for 30 s, flow through was discarded and 70  $\mu$ l RDD buffer with 10  $\mu$ l DNase I was added to digest the DNA. After a 20 min incubation at room temperature, the sample was washed with 350  $\mu$ l RW1 and subsequently with 500  $\mu$ l RPE buffer. Then, 500  $\mu$ l 80% ethanol was added, the sample was centrifuged as before, and the collection tube was changed. Dry centrifugation followed at 24,000 x g for 5 min and open lid. The collection tube was exchanged by a 1.5 ml microtube, and 14.5  $\mu$ l RNase-free water was added to the middle of the column. After centrifugation at 20,000 x g for 1 min, 14  $\mu$ l RNA was collected in a microtube and stored at 4 °C. In the next step, the RNA concentration was determined with a NanoDrop 2000 spectrophotometer (Thermo Fisher Scientific, Darmstadt, Germany). The absorption of 1  $\mu$ l isolated RNA was measured at 260 nm, and RNA concentrations were calculated in ng/ $\mu$ l by the software. According to the manufacturer's instructions, reverse transcription was performed with the High-Capacity cDNA Reverse Transcription kit (Fisher Scientific, Schwerte, Germany). For each reaction, 250 ng RNA was used. Two negative controls, the RNase-free water and one sample without reverse transcriptase, were mandatory to exclude contamination in the isolated RNA. Reverse transcription was done in the Thermocycler SimpliAmp (Thermo Fisher Scientific, Darmstadt, Germany) with the following program: 24 °C for 10 min, 37 °C for 2 h, 85 °C for 5 min and 4 °C until sample collection.

The generated cDNA was multiplied and simultaneously quantified via RT-qPCR based on the detection of the fluorescence signal from TaqMan assays (Thermo Fisher Scientific, Darmstadt, Germany), which increases proportionally to the amount of DNA. First, the desired genes (TaqMan assays) were selected (Tab. 8 and 9). The housekeeping genes *GAPDH* and *HPRT1* served as a reference for endogenous positive control. For qPCR, an appropriate mastermix was prepared with 0.5  $\mu$ l TaqMan assay, 5  $\mu$ l TaqMan Fast Advanced Master Mix (Fisher Scientific, Schwerte, Germany), 0.2  $\mu$ l cDNA and 4.3  $\mu$ l RNase free water per one well of a 96-well qPCR-plate. For each reaction, three technical replicates were performed. After sealing the plate

with an adhesive film and short centrifugation, the samples were analysed with QuantStudio 7 Flex Real-Time PCR System (Thermo Fisher Scientific, Darmstadt, Germany). Their graphs should not deviate from each other by more than 0.5 cycles. The gene expression data was evaluated with QuantStudio Real-Time Software following the mathematical analysis by Pfaffl 2001. In a typical PCR, about 40 cycles are run, and new DNA is amplified with each cycle. The exponential increase is detected by the increase of the fluorescence signals. The software calculates the threshold (Ct value), i.e. the number of PCR cycles in the linear range of the rise. The higher the Ct value, the less mRNA is present in the original sample, as more cycles are required to reach the linear range. The corresponding gene is strongly expressed at low values, which is usually the case for endogenous controls. For relative gene expression quantification between a sample and an untreated calibrator sample, the RQ-value was calculated as follows:

$$\begin{aligned} \Delta Ct_{\text{Calibrator or sample}} &= Ct_{\text{Calibrator or sample}} - Ct_{\text{endogenous ctrl}} \\ \Rightarrow \Delta\Delta Ct &= \Delta Ct_{\text{sample}} - \Delta Ct_{\text{Calibrator}} \Rightarrow RQ = 2^{-\Delta\Delta Ct} \end{aligned} \quad (1)$$

Table 8: List of TaqMan assays for RT-qPCR of NSCs from Thermo Fisher Scientific, Darmstadt, Germany.

TaqMan primer (assay ID)	Protein	Function
<i>GAPDH</i> (Hs99999905_m1)	Glyceraldehyd-3-phosphate-Dehydrogenase	Housekeeping marker (Reference)
<i>HPRT1</i> (Hs99999909_m1)	Hypoxanthine-Phosphoribosyl-Transferase 1	Housekeeping marker (Reference)
<i>HES1</i> (Hs00172878_m1)	Hairy and enhancer of split-1	Neural marker
<i>NES</i> (Hs04187831_g1)	Nestin	
<i>PAX6</i> (Hs01088114_m1)	Paired box protein Pax-6	
<i>CDH1</i> (Hs01023894_m1)	Epithelial cadherin (E-cadherin)	Cell adhesion marker
<i>OCN</i> (Hs01049883_m1)	Occludin	
<i>NOTCH1</i> (Hs01062014_m1)	Neurogenic locus notch homolog protein 1	
<i>BAX</i> (Hs00180269_m1)	Bcl-2 Associated X-protein	Stress marker
<i>P53</i> (Hs01034249_m1)	Tumor suppressor protein	
<i>SOD1</i> (Hs00533490_m1)	Superoxide dismutase 1 protein	
<i>HSF1</i> (Hs01027616_g1)	Heat shock protein factor 1	

A significant change in expression is defined as at least a twofold change, resulting in RQ-values of more than 2 or less than 0.5.

Table 9: List of TaqMan assays for RT-qPCR of hepatocytes from Thermo Fisher Scientific, Darmstadt, Germany.

TaqMan primer (assay ID)	Protein	Function
<i>HNF4A</i> (Hs00230853_m1)	Hepatocyte nuclear factor 4 $\alpha$	Hepatocyte progenitors
<i>AFP</i> (Hs01040598_m1)	$\alpha$ -fetoprotein	
<i>TTR</i> (Hs00174914_m1)	Transthyretin	
<i>ALB</i> (Hs00609411_m1)	Albumin	Hepatocytes
<i>CYP2C9</i> (Hs00426397_m1)	Cytochrome P450 2C9	CYP enzymes
<i>CYP3A4</i> (Hs00604506_m1)	Cytochrome P450 3A4	

### 3.5.6 Protein expression analysis with flow cytometry (FC)

Flow cytometry (FC) enables protein expression analysis via specific antibody binding labelled with a fluorescence dye. With this method, the maturation status of differentiated NSCs-derived from hiPSCs and NSC spheroids was evaluated. NSC spheroids were dissociated by incubating them with pre-warmed Accutase (Fisher Scientific, Schwerte, Germany) at 37 °C and 5% CO<sub>2</sub> for 5 minutes, followed by mechanical dissociation using pipetting. Dissociated cells were centrifuged at 400 x g for 3 min. A cell pellet of 1x10<sup>6</sup> cells was resuspended in 300  $\mu$ l BD Fixation Buffer (BD Biosciences, Heidelberg, Germany) and incubated at 4 °C for 30 min. Cells were permeabilised by washing twice with 1 ml 1x BD Perm/Wash buffer for 3 min. After centrifugation at 400 x g for 3 min, the supernatant was discarded, and cells were resuspended in 100  $\mu$ l filtrated FC staining buffer containing 2% FBS, 15.4 mM sodium azide and 0.5 mM EDTA (all Fisher Scientific, Schwerte, Germany). Cells were split into unstained control, isotype control, and staining samples. Isotype controls and samples were incubated with the isotype markers or direct antibodies (Tab. 10) for 30 min at 4 °C in the dark. Then, all controls and samples were washed and resuspended in 300  $\mu$ l FC staining buffer. The unstained controls were used to adjust the device to visualise the cell type-specific forward scatter (FSC) and side scatter (SSC) plots and to adjust the photomultiplier tube (PMT) voltages. The isotype controls served as negative controls with matching host species, IgG subclass and fluorophore of the respective primary antibody to detect unspecific antibody bindings. To analyse protein expression with antibody samples, 10,000 events were measured using the BD FACS Canto™ II flow cytometer (BD Biosciences, Heidelberg, Germany) according to the manufacturer's instructions. The data was analysed using the BD FACS Diva software (BD Biosciences, Heidelberg, Germany).

Table 10: Direct antibodies and isotype controls for FC.

<b>Antibody/Isotype</b>	<b>Volume per sample</b>	<b>Manufacturer</b>
Alexa Fluor 488 anti-human CD324 (E-cadherin)	5 $\mu$ l	BioLegend, Koblenz, GER
Alexa Fluor 488 Mouse IgG1, k Isotype Ctrl	5 $\mu$ l	BioLegend, Koblenz, GER
Alexa Fluor 488 Mouse anti-Sox2	5 $\mu$ l	BD Biosciences, Heidelberg, GER
Alexa Fluor 488 Mouse IgG2a, k Isotype Ctrl	5 $\mu$ l	BD Biosciences, Heidelberg, GER
Alexa Fluor 647 Mouse anti-Oct3/4 (POU5F1)	5 $\mu$ l	BD Biosciences, Heidelberg, GER
Alexa Fluor 647 Mouse IgG1, k Isotype Ctrl	5 $\mu$ l	BD Biosciences, Heidelberg, GER
PE Mouse anti-Nestin	5 $\mu$ l	BD Biosciences, Heidelberg, GER
PE Mouse IgG1, k Isotype Ctrl	5 $\mu$ l	BioLegend, Koblenz, GER
Per CP-CyTM 5.5 Mouse anti-Oct3/4 (POU5F1)	20 $\mu$ l	BD Biosciences, Heidelberg, GER
Per CP-CyTM 5.5 Mouse IgG1, k Isotype Ctrl	20 $\mu$ l	BioLegend, Koblenz, GER

### 3.6 Data and image processing

Image processing was performed by open-source ImageJ1.52a, Inkscape 1.3 and NIS Elements AR (Nikon, Düsseldorf, Germany). Data processing was done by Microsoft Office Excel Professional Plus 2016 and OriginPro 2020.

Unless otherwise stated, all data have been obtained from at least three independent experiments, i.e. three biological replicates ( $N=3$ ) and three technical replicates ( $n=3$ ). The mean values were presented as  $\bar{x} \pm$  standard deviation ( $SD$ ). The Student's  $t$ -test was used to compare differences between two groups.  $P < 0.05$  was considered statistically significant (\* $p < 0.05$ , \*\* $p < 0.01$ , \*\*\* $p < 0.001$ ).

## 4 Results

Next-generation biobanking of living diagnostically and therapeutically relevant cell systems has become increasingly popular. In this context, the long-term preservation of 3D cell systems, like primary tissues or stem cell-derived organoids, is an emerging research field. Easy and constant access to ready-to-use, functional 3D cell systems is essential for on-demand availability in biotechnological research and medical applications. Hence, the establishment of efficient and standardised cryopreservation protocols for 3D cell models is required. The aim is to examine and understand the underlying factors of cryo-related effects in 3D cell systems with quality and functional analyses. By gaining an extended understanding of biological mechanisms after cryopreservation, new, innovative processes can be established.

In this thesis, the effects of cryopreservation on precursor organoids, like the neural stem cell (NSC) and hepatocyte progenitor (HP) spheroids, as well as heterogeneous matured hepatocyte-like cell (HLC) organoids, were analysed comparatively. The focus was to elucidate the impact of different organoid diameters and volumes on cryo-induced injury mechanisms. In this context, the cryo effects on cell structures and CPA diffusion kinetics were analysed in detail.

### 4.1 Comparative investigations on cryopreservation effects on metabolic properties in precursor organoids of defined volumes

In this work, human induced pluripotent stem cells (hiPSCs) derived NSC spheroids serve as a reproducible, legally and ethically less restricted precursor of matured human brain organoids. In the first step, the differentiation of NSCs was established and static and dynamic 3D generation processes were comparatively analysed. Subsequently, the metabolic effects of the incubation of different cryopreservation media before cryopreservation on NSC spheroids were investigated, as it is crucial for effective cryopreservation to ensure sufficient distribution of CPAs throughout the 3D cell models while minimising cytotoxic effects on the peripheral cell layers. In the next step, the cryo-induced metabolic effects in NSC spheroids with different volumes were analysed in detail after thawing.

#### 4.1.1 Differentiation and 3D generation techniques of NSC spheroids

The differentiation of hiPSCs to NSCs was induced by the neural induction medium following the protocol of Reinhardt et al. 2013. The hiPSCs line UKKi011-A was differentiated into ectodermal cells via EBs. Stimulating the WNT and SHH signalling pathway induces the formation of epithelial cells with neural progenitor characteristics. During further maturation, NSCs arise from neural rosettes formed by the EBs. After the differentiation of UKKi011-A to NSCs, the neural fate was verified by flow cytometry (FC) analysis for cell passage P6 and P14 (Fig. 11 A). The pluripotency of NSCs, indicated by OCT3/4 expression, was decreased to 2.5% positive cells for both passages. In comparison, over 96% of the differentiated cells from both passages were positive for the neural markers Sox2 and Nestin. Additionally, the neural status and cell

proliferation of NSC spheroids (P16) were verified by ICC staining of Nestin and Ki67 (Fig. 11 B). After verifying the neural fate of the differentiated NSCs, spheroids were generated statically with ULA 96-well plates and dynamically with the CERO 3D bioreactor. The proliferation was determined by tracking the spheroids' morphological area over time. Due to high circularity ( $\psi > 0.9$ ), the diameters and volumes were calculated by the spheroid areas. The proliferation rate of NSC spheroids, i.e. the increase of volume over time, which were cultured in ULA plates was reproducible across three different passages for each initial cell number (Fig. 11 C). Small spheroids were defined as spheroids with an initial cell number of 2,500 NSCs/well, resulting in a mean diameter of  $\bar{x} = 323 \mu\text{m} \pm 15 \mu\text{m}$  after 5 d of cultivation. To generate medium or large spheroids, the initial cell number was 7,500 NSCs/well or 12,000 NSCs/well, resulting in mean diameters of  $\bar{x} = 463 \mu\text{m} \pm 12 \mu\text{m}$  or  $\bar{x} = 613 \mu\text{m} \pm 12 \mu\text{m}$ . Unless otherwise stated, these conditions consistently remained the same in the following sections. The mean volumes were 25-fold higher in medium and 318-fold higher in large spheroids compared to small spheroids after 5 d of cultivation. After cultivation for 12 d, the mean volumes of the medium and large spheroids were only 2-fold and 4-fold higher compared to the small spheroids. In comparison, NSC spheroids generated in a CERO 3D bioreactor reached a mean diameter of  $471 \mu\text{m} \pm 67 \mu\text{m}$  after 5 d and  $772 \mu\text{m} \pm 65 \mu\text{m}$  after 12 d. The coefficient of determination  $R^2$  of the regression of the mean values from five passages cultured in the CERO 3D bioreactor was 0.90. The reproducibility of spheroids cultured in ULA plates was higher, causing  $R^2$  values of 0.944 for 2,500 NSCs/well, 0.990 for 7,500 NSCs/well and 0.963 for 12,000 NSCs/well initial cell number.

#### 4.1.2 Effects of cryopreservation media diffusion in NSC spheroids

The effect of cryopreservation media incubation before cryopreservation was evaluated by analysing the NSC spheroid morphology, viability, and expression of genes and proteins. Fig. 12 depicts representative microscopic images of NSC spheroids, cultured for 5 d with different initial cell numbers, after incubation in CryoStor CS10 for 5 min, 15 min and 30 min. After incubation for 5 min, the measured mean spheroid areas and, correspondingly, the spheroid diameters were decreased by  $-25\% \pm 5\%$  in small,  $-22\% \pm 5\%$  in medium and  $-23\% \pm 4\%$  in large spheroids compared to non-treated spheroids. After incubation for 30 min, the morphology and circularity were not changed. The mean diameters were slightly increased again to  $-22\% \pm 5\%$  in small,  $-18\% \pm 4\%$  in medium and  $-22\% \pm 5\%$  in large spheroids compared to non-treated spheroids. Analogue morphology analyses were carried out and quantified for 14 different cryopreservation media (NSC medium with 20% DMSO, 10% DMSO, 5% DMSO, 2% DMSO, 20% EG, 10% EG, 20% glycerol, 10% glycerol, 0.3 M trehalose or 0.3 M sucrose and 100% Cryostor CS10, 100% HypoThermosol FRS, VS1, VS2). The mean diameters of spheroids after media incubation were normalised to the mean diameters of spheroids without treatment. Thus, mean diameter changes according to each media composition were assessed for small (Fig. 13 A), medium (Fig. 13 B) and large (Fig. 13 C) spheroids. Similar trends in relative diameter changes over

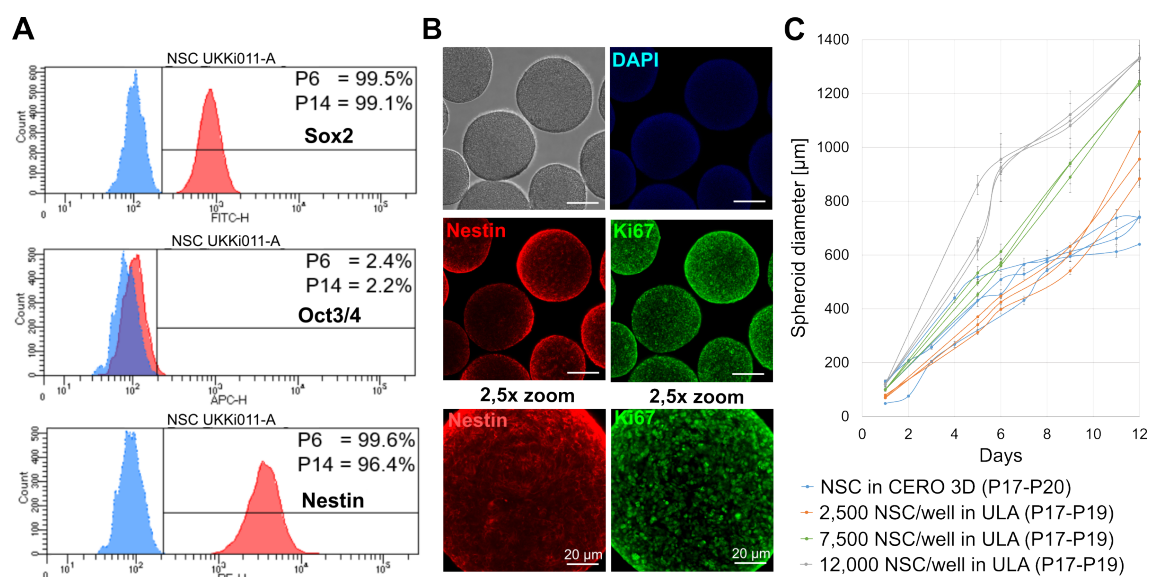


Figure 11: **Differentiation of UKKi011-A into NSCs and proliferation of NSC spheroids.** (A) FC analysis of differentiated NSCs (cell passage 6 (P6) and cell passage 14 (P14) from UKKi011-A. NSC state was verified by Sox2 and Nestin markers. (B) ICC analysis of NSC spheroids cell passage 16 (P16) was used to analyse the NSC state by Nestin and proliferation by Ki67 marker expression. (C) Spheroid diameters as an indicator of proliferation rates of different passages of NSC spheroids in the CERO 3D bioreactor and ULA plates.

incubation time were observed for all spheroid volumes. After 5 min incubation in permeable CPAs (DMSO and EG), the relative spheroid diameters were decreased compared to the non-treated control. With increasing incubation time, the diameters were again linearly increased by about 10-20% after 30 min. The incubation with non-permeable disaccharides trehalose and sucrose caused an opposite trend. After 5 min incubation, the relative diameters were decreased by about 20% and after 30 min incubation by 30-35%. The incubation with both glycerol concentrations caused a diameter decrease of about 20% in all spheroids. After incubating with the commercial media CryoStor CS10 and HypoThermosol FRS, a constant decrease in diameter of about 20-25% within 30 min was observed. The incubation with VS1, containing 10% DMSO and 10% EG, caused an initial diameter decrease of about 10-15% after 5 min and a subsequent equal increase for all diameters. In contrast, after the incubation with VS2, containing 30% 1 M sucrose, 20% DMSO and 20% EG, the relative diameters of small spheroids were decreased over incubation time by 15% after 5 min to 28% after 30 min. The relative diameters of medium spheroids were constantly decreased by 30-35% and those of large spheroids by 15%.

Additionally, the mean cell viability values of NSC spheroids after cryopreservation media incubation were normalised to non-treated controls. As measured by ATP activity, the relative cell viability provided information about the influence of a 30 min cryopreservation media incubation on ATP production in NSC spheroids. Fig. 14 shows the relative cell viability values of NSCs spheroids with different initial volumes after cryopreservation media incubation. Comparing different DMSO concentrations, the mean relative viability after incubation in 10%, 5%

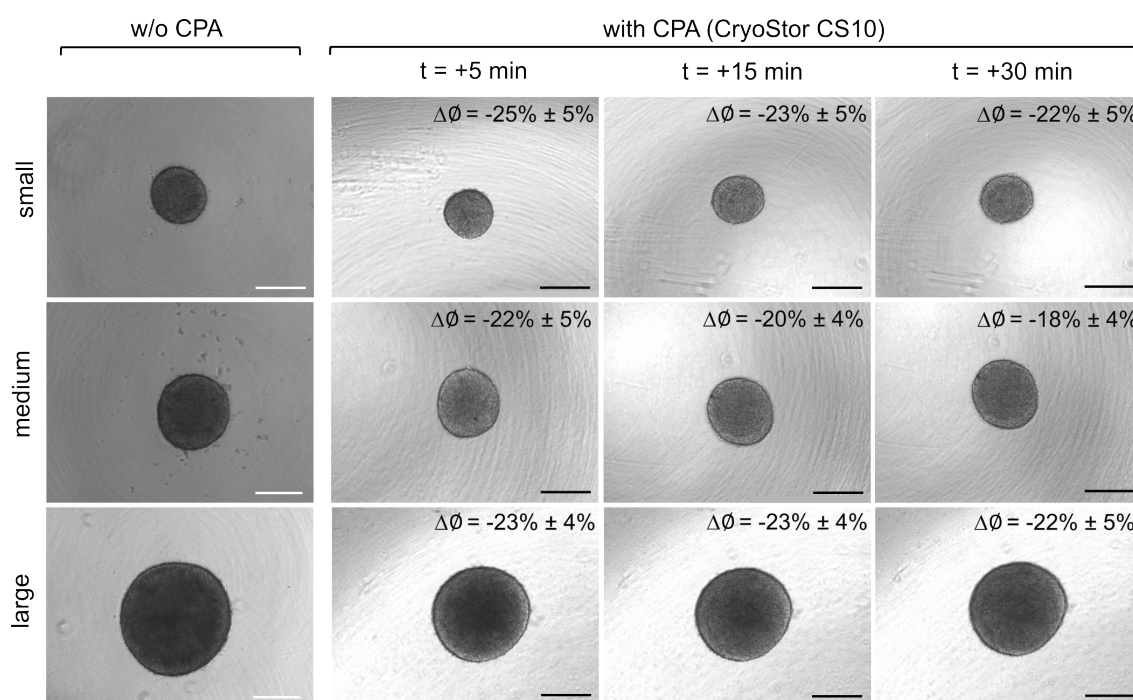


Figure 12: **Representative morphological characterisation of small, medium and large NSC spheroids without (w/o) and with incubation in CryoStor CS10.** Mean spheroid diameter changes ( $\Delta\emptyset$ ) compared to non-treated control were determined after cryopreservation media incubation for 5 min, 15 min and 30 min. The quantification of the relative diameter analyses with all cryopreservation media is shown in Fig. 13; scale bar represents 300  $\mu\text{m}$ , N=3, n=4-5.

and 2% DMSO decreased with increasing spheroid volumes. Small spheroids have a relative cell viability of 88-94%, whereas the large spheroids exhibited a mean viability of 60% with 10% DMSO, 86% with 5% DMSO and 65% with 2% DMSO. After incubation in 20% DMSO, the trend was contrary, with lower relative cell viability in small spheroids (71%) than in medium (77%) or large (86%) spheroids. Regarding the relative cell viability after incubation with EG, viability values ranged between 90% for medium spheroids with 20% EG and 40% for large spheroids with 10% EG. In contrast, the relative cell viability after glycerol incubation only varied between 85% for small spheroids with 20% glycerol and 71% for medium spheroids with 10% glycerol. Striking were the low relative cell viability values after incubation with disaccharides. The minimum relative value was 29% for large spheroids with trehalose, and the maximum was 62% for small spheroids with sucrose. The lowest relative cell viability was measured after incubating with HypoThermosol FRS, with values of 28%. Besides the ATP-based viability analysis, active esterases in viable cells of small spheroids were investigated using the viability staining with FDA/EtB. Spheroids were analysed after the incubation in representative cryopreservation media with permeable CPA (10% DMSO) or impermeable CPA (0.3 M sucrose) and in a commercial medium (CryoStor CS10). In comparison to the non-treated control, no differences in viability could be observed (Fig. 14 B).

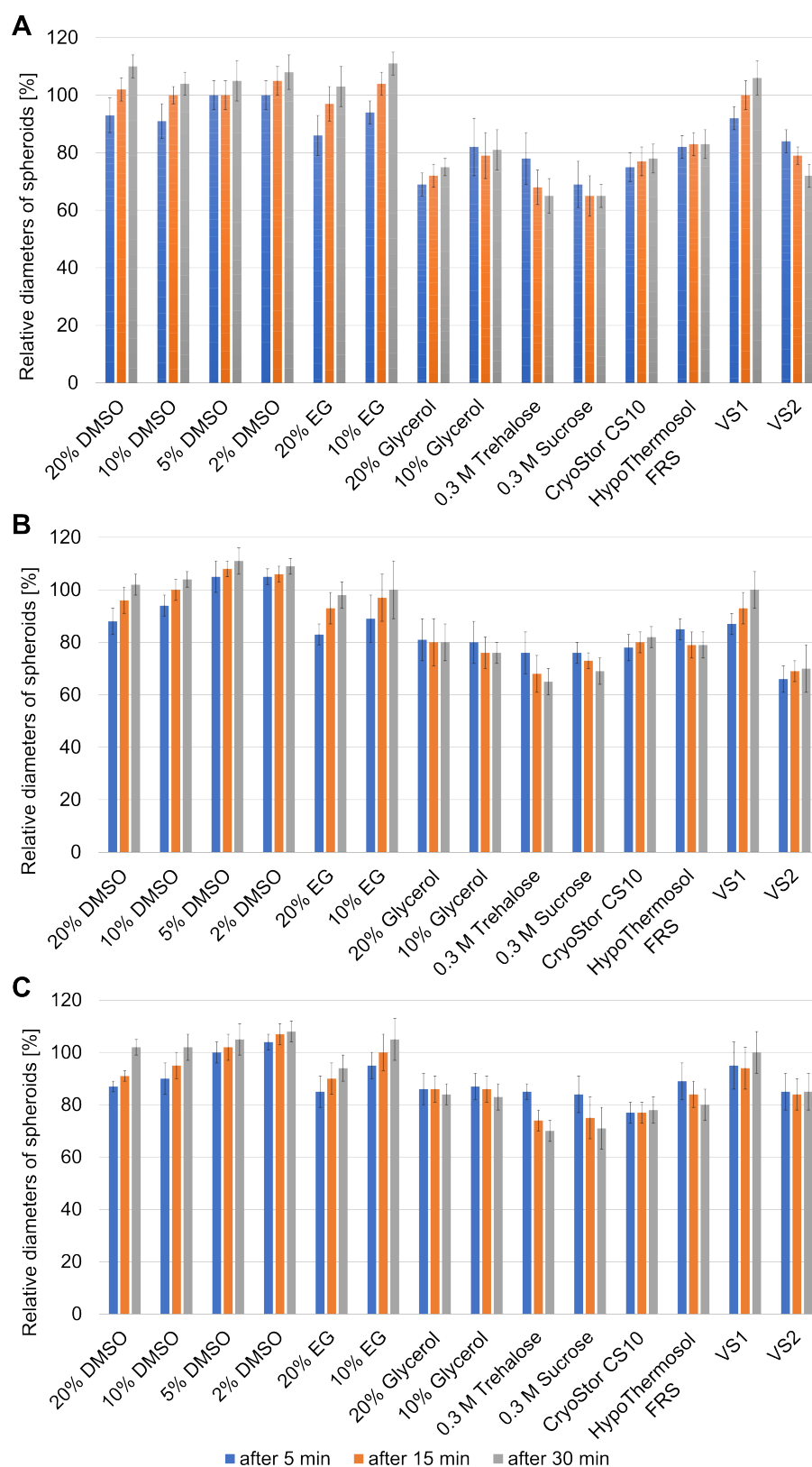


Figure 13: **Relative mean diameters of NSC spheroids after incubating for 5 min, 15 min and 30 min in different cryopreservation media.** The mean diameters of (A) small ( $\text{\O} 300 \mu\text{m}$ ), (B) medium ( $\text{\O} 450 \mu\text{m}$ ) and (C) large ( $\text{\O} 600 \mu\text{m}$ ) spheroids after media incubation were normalised to the non-treated controls,  $N=3$ ,  $n=4-5$ .

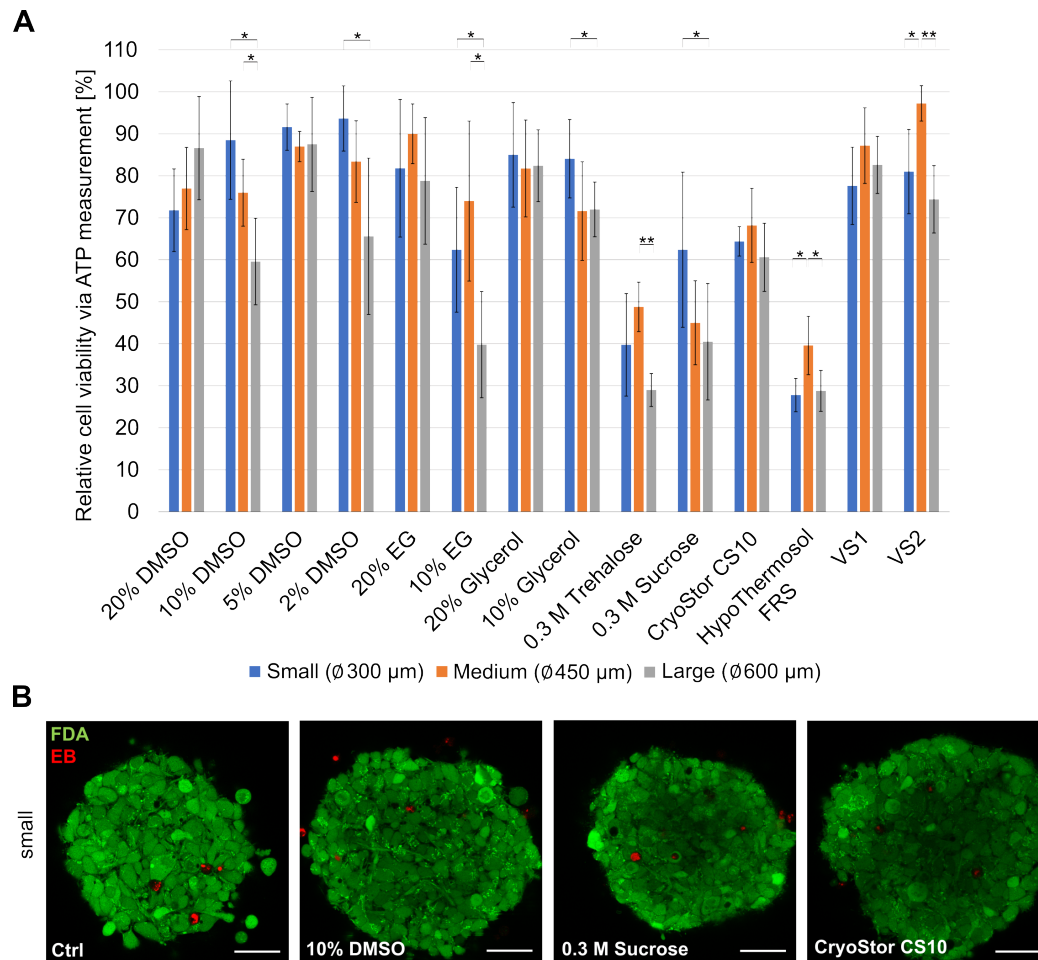
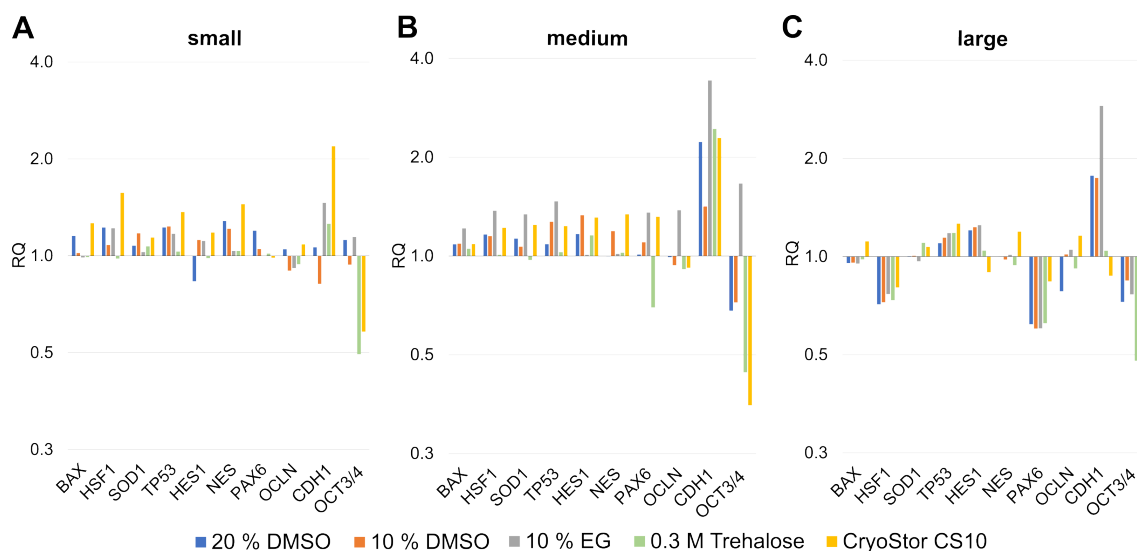


Figure 14: **Relative mean cell viability of NSC spheroids after 30 min incubation in different cryopreservation media.** (A) The mean viability values of small, medium and large spheroids after cryopreservation media incubation were normalised to non-treated controls,  $N=3$ ,  $n=3-5$ . (B) Viability staining with FDA/EtB of small spheroids without and with cryopreservation media incubation (10% DMSO, 0.3 M sucrose and CryoStor CS10); scale bar represents 50  $\mu\text{m}$ ,  $N=2-3$ ,  $n=3$  ( $t$ -test, \* $p$  value < 0.05, \*\* $p$  value < 0.01).

The impact of cryopreservation media was further evaluated with gene and protein expression analyses. Therefore, NSC spheroids with different diameters were incubated in cryopreservation media with permeable CPAs (20% DMSO, 10% DMSO and 10% EG) or non-permeable CPA (0.3 M trehalose) and in commercially available media (CryoStor CS10) for 30 min. Fig. 15 depicts the results of the RT-qPCR analysis. None of the stress markers (*BAX*, *HSF1*, *SOD1* and *TP53*) and none of the neural markers (*HES1*, *NES* and *PAX6*) were significantly changed ( $\geq 2$ -fold change) for all spheroids. A striking aspect here was the significant increase of *CDH1* expression in medium spheroids after the incubation in 20% DMSO (2.2-fold), 10% EG (3.4-fold), 0.3 M trehalose (2.4-fold) and CryoStor CS10 (2.3-fold) (Fig. 15 B). In small spheroids, the cadherin marker expression (*CDH1*) was significantly increased by 2.2-fold after the incu-

bation in CryoStor CS10 (Fig. 15 A). In large spheroids, the *CDH1* expression was significantly increased by 2.9-fold after the incubation in 10% EG (Fig. 15 C). Another striking aspect is the significant 0.4-fold expression decrease of *OCT3/4* in medium spheroids after incubation in 0.3 M trehalose and CryoStor CS10.



**Figure 15: Gene expression analysis of NSC spheroids after 30 min incubation in cryopreservation media.** The gene expression of different stress (*BAX*, *HSF1*, *SOD1* and *TP53*), neural (*HES1*, *NES* and *PAX6*), cell adhesion (*OCLN* and *CDH1*) and pluripotency marker (*OCT3/4*) were analysed by RT-qPCR after the incubation in cryopreservation media (20% DMSO, 10% DMSO, 10% EG, 0.3 M trehalose and CryoStor CS10). *GAPDH* and *HPRT1* served as housekeeping markers. Data is shown as fold-change (RQ) normalised to the calibrator, the non-treated spheroids, N=3, n=3.

To verify the significant gene expression changes of *CDH1* and *OCT3/4*, the protein expressions of these markers were investigated by flow cytometry. In addition, the expression of the neural marker Nestin was analysed as a positive control (Fig. 16). After the incubation of 30 min in cryopreservation media (20% DMSO, 10% DMSO, 10% EG, 0.3 M trehalose and CryoStor CS10), all NSC spheroids showed high protein expression levels of Nestin with > 90% positive cells and low expressions of *OCT3/4* with < 1% positive cells compared to the untreated, unstained control. The relative values for the E-cadherin marker ranged with high standard deviations. The lowest mean values were measured for medium spheroids after incubation in 10% EG with only 30% positive cells (Fig. 16 C). The highest mean values were observed for small spheroids after incubation in 0.3 M trehalose with 78% positive cells (Fig. 16 B). However, no significant protein expression changes were detected between the stained, untreated control and the cryopreservation media-treated spheroids.

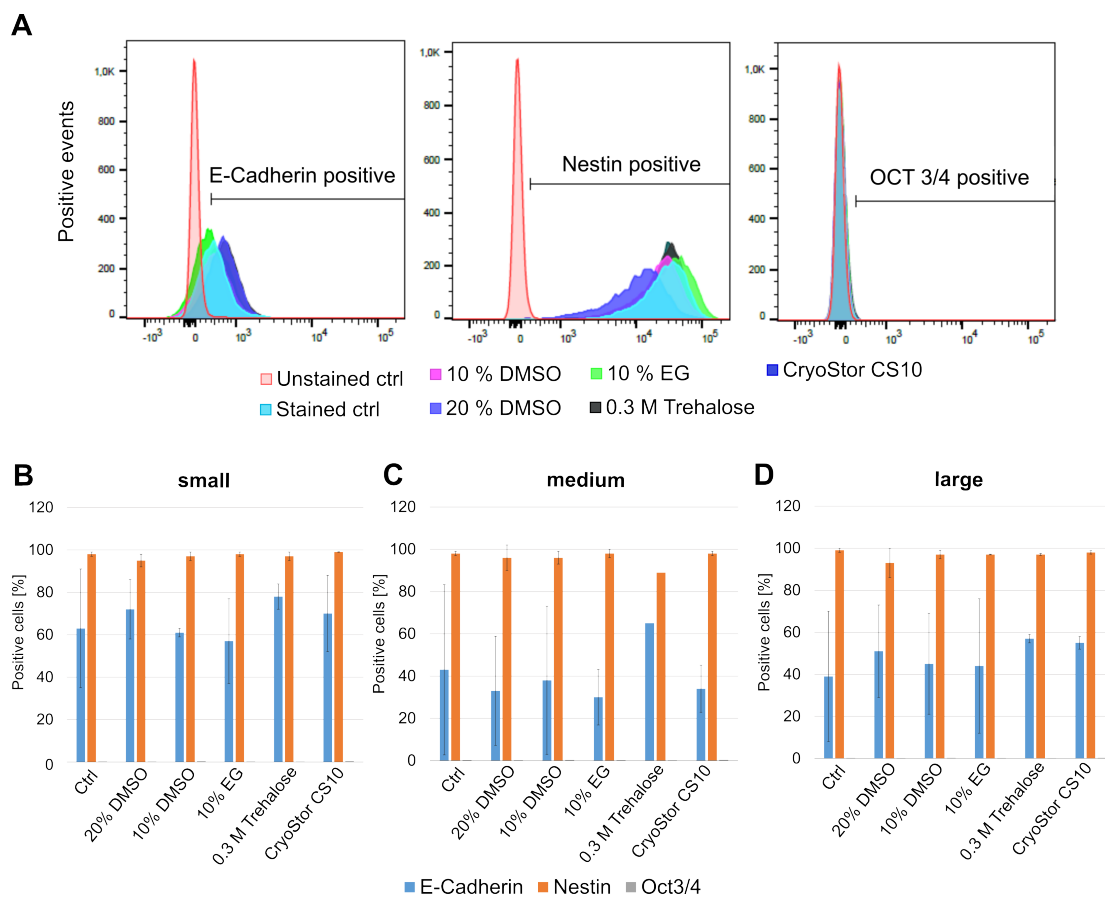


Figure 16: **Quantitative protein expression analysis of NSC spheroids after 30 min incubation in cryopreservation media.** (A) Representative graphs of fluorescence intensity distribution for E-cadherin, Nestin and OCT3/4 positive cells. The analysis was carried out by flow cytometry with 10,000 cells (events) of small spheroids after incubating in cryopreservation media. The relative mean fluorescence signal of E-Cadherin, Nestin and OCT3/4 positive cells was quantified for (B) small ( $\varnothing$  300  $\mu\text{m}$ ), (C) medium ( $\varnothing$  600  $\mu\text{m}$ ) and (D) large spheroids compared to unstained, untreated control, N=1-3, n=3.

#### 4.1.3 Cryo-induced metabolic effects in NSC spheroids of defined volumes

NSC spheroids were cultured for 5 d in ULA plates or the CERO 3D bioreactor. The conditions for slow-rate freezing of spheroids were adapted from single-cell protocols. NSC spheroids cultured in the ULA plate with initial cell numbers of 2,500 NSCs/well, 7,500 NSCs/well and 12,000 NSCs/well were frozen and recovered as single spheroids directly in the plate. Spheroids generated in the CERO 3D bioreactor were frozen in cryovials and recovered in the CERO 3D bioreactor. After thawing, the spheroids were recovered for 7 d, i.e., they were cultured for up to 12 d in total (Fig. 17 and 18). All spheroids, before freezing and after thawing (a.t.), showed a regular and spherical shape with a constant mean circularity of  $\psi > 0.97$ . Only 24 h a.t., the circularity decreased to  $\psi = 0.93 \pm 0.03$  for small spheroids and  $\psi = 0.89 \pm 0.05$  for medium and large spheroids. This is related to the detachment of the peripheral cell layer, which was observed for all spheroid diameters 24 h and 3 d a.t.

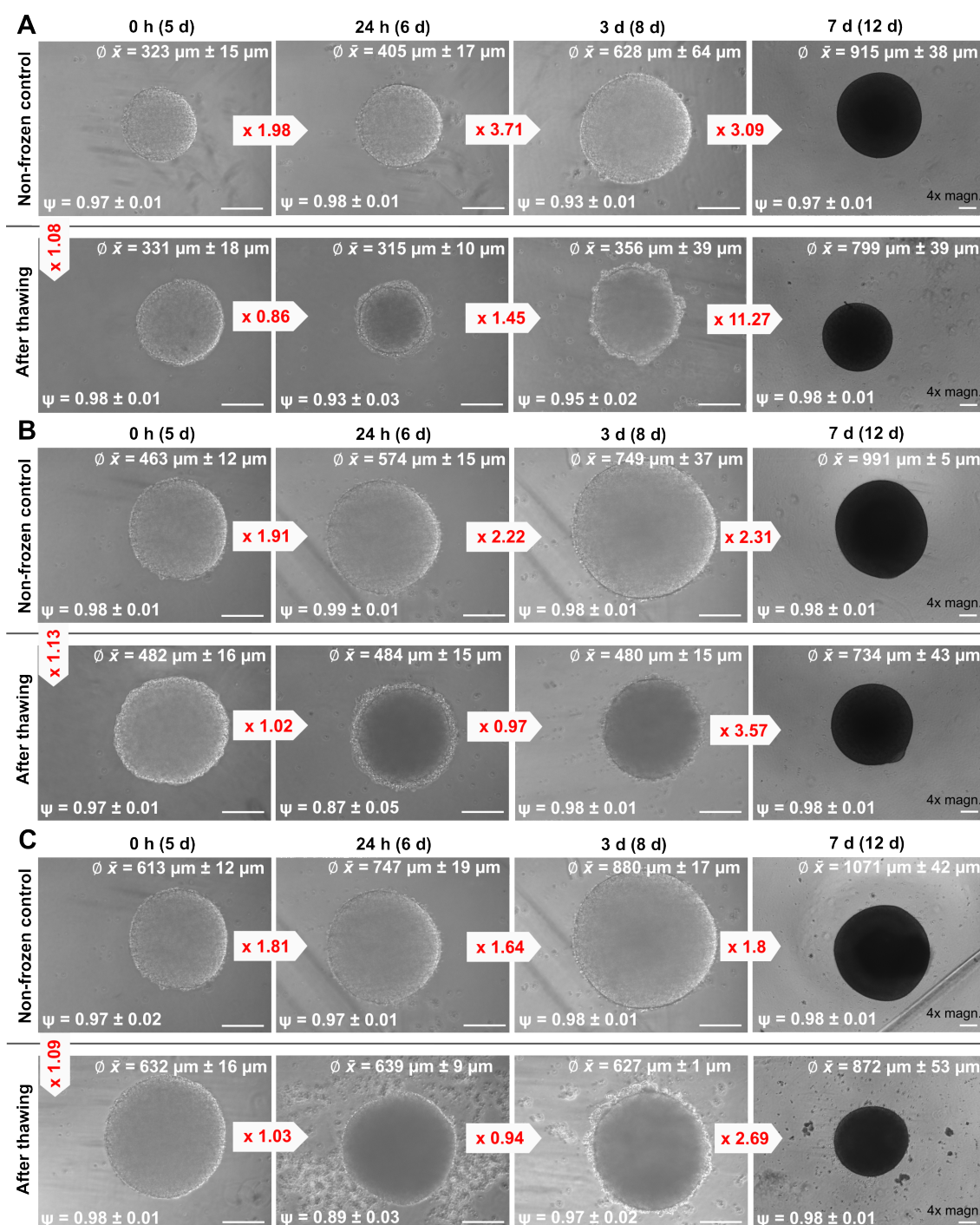


Figure 17: Morphological characterisation of small, medium and large NSC spheroids nfc and a.t., cultured and recovered in ULA plates. The initial cell numbers were (A) 2,500 NSCs/well, (B) 7,500 NSCs/well and (C) 12,000 NSCs/well. Mean spheroid diameters ( $\bar{x}$ ) and circularity ( $\psi$ ) were determined at different cultivation times in nfc and a.t. After 0 h to 3 d recovery, spheroids are shown with 10-fold and after 7 d with 4-fold magnification (magn.). The respective-fold change of mean spheroid volumes is indicated in red; scale bar represents 200  $\mu\text{m}$ , N=3, n=8

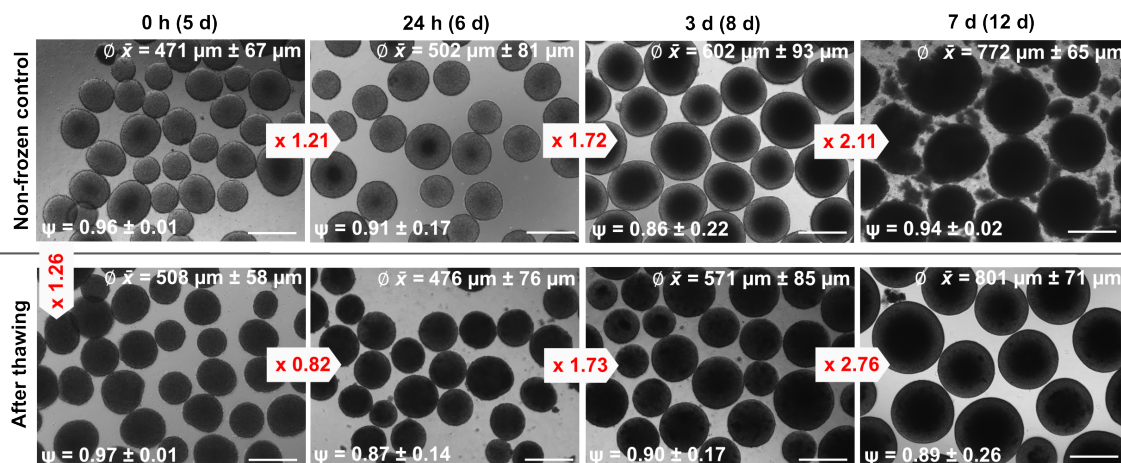


Figure 18: Morphological characterisation of NSC spheroids nfc and a.t., cultured and recovered in the CERO 3D bioreactor. The initial cell number was  $7.5 \cdot 10^5$  NSCs/ml. Mean spheroid diameters ( $\bar{x}$ ) and circularity ( $\psi$ ) were determined at different cultivation times in nfc and a.t. The respective-fold change of mean spheroid volumes is indicated in red; scale bar represents  $500 \mu\text{m}$ ,  $N=3$ ,  $n=5$ .

To quantify these morphologically analysed data, the mean volumes of non-frozen controls (nfc) and spheroids after thawing were calculated by spheroid areas and normalised to values of nfc before freezing after 5 d of cultivation. Therefore, the spheroids were assumed to be spherical, and their mean volumes were determined by the areas measured with microscopic images (see section 3.2.1). The relative volumes in Fig. 19 A show the progression of volume changes of spheroids to clarify the differences between nfc and after thawing at the respective point in time. Immediately after thawing, the relative volumes of the spheroids were increased by 1.08-fold for small, 1.13-fold for medium and 1.09-fold for large spheroids compared to nfc, but without statistically significant difference. After further recovery for 24 h, 3 d and 7 d, the relative volumes were significantly decreased in small, medium and large spheroids after thawing compared to respective nfc at the same time. During the recovery between 0 h and 24 h a.t., the mean volumes were 0.14-fold reduced in small and not changed in medium and large spheroids. In comparison, the proliferation of nfc was increased over time, and the volumes were altered by 1.98-fold in small, 1.91-fold in medium and 1.81-fold in large spheroids between 5 d and 6 d. However, the mean volumes of the spheroids after thawing were significantly increased again between 3 h and 7 d a.t. by 11.27-fold in small, 3.57-fold in medium and 2.69-fold in large spheroids. After a cultivation time of 12 d, the small spheroids reached 0.67-fold volume, the medium spheroids 0.41-fold and the large spheroids 0.54-fold a.t. compared to the nfc. NSC spheroids, cultured for 5 d in the CERO 3D bioreactor, showed a mean diameter of  $\bar{x} = 471 \mu\text{m} \pm 67 \mu\text{m}$  (Fig. 18). Compared to spheroids from the ULA plate, the homogeneity is decreased, indicated by high standard deviations at all cultivation times ( $SD > 58 \mu\text{m}$ ). Additionally, the circularity is reduced with  $\psi < 0.97$  and the maximum mean diameter after 12 d of cultivation was  $\bar{x} = 772 \mu\text{m} \pm 65 \mu\text{m}$ . However, the cell debris was reduced after thawing, and only a slight

decrease in volume of about  $20 \cdot 10^6 \mu\text{m}^3$  was observed between 24 h and 3 d a.t. compared to nfc (Fig. 19 B). No significant differences between relative volumes of nfc and spheroids after thawing were detected at all respective points in time (Fig. 19 C).

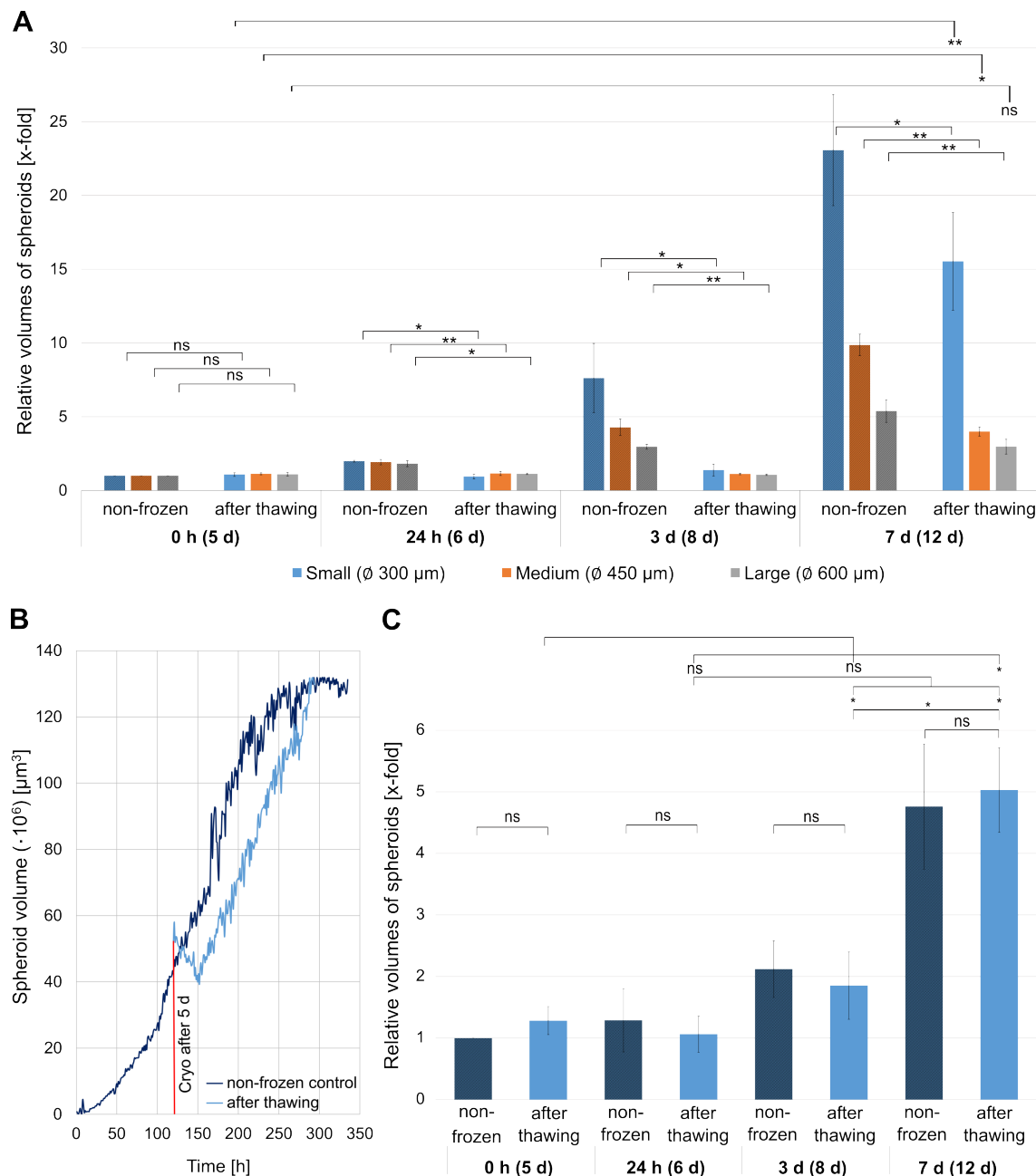


Figure 19: **Relative volumes of NSC spheroids nfc and a.t., cultured and recovered in ULA plates and the CERO 3D bioreactor.** The mean volumes of nfc and spheroids a.t. at different times were normalised to nfc after 5 d of cultivation. (A) Relative volumes of spheroids from ULA plate. The values were calculated respectively for small, medium and large spheroids,  $N=3$ ,  $n=8$ . (B) Volume tracking of spheroids nfc and a.t. over time in the CERO 3D bioreactor,  $N=4$ ,  $n>100$ . (C) Relative volumes of spheroids from CERO 3D bioreactor,  $N=3$ ,  $n=5$  ( $t$ -test, ns: not significant, \* $p$  value  $< 0.05$ , \*\* $p$  value  $< 0.01$ ).

The viability of NSC spheroids after thawing was evaluated by ATP measurements using the CellTiter-Glo 3D Cell Viability Assay, by viable cell number measurements based on membrane integrity using the NucleoCounter and by viability staining. The mean cell viability values of nfc and spheroid after thawing were normalised to values of nfc before freezing after 5 d of cultivation. The relative values in Fig. 20 - 22 show the progression of the viability of nfc and spheroids after thawing during the cultivation and recovery. The increase in relative viability of nfc over cultivation time coincided with the rise in relative volumes over time derived from the morphological analysis. Hence, relative cell viability analyses of nfc support the statement of exponential proliferation for small, linear proliferation for medium and logarithmic proliferation for large spheroids. This trend could not be observed in spheroids after cryopreservation and thawing. Regarding the relative viability measured by ATP activity, a significant decrease in metabolic activity was observed in all spheroids immediately after thawing compared to nfc. After the recovery of 3 d, the relative viability was significantly decreased under 0.7 for all diameters compared to nfc. In contrast, the values in nfc were increased 4.3-fold  $\pm$  1.04 in small, 2.5-fold  $\pm$  0.56 in medium and 1.7-fold  $\pm$  0.11 in large spheroids. Despite the decrease in viability at 0 h to 3 d a.t., a recovery was detected after 7 d. The relative cell viability was significantly increased for all diameters compared to 0 h a.t. (Fig. 20).

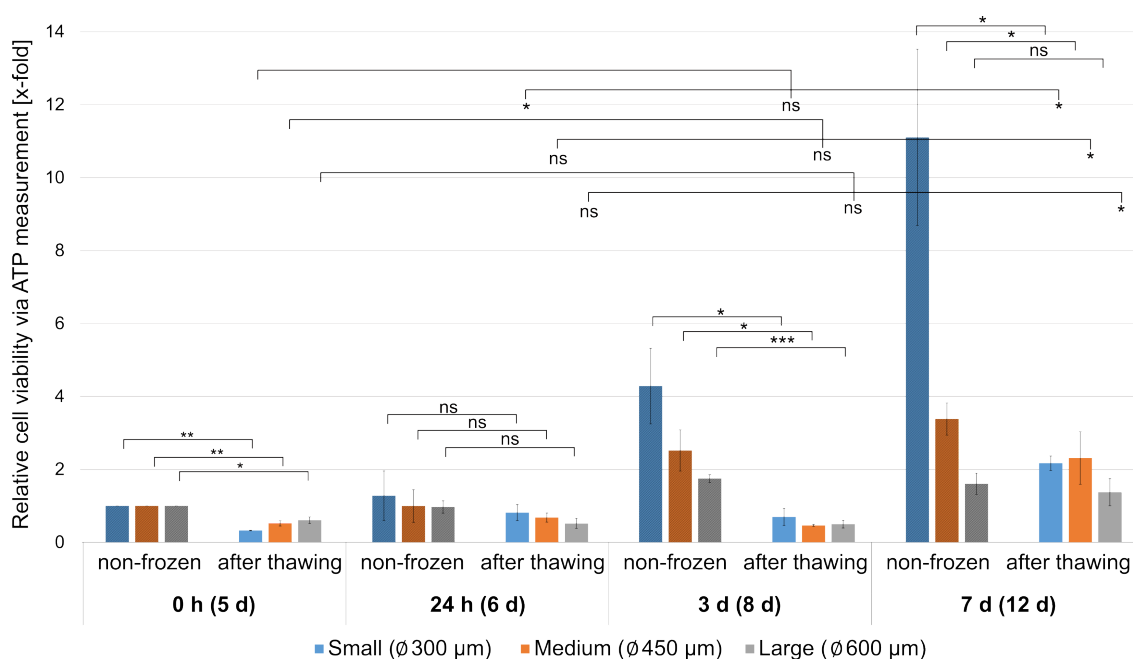


Figure 20: **Relative cell viability of NSC spheroids nfc and a.t. analysed by ATP measurement, cultured in ULA plates.** The mean cell viability of nfc and spheroids a.t. at different times were normalised to nfc after 5 d of cultivation, N=3, n=3 (*t*-test, ns: not significant, \**p* value < 0.05, \*\**p* value < 0.01, \*\*\**p* value < 0.001).

Concerning the analysis of the relative viability by membrane integrity, a similar trend to the values based on ATP measurement was observed (Fig. 21). After recovery of 24 h, small and large spheroids after thawing showed a very significant difference in the relative viability

measured by membrane integrity to nfc. An increase in proliferation was observed after the recovery of 7 d with a rise in relative viability values of 2.5-fold  $\pm$  0.96 in small, 1.8-fold  $\pm$  0.23 in medium and 1.3-fold  $\pm$  0.09 in large spheroids.

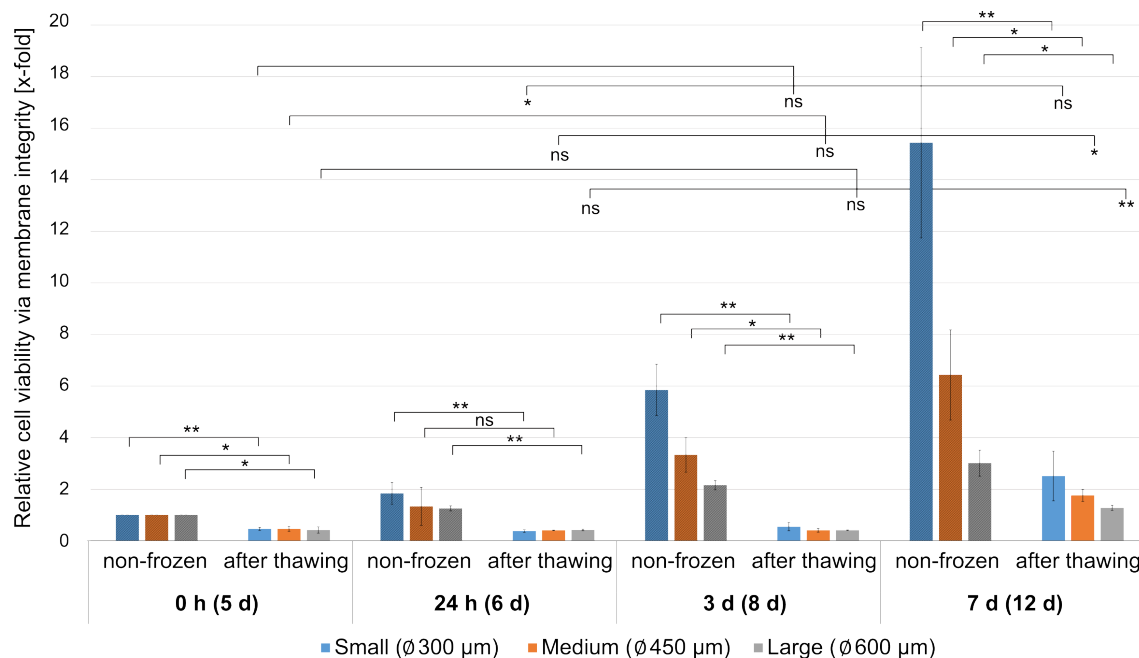


Figure 21: **Relative cell viability measured by membrane integrity of NSC spheroids nfc and a.t., cultured in ULA plates.** The mean relative viability of nfc and spheroids a.t. at different times were normalised to nfc after 5 d of cultivation, N=3, n=3 (*t*-test, ns: not significant, \**p* value < 0.05, \*\**p* value < 0.01).

In spheroids cultured in the CERO 3D bioreactor, the relative cell viability values measured by ATP activity and membrane integrity were decreased by about 50% at 0 h a.t. compared to nfc (Fig. 22). The cell viability increased significantly over time and ran linear to 1-fold  $\pm$  0.17 at 24 h a.t., to 1.7-fold  $\pm$  0.15 at 3 d a.t. and to 3.1-fold  $\pm$  0.2 at 7 d a.t. The progression of the values determined by membrane integrity analysis was comparable, except that the value 24 h a.t. was not significantly increased compared to 0 h a.t.

With the viability staining, a high number of viable cells was detected for small and large nfc compared to the assay controls (Fig. 23 A). During the recovery phase after thawing, the number of apoptotic cells was increased (Fig. 23 B). Immediately after thawing, an apoptotic peripheral cell layer of  $37 \mu\text{m} \pm 2.1 \mu\text{m}$  was observed for small spheroids. For large spheroids, an apoptotic peripheral cell layer of  $35 \mu\text{m} \pm 3.8 \mu\text{m}$  was detected. The width of the peripheral apoptotic cell layer decreased during the recovery of 7 d. As for the volume and viability analysis, the increased proliferation between 3 d and 7 d a.t. was also detected. To quantify these results, the number of apoptotic cells analysed by caspase-3/7 activity using the Caspase Glo 3/7 3D Assay was normalised to the number of viable cells analysed with the CellTiter-Glo 3D Cell Viability Assay (Fig. 23 C). The ratio of viable to apoptotic cells at 24 h a.t. is 35% lower for small, 45% lower for medium and 23% lower for large spheroids compared to nfc.

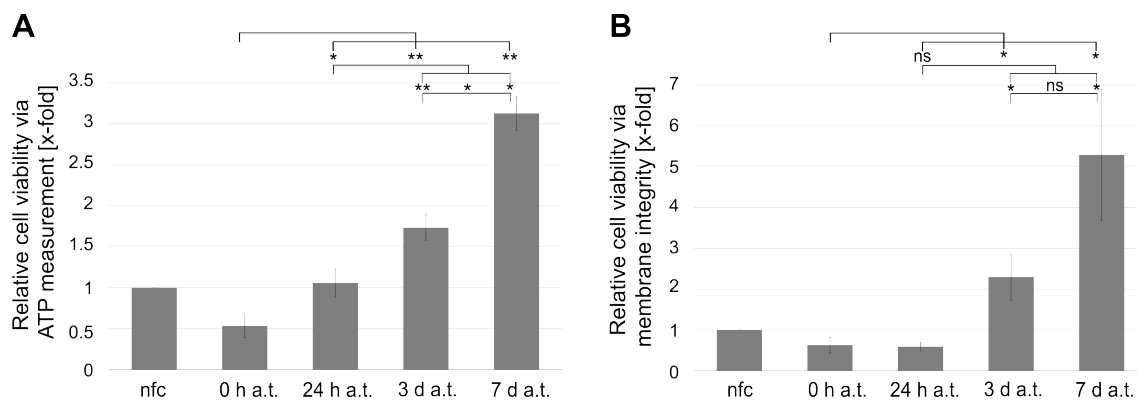


Figure 22: **Relative cell viability of NSC spheroids nfc and a.t., cultured in the CERO 3D bioreactor.** The viability values of nfc and spheroids a.t. at different times, measured by (A) ATP activity and (B) membrane integrity, were normalised to nfc after 5 d of cultivation, N=3, n=3 (*t*-test, ns: not significant, \**p* value < 0.05, \*\**p* value < 0.01).

RT-qPCR was performed to further investigate the effects of slow freezing on the genetic level in NSC spheroids. The gene expression of neural, cell adhesion, stress, and pluripotency markers were investigated (Fig 24). Therefore, nfc and spheroids after thawing were analysed at different cultivation and recovery times (0 h nfc/a.t., 24 h nfc/a.t., 3 d nfc/a.t., 7 d nfc/a.t.). The nfc after 5 d of cultivation served as calibrator sample. No significant expression changes were observed for the neural or stress markers. For the adhesion marker, only *CDH1* was 5.8-fold higher expressed at 24 h a.t. compared to the calibrator. Striking were the significantly higher expressions ( $\geq 2$ -fold change) of the pluripotency marker *OCT3/4* in the samples at 24 h nfc (7.7-fold), 24 h a.t. (20.9-fold), 3 d nfc (23.1-fold), 3 d a.t. (12.7-fold), 7 d nfc (18.1-fold) and 7 d a.t. (43.0-fold).

In the next step, the effect of Rho-associated protein kinase (ROCK) inhibitors Chroman 1 and Y-27632 on the viability of NSC spheroids after cryopreservation was analysed by ATP measurement and caspase-3/7 activity. Relative cell viability and relative apoptosis of NSC spheroids with different volumes were measured at various times after thawing (0 h a.t., 24 h a.t., 3 d a.t., 7 d a.t.) (Fig. 25). Both ROCK inhibitors were added immediately after thawing and were incubated for 24 h. Regarding the relative cell viability and apoptosis values of nfc, no significant difference was found between the samples treated with Chroman 1, Y-27632 and without additive. After thawing, spheroids with all volumes showed a decreased relative cell viability for all conditions at different times. However, no significant effect was observed between the samples with ROCK inhibitor and without additive (Fig. 25 A). The relative apoptosis values of spheroids after thawing were also not significantly changed compared to values of nfc (Fig. 25 B). No differences between the conditions with ROCK inhibitor and without additive were detected.

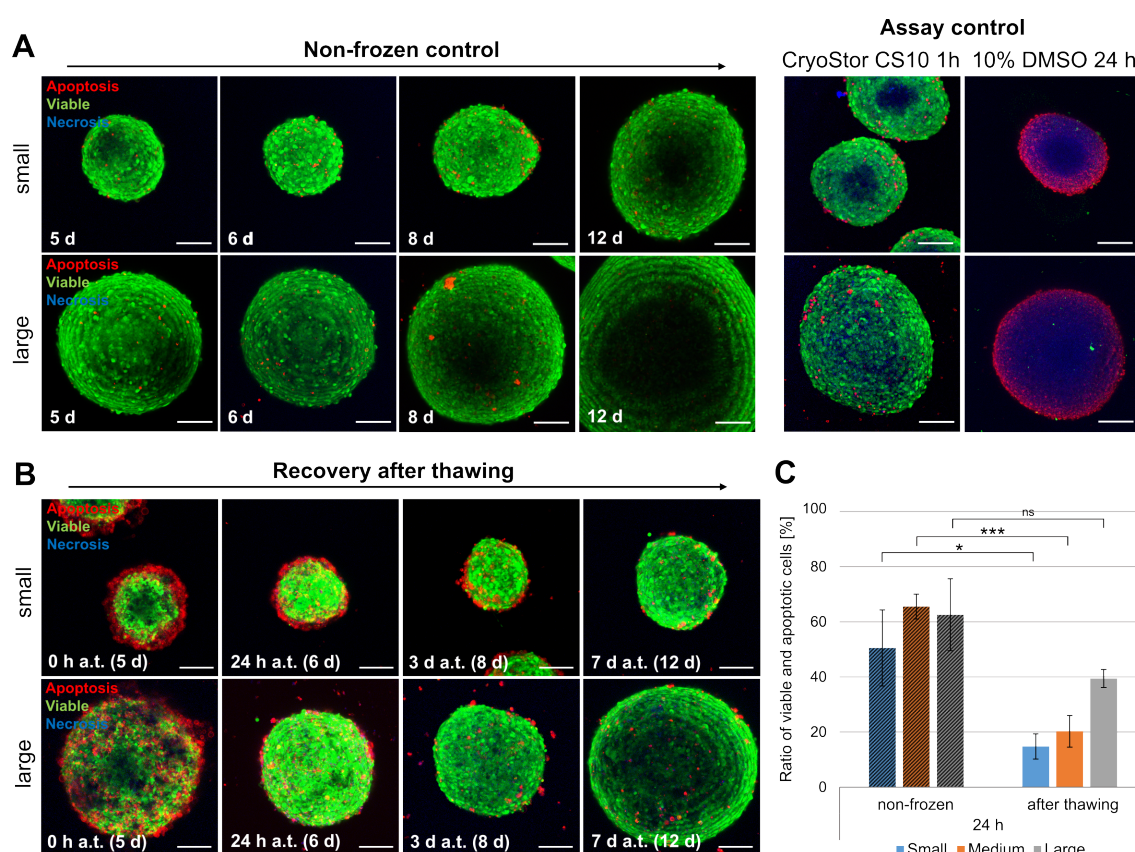


Figure 23: **Representative viability stainings of NSC spheroids nfc and a.t.** (A) Viability staining of nfc small ( $\varnothing$  300  $\mu\text{m}$ ) and large ( $\varnothing$  600  $\mu\text{m}$ ) NSC spheroids at different cultivation times to indicate apoptotic (red), necrotic (blue) and viable (green) cells. For assay control, spheroids were incubated in CryoStor CS10 for 1 h and 10% DMSO for 24 h. (B) Viability staining of small and large spheroids a.t. after different recovery times. Images are z-stacks with a z-step size of 10  $\mu\text{m}$  and 10 steps; scale bar represents 150  $\mu\text{m}$ . (C) The ratio of apoptotic and viable cell number of nfc and spheroids 24 h a.t. Apoptosis was measured by caspase-3/7 and viability by ATP activity, N=3, n=3 (*t*-test, ns: not significant, \**p* value < 0.05, \*\*\**p* value < 0.001).

#### 4.2 Comparative investigations on cryopreservation effects on metabolic properties in organoids from distinct germ layers and with different maturity

Hepatocytes derived from hiPSCs, cultivated in 3D, are of particular interest in biomedical research concerning pharmaceutical drug screenings, disease modelling and in vitro toxicology. These hiPSC-derived 3D models provide a theoretically unlimited available alternative to primary human hepatocyte (PHH) in vitro models while representing the physiology and functions of a human liver. In this thesis, a successful translation from 2D into 3D differentiation in the CERO 3D bioreactor was established. The upscaling by standardised 3D cultivation enables higher biomass yields in terms of cell number per millilitre of cell culture medium and per batch. However, successful long-term storage via cryopreservation to ensure the supply of hiPSC-derived hepatic 3D models has not been published yet. In this work, HP spheroids and

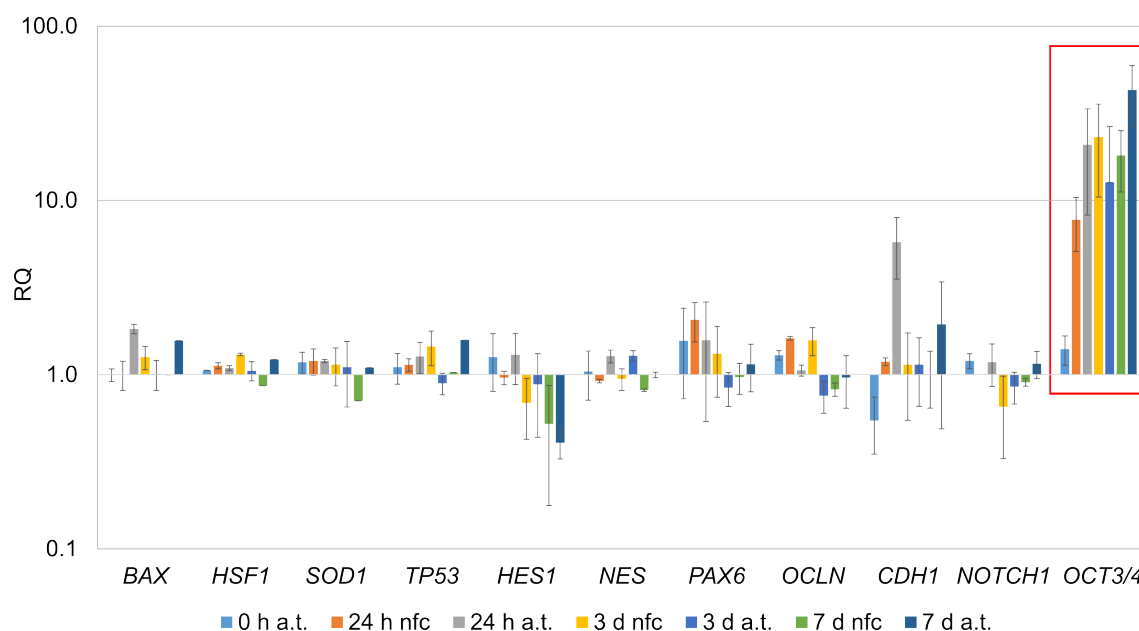


Figure 24: **Gene expression analysis of cells from NSC spheroids nfc and a.t.** Expression of different stress (*BAX*, *HSF1*, *SOD1* and *TP53*), neural (*HES1*, *NES* and *PAX6*), cell adhesion (*OCLN*, *CDH1* and *NOTCH1*), and pluripotency marker (*OCT3/4*) were analysed by RT-qPCR at different times in nfc and spheroids a.t. *GAPDH* and *HPRT1* served as housekeeping markers. Data is shown as fold-change (relative quantification (RQ)) normalised to the calibrator (nfc after 5 d cultivation), N=3, n=3.

matured HLC organoids served as alternative 3D cell models to NSC spheroids to investigate the cryo effects regarding cell type and maturation specificity and heterogeneity. First, cell-type-specific differences between cryo-induced effects in uniform NSC and HP spheroids were comparatively investigated by morphology and viability analyses. Second, the cryopreservation and recovery potential of HP spheroids and HLC organoids were investigated by specific quality controls, including the assessment of organoid morphology, the measurement of *CYP3A4* metabolic activity and the analysis of hepatic gene and protein expressions. These studies provide new insights into the impact of the maturation state on cryopreservation outcomes of 3D cell models.

#### 4.2.1 3D differentiation and upscaling of hepatic organoids

The 2D differentiation protocol from hiPSCs to HLC was successfully translated into a 3D protocol in the suspension CERO 3D bioreactor. This was realised by adapting the seeding density of hiPSCs, the cultivation program and the medium composition (see section 3.2.2, Altmaier et al. 2022.). Fig 26 A shows representative microscopic images and the morphological changes during the 3D differentiation from day 1 to day 21. Due to the heterogeneous and non-spherical shape, respective diameters and volumes could not be derived like in NSC spheroids. Thus, spheroid and organoid areas were measured using NIS Elements AR (see section 3.2.2) and are shown below (Fig. 26). During the 3D differentiation process, between days 3 to 4,

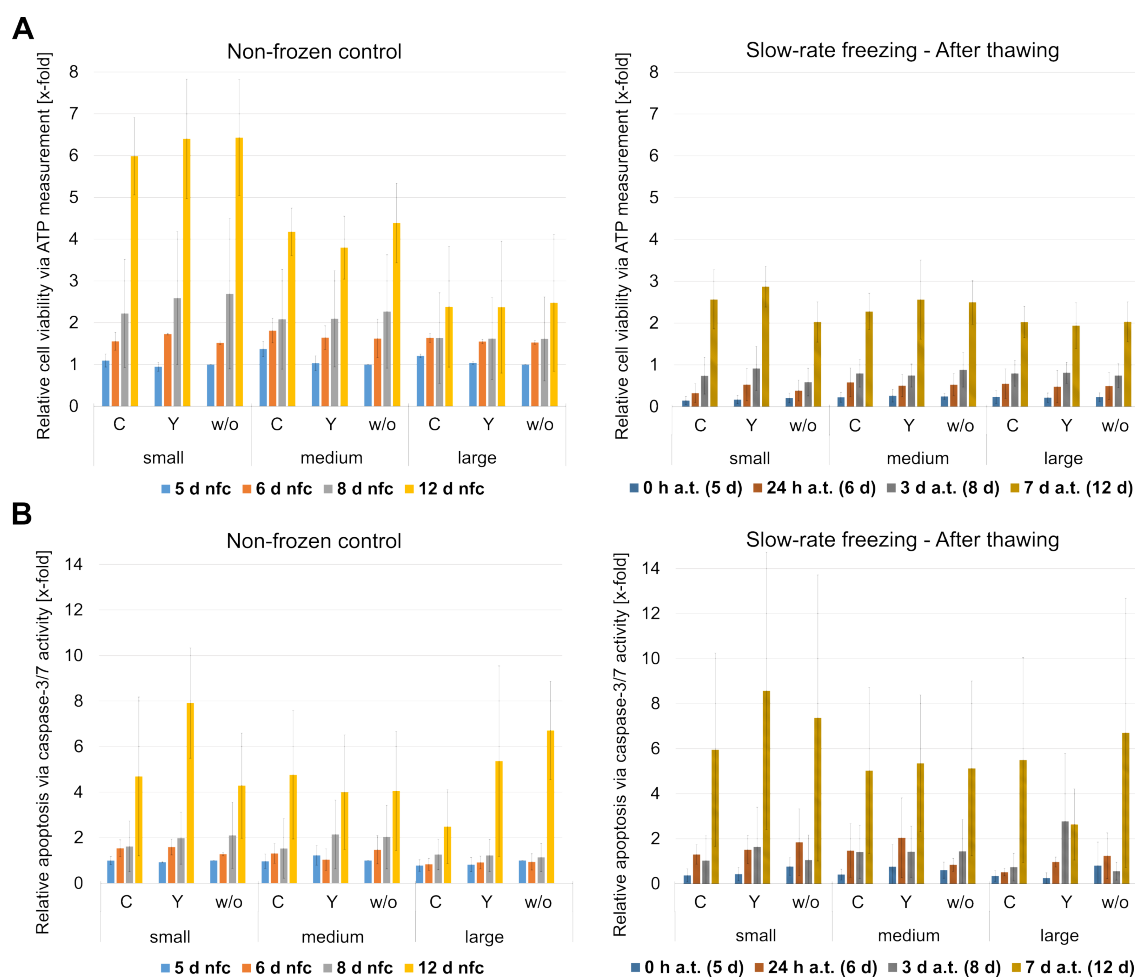


Figure 25: **Relative cell viability and apoptosis of NSC spheroids nfc and a.t. after treatment with Chroman 1 (C), Y-27632 (Y) and without (w/o) additive.** Both the relative (A) viability and (B) apoptosis values of spheroids ( $\varnothing$  300  $\mu\text{m}$ ,  $\varnothing$  450  $\mu\text{m}$ ,  $\varnothing$  600  $\mu\text{m}$ ) with C, Y, and w/o additives at different points in time were normalised to nfc w/o additive after 5 d of cultivation,  $N=3$ ,  $n=3$ .

the light reflection from the aggregates was reduced, indicating a more compact and dense structure, and the mean area decreased. In the following differentiation via DE- (4 d) and HP spheroids (8 d) to HLC organoids (21 d), the mean areas slowly increased. After the 21 d of differentiation, hepatic organoids showed a mean area of 30,000  $\mu\text{m}^2$  (Fig. 26 B). The number of 3D cell systems constantly decreased from 523 DE spheroids/ml (3 d) to 232 HLC organoids/ml (21 d) (Fig. 26 C).

#### 4.2.2 Cryo-induced metabolic effects in hepatic organoids of different maturity

To elucidate the impact of the cell type-specific maturation level on cryopreservation, hepatic 3D cell models were slow-rate frozen at an early differentiation status at day 8 (HP spheroids) and at the end of 3D differentiation at day 21 (HLC organoids). The quality and functional analyses were carried out after different recovery times and accordingly for the nfc. Fig. 27

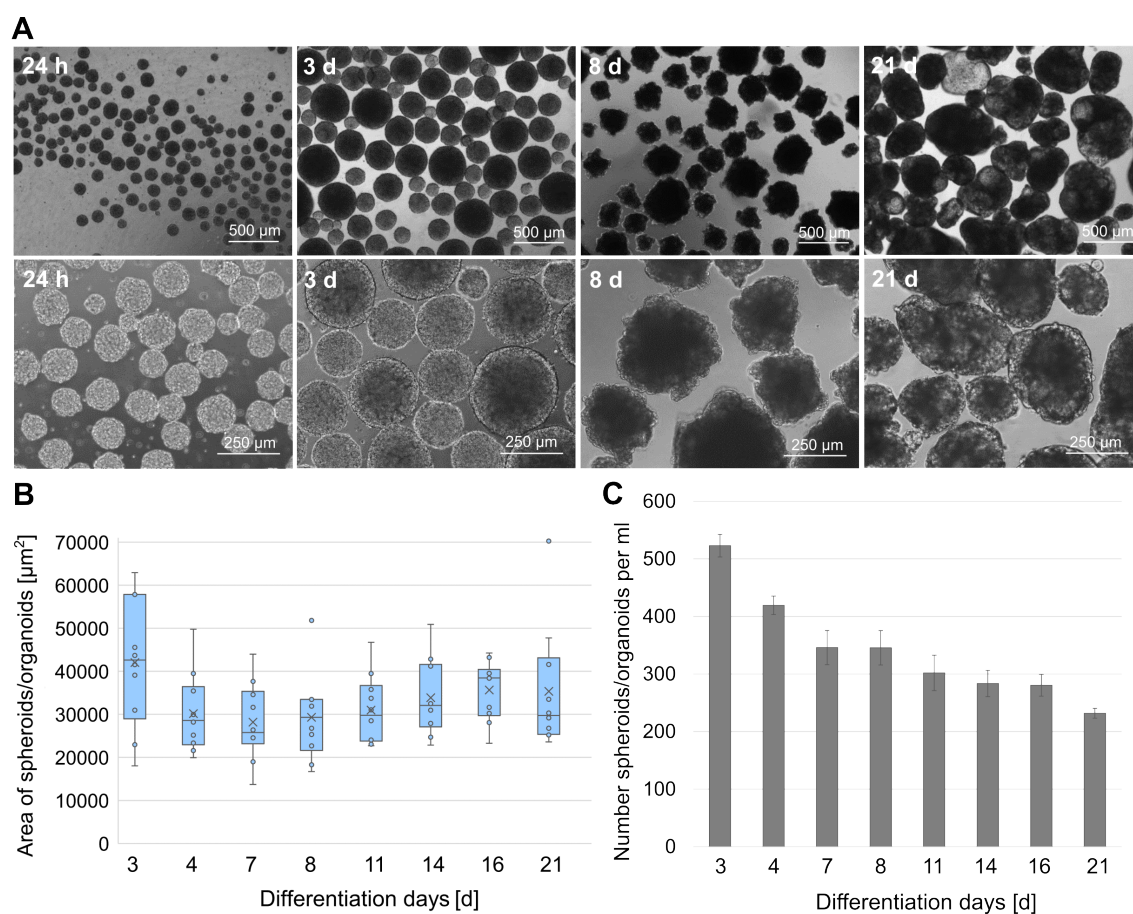


Figure 26: **Characterisation of HLC organoids differentiated via DE- and HP spheroids.** (A) Representative microscopic images of spheroids and organoids during the differentiation from hiPSCs to HLC. (B) Mean areas of 3D cell systems throughout the differentiation from day 3 to 21. (C) Number of 3D cell systems per ml during differentiation from day 3 to 21,  $N=3$ ,  $n=3$ . Data published in Kwok et al. 2022.

A shows representative microscopy images of HP spheroids and HLC organoids before freezing and 24 h and 7 d a.t. HP spheroids before freezing exhibited a more uniform shape among themselves with areas of about  $29,300 \mu\text{m}^2 \pm 6545 \mu\text{m}^2$  compared to HLC organoids. The morphology of different HLC organoids was more heterogeneous with mean areas of  $35,400 \mu\text{m}^2 \pm 14,493 \mu\text{m}^2$ . On day 1 after thawing, the areas of both samples were decreased, and the outer cell layers had an irregular shape. Cell debris was detected in the suspension of both samples (see white arrows in Fig. 27 A). After a recovery of 7 d, both samples showed a more regular shape and increased areas. These morphological effects after cryopreservation were comparable to the detected effects in NSC spheroids during the recovery. In NSC and hepatic 3D cell systems, the areas were reduced 24 h a.t., and cell debris was observed. A recovery of the area and proliferation followed this.

As further quality analysis, the *CYP3A4* expressions in HP spheroids and HLC organoids were analysed with the Nano-Glo Luciferase Assay. For this purpose, the spheroids and organoids

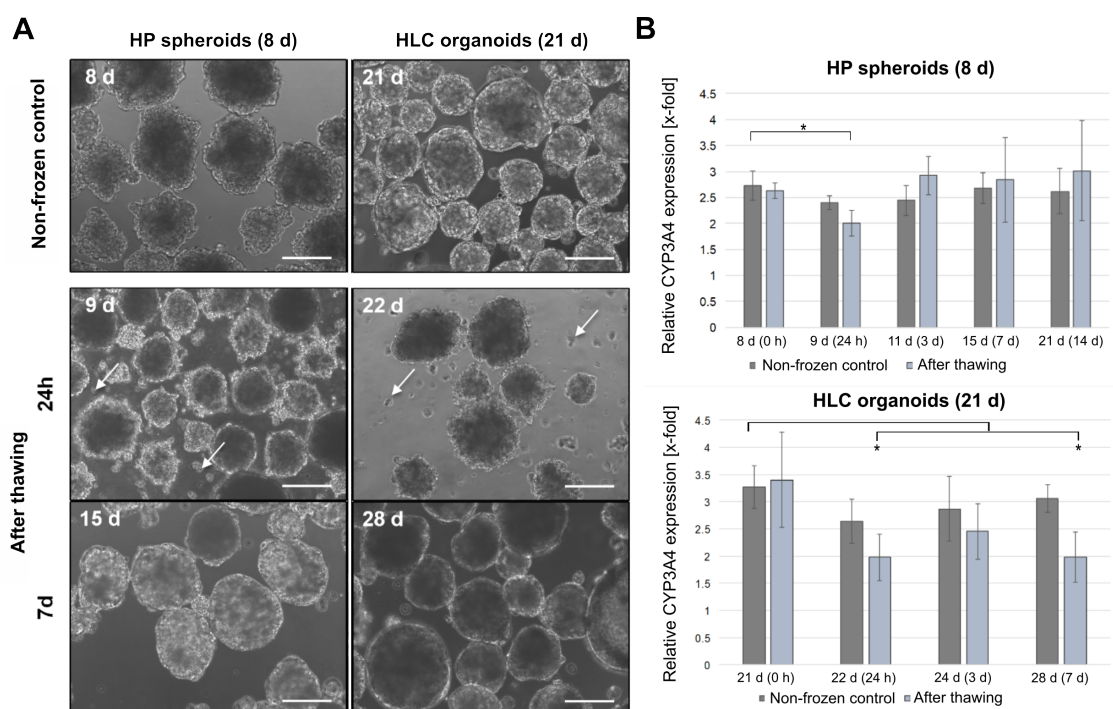


Figure 27: **Morphological and metabolic characterisation of HP spheroids and HLC organoids nfc and a.t.** (A) Representative microscopic images of HP spheroids (8 d) and HLC organoids (21 d) before freezing and respectively 24 h and 7 d a.t.; scale bar represents 200  $\mu\text{m}$ . (B) Relative *CYP3A4* expression during the recovery of day 8 frozen HP spheroids and day 21 frozen HLC organoids. The assays were performed 0 h (reflecting 8 d or 21 d of differentiation), 24 h (9 d or 22 d), 3 d (11 d or 24 d), 7 d (15 d or 28 d) and only for day 8 frozen samples 14 d (28 d) after thawing. Respective nfc was measured at the accordant points in time,  $N=3$ ,  $n=3$  (*t*-test, \**p* value < 0.05). Data published in Altmaier et al. 2022.

were derived from the hepatocyte-specific reporter hiPSC line BIONi010-C-64, which contains a Nanoluciferase gene downstream of *CYP3A4*, a hepatocyte-specific gene. The Nano-Glo luminescence values were normalised to the respective viable cell number to obtain a relative *CYP3A4* expression. Fig. 27 B shows the relative *CYP3A4* expression of nfc, intermediate frozen HP spheroids, and HLC organoids during the differentiation. The relative *CYP3A4* expression of nfc HP spheroids only varied between 2.4-fold and 2.7-fold at all times. Immediately after thawing, the HP spheroids showed a similar expression level of 2.6-fold  $\pm$  0.14. However, 24 h a.t., the expression significantly decreased by 26% compared to before freezing. At later recovery times, the expression of the marker increased again to levels similar to those of nfc. During the recovery at day 14, the HP spheroids differentiated into HLC organoids and showed comparable *CYP3A4* expression to nfc. However, analyses by ATP measurement showed a 43% reduction in cell viability in HP spheroids at 14 days compared to nfc, but standard deviations between biological replicates were high (data not shown). The HLC organoids, cryopreserved at day 21, exhibit similar *CYP3A4* expressions before freezing and immediately after thawing. As with HP spheroids, marker expression was significantly reduced by around 40% at 24 h

a.t. In contrast to the HP spheroids, the marker expression was still reduced at 3 d and 7 d a.t. Unlike HP spheroids, which were collected for 14 d a.t. to day 21, HLC organoids were collected and analysed for only 7 d a.t. to day 28. Longer cultivation after thawing would not be consistent with the goal of a potentially rapidly available product. In summary, a fast recovery of *CYP3A4* expression from 3 d a.t. with similar levels compared to the nfc was only observed in HP spheroids. In contrast, HLC organoids recovered 3 d a.t. more slowly and showed continuously lower expression levels compared to nfc.

To further characterise cryopreserved HP spheroids and HLC organoids, gene and protein expressions were determined. Hepatocyte-specific gene expression was analysed by RT-qPCR, including the HP-specific markers *HNF4A*, *AFP* and *TTR* and HLC-specific markers *ALB*, *CYP2C9* and *CYP3A4* (Fig. 28 A and 29 A).

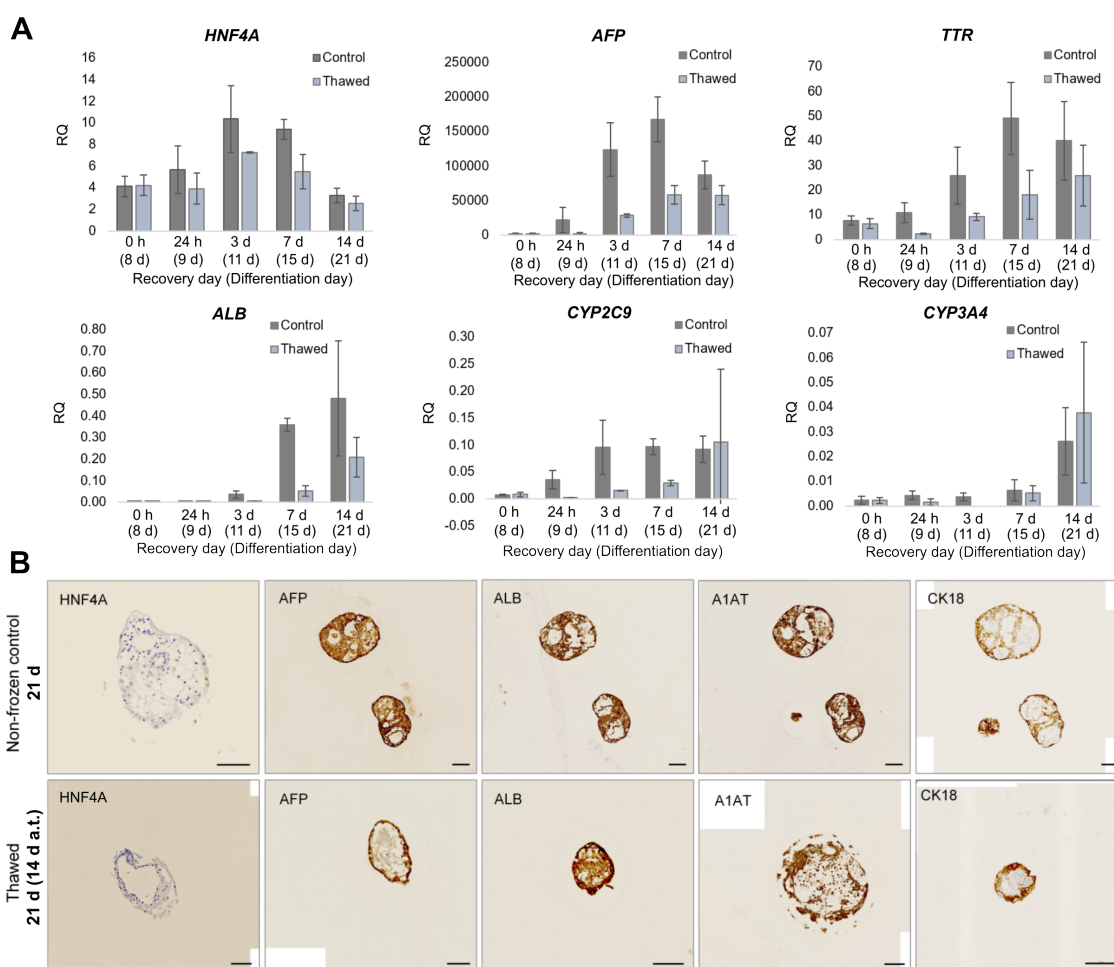


Figure 28: **Gene and protein expression of HP spheroids nfc and a.t.** (A) RT-qPCR analyses with HP-specific markers *HNF4A*, *AFP* and *TTR* and HLC-specific markers *ALB*, *CYP2C9* and *CYP3A4*. Analyses were performed at 8 d (0 h a.t.), 9 d (24 h a.t.), 11 d (3 d a.t.), 15 d (7 d a.t.) and 21 d (14 d a.t.). Data is shown as fold-change (RQ) normalised to *HPRT1* with PHH as a reference. (B) Representative ICC images of nfc and day 8 frozen organoids at differentiation day 21 with HNF4A, AFP, ALB, A1AT and CK18; scale bar represents 100  $\mu\text{m}$ , N=3, n=3. Data published in Altmaier et al. 2022.

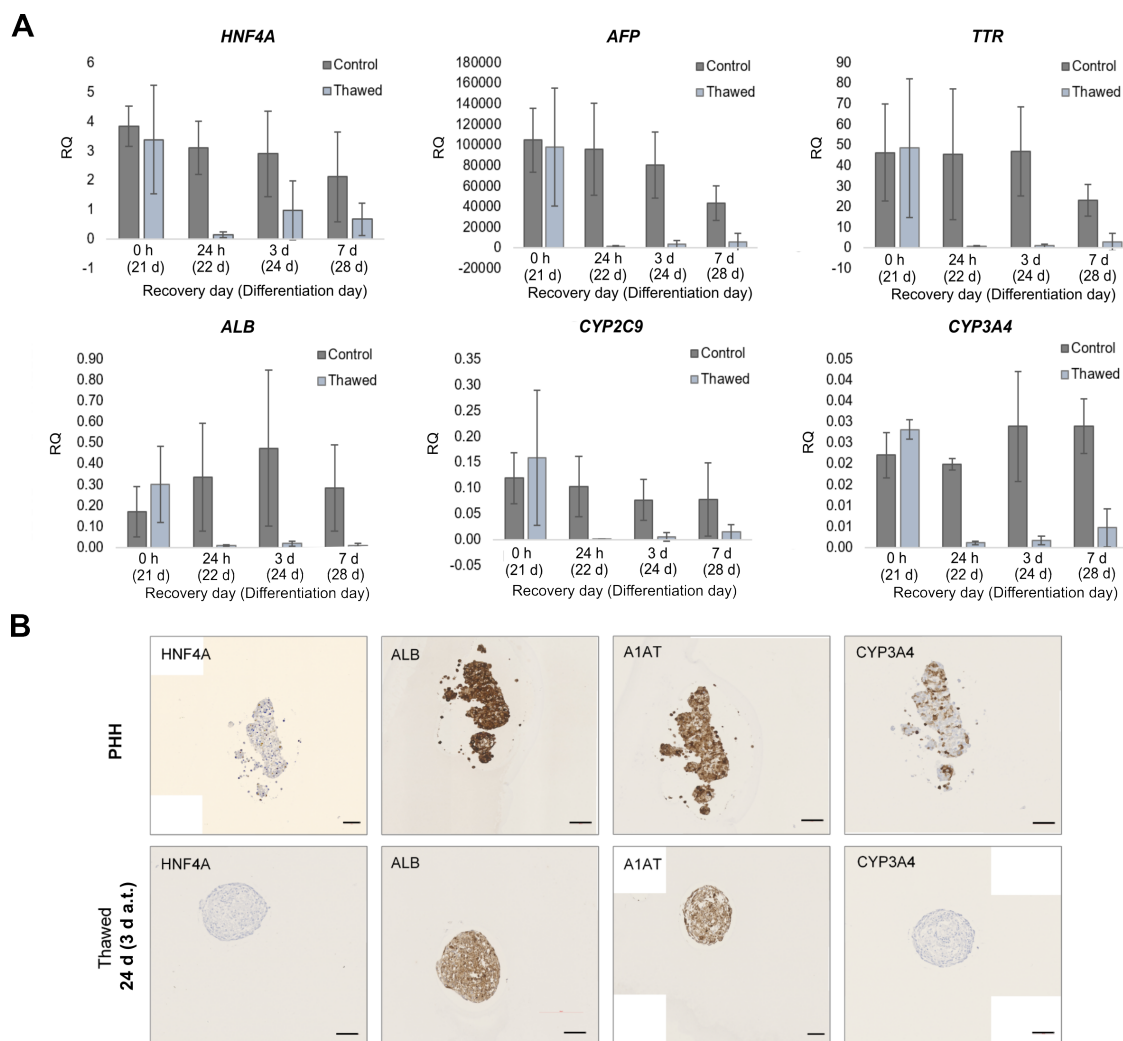


Figure 29: **Gene and protein expression of HLC organoids nfc and a.t.** (A) RT-qPCR analyses with HP-specific markers *HNF4A*, *AFP* and *TTR* and HLC-specific markers *ALB*, *CYP2C9* and *CYP3A4*. Analyses were performed at 21 d (0 h a.t.), 22 d (24 h), 24 d (3 d a.t.), and 28 d (7 d a.t.). Data is shown as fold-change (RQ) normalised to *HPRT1* with PHH as a reference. (B) Representative ICC images of PHH and day 21 frozen organoids 3 d a.t. with HNF4A, ALB, A1AT and CYP3A4; scale bar represents 100  $\mu$ m, N=3, n=3. Data published in Altmaier et al. 2022.

The HP spheroids after thawing and the respective nfc showed high levels of HP- and HLC-specific markers during the differentiation from day 8 to 21 (Fig. 28 A). All HP-specific marker expressions were increased steadily until day 11 for *HNF4A* and until day 15 for *AFP* and *TTR*. They dropped off with increasing maturation. Increasing levels of HLC-specific markers were observed at later stages of the differentiation. The highest levels were measured at the end of differentiation on day 21. These developments in gene expression were observed in cryopreserved samples after thawing and nfc. However, the expression values of samples after cryopreservation were consistently lower compared to the controls. Notably, higher expressions of *CYP2C9* and *CYP3A4* were detected in the cryopreserved HP spheroids at day 21, albeit

with a high standard deviation. In the non-frozen HLC organoids, a decrease in HP-specific and increased HLC-specific marker expression was observed as differentiation progressed (Fig. 29 A). However, HLC organoids frozen on day 21 do not express HP- or HLC-specific markers 24 h a.t. and later in recovery.

The HP spheroids and HLC organoids were further validated by ICC with hepatocyte-specific markers HNF4A, AFP, ALB, A1AT, CK18 and CYP3A4 (Fig. 28 B and 29 B). Therefore, HP spheroids were frozen at differentiation day 8 and recovered for 14 days. The protein expressions were comparatively analysed in these intermediate frozen organoids and non-frozen HLC organoids at the end of differentiation on day 21 (Fig. 28 B). Except for HNF4A, all hepatic markers were expressed in both conditions. These expression patterns were comparable to the staining of PHH (Fig. 29 B). HLC organoids frozen on day 21 showed only low expression of ALB and A1AT 3 d a.t., and HNF4A and CYP3A4 were not identified (Fig. 29 B).

### 4.3 Comparative investigations on cryopreservation effects on structural and functional properties in precursor organoids

Comparative analyses of the morphology of NSC and HP spheroids revealed a reduction in the spheroid area 24 h a.t. and increased cell debris in the suspension. In addition, the circularity was decreased and the outer cell layers were irregularly shaped. This indicates a detachment of peripheral cells between 0 h and 24 h after thawing. The structural integrity of cells in NSC spheroids was further assessed to investigate these effects after cryopreservation. This included the comparative analysis of the ultrastructures using SEM and structure protein expressions by clearing and ICC in peripheral and inner cells of NSC spheroids. In this context, the adhesion functionality of cell junctions and the effect of potential cell contact-supporting additives on reducing cell detachment were investigated.

#### 4.3.1 Crystallisation effects on cell structure and adhesion in NSC spheroids

The ultrastructure was examined using SEM to analyse the outer spheroid cell layer. The nfc showed tightly connected peripheral cells with widely spread cell-cell junctions (Fig. 30). In contrast, the peripheral cells of slow-rate frozen spheroids exhibited a more circular shape and a loose structure with fewer cell-cell junctions. In addition, broken cell-cell connections and the structure of dehydrated or apoptotic cells were observed. However, the cell-cell junctions started to recover 24 h a.t. These results were detected for small (Fig. 30 A) and large NSC spheroids (Fig. 30 B). Only the peripheral cells appeared more densely packed and connected in large spheroids.

Additionally, the expression of the cytoskeleton and adhesion proteins F-actin and N-cadherin was investigated by ICC. Fig. 31 depicts the F-actin and N-cadherin expression in the outer cell layer of nfc and NSC spheroids after thawing. For assay control, spheroids were incubated in CryoStor CS10 for 1 h and 10% DMSO for 24 h to induce apoptosis. Both marker expressions were decreased in the outer cells 24 h a.t. compared to nfc. The lowest N-cadherin expression



was observed at 6 h a.t. However, during the recovery phase, the N-cadherin expression increased and at 7 d a.t., the expression levels were comparable to cells of nfc with both diameters. These results were supported by the functional analyses of spheroid fusion after cryopreservation. Three NSC spheroids were incubated in one ULA well to attach to each other and fuse (Fig. 32). The fusion of 5 d cultured nfc started after a pooled incubation of 4 h, and after 24 h, the spheroids were completely merged. This was not detected for spheroids which were pooled immediately and 24 h after thawing. However, spheroids that were separately recovered for 7 d a.t. showed similar adhesion properties to nfc after pooled incubation. First agglomeration was observed after a separate recovery for 48 h a.t. after a pooled incubation of 24 h and after a separate recovery for 3 d a.t. after a pooled incubation of 4 h.

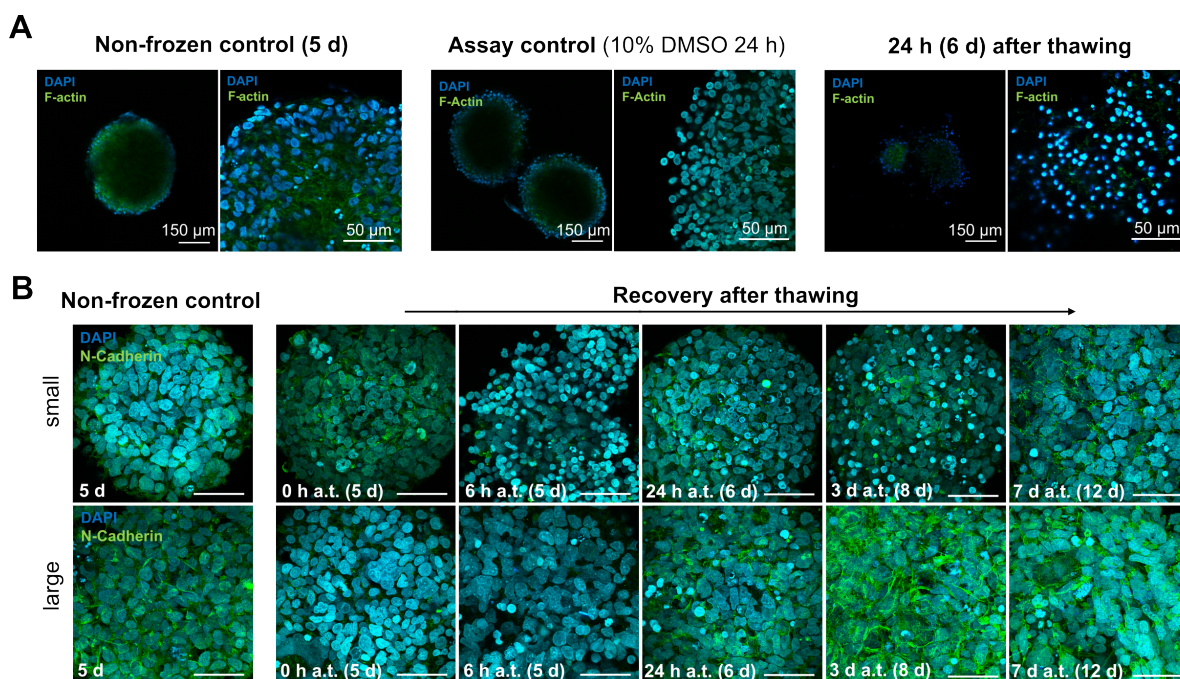


Figure 31: **Characterisation of cytoskeleton and adhesion proteins of NSC spheroids nfc and a.t.** (A) ICC staining of small ( $\varnothing$  300  $\mu$ m) spheroids nfc and 24 h a.t. with the cytoskeleton protein F-actin. For assay control, the spheroids were incubated in 10% DMSO for 24 h. (B) ICC staining of small and large spheroids with N-cadherin at different cultivation and recovery times (0 h nfc and 0 h, 6 h, 24 h, 3 d, 7 d a.t.); scale bar represents 50  $\mu$ m, N=2, n=3.

To investigate not only the outer cell layers but also the inner cells, the peripheral cell layers of the NSC spheroids were detached stepwise with Accutase and the relative viability of the cells from three separate layers was analysed. The first cell layer was detached after incubation for 25 min. Fresh Accutase was added, and after 10 min, the second cell layer was detached. After another 10 min incubation in fresh Accutase, the third cell layer was resuspended. The cell viability measurements by membrane integrity showed a percentage cell viability of 91% for the first, 65% for the second and 54% for the third cell layer (Fig. 33 A). However, an exact

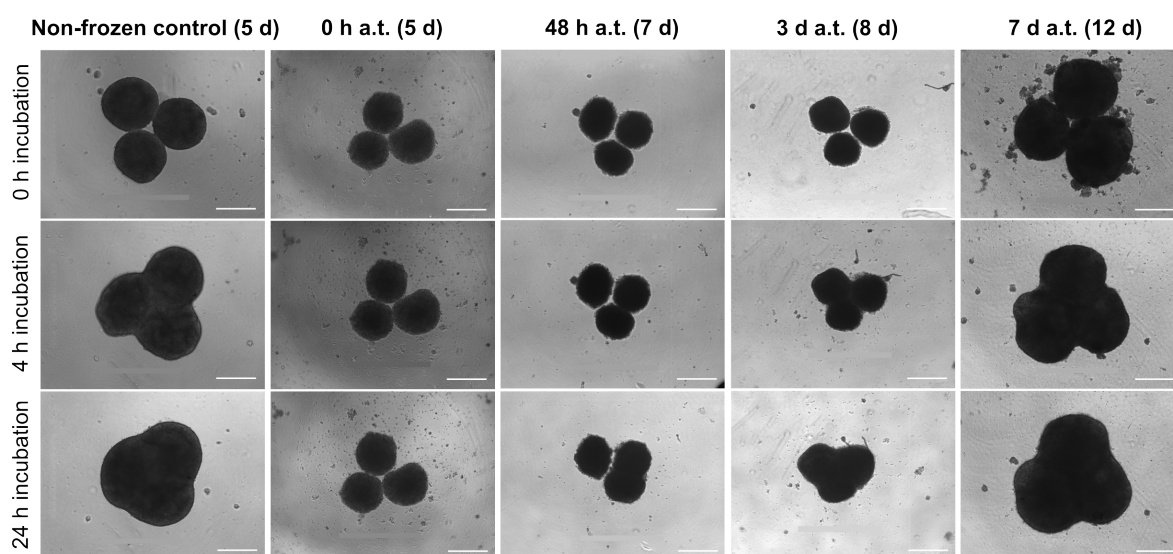


Figure 32: **Morphological assessment of fusion properties of NSC spheroids nfc and a.t.** Starting attachment of nfc and NSC spheroid 3 d a.t. to each other after 4 h incubation and complete fusion after 24 h. No attachment and fusion of spheroids immediately after thawing; scale bar represents 500  $\mu\text{m}$ , N=3, n=3

depth measurement could not be determined with this method. To analyse the proliferation status of the inner cell at a precise depth, the spheroids were cleared after ICC staining. The clearing process chemically homogenised the refractive indices of cells, resulting in transparent spheroids. The method included steps for dehydration so that the original diameter of about 500  $\mu\text{m}$  of spheroids cultivated for 7 d was reduced to about 200  $\mu\text{m}$ . Thus, a measurement of a cell layer at a depth of 30  $\mu\text{m}$  mapped cells with an original depth of 75  $\mu\text{m}$ . To analyse inner cells' proliferation status before freezing and after cryopreservation, NSC spheroids were stained with the proliferation marker Ki67, the nucleus marker DAPI and the transmembrane protein marker N-cadherin. Fig. 33 D depicts representative confocal microscopic images of stained cell layers in a depth of 10  $\mu\text{m}$ , 30  $\mu\text{m}$ , and 60  $\mu\text{m}$ . The negative antibody control excluded unspecific antibody bindings. DAPI was excited with UV light, and the emission maximum was measured at 461 nm. The emission of Ki67 and N-cadherin binding antibodies coupled with different fluorophores were detected at a wavelength of 671 nm and 525 nm. Light with higher wavelengths penetrates deeper into the spheroids, whereas the detection of UV light in deeper cell layers is limited. Thus, detecting DAPI was the limiting factor for the successful analysis of cleared spheroids. Further improvements in the clearing protocol and a z-adaptation of the laser intensity could enable the analyses of deeper regions (data not shown). With the clearing method, DAPI could be reliably detected in all technical and biological replicates until a depth of 60  $\mu\text{m}$ , which corresponds to the inner region with an original depth of 150  $\mu\text{m}$ . The staining of N-cadherin served as a positive control for successful staining and as proof of the NSC status of the spheroids. The expression of Ki67 was decreased with progressing spheroid depth. To quantify these results, the pixel number of cells with positive Ki67 signal

was normalised to the pixel number of DAPI-stained nuclei. The relative proliferation of cell layers was calculated from 0  $\mu\text{m}$  to 60  $\mu\text{m}$  depth in 5  $\mu\text{m}$  steps (Fig. 33 B). The percentage of proliferating cells was logarithmically decreased from a mean value of 80% (0  $\mu\text{m}$ ) to 37% (60  $\mu\text{m}$ ). This indicates more proliferating cells in the outer layers than in the intermediate zone.

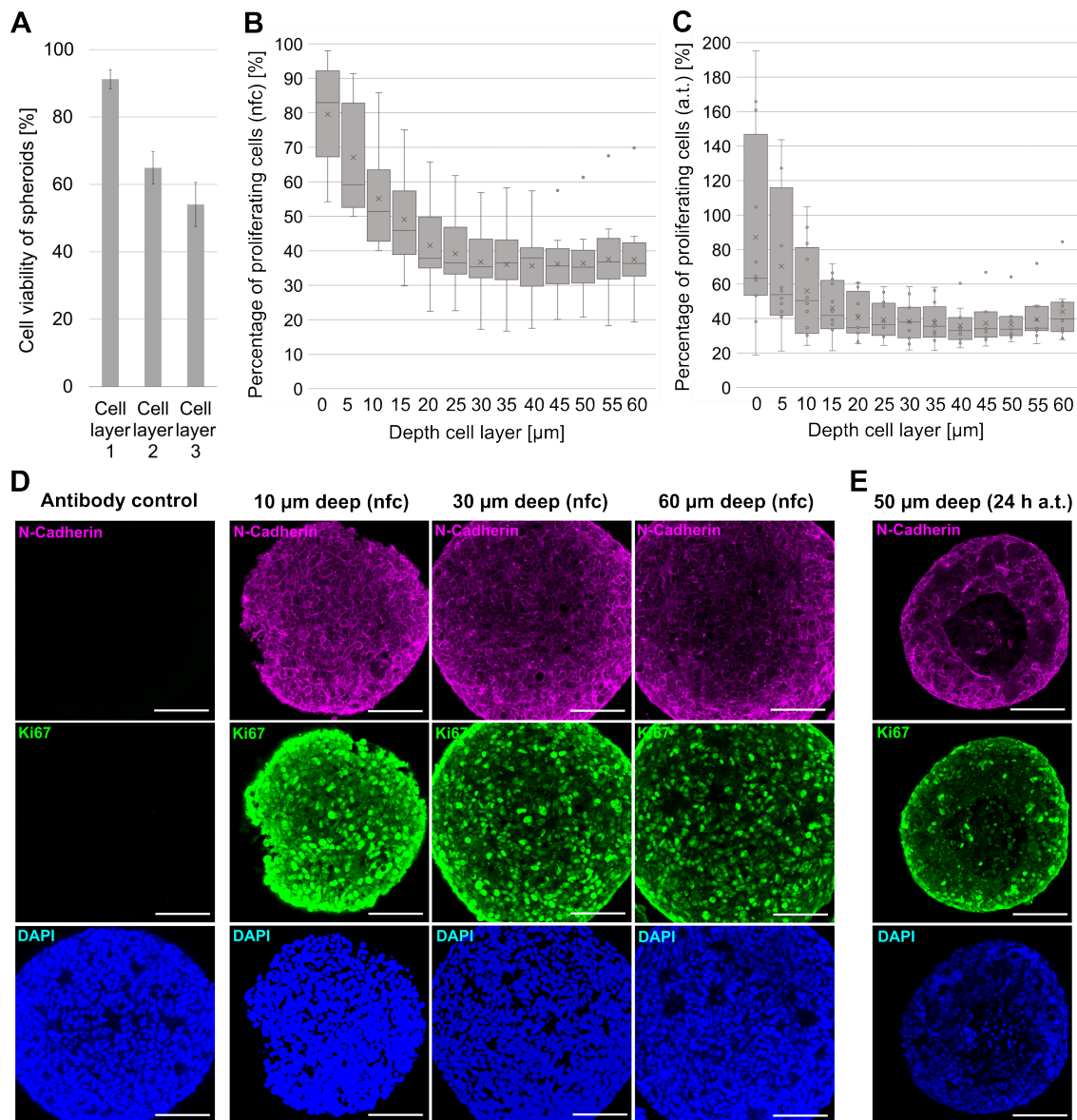


Figure 33: **Viability and proliferation analysis of inner cell layers of NSC spheroids nfc and a.t.** (A) Cell viability of outer, intermediate and core cell layers measured by cell membrane integrity. The percentage of proliferating cells in (B) nfc and (C) a.t. was detected in 5  $\mu\text{m}$  steps between 0  $\mu\text{m}$  and 60  $\mu\text{m}$  depth by ICC image analyses. Representative ICC images of NSC spheroids in a depth of 10, 30 and 60  $\mu\text{m}$  for (D) nfc and (E) in 50  $\mu\text{m}$  for 24 h a.t. after ICC and clearing, stained with N-cadherin, Ki67 and DAPI marker; scale bar represents 50  $\mu\text{m}$ , N=2-3, n=3-8

In comparison, the slow-rate frozen spheroids also showed a logarithmic decrease in proliferation from the outer to the inner cells. The mean values of proliferating cells decreased from 87% in the outer layer to about 40% in inner cells (Fig. 33 C). The progression of the percentage of proliferating cells 24 h a.t. at increasing depth is comparable to nfc, but the standard deviations in the first three outer cell layers from 5  $\mu\text{m}$  (41 %) to 15  $\mu\text{m}$  (16 %) were high. A striking aspect of the analyses of cryopreserved spheroids after clearing was the detection of a clearly defined circular core region in a depth of about 50  $\mu\text{m}$ , with lower N-Cadherin expression than in the outer cell layers (Fig. 33 E). Ki67 and DAPI marker expressions were also reduced in this region but still detectable.

In the next step, two additives were analysed that might have a beneficial influence on the preservation of peripheral cell structures of NSC spheroids after cryopreservation. Therefore, the effects of the myosin inhibitor (S)-4'-nitro-Blebbistatin (Blebb) and the foam-reducing, non-ionic surfactant Poloxamer 188 (PO) on the cells were investigated by relative cell viability (ATP measurement) and caspase-3/7 activity analyses. Blebb was added to NSC spheroids 30 min before slow-rate freezing, and PO was added after thawing and incubated for 24 h. The relative cell viability and apoptosis of nfc and spheroids after thawing were measured at different cultivation and recovery times in the CERO 3D bioreactor or ULA plate (Fig. 34 and 35). No significant difference in relative cell viability was observed between the samples without additive and neither with Blebb (Fig. 35 A) nor with PO (Fig. 34 A and 35 B). In addition, no significant differences in the relative apoptosis were detected between the treated and non-treated samples in the CERO 3D bioreactor (Fig. 34 B). Only a 3.3-fold increase of relative cell apoptosis without PO at 24 a.t. was observed (Fig. 34 B). However, no significance was detected.

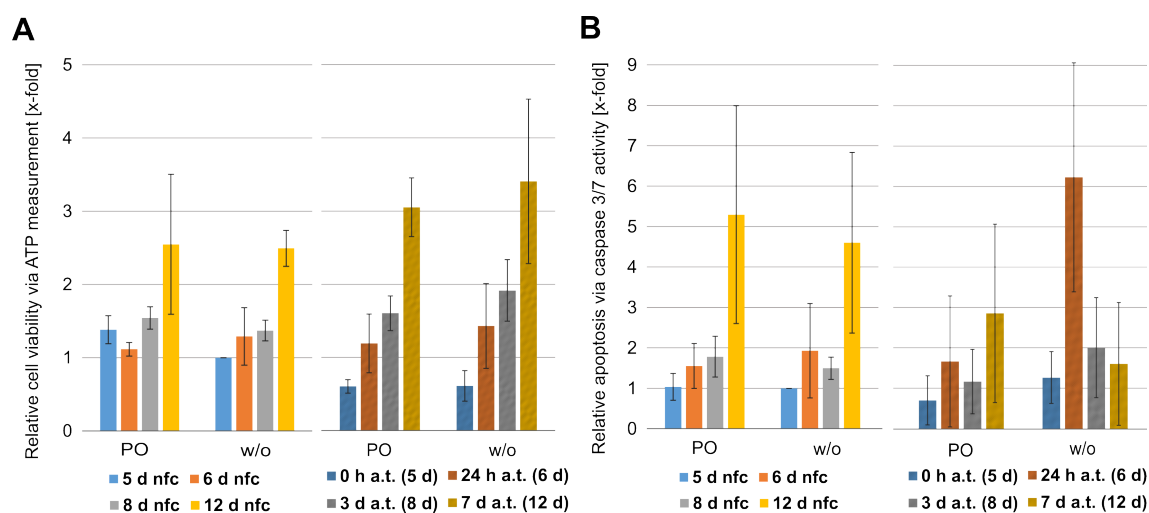


Figure 34: **Relative cell viability of NSC spheroids nfc and a.t. with and without (w/o) treatment of PO, cultured in the CERO 3D bioreactor.** Both, the relative (A) viability and (B) apoptosis values of spheroids with PO and w/o additive at different cultivation and recovery times were normalised to nfc w/o additive after 5 d of cultivation, N=3, n=3.

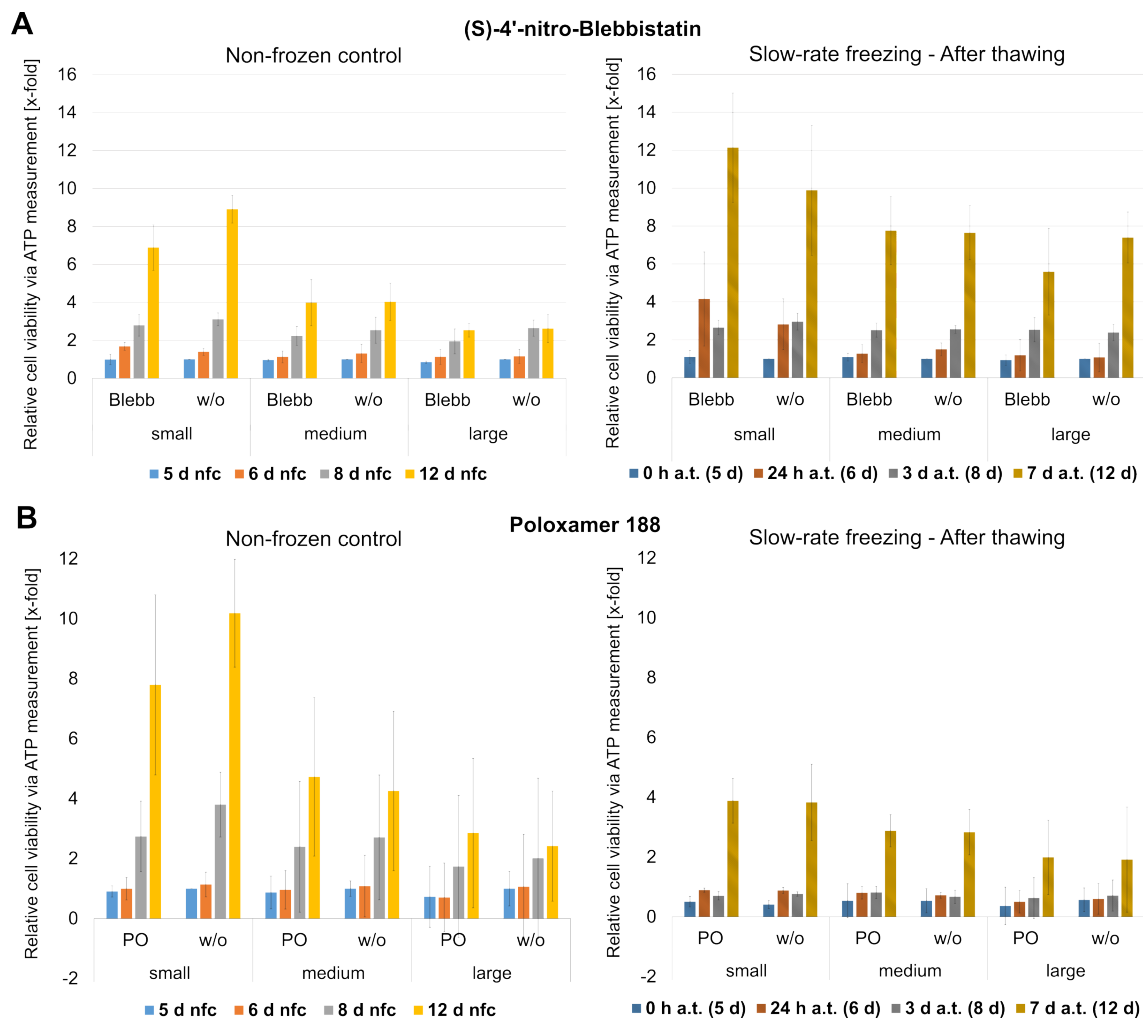


Figure 35: **Relative cell viability of NSC spheroids nfc and a.t. after treatment with Blebb, with PO and without (w/o) additives.** The relative viability values of spheroids w/o and with (A) Blebb or (B) PO at different cultivation and recovery times were normalised to nfc w/o additive after 5 d of cultivation, N=3, n=3.

#### 4.3.2 Vitrification effects on cell structure and metabolism in NSC spheroids

The previously described structural analyses of NSC spheroids after slow-rate freezing revealed the detachment of peripheral cells between 0 h and 24 h after thawing. Additional investigations should clarify whether crystallisation is causative and if vitrification as an alternative cryopreservation method could reduce these effects. The structural cell integrity was investigated in NSC spheroids after warming (a.w.) by analysing the morphology, viability, ultrastructures and gene expressions.

Two vitrification approaches were comparatively analysed. For the first method, small spheroids were collected in a cell strainer, which was directly immersed into LN<sub>2</sub>. For the second approach, spheroids were collected in a Twist device and were vitrified by pouring the LN<sub>2</sub> on the ultra-thin bottom (see section 3.3.4). Thus, direct cell contact with LN<sub>2</sub> was avoided. The morphology

of spheroids a.w. were similar for both vitrification devices (Fig. 36 A). The outer cell layers' circularity and shape were preserved, and no cell debris was detected in the suspension. Only 3 d a.w., the peripheral cells of the spheroids, which were vitrified in the cell strainer, showed an irregular shape. However, the proliferation of 24 h a.w. was increased in both approaches. These results correspond to the relative cell viability analyses by ATP measurement (Fig. 36 B). After vitrification with both devices, the NSC spheroids showed significantly higher viability values during the recovery than after slow-rate freezing. Since the viability after vitrification with a Twist is increased compared to the cell strainer method, the following quality and structural analyses were carried out with spheroids after vitrification with a Twist. The viability staining was performed with small and large NSC spheroids during the recovery after Twist vitrification (Fig. 36 C). Immediately after warming a slight increase of apoptotic peripheral cells was observed compared to nfc as depicted in Fig. 23 A. Compared to spheroids after slow freezing (Fig. 23 B), the outer cell layers were more viable after vitrification. The proliferation progression during the recovery after warming is comparable to that of nfc.

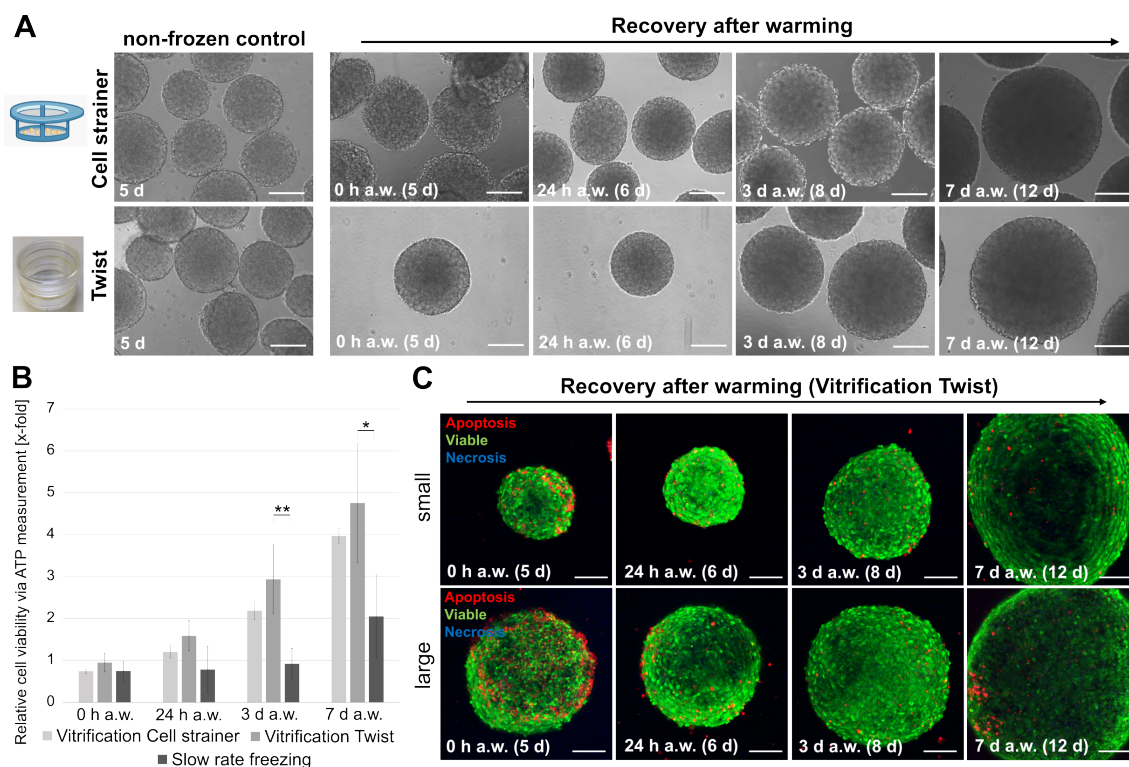


Figure 36: **Morphology and viability analysis of vitrified NSC spheroids a.w.** (A) Representative microscopic images of NSC spheroids a.w., which were vitrified with a cell strainer or Twist; scale bar represents 200 µm. (B) Relative cell viability of spheroids after vitrification or slow-rate freezing. (C) Viability staining of small (Ø 300 µm) and large (Ø 600 µm) vitrified spheroids a.w. at respective points in time during the recovery. Images are z-stacks with a z-step size of 10 µm and 10 steps; scale bar represents 50 µm, N=3, n=3 (*t*-test, \**p* value < 0.05, \*\**p* value < 0.01).

In addition, the gene expression of vitrified spheroids at 24 h a.w. is similar to that of nfc concerning different stress, neural, cell adhesion and pluripotency markers (Fig. 37). In contrast, spheroids after slow-rate freezing showed significantly higher expressions of *CDH1* and *OCT3/4* at 24 h a.t. compared to vitrified samples and nfc.

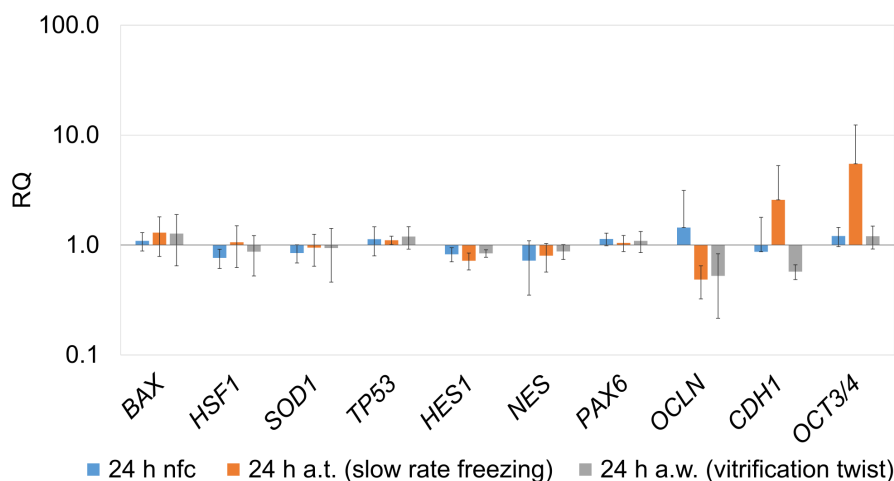


Figure 37: **Gene expression of nfc and vitrified NSC spheroids a.w.** Expression of different stress (*BAX*, *HSF1*, *SOD1* and *TP53*), neural (*HES1*, *NES* and *PAX6*), cell adhesion (*OCLN* and *CDH1*) and pluripotency marker (*OCT3/4*) were analysed by RT-qPCR at different times in nfc and a.w. *GAPDH* and *HPRT1* served as housekeeping markers. Data is shown as fold-change (RQ) normalised to the calibrator (nfc after 5 d cultivation), N=3, n=3.

To confirm previous findings of the regular cell morphology, the ultrastructures of NSC spheroids after vitrification were analysed using SEM. For nfc (small and large spheroids), tightly connected peripheral cells with widely spread cell-cell junctions were observed (Fig. 38). In peripheral cells of vitrified spheroids, the cell-cell junctions remained intact, and the cells were strongly interconnected. However, dehydrated or apoptotic cell structures were observed in a few cells. These results were detected for small (Fig. 38 A) and large (Fig. 38 B) spheroids. In summary, the studies on the influence of vitrification on cell structures of NSC spheroids revealed an intact and regular morphology and high viability after warming. However, only a small number of about 50-100 spheroids per batch could be preserved with the Twist vitrification device.

#### 4.4 Comparative investigations on the diffusion kinetics of cryoprotective agents in different 3D cell systems

A sufficient supply of cryopreservation media before cryopreservation is essential for ensuring adequate protection of the biological samples. Particularly in 3D cell models, adequate diffusion of CPA solutions into inner cells while avoiding cytotoxicity due to prolonged incubation time in the peripheral cells is critical. However, the diffusion kinetics of different compounds in 3D cell systems are very diverse due to the different chemical and mechanical properties of the cell network and the compounds. In the following studies, the diffusion kinetics of DMSO in NSC,

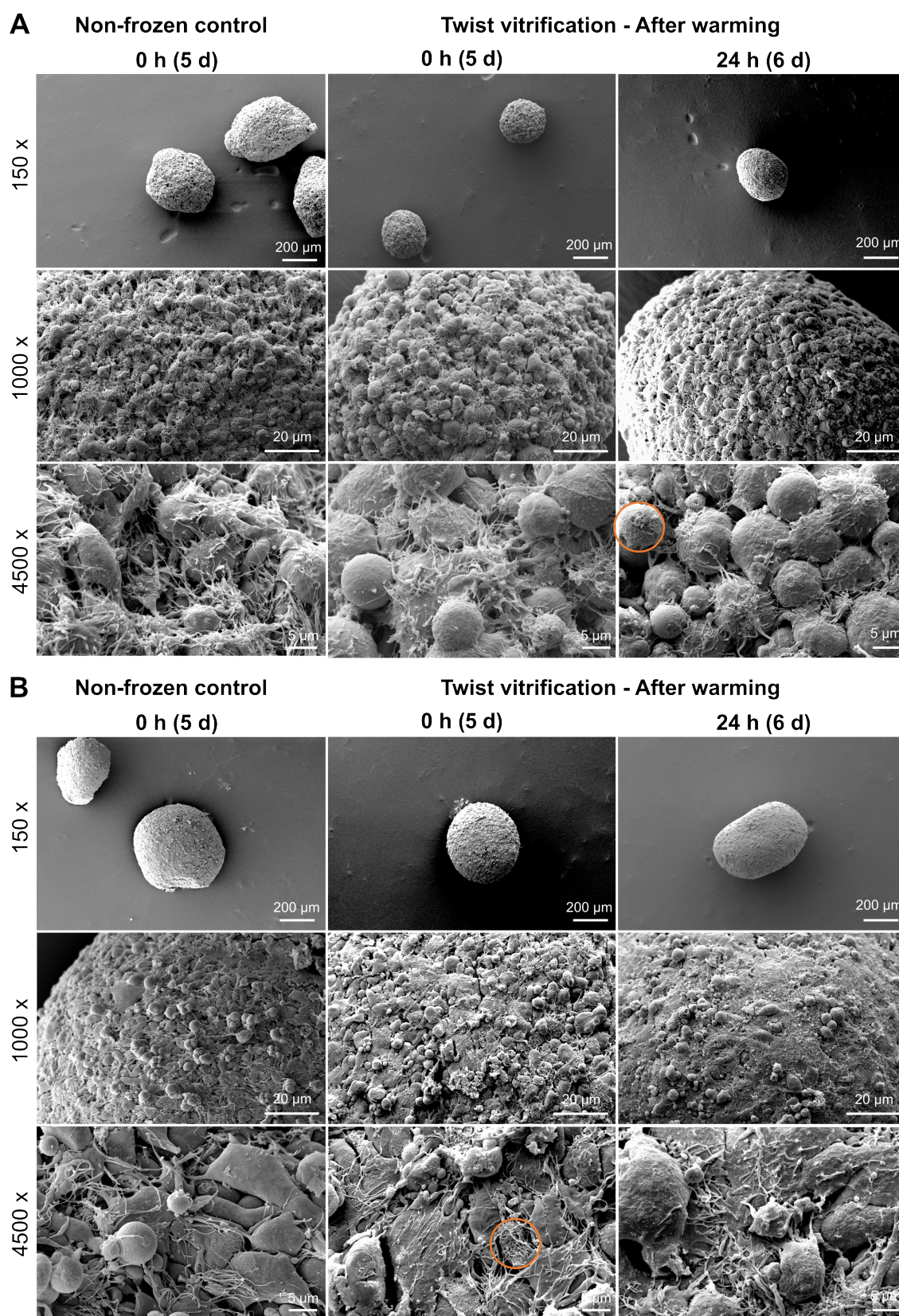


Figure 38: **Characterisation of the peripheral ultrastructure of nfc and vitrified NSC spheroids a.w.** Orange circles mark dehydrated or apoptotic cells on the outer layer of (A) small ( $\text{\O} 300 \mu\text{m}$ ) and (B) large ( $\text{\O} 600 \mu\text{m}$ ) spheroids. Magnification was 100x, 1000x and 4500x, N=2, n=3.

HP and HLC 3D cell models were studied using Raman micro-spectroscopy. Based on this, the perfusion times of DMSO were adapted to shorten the incubation times before cryopreservation.

#### 4.4.1 Diffusion kinetics of DMSO in organoids using Raman micro-spectroscopy

For successful cryopreservation, it is essential to ensure an adequate supply of CPAs throughout the entire 3D cell system while controlling cytotoxic effects in the outer layers via adapted incubation times. In the following, incubation times derived from the diffusion rate of DMSO, as the most frequently used and effective permeable CPA, were evaluated in NSC and HP spheroids and HLC organoids by bioorthogonal Raman micro-spectroscopy (Altmaier et al. 2024). In particular, deuterated dimethyl sulfoxide (DMSO-d6) penetration was analysed in spheroids with different diameters and cultivation times. Due to the bioorthogonal exchange of the hydrogen against the deuterium, the vibration bands of DMSO-d6 were detectable in a spectral range with less interference (Fig. 39 A). The spectral bands of DMSO-d6, which were detected in the spheroid centre, were quantified by integration (Fig. 39 B). First, each spectrum  $i(\Delta v)$  was background-corrected by subtracting a baseline  $b(\Delta v)$  that was generated by 7-point B-spline interpolation in the spectral area. The Raman band integral was calculated from the highlighted spectrum range  $v_0 = 2124$  to  $v_1 = 2233$   $\text{cm}^{-1}$  (Fig. 39 B).

$$A(t) = \int_{v_0}^{v_1} [i(\Delta v) - b(\Delta v)] d\Delta v \quad (2)$$

The integral of Raman band  $A(t)$  was assumed to be proportional to the DMSO-d6 concentration in the spheroid centre  $c(0, t)$ . Based on this, a fit equation was derived, which is based on the model of uniform diffusion of a compound from an infinite source into a sphere (Crank 2009). The general differential diffusion equation is solved for the specified geometry, resulting in a Laplace series expansion. The series of this fit function is aborted at  $n=8$ . Higher elements primarily influence the initial phase of the sigmoidal function. No data was recorded in this phase, as the measurement had to be started with a delay of  $t_0 = 20\text{-}30$  s.

$$\frac{c(0, t)}{c_0} = \frac{A(t)}{A_0} = 1 + 2 \sum_{n=1}^8 (-1)^n \exp\left[-Dn^2 \frac{\pi^2}{a^2} (t - t_0)\right] \quad (3)$$

Fig. 39 C shows a sigmoidal increase of the integrated spectral bands of DMSO-d6 for all spheroid diameters and ages. The fit curve for each graph is shown in red. In small spheroids after a cultivation time of 3 d, the early part of the sigmoidal curve shape is often invisible due to a fast influx of DMSO-d6 during the setup time  $t_0$ . For larger spheroids after 7 d and 14 d of cultivation, the slope of the first parts is decreased as the penetration of DMSO-d6 into the spheroid centre takes more time. External effects, such as sample drift or convection of the medium, affected some of the data. However, plausible fits with unaffected data in the first part were fitted to obtain diffusion parameters and were included in the analysis (Fig. 39 D). If a plausible model fit was not possible, the data was discarded from the study (11 out of 94 runs in total).

Based on these analyses, first, the diffusion coefficient  $D$  [ $\mu\text{m}^2\text{s}^{-1}$ ] as a tissue-specific parameter was determined. For this purpose, it was assumed that the spheroids were perfectly spherical, and the mean radii  $a$  were determined based on microscopic images. Second, the perfusion time of DMSO-d6, as a spheroid-specific parameter, was calculated. The diffusion time was defined as the time the relative concentration  $c/c_0 = A/A_0$  at the spheroid centre reaches 90% ( $t_{90\%}$ ) [s]. In this late stage of the process, the sigmoidal curve is primarily influenced by the first term (n=1) of the Laplace expansion:

$$t_{90\%} = -\frac{a^2}{D\pi^2} \cdot \ln\frac{1}{2}\left(1 - \frac{A}{A_0}\right) = \frac{\ln 20}{D} \cdot \frac{a^2}{\pi^2} \quad (4)$$

The diffusion coefficient  $D$  was calculated for each spheroid and was plotted against the diameters (Fig. 39 E). The data indicate that diffusion constants vary depending on the diameter of the samples. Up to an NSC spheroid diameter of 500-600  $\mu\text{m}$ , constant diffusion coefficients in order of  $D = 88.8 \pm 14.4 \mu\text{m}^2\text{s}^{-1}$  were calculated. NSC spheroids with diameters of 800  $\mu\text{m}$  exhibited diffusion coefficients of about  $D = 178.6 \pm 38.5 \mu\text{m}^2\text{s}^{-1}$ . With increasing diameter and age,  $D$  was further increased up to about  $D = 206.6 \pm 52.6 \mu\text{m}^2\text{s}^{-1}$  with a positive curvature in spheroids with an initial cell number of 2,500 cells (circles). At the same time, a reduced  $D$  of  $154.6 \pm 6.6 \mu\text{m}^2\text{s}^{-1}$  with a negative curvature was observed in NSC spheroids with diameters above 800  $\mu\text{m}$  and an initial cell number of 12,000 (boxes). HP spheroids and HLC organoids showed a similar trend with increased diffusion coefficients at higher diameters. HP spheroids with a mean diameter of 389  $\mu\text{m}$  had a  $D = 48.8 \pm 6.4 \mu\text{m}^2\text{s}^{-1}$  and HLC organoids with a mean diameter of 606  $\mu\text{m}$  showed a  $D = 130.5 \pm 11.1 \mu\text{m}^2\text{s}^{-1}$  (triangles). The adaptation of respective  $D$  values to spheroid and organoid diameters resulted in a linear increase of the perfusion times  $t_{90\%}$  with diameter. Thus, the DMSO perfusion is not quadratically dependent on the spheroids' diameter, which was expected with a constant  $D$ . The perfusion times range from about  $t_{90\%} = 1$  min for the radii of  $a = 125 \mu\text{m}$  to  $t_{90\%} = 8$  min for  $a = 500 \mu\text{m}$ . Corresponding perfusion times of the respective cell model, the diameter and the cultivation time can be taken from Fig. 39 F.

Supplementary to these results, two-photon excitation microscopy was performed to visualise diffusion routes and mechanisms qualitatively. Fig. 40 depicts the fluorescence staining of spheroids with fluorescein, rhodamine B and Hoechst 33342. Negatively charged, non-permeable fluorescein was detected along intercellular pathways within the extracellular space. Positively charged, membrane-permeable rhodamine B was observed extra- and intracellularly except within the nuclei. The nuclei of the peripheral cell layer were stained with membrane-permeable Hoechst 33342.

#### 4.4.2 Cryo-induced metabolic and adhesion effects with adapted CPA incubation

Before testing the effects of derived DMSO-d6 perfusion times using Raman micro-spectroscopy, the cryoprotective properties of DMSO-d6 compared to DMSO were evaluated. Large NSC spheroids were incubated in 10% DMSO, 10% DMSO-d6 or 10% DMSO/DMSO-d6 1:1 mix-

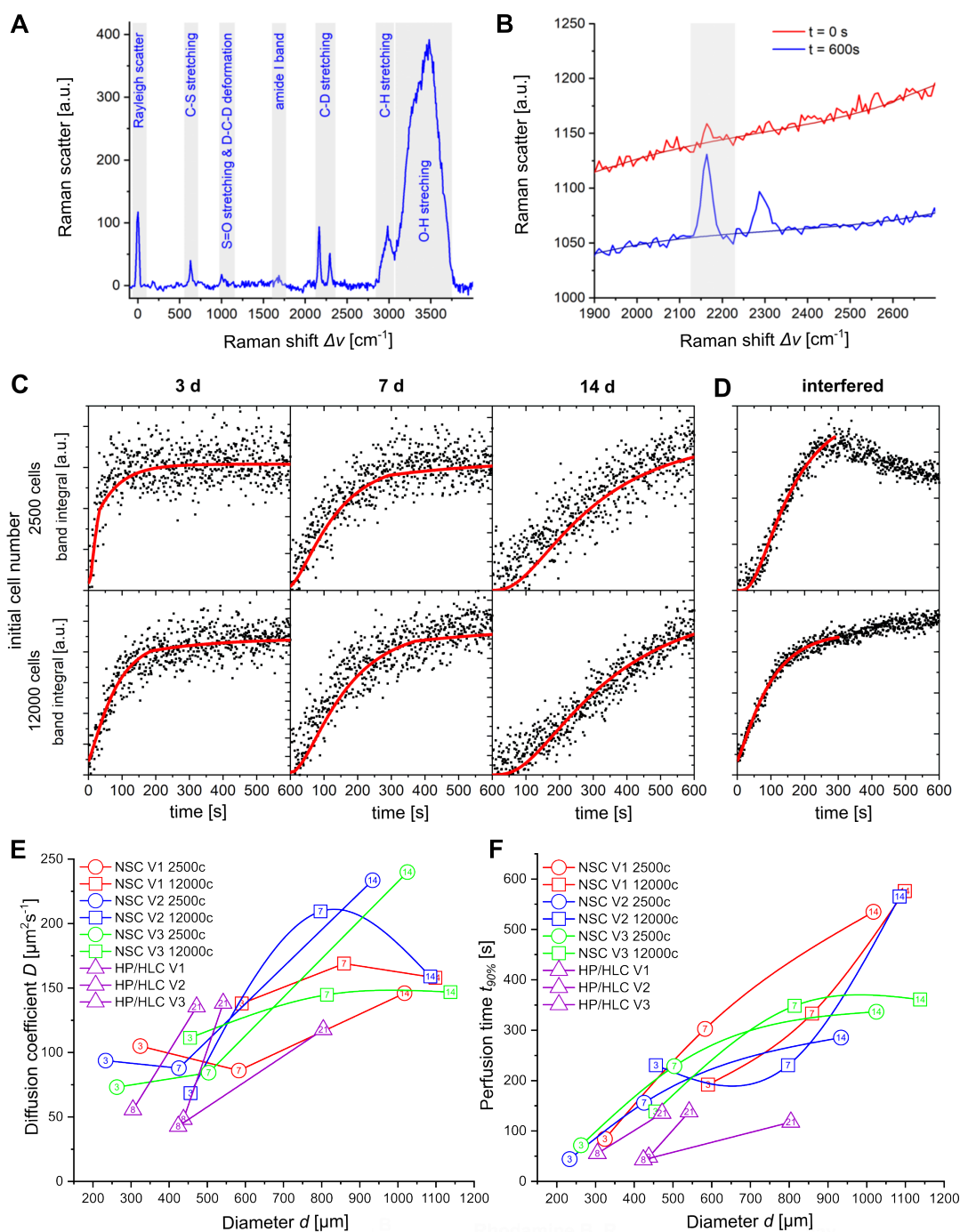


**Figure 39: Bioorthogonal Raman micro-spectroscopy to analyse DMSO-d6 perfusion in organoids.** (A) Representative background-corrected Raman spectrum of an NSC spheroid centre with vibration band assignments. (B) A relevant section of an early ( $t = 0$  s) and late Raman spectrum ( $t = 600$  s) after DMSO-d6 incubation. Band integral was calculated from the highlighted section after background correction. (C) Representative DMSO-d6 perfusion courses for spheroids with different initial cell numbers and ages. Each data point  $A(t)$  was obtained by integrating a section of the Raman spectrum as described by Eq. 2. The red fit curve was calculated according to Eq. 3. (D) Representative interfered data sets with partial fits. (E) Plot of diffusion coefficient  $D$  [ $\mu\text{m}^2\text{s}^{-1}$ ] and (F) perfusion times  $t_{90\%}$  [s] against the spheroid diameter  $d$  [ $\mu\text{m}$ ]. Circles represent data of spheroids with an initial NSC number of 2,500 cells and boxes of 12,000 cells. Triangles represent HP spheroids and HLC organoids. Cultivation days are given within the symbol,  $N=3$ ,  $n=4-6$ . Data published in Altmaier et al. 2024.

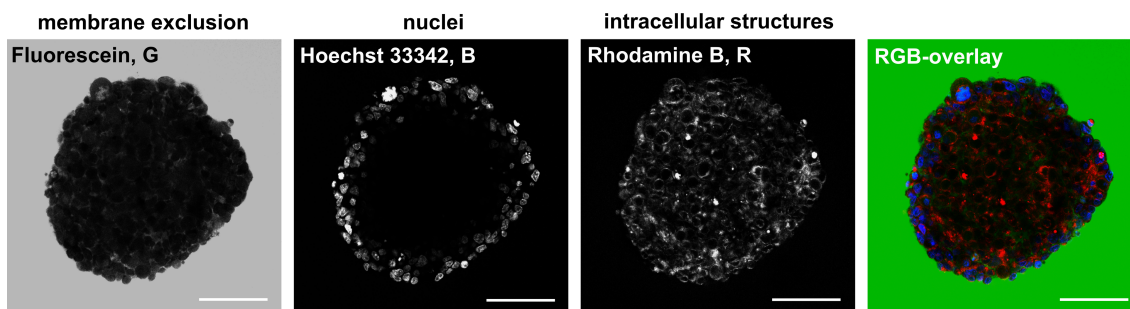


Figure 40: **Two representative multichannel images of NSC spheroids acquired by two-photon excitation microscopy.** Fluorescein highlights extracellular interspaces, while Hoechst 33342 and rhodamine B indicate intracellular structures. Images were recorded at a depth of 50  $\mu\text{m}$ ; scale bar represents 100  $\mu\text{m}$ ,  $N=3$ ,  $n=3$ . Data published in Altmaier et al. 2024.

ture for 5 min before slow-rate freezing. The samples incubated in NSC medium served as a negative control. Fig. 41 A shows the relative cell viability of spheroids during the recovery. A significant increase in viability was observed in all samples treated with DMSO 24 h, 3 d and 7 d a.t. compared to the medium control without DMSO. However, no significant difference was found between the samples pre-incubated with DMSO, DMSO-d6 and the mix. The analysis of adhesion functionality of three spheroids 7 d a.t. also showed successful fusion after DMSO-d6 pre-treatment. In comparison, spheroids only incubated in NSC medium before cryopreservation did not show adhesion properties (Fig. 41 B). These results showed no significant differences in the cryoprotective properties of DMSO-d6 and DMSO.

In the next step, based on the calculated DMSO-d6 diffusion kinetic derived from Raman micro-spectroscopy data, optimal incubation times for NSC spheroids with different volumes were determined to ensure a 90% diffusion of 10% DMSO in the spheroid core before cryopreservation. The incubation times ( $t_{90\%}$ ) should be as short as possible but as long as necessary to ensure sufficient supply while reducing DMSO-induced cytotoxic effects in the peripheral cells. Different NSC spheroids were incubated with 10% DMSO for 0 min, their respective  $t_{50\%}$  and  $t_{90\%}$  times and 15 min before cryopreservation. The 0 min and 15 min incubated samples served as controls, in which an insufficient or an excessive supply of DMSO was assumed. For small spheroids, the  $t_{90\%}$  was detected at 4:18 min and the  $t_{50\%}$  at 55 s. These values were increased in medium and large spheroids to  $t_{90\%}$  of 5 min and 5:41 min and  $t_{50\%}$  of 1:10 min and 1:25 min. Fig. 42 A shows the relative cell viability of NSC spheroids after thawing, which were incubated in 10% DMSO for different times at 4  $^{\circ}\text{C}$  before slow-rate freezing. No significant differences were observed between the pre-incubation times for all spheroids after thawing and at all recovery times. In addition, the viability staining of a medium spheroid at 18 h a.t. did not show any difference between all adapted DMSO incubation times before slow-rate freezing (Fig. 42 B). The perfusion times were previously determined at room temperature using Raman micro-spectroscopy, so the corresponding pre-incubation times were also tested at 20  $^{\circ}\text{C}$ . However, after increasing the incubation temperature from 4  $^{\circ}\text{C}$  to 20  $^{\circ}\text{C}$ , the relative

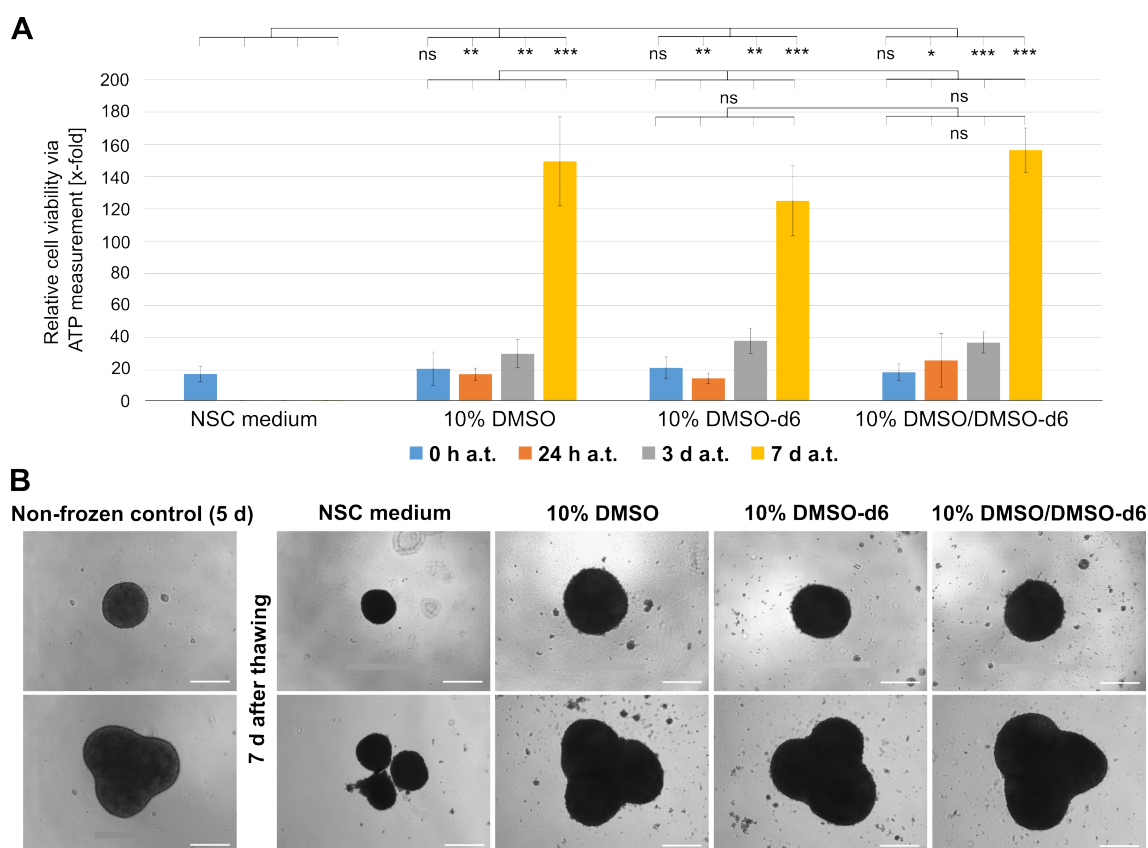


Figure 41: **Relative cell viability and fusion properties of NSC spheroids incubated in DMSO and DMSO-d6 before slow-rate freezing.** (A) Relative cell viability of spheroids during the recovery, incubated for 5 min in NSC medium, 10% DMSO, 10% DMSO-d6 or 10% DMSO/DMSO-d6 mixture before slow-rate freezing. (B) 24 h fusion of spheroids 7 d a.t., incubated for 5 min in DMSO variants before slow-rate freezing; scale bar represents 500  $\mu\text{m}$ ,  $N=3$ ,  $n=3$  ( $t$ -test, ns: not significant, \* $p$  value < 0.05, \*\* $p$  value < 0.01, \*\*\* $p$  value < 0.001).

viability of the cells in the medium NSC spheroids was reduced by about 50% for each condition (Fig. 42 C). No significant changes between the conditions were recorded. Additionally, the pre-treatment with 0.15 M sucrose for 1 or 24 h before 5 min DMSO incubation in medium spheroids did not affect the relative cell viability compared to non-treated spheroids (Fig. 42 D). After pre-treatment with 0.3 M sucrose, the relative cell viability decreased (Fig. 42 D).

In the next step, NSC spheroids were also cryopreserved by vitrification after DMSO incubation with the derived times  $t_{90\%}$  and  $t_{50\%}$ . In this experimental setup, spheroids were incubated in VS1 (10% DMSO and 10% EG) for their corresponding  $t_{90\%}$  and  $t_{50\%}$ . Then, the samples were incubated in VS2 (20% DMSO, 20% EG and 30% 1 M sucrose) for 20 sec, and vitrification was performed. The relative cell viability was significantly increased at 0 h and 24 h a.t. in all spheroids which were incubated with VS1 for their  $t_{90\%}$  compared to  $t_{50\%}$  (Fig. 43). In medium spheroids, a significant change in the relative viability of the cells was still observed 3 d a.t. These results indicate that the cell viability was significantly increased with the Raman micro-spectroscopy-derived DMSO incubation time  $t_{90\%}$ .

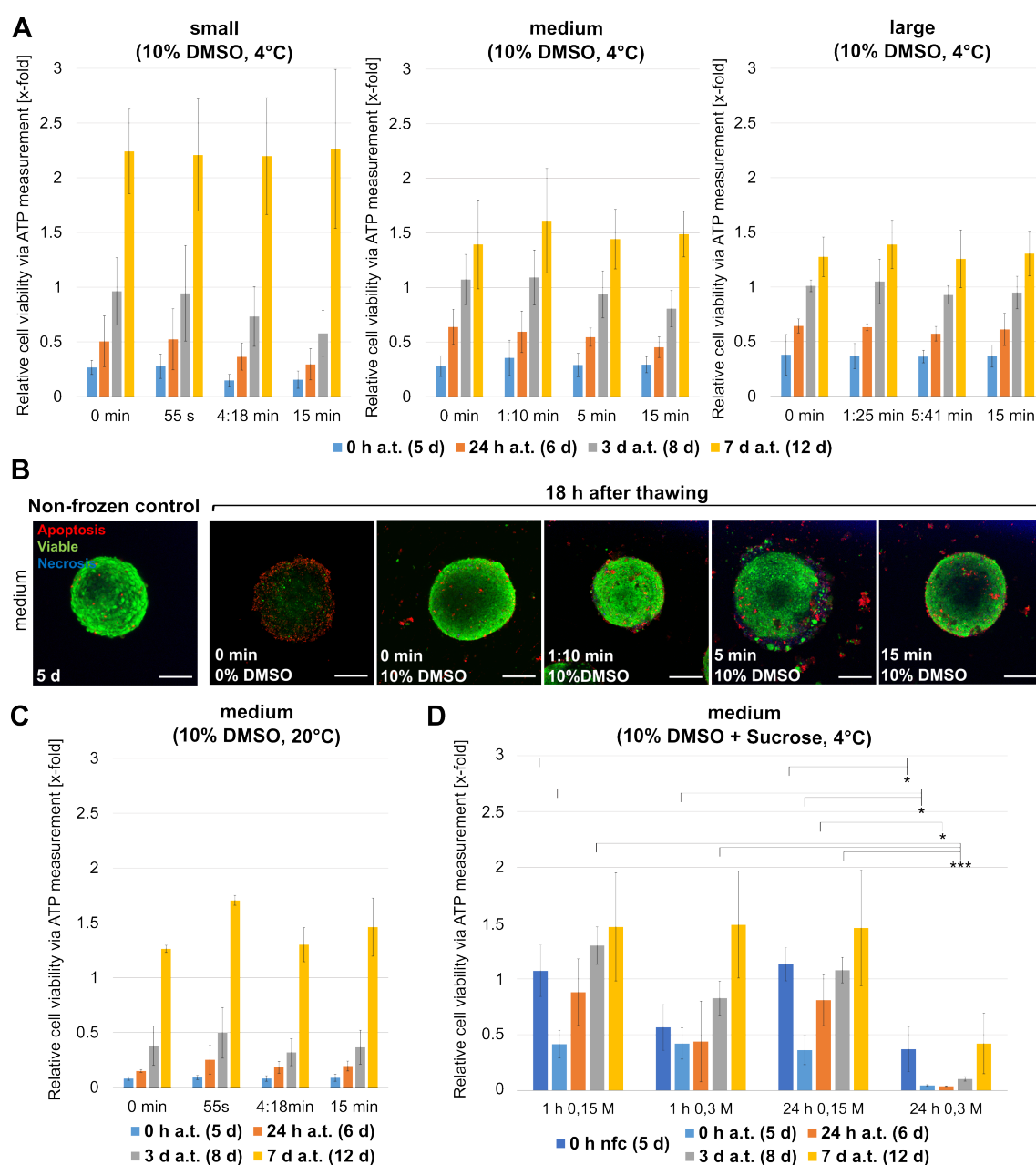


Figure 42: Viability analyses of NSC spheroids a.t., incubated in 10% DMSO for different times before slow-rate freezing. (A) Relative cell viability of small ( $\varnothing$  300  $\mu$ m), medium ( $\varnothing$  450  $\mu$ m) and large spheroids ( $\varnothing$  600  $\mu$ m) after DMSO incubation at 4 °C for 0 min, corresponding  $t_{50\%}$  and  $t_{90\%}$  times and 15 min before slow-rate freezing. (B) Viability staining of medium spheroids at 18 h a.t., treated with different DMSO incubation times; scale bar represents 150  $\mu$ m. (C) Relative cell viability of medium spheroids after DMSO treatments at 20 °C and (D) after pre-treatment with 0.15 M and 0.3 M sucrose and 5 min DMSO incubation at 4 °C before slow-rate freezing, N=3, n=3 ( $t$ -test, \*p value < 0.05, \*\*p value < 0.01, \*\*\*p value < 0.001).

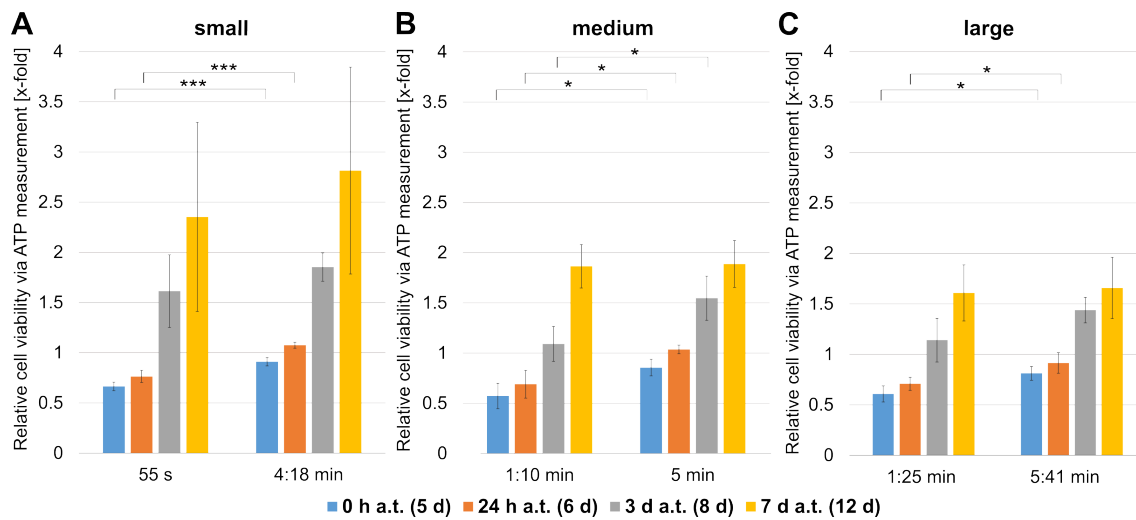


Figure 43: Viability analyses of NSC spheroids a.w., which were incubated in 10% DMSO for different times before vitrification. (A) Small ( $\varnothing$  300  $\mu\text{m}$ ), (B) medium ( $\varnothing$  450  $\mu\text{m}$ ) and (C) large ( $\varnothing$  600  $\mu\text{m}$ ) NSC spheroid were incubated with 10% DMSO for respective  $t_{50\%}$  and  $t_{90\%}$  incubation times,  $N=3$ ,  $n=3$  ( $t$ -test, \* $p$  value < 0.05, \*\*\* $p$  value < 0.001).

## 5 Discussion

The application potential of 3D cell models has significantly increased in the last decade (Jensen and Teng 2020, Silva-Pedrosa et al. 2023). Hence, the establishment of next-generation, function-maintaining, living biobanking of 3D cell systems would be groundbreaking for various biomedical research fields (Xie et al. 2023, Rogulska et al. 2023). A robust and standardised stock-keeping by cryopreservation would ensure a constant supply of complex 3D cell systems while facilitating the timing of long-term differentiation and maturation steps when the samples are needed. This thesis focuses on the understanding of cryo-related mechanisms to bridge a gap between the cryopreservation of 2D and 3D cell models and advance next-generation biobanking. The workflow to improve and accelerate the applications of ready-to-use 3D cell models by biobanking is summarised in Fig. 44. This process can be divided into five steps:

1. Extraction and cultivation of specific samples, such as cells extracted from primary tissues or stem cells (e.g. ESCs or hiPSCs).
2. Generation and cultivation of 3D cell models using a static or dynamic approach, depending on the requirements of the application.
3. Model-specific quality and functionality controls to ensure cell type specificity.
4. Cryopreservation and biobanking of 3D cell models to enable stock-keeping.
5. Warming and subsequent model-specific application of ready-to-use 3D cell systems in respective research fields.

The first three steps can be summarised as essential work to define the model system required for specific downstream applications before biobanking. In the first step, the cell source of the respective model has to be selected, extracted if necessary and cultivated. In this work, hiPSCs were selected as cell source with the potential to mimic human organ-like structures and physiology after differentiation and maturation. Following cell expansion, spheroids and organoids were generated by 3D cell culture. Depending on the requirements for homogeneity, reproducibility and throughput, different static or dynamic approaches were used (see section 4.1.3). Within the scope of this work, the protocols for 3D cell culture and characteristic quality controls of NSCs, HPs and HLCs were improved. The following step four is the cryopreservation and long-term storage of 3D cell models. The evaluation of samples after cryopreservation and warming with characteristic quality and functionality controls is an essential part of step five. In the following sections, the factors affecting the cryo injury effects in specific 3D cell systems are discussed in detail. In particular, the focus is on the influence of the volumes and maturation of the organoids, the cryopreservation regime and the diffusion kinetics of CPAs on the structural and functional integrity after cryopreservation. These studies provide new insights into the evaluation of 3D cell models after cryopreservation to enable various biomedical and pharmaceutical research and diagnostic applications.

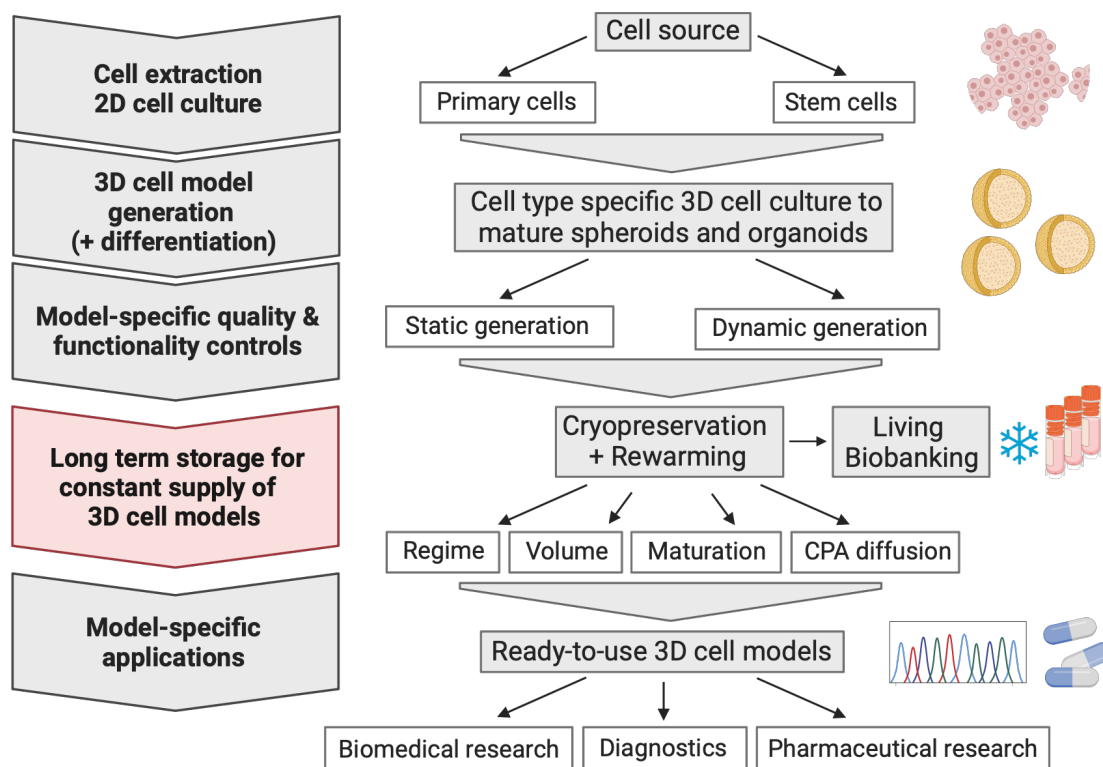


Figure 44: **Workflow to enable a constant supply of complex 3D cell models for biomedical and pharmaceutical research and diagnostics using living biobanking.** The process can be divided into 3D cell model generation before cryopreservation, long-term storage after cryopreservation and model-specific applications after thawing. Created with biorender.

### Different volumes of uniform precursor organoids influence the recovery after cryopreservation

Cryobiology aims to establish readily available and adaptable cryopreservation protocols for different cell models, including 2D and 3D cell systems, depending on characteristic model-specific factors. Influencing factors are cell type-specific, such as cell volumes, structural and membrane integrity or maturation stage. However, the influences of these factors on cryo mechanisms have hardly been considered in research to date. Thus, in the following discussion, the aspects of cell-model specificity on cryo effects were studied on 3D cell systems.

The first part of the discussion focuses on the influence of different diameters of uniform, single-cell-typed precursor organoids on cryo injury effects after cryopreservation. In a spherical 3D cell structure, like the NSC or HP spheroids, the diameters are directly correlated to the spheroid volume, affecting the thermal and mass transfer throughout the cell system. The radial distance from inner to peripheral cells is bigger in larger spheroids than in smaller spheroids. In theory, based on the calculation of the volume of the spheroid ( $V = \frac{4}{3} \cdot \pi \cdot r^3$ ), the volume

increases by the power of three when the radial distance (= radius) of the spheroids increases. Consequently, an exponential rise in spheroid volume due to cell proliferation theoretically leads to a proportional increase in the perfusion time of CPAs and increases the thermal gradient during freezing and thawing. This restricts the application of appropriate cooling and thawing rates and limits the CPA diffusion, both essential for an optimal cryopreservation result. The postulation is that the ice crystallisation becomes more challenging to balance by using standard cooling and thawing rates and conventional CPA concentration and perfusion times in larger spheroids. This implies the initial hypothesis that the spheroid volume significantly impacts cryo injury effects. However, since the generation and maturation of 3D cell models are constantly evolving to imitate more complex organ-like structures, the cell systems continue growing. Thus, investigations on the cryopreservation of spheroids with different volumes are becoming increasingly important. In addition, larger spheroids would maximise the cell throughput to achieve a higher quantity of functional cells depending on the applications, like for cell therapy in regenerative medicine (Rossi et al. 2018). Furthermore, with the long-term goal of enabling the preservation of whole or partial organs with adapted cryopreservation protocols to different volumes, associated cryo injury effects must be researched. One of the essential areas of research in this context is reproductive biology. To ensure adequate CPA penetration and reduce the thermal gradient, most publications about cryopreservation of ovarian tissue describe the use of cut tissue slices of 1-10 mm<sup>2</sup> with a maximum thickness of 2 mm (Diaz et al. 2022). Although larger tissue pieces would facilitate cutting and handling, cryopreserved tissue fragments larger than 2 mm that were slowly frozen according to the protocol of Lucci et al. 2004 showed abnormal follicular morphology (Ferreira et al. 2010). This is an exclusion criterion for the transplantation of these samples. The application aims to restore fertility by maintaining the functionality of the ovaries in the tissue and not necessarily the exact intercellular integrity (Agca 2000). According to Gellert et al. 2018, the endocrine function of cryopreserved ovarian tissue has been restored in 95% of women in 21 countries after different cryopreservation and transplantation methods. However, studies of the ultrastructure of ovarian tissue slices have shown that, depending on the cryopreservation protocol, changes in the cell structure can occur, e.g. shrinkage and detachment of oocytes, although functionality can be restored (El Cury-Silva et al. 2021, Mahmoudi Asl et al. 2021). In comparison, the diameters of successfully cryopreserved spheroids or organoids only range between 30 to 200 µm (Han et al. 2017, Beaumont et al. 2021, B. E. Lee et al. 2022). This may be explained by the limited preservation of the multicellular integrity with characteristic cell-cell interactions, which is often essential for maintaining the typical metabolism and functionality of many spheroids and organoids. Due to the increasing importance of 3D cell models, the number of studies focusing on the cryopreservation of spheroids and organoids has increased in recent years (Rogulska et al. 2023). Regarding the analysis of the influence of spheroid volumes on recovery after cryopreservation, only Jeong et al. 2020 investigated mesenchymal stem cell spheroids of various diameters (200-900 µm) after cryopreservation. Their analyses focus on the viability assessments post-thawing without emphasising the spheroid volumes.

In this thesis, it is hypothesised that spheroids of varying volumes contain distinct cell layers from the periphery to the centre, each with unique diffusion properties that influence cryopreservation. Thus, structural and metabolic analyses were carried out to investigate cryo injury mechanisms in uniform NSC spheroids with three different diameters (300  $\mu\text{m}$ , 450  $\mu\text{m}$  and 600  $\mu\text{m}$ ). Firstly, the effects of different spheroid volumes on the diffusion characteristics of the distinct cell layers were investigated. Therefore, the spheroids were generated with varying cell numbers at the same cultivation time based on the linear relationship between spheroid volume and cell number (Schmitz et al. 2017). Different cultivation times to generate different spheroid volumes by cell proliferation were avoided to ensure comparability between the samples in terms of the maturation of cell junctions and cell density. To ensure the reproducibility of the diameters, which was confirmed by high coefficient of determination ( $R^2$ ) values, the spheroids were generated in ULA plates (Fig. 11) (D. Liu et al. 2021, Wanigasekara et al. 2023). During the spheroid cultivation, a convergence of mean diameters from small spheroids to medium and large spheroids was observed, indicating an increased proliferation rate in spheroids with lower seeding cell numbers over time. The proliferation rate of small spheroids, which is defined as the increase of spheroid volume over time, increased exponentially, while the medium spheroids showed a linear and the large spheroids a more logarithmic diameter growth (Fig. 11 C). This is due to the maximum growth of spheroids, which is reached when the inner cells can no longer be supplied by radial diffusion and proliferation is slowed down. These results are consistent with those of Costa et al. 2016 or Rossi et al. 2018. Generally, avascular spheroids above a certain diameter consist of viable cell layers and a necrotic zone at a certain depth (Costa et al. 2016). The thickness of the viable cell layers depends on the diffusion coefficient and the cell network consumption of small molecules such as oxygen and glucose. Basically, the properties of these small molecules, such as size, charge and mass, are decisive for their diffusion kinetics in cells (Sokoloff 1977). The kinetics are further influenced by the temperature and cell type characteristics, such as the membrane permeability, the density of cells or specific cellular structures, like the number of tight junctions which serve as a physical barrier against intercellular diffusion of molecules (McMurtrey 2016, Saito et al. 2023). In general, the diffusion of molecules in tissues, such as cartilage, has been published to be about 40% of that found in solutions (McMurtrey 2016). The diffusion coefficients of various small molecules in tissues are typically around  $10^{-9}$  to  $10^{-10}$   $\text{m}^2/\text{s}$ . Values of smaller molecules like oxygen are closer to  $10^{-9}$   $\text{m}^2/\text{s}$  and larger molecules like glucose are closer to  $10^{-10}$   $\text{m}^2/\text{s}$ . The consumption of oxygen in human brain tissue is about 0.035 oxygen use per gram ( $\text{ml}/\text{g}\cdot\text{min}$ ), and the consumption of glucose is 0.31 glucose use per gram ( $\mu\text{mol}/\text{g}\cdot\text{min}$ ) (Herculano-Houzel 2011). These values are very variable in different tissues. However, the cellular network characteristics of human brain tissue are closest to those of NSC spheroids. Assuming maximum oxygen and glucose consumption values and a diffusion coefficient at the lower range, the thickness of viable neuronal cell layers is only about 250  $\mu\text{m}$  (McMurtrey 2016). With an average metabolic activity and diffusivity, the thickness of viable tissue is estimated at a maximum of 1.4 mm (McMurtrey 2016). Dynamic

cultivation approaches can improve these dimensions (Volkmer et al. 2008). However, cell viability decreases exponentially with increasing distance to the spheroid surface and proliferation is reduced in still viable but quiescent zones. Glicklis et al. 2004 reported oxygen limitation in hepatic spheroids above a radial depth of 100  $\mu\text{m}$ , resulting in an exponential increase in cell death. This indicates the significant variability in the thickness of viable cell layers, which depends on metabolic activity and nutrient diffusion correlated to the cell types, tissue shape and temperature. In addition, the growth of spheroids or tissues also induces the accumulation of by-products of cellular respiration during ATP formation, such as  $\text{CO}_2$ . The limited diffusion and removal of cellular waste products and the increase of  $\text{CO}_2$  concentration lead to decreased pH that impairs cell metabolism (Busa 1986). Besides the radial diffusion of extracellular molecules, the growth kinetic of avascular spheroids is also restricted by internal waste agglomeration. So far, the thickness of the viable cell layers of NSC and HP spheroids can only be estimated by the nutrient diffusion and consumption analyses in human brain tissue and hepatic spheroids (Glicklis et al. 2004, McMurtrey 2016). Based on these reports, it can be assumed that these single-cell-type, spherical precursor organoids with a diameter of 300-600  $\mu\text{m}$  consist of outer proliferating, viable cell layers of 100-250  $\mu\text{m}$  before cells start to quiescent and undergo diffusion-induced necrosis. Thus, in small spheroids with a diameter of 300  $\mu\text{m}$ , there should be fewer necrotic cells, whereas in medium ( $\text{Ø}$  450  $\mu\text{m}$ ) and large ( $\text{Ø}$  600  $\mu\text{m}$ ) spheroids, there is probably a necrotic core with a diameter of about 50  $\mu\text{m}$  up to 300  $\mu\text{m}$ . The proliferation analyses of inner NSCs in spheroids support this estimation (Fig. 33). The percentage of proliferating cells decreases with the depth of the cell layer. However, the necrotic status of the core cells could not be identified due to the limitations of the clearing technique. The integration of microsensors into avascular spheroids would be advantageous to determine the model-specific oxygen and glucose consumption (Dornhof et al. 2022, Rousset et al. 2022). Microsensors could also measure osmotic-induced tension on the plasma membranes or the pH shift in undersupplied cells (Charras and Yap 2018, Rizzo et al. 2022). This approach would help to accurately predict the thickness of the viable cell layer in different avascular 3D cell models. According to the current assumptions, the thickness of the viable, proliferating cell layers remains the same in different spheroid diameters, but the volume of viable cells increases by the power of three with radial spheroid growth. The quiescent zone and necrotic core grow to a maximum, depending on the avascular growth kinetics. Schmitz et al. 2017 also postulated that the diameter of the necrotic core region is not proportional to the diameter of the spheroid. The peripheral viable cell layers are relatively thinner in larger spheroids but have a larger volume than in small or medium spheroids.

In the next step, the impact of the different thicknesses and diffusion characteristics in the distinct cell layers on cryo injury effects were analysed comparatively with precursor organoids of different diameters. After cryopreservation, a decrease in all spheroid diameters and corresponding volumes was observed during the recovery compared to the nfc at the respective cultivation times (Fig. 19 A). Most mammalian cells can lose about 50% of their intracellular

water before severe dehydration damages occur (Meryman 1970, Clegg et al. 1982). According to the measurements of individual NSCs in suspension, the NSCs have a mean diameter of  $13 \mu\text{m} \pm 1 \mu\text{m}$ . Assuming that a 50% water efflux also causes a volume decrease of 50%, the diameter of the cells would shrink to approx.  $6 \mu\text{m}$ . Additionally, interconnected, flat cells have even smaller radial diameters than spherical-shaped single cells. Thus, only osmotically-induced shrinkage of single cells in the surface layer cannot explain the observed loss of spheroid diameters in a range of about  $60 \mu\text{m}$ . The spheroid volume decrease is more likely due to the delayed proliferation by cryopreservation and the complete detachment of the peripheral cells between 24 h and 3 d a.t. The suppression of proliferation after cryopreservation has already been shown in granulosa cells of ovarian tissue by the reduction of specific cyclin expression levels. This could be related to the delayed follicle development in cryopreserved ovarian tissue (Choi et al. 2008). In other cell types, such as mononuclear blood cells, a 48 h delay in proliferation was also observed after cryopreservation, causing a change in cytokine levels (Kvarnström et al. 2004, Jeurink et al. 2008). In the precursor organoids studied here, this effect is further enhanced by the additional detachment of the peripheral cells. Thus, the proliferation-induced increase in spheroid volume in medium and large spheroids only begins after 3 d of recovery. In small spheroids, the proliferation rate is higher, and there is no growth-inhibiting necrotic core. Thus, the spheroid volume increases between 24 h and 3 d a.t. (Fig. 19).

The results were confirmed by analysing the proliferation of peripheral and inner NSCs in spheroids after thawing (Fig. 33 C). The percentage of proliferating cells after 24 h in the outer cell layers was similar to that of nfc, but the volumes of the spheroids were smaller (Fig. 33 E). This indicates that the peripheral cell layers detached after 24 h, and the new outer cells showed a high proliferation rate, which explains the increase in volume between 24 h and 3 d a.t. The viability staining revealed that the detaching, apoptotic cell layers had a diameter of  $37 \mu\text{m} \pm 2 \mu\text{m}$  in small,  $36 \mu\text{m} \pm 4 \mu\text{m}$  in medium and  $35 \mu\text{m} \pm 4 \mu\text{m}$  in large spheroids (Fig. 17, Fig. 23). Although the spheroids were generated with different diameters, the detached surface cell layers had approx. the same diameter. Assuming that contiguous NSCs in a spheroid are less spherical than in suspension with a mean diameter of  $13 \mu\text{m} \pm 1 \mu\text{m}$ , about three cell layers will probably detach in each case. Hence, the initial hypothesis that the spheroid volume significantly impacts cryo injury effects based on limited CPA diffusion and increased thermal gradients was not confirmed for avascular, spherical precursor organoids up to a diameter of  $600 \mu\text{m}$ . Both small and large spheroids showed similar cryo-damaging effects, such as the detachment of the peripheral cell layer with similar thickness and comparable proliferation recovery trends. This indicates that the percentage ratio of the volume of viable cells before freezing ( $V_1$ ) to the volume of apoptotic, peripheral cells ( $V_{cryo}$ ) is increased in smaller spheroids. Thus, the percentage of viable cell loss is not proportional to the spheroid diameters or volumes. The relative cell loss is higher in smaller spheroids and increases logarithmically with increasing volume (Fig. 45). Only considering the loss of cell volume of the three outer cell layers, small spheroids lose 45% of their cell volume, whereas medium and large spheroids are decreased by 40% and 31%. However, the proliferation of the inner viable cells compensates for

the loss of volume, and the maximum spheroid volume can be reached with a delay of about 2 d in small and 3 d in medium and large spheroids. The analyses of the relative cell viability over recovery time confirm the previously described conclusions (Fig. 20 and Fig. 21). The viability was significantly reduced after thawing compared to nfc. This was also shown by the lower ratio of viable and apoptotic cells in small spheroids 24 h a.t. compared to large spheroids (Fig. 23 C). Nevertheless, a delayed, similar increase between 3 d and 7 d was detected in all spheroid diameters (Fig. 20 and 21). In addition, the *CDH1* expression was significantly up-regulated 24 h a.t. (Fig. 24). This gene encodes for Cadherin-1, a cell-cell adhesion glycoprotein that acts as a transmembrane protein in adherens junctions. This leads to the assumption that the adherens junctions started to recover after cell detachment and new cell-cell connections are formed.

In summary, the static recovery of cell proliferation and viability in ULA plates after slow freezing of precursor organoids was achieved by cooling rates of  $-1\text{ }^{\circ}\text{C}/\text{min}$  and by adding cryopreservation media with 10% DMSO. However, the proliferation was delayed, and peripheral cells were detached in each condition. The cryo injury effects were similar in different spheroid volumes, but in principle, the volume of spheroids is an important parameter that must be considered for the subsequent application before cryopreservation. The cryopreservation of large spheroids is suitable if the subsequent application requires a large quantity of viable, functional cells, such as for cell therapies following spheroid dissociation (Rossi et al. 2018), or for the production of desired molecules like insulin (Dayem et al. 2019). In contrast, the preservation of small spheroids is more suitable when high proliferation rates are required after thawing, like for differentiation protocols. However, these conclusions were only drawn for avascular, spherical spheroids with homogeneous cell densities and radial diffusion and heat transfer. Schmitz et al. 2017 postulated heterogeneous cell densities ranging from  $5\cdot 10^5$  to  $1\cdot 10^6/\text{mm}^3$  in the outer cell layer of breast carcinoma spheroids. This can lead to inhomogeneous CPA penetration and non-uniform thermal transfer, which can impair cryopreservation in denser regions of the spheroid. Hence, in addition to the effects of different spheroid diameters, the influence of other crucial factors on the mechanisms of cryo injury, such as heterogeneous cell densities and asymmetric shapes of 3D cell systems must be investigated further in the future.

### **Static and dynamic cell culture influence the recovery of precursor organoids after cryopreservation**

Regarding the proliferation of spheroids generated and recovered in the CERO 3D bioreactor, a volume reduction of about  $20\cdot 10^6\text{ }\mu\text{m}^3$  corresponding to a diameter reduction of about  $60\text{ }\mu\text{m}$  was detected 24 h a.t. (Fig. 18 and 19 B). Also, in this setup, a cell layer of approx.  $30\text{ }\mu\text{m}$  was detached after thawing. This confirms the hypothesis that a cell layer of the same thickness undergoes apoptosis and detaches, regardless of the spheroid diameter and the type of generation or recovery. After 48 h, the spheroid volumes increase linearly until the growth slows down

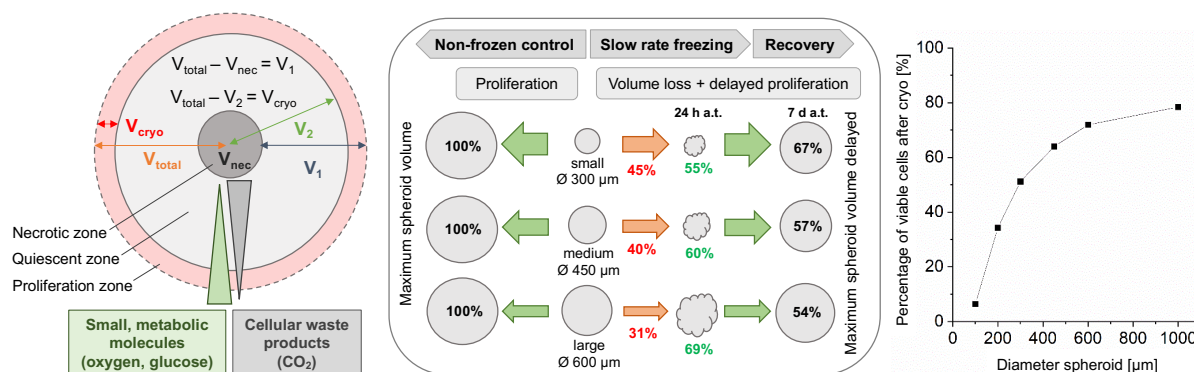


Figure 45: **Percentage volume decrease of spheroids with different diameters due to the detachment of peripheral cells in the proliferating zone after cryopreservation ( $V_{cryo}$ ).** The percentage volumes of detached, peripheral cell layers in all spheroids are shown in red, indicating a percentage higher cell loss in smaller spheroids. The remaining percentage volumes of spheroids 24 h after thawing are indicated in green and the percentage volumes of spheroids 7 d after thawing and the respective nfc are shown in black.

with a logarithmic progression 6 d a.t. However, compared to nfc, no significant differences in the relative volumes were detected (Fig. 19 C). These differences compared to static recovery in ULA plates can be explained by the improved perfusion of nutrients and oxygen through the bioreactor system (Malda et al. 2007, Volkmer et al. 2008). Additionally, spheroids collide with each other during the dynamic rotation of the bioreactor, which enables a faster detachment of the apoptotic cell layers after thawing and thus a quicker supply of inner cells and higher proliferation rates (Martin et al. 2004, Zhao et al. 2016). The results of the relative cell viability analyses support this fact (Fig. 22). Already 3 d a.t., the viability was 1.8-fold (viability by ATP measurement) and 2.2-fold (viability by membrane integrity) higher than in the nfc.

In addition to the improvements in dynamic 3D cultivation methods, the influence of cryopreservation formats must also be considered in this context. Spheroids cultivated in the CERO 3D bioreactor were cryopreserved in cryovials, which are specifically designed for the cryopreservation of cells, while spheroids from ULA plates were cryopreserved in the same plates. The polystyrene of the ULA plate is thicker than the polypropylene of cryovials, and the wells are separated by air. This impairs the heat-conducting properties so that the cooling or heating rates generated by the freezer or incubator are not transferred fast and homogeneously to the samples (Meneghel et al. 2020). This inhomogeneous thermal profile across the plate can lead to different recoveries between the samples and experiments. So far, no optimised container or device for the cryopreservation of spheroids or organoids exists. However, the demand for assay-ready cryopreserved plates with single spheroids per well is increasing (TerWee et al. 2011, Tomás et al. 2022). Therefore, these comparative studies on different cryopreservation containers and static and dynamic 3D cell cultures for recovery are essential for developing application-oriented formats for the cryopreservation of 3D cell systems.

In summary, NSC spheroids, generated and recovered in the CERO 3D bioreactor, also showed a detachment of the outer cell layers but no significant differences in relative volumes and viability in nfc and after thawing, indicating higher proliferation rates during dynamic than static recovery.

### **Pro-apoptotic stress factors influence precursor organoids after cryopreservation**

To improve the recovery of cell viability, further investigations on apoptosis-suppressing additives were carried out. Apoptosis is referred to as programmed cell death by an extrinsic or intrinsic trigger of caspases. The induction of this complex biochemical pathway inactivates cell survival and activates cell death (D'Arcy 2019). A network of many cryopreservation-related osmotic and cold stress factors is assumed to trigger apoptosis in mammalian cells by activating the caspase-8 and caspase-9 pathways. This includes the formation of reactive oxygen species (ROS), the activation of the ROCK pathway, F-actin rearrangements and the activation of *TP53* by DNA stimulation (Xu et al. 2010, Vining et al. 2021). However, the complete mechanism of apoptosis induction by cryopreservation is still unclear. It has been shown that the presence of ROCK inhibitors suppresses the activity of caspase-8 and caspase-9, leading to an inhibition of apoptosis and higher recovery (Bishop and Hall 2000, Etienne-Manneville and Hall 2002). The ROCK inhibitors Y-27632 and Chroman 1 are known as potent additives to regulate ROCK pathways, including proliferation, migration, and apoptosis through control of the actin cytoskeleton. The use of ROCK inhibitors leads to a decrease of stress fibres and facilitated interactions of myosin with F-actin, causing an enhanced actomyosin contraction and an increase of focal adhesion (Liao et al. 2007). X. Li et al. 2008, Claassen et al. 2009 and others showed an improved recovery of cryopreserved hESCs and hiPSCs using ROCK inhibitors, as they promote the formation of focal contacts. These positive effects were also observed in 2D NSC culture (Rungsiwut et al. 2013). However, in this work, the application of ROCK inhibitors did not improve the cell viability of cryopreserved NSC spheroids after thawing (Fig. 25). This leads to the conclusion that the activation of ROCK pathways plays a minor role in the cryopreservation of NSC spheroids compared to other cryo-induced factors. ROCK inhibition could not stop the induction of apoptosis and detachment of peripheral cells after thawing.

Furthermore, the activation of other cryo stress factors was investigated using RT-qPCR (Fig. 24). Even though apoptosis was shown in peripheral cells, both apoptosis regulator genes *BAX* and *TP53* were not significantly higher expressed after cryopreservation. Similarly, there was no up-regulation of the stress marker *HSF1*, which regulates the heat shock response, and *SOD1*, which controls the cellular response to ROS. This leads to the initial assumption that typical cryo-induced stress factors, such as apoptosis and ROS, were less prevalent in NSC spheroids after freezing and thawing. However, it is important to emphasise that all cells of the spheroids were lysed and analysed using RT-qPCR. Since the volume of peripheral apoptotic cells after

thawing is lower compared to the inner cells, their gene expressions were less significant. This implies that mostly the inner cells were not affected by apoptosis or ROS. Gene expression analyses using only the peripheral cells were not successful due to the limited possibility of isolating only the outer cell layer and the insufficient number of cells. In the next step, single-cell RNA sequencing could be performed to analyse the expression of specific markers in all individual cells of the spheroids and to identify related groups of peripheral and inner cells. Another striking result was the significant up-regulation of *OCT3/4* expression in all samples. This gene is typically expressed in stem cells and verifies pluripotency. Higher expression of *OCT3/4* indicates de-differentiation of NSCs to hiPSCs. It has been shown that in mammalian cells and tissues, de-differentiation pathways can be initiated by severe stress factors, especially oxidative stress (Ren et al. 1998, Shoshani and Zipori 2011). This reaction may protect the cells to maintain essential functions and initiate cell recovery. In this context, the effect can be explained by intracellular mechanical and metabolic cell stress during spheroid proliferation, which may cause this reprogramming (McEvoy et al. 2020). After cryopreservation, the cells are additionally exposed to various cryo-induced stress factors, like oxidative stress. However, the relationship between stress-induced de-differentiation by proliferation or cryopreservation in spheroids has not been published elsewhere.

In conclusion, the viability staining confirmed the apoptotic state of the outer cells, however, the application of ROCK inhibitors did not significantly improve the recovery of the cell viability after thawing. Furthermore, analysis of the expression of pro-apoptotic and oxidative stress genes in all cells of the spheroids showed no upregulation, indicating a low level of apoptosis and ROS in the inner cells, which was not possible to detect only for the peripheral cells. Single-cell RNA sequencing could be the next step to prove this hypothesis.

### **Structural 3D cell integrity of precursor organoids changes after slow freezing**

Initial quality control of precursor organoids revealed decreased adhesion and viability of the peripheral cells after slow-rate freezing and thawing. Detailed investigations on the structural cell integrity should clarify the induction of apoptosis and detachment. According to the Two-factor hypothesis from Mazur (Mazur et al. 1972), successful cryopreservation of cells depends, among other things, on the optimal cooling rate, which is influenced by cell type characteristics. Intracellular super-cooled water has a higher chemical potential than the extracellular frozen compartment, creating a balance between the dehydration of the cells and the concentration of intracellular solutes (Mazur 1963). Non-optimal cooling and thawing rates, together with CPA cytotoxicity, can lead to osmotic stress, intracellular ice formation and solution effects. In this case, harmful cryo injuries, such as ruptures of membranes, damaged cytoskeleton, biochemical alterations and DNA fragmentation, can cause apoptotic cell death (Lovelock 1953, Mazur 1977, Lin and Tsai 2012, Chatterjee et al. 2017). Compared to single cells, 3D cell systems consist of a network of different cell types, cell densities and cell-cell interactions, significantly

influencing cryopreservation success (McEvoy et al. 2020). Constant cooling and thawing rates in 3D cell systems lead to inhomogeneous cooling and heat transfer through the cell layers, resulting in harmful temperature gradients from the periphery to the core. In consequence, cells are exposed to different, non-optimal cooling and thawing rates. Hence, cooling-induced dehydration is suboptimal and inhomogeneous between different cell layers leading to osmotic stress that causes cell deformations and tensile stress between adjacent cells and the ECM. This may result in broken cell junctions, damaged membranes or impaired cytoskeleton components that compromise the structural cellular integrity (Karlsson and Toner 1996). Furthermore, gap junctions between cells promote ice propagation through the system, enhancing shear stress and mechanical disruptions (Acker et al. 2001, Irimia and Karlsson 2002). This increases the cryo-induced stress factors in 3D cell systems compared to 2D single cells. These adverse cryo effects have been shown in adherent cell monolayers and some 3D cell systems. For instance, reduced viability and altered cell ultrastructures of primary rat hepatocyte spheroids after slow freezing were published in Magalhães et al. 2012. As another example, in Stokich et al. 2014, only a 10% recovery of human hepatocellular carcinoma cells that were slowly frozen in an adherent monolayer was observed, compared to a 90% recovery after freezing in a cell suspension. These studies show that 3D cell networks are more severely damaged by cold injury than single cells due to limited dehydration and disruption of cell connections. The investigations on the structural cell integrity in this thesis support these results. The ultrastructure analyses of the peripheral NSCs after slow-rate freezing revealed a reduction of cell-cell junctions in small and large spheroids (Fig. 30). The disruptions of cell-cell junctions indicate a loss of cell adhesion. Consequently, the cells took on a spherical shape like detached single cells in suspension. In addition, the ultrastructure of these cells is probably comparable to that of apoptotic cells in terms of condensation, segmentation from other cells and fragmentation (Falcieri et al. 1994), which could confirm apoptotic cell death in the periphery. Further studies on nuclear changes, such as the irregular condensation of chromatin and the formation of apoptotic bodies (Ihara et al. 1998), could support this assumption. The accumulation of disruptions in the peripheral cell layer can be explained by the spheroid model of McEvoy et al. 2020. They presented a spheroid model with non-uniform solid growth stress that influences the cell volumes in multicellular spheroids. The proliferation-induced mechanical stress leads to a water efflux from core cells by ion transportation to reduce membrane tension. The controlled ion flow through gap junctions causes an increase in the osmolarity in adjacent cells. Water from inner cells is transported to the periphery. Therefore, due to the larger volume of dynamic water, the adaptation to osmotic stress during freezing and thawing by shrinkage is more extreme in the peripheral cell layer. The larger the cell volume, the higher the gradient and the osmosis rate due to increased water potential (Maffly and Leaf 1959). The cells shrink relatively more to increase the intracellular concentration of solutes and prevent intracellular ice formation. However, most mammalian cells can only lose about 50% of their intracellular water before lethal effects occur, such as harmful deformations by plasma membrane and cytoskeleton ruptures (Meryman 1970, Clegg et al. 1982). Thus, intracellular ice formation or extensive adaptations of the cytoskeleton and

membranes can disrupt cell connections in the periphery and trigger apoptosis. The inner cells are smaller and have a lower water volume, which reduces deformation. This finding is part of the hypothesis shown in Fig. 46.

### **Cell-cell junctions of peripheral cells rupture in organoids after slow freezing**

In summary, attached and cross-linked cells have a limited ability to regulate volume during cryo-induced excessive osmotic dehydration, leading to disruption of cell connections, reduced viability and cell loss. The characterisation of F-actin and N-cadherin has confirmed these results after thawing (Fig. 31). N-cadherin is a transmembrane glycoprotein and functions as a calcium-dependent adhesion protein. This protein is part of desmosomes and adherens junctions to stabilise cell contacts, support migration and promote embryonic development in early neural tissues (Blaschuk 2022). The expression of N-cadherin is reduced directly and at 6 h a.t. while recovery was observed after 24 h. Together with the fact that the cells took on a spherical shape, it is reasonable to assume that the peripheral cell layers had already detached after 24 h, which was probably facilitated by several washing steps for the staining. The rapid decrease in N-cadherin also supports the hypothesis that the outer cell layer detaches and no transport of the inner cells to the periphery occurs. F-actin expression was also reduced, with only a slight recovery at 24 h a.t. This cytoskeleton protein is an essential component of the cytoskeleton in eukaryotes and is responsible for various cytoskeleton-related functions such as migration or volume regulations (Kadzik et al. 2020). In adherens junctions, N-cadherin is connected indirectly via other adhesion proteins with F-actin. Together with the loss of cell-cell connections, the cell rounding triggers the re-organisation of F-actin up to degradation and phagocytosis at the final stage of apoptosis (Desouza et al. 2012, Charras, C.-K. Hu, et al. 2006). In comparison, the adhesion proteins in inner cells remained intact due to more appropriate dehydration and fewer ruptures of the cell junctions. This assumption is supported by the analysis of the inner cells in spheroids 24 h a.t. after clearing (Fig. 33 E). The clearly defined circular region of reduced marker expression in a depth of 50  $\mu\text{m}$  suggests a decreased diffusion of the antibodies in these zones. The intensity of marker expression in this depth is comparable to nfc. It can be hypothesised that the apoptotic peripheral cell layer with a thickness of about 30  $\mu\text{m}$  is already detached 24 h a.t. and the new peripheral layers are still proliferating, but cells are less densely packed due to cryo injury effects. This can accelerate the diffusion of the antibodies in the outer zones, leading to higher antibody concentrations and an increase in antigen bindings. Hence, these results indicate that besides the apoptotic peripheral cell layer that detaches between 0 h and 24 h, the previous intermediate zone is also affected by the cryo injury effects. However, after recovery and detachment of apoptotic cells, the adhesion properties of these cells can be restored. These findings correspond to the morphological assessment of the fusion properties of NSC spheroids after thawing (Fig. 32). The spheroids did not grow together directly after thawing, whereby after a recovery of 7 d, the fusion of the spheroids was comparable to nfc. This confirms the apoptotic state of the peripheral cells, which is directly associated with the

loss of functionality of the adhesion proteins at the cell junctions but also shows the recovery of the new outer cells.

In this context, the influence of the myosin II inhibitor Blebb and PO was investigated to improve the adhesion of peripheral cells after slow-rate freezing (Fig. 34 and 35). Blebb stabilises the myosin-ADP-Pi complex, inhibiting the myosin ATPase activity, which relaxes the interactions between the actomyosin filaments. With this relaxation, the stiffness of the cells decreases. The hypothesis is that the peripheral cells can better adapt to the cryo-induced rearrangements and deformations of the cytoskeleton with Blebb, which leads to higher adhesion and viability. Positive effects of Blebb for cryopreservation have been shown for retinal organoids (Luo et al. 2021). However, in their study, a Blebb-containing medium was examined, but no medium without Blebb was analysed comparatively. In this thesis, a positive effect of Blebb on cell viability of cryopreserved spheroids was only observed in small spheroids 24 h a.t., but without statistically significant difference (Fig. 35 A). This suggests that a 30 min pre-incubation before cryopreservation may not be sufficient to relax the actomyosin filaments to improve post-thaw viability. However, a significant inhibitory effect of 10  $\mu$ M Blebb was detected in M2 macrophages already after incubation for 30 min (Várkuti et al. 2016), which suggests that a longer incubation period is very unlikely to produce stronger effects. There may be a different reaction time in cross-linked NSCs in spheroids, but probably the cryo-induced dehydration of the cells was too intense, so the blebbistatin-induced actomyosin relaxation was not sufficient to support the adhesion of the cell and prevent detachment. Nevertheless, these analyses investigated the viability of complete spheroids and not only the peripheral cell layer. Hence, additional studies on the ultrastructure or fusion properties after Blebb treatment would be beneficial in proving the hypothesis. The addition of non-ionic surfactant PO for 24 h a.t. also showed no significant positive effects. PO lowers surface tension and reduces the formation of bubbles and foam in cell culture media (Apostolidis et al. 2015). The incorporation of PO into the plasma membrane of mammalian cells increases the membrane fluidity, which protects the cells from hydrodynamic shear stress, especially in bioreactors (Chang et al. 2017, Safta et al. 2024). Positive cryoprotective properties through the stabilisation of cell membranes have already been demonstrated, e.g. with an increase in the viability of human colorectal adenocarcinoma cells after cryopreservation (González Hernández and Fischer 2007, Kerleta 2010). Theoretically, PO should improve the viability of cells by preventing membrane rupture resulting from cryo-induced mechanical stress. However, in NSC spheroids, no significant differences were found in the viability of the cells with or without PO addition after thawing. This was independent of the static or dynamic recovery (Fig. 35 B, 34). This indicates that the protective properties of the surfactant PO are insufficient to prevent detachment, like for Blebb addition. Additional structural studies and investigations of pre-incubation before freezing would provide further insights into the effects of PO on spheroids' recovery.

To summarise, the analyses of structural cell integrity confirm the previous conclusion of pe-

peripheral cell detachment by proliferation and viability assessments. In general, cell adhesion is essential for communication between cells and their environment to maintain and develop their characteristic physiology. These connections get lost in peripheral cells of precursor organoids after slow-rate freezing. Promising approaches to overcome this problem combine a gradual slow cooling with directional freezing (see section 2.2.4). Peripheral cells would have more time to slowly adapt their membrane and cytoskeleton to the osmotically-induced dehydration. Membrane ruptures and IFF could be reduced, while at the same time, solution effects were avoided by sufficiently rapid dehydration in the inner cells (Arav and Natan 2012, Maffei et al. 2014). Another approach to maintaining structural integrity is vitrification, which is discussed in one of the following sections (see pages 96-98).

### **Cryo-induced effects are comparable in uniform precursor organoids with ectodermal and endodermal origin**

To elucidate the effects of tissue specificity on cryo-damage mechanisms, the effects in HP precursor organoids of endodermal origin (Fig. 26) were compared with those in NSC spheroids of ectodermal origin. The morphological analyses according to the cell debris and reduced spheroid area 24 h a.t. indicate apoptotic cell death in both models (Fig. 27 A). Like in NSC spheroids, the proliferation and viability of HP spheroids were increased again during the dynamic recovery. In addition, cryopreserved HP spheroids showed a significant decrease in the relative expression of the metabolic marker *CYP3A4* 24 h a.t. with a following increase after 3 d. During the recovery after 7 d and 14 d, the marker expressions were comparable to the nfc (Fig. 27 B). As a member of the cytochrome P450 family, the protein CYP3A contributes to the oxidation of small organic molecules, such as drugs or toxins (Michaletts 1998). It is mainly expressed in primary hepatocytes and indicates metabolic activity in successfully differentiated hepatocytes. Due to the recovery of *CYP3A4* expression after thawing to the nfc level, a regeneration of metabolic activity can be assumed (Altmaier et al. 2022). Other studies with cryopreserved human single hepatocytes (Yajima et al. 2014, Sudo et al. 2017) or human liver hepatocellular carcinoma cells spheroids (Bissoyi et al. 2023) support these results by reporting a similar successful recovery of the metabolising activity of CYP3A4 after slow-rate freezing. Furthermore, all hepatic gene markers were increased again in HP spheroids after thawing. Although the expression generally remained lower than in nfc, the trend of the expressions developed similarly to the nfc according to their maturation status (Fig. 28 A). Comparable gene expression patterns for *ALB*, *HNF4A* and *CYP3A4* in cryopreserved hiPSCs-derived hepatocytes were also shown in Inui et al. 2023. An overview of the gene expression of six hepatic markers in cryopreserved HP spheroids and HLC organoids at different maturation times has been published in Altmaier et al. 2022. In addition, the expression of hepatocyte-specific ICC markers AFP, ALB, A1AT and CK18 after thawing confirms the successful recovery and further maturation of functional protein activity in HP spheroids.

These findings indicate a successful recovery of proliferation, metabolic activity, gene and pro-

tein expression, and differentiation and maturation properties. Comparable recovery trends in morphology and proliferation were shown in NSC spheroids. The basic cryo-damaging effects, such as cell detachment and loss of viability, were observed in both precursor organoids regardless of their origin from different germ layers. These effects also appeared to be independent of the fact that the NSCs were differentiated by 2D cell culture and subsequently formed in spheroids, and the HP were differentiated by 3D cell culture in a bioreactor. This indicated that cryo damage on cell-cell junctions occurs in different 3D cell networks and is unrelated to the culture type during differentiation. However, characteristic gene and protein expressions and functional properties must always be analysed in relation to the respective tissue.

### **Maturation status of 3D cell systems influences the preservation of cell structures and functions during cryopreservation**

Cryopreservation of hiPSCs-derived HP spheroids can serve as a time-saving option to ensure a rapid supply of differentiated and partly matured precursor organoids to promote toxicity studies. Due to their human 3D physiology, their ability to self-renew and their high-throughput generation in bioreactors, they represent an attractive alternative to limited available PHHs, which can only represent 2D cell network interactions (Yi et al. 2012, Hu and Li 2015). To speed up the production process and enable a stock-keeping of ready-to-use, further matured hepatic 3D models, HLC organoids were cryopreserved after differentiation of 21 d. As with the HP spheroids, the morphological analyses showed similar results with cell debris in suspension at 24 h a.t. However, the CYP3A4 expression in HLC organoids remained always lower than that of *nfc* at a similar level as 24 h a.t. This implies that the recovery of the metabolic hepatocyte marker is less successful than in cryopreserved HP spheroids (Fig. 27 B). These results were supported by the significant decrease of all hepatic gene markers after thawing (Fig. 29 A). Immediately after thawing, the expression was comparable to that of *nfc*, but from 24 h a.t., gene expression was almost absent throughout the recovery period. Furthermore, the representative hepatocyte ICC markers ALB and A1AT were only identified with low expressions in HLC organoids 3 d a.t. and CYP3A4 was not detected compared to PHH (Fig. 29 B). These findings are not comparable with the previously described results of cryopreserved HP spheroids. Hence, the recovery of metabolic activity and hepatocyte gene and protein expressions were more successful in intermediate-frozen HP spheroids than in matured frozen HLC organoids. These results can be explained by differentiation- and maturation-induced changes regarding the structural integrity and cell-cell interactions of the HLC organoids (Mun 2019). The increase of tissue density mediated by cell-cell interactions and cellular condensation has been shown in the mesodermal progenitor zone during the vertebrate body axis elongation (Mongera et al. 2018). According to these studies, the further differentiation of HP spheroids to HLC organoids probably leads to an increase in cell-cell interactions, and the cells are more densely packed. Water efflux and the diffusion of solutes and CPAs are more restricted in matured organoids. This means that the possibility of sufficient dehydration to prevent IFF is reduced, and the

cells in HLC organoids are less protected by CPAs. As a result, the increase of osmotic stress leads to ruptures of the plasma membrane, which facilitates the propagation of extracellular ice crystals into the cells. In consequence, more damaging IIF occurs, which is often associated with lethal cell injuries (Morris and Acton 2013). Furthermore, due to the additional reduction of the effective surface area of water transport by the higher amount of cell-cell contacts, the paracellular ice penetration or gap junction propagation through nanoscaled apertures between connected cells is even facilitated. Thus, the nucleation kinetics of intracellular ice are faster in 3D systems with more cell-cell interactions (Berger and Uhrík 1996, Acker et al. 1999, Higgins and Karlsson 2013). Hence, the cellular architecture of HLC organoids with increasing density and complexity, which develops during differentiation, is not only influenced by osmotic imbalances but also represents a target for IIF due to an increased number of cell junctions (William and Acker 2020). Both lead to cytoskeleton changes and fatal cell-cell disruptions that are critical for cellular integrity and functionality in HLC organoids. In contrast, the HP precursor organoids, only differentiated for 8 d, exhibit a lower degree of maturity with probably fewer and less dense intercellular connections. It can be assumed that HP cells adapt more dynamically to the effects of cryo injuries. Additional investigations on cellular density and cell junctions could further confirm this theory. However, HP precursor organoids might serve as a starting point for developing high-quality living biobanks of hepatic 3D cell models. The settings of the current freezing process of HLC organoids need to be adjusted to ensure the recovery of metabolic CYP3A4 activity and gene and protein expressions of hepatic markers. Possible approaches would be the application of AFPs or IRIs during freezing and thawing (Tomás et al. 2022, Poisson et al. 2019, William and Acker 2020) or alternative cryopreservation methods, such as directional freezing (Maffei et al. 2014) or isochoric cryopreservation (Taylor et al. 2019).

### **Vitrification improves preservation of structural integrity of precursor organoids**

Structural analyses of NSC spheroids after slow-rate freezing revealed the detachment of peripheral cells and the decrease of cell junction proteins between 0 h and 24 h a.t. This could be shown for spheroids with three different diameters. Further investigations should clarify whether osmotic effects and ice crystallisation induced by slow-rate freezing and thawing affect the peripheral cell structures. Thus, NSC spheroids were cryopreserved by vitrification as an alternative cryopreservation method. With vitrification, samples were transformed into an amorphous, solid state without ice crystallisation and osmotic cell dehydration (Fahy et al. 1984, Bojic et al. 2021). The application of very potent cooling agents, such as LN<sub>2</sub>, leads to ultra-fast cooling rates in the periphery, and together with high CPA concentrations, a glassy state can be achieved. For instance, for the vitrification of oocytes with 10% DMSO, a cooling rate of  $3 \cdot 10^6$  °C/min is needed to avoid the growth of intracellular ice to 10 µm in the cooling phase between -40 °C to -100 °C (Arav 2022). Higher CPA concentrations decrease the required cooling rates (Karlsson 2010) but increase cytotoxic effects. Compared to slow-rate freezing, the thermal gradient and CPA penetration are even more challenging in 3D cell systems during

vitrification due to the high cooling rates and CPA concentrations required. Accordingly, the cooling rate and CPA supply in the inner cells are reduced compared to peripheral cells, and ice formation can occur. However, preserving viable and proliferating cells in the peripheral layers is of greater importance than the necrotic cells in the core of the spheroid. The viable cell layers should be adequately supplied with high CPA concentrations and cooling rates. In theory, due to the ultra-fast transfer into a vitrified status, ice crystallisation and osmotic-induced dehydration or cytoskeleton rearrangements should not occur, and peripheral cell detachment should be reduced.

This hypothesis could be confirmed by the analyses of the morphology and ultrastructures of NSC spheroids after vitrification (Fig. 36 A, Fig. 38). In comparison to slow-rate frozen spheroids, fewer detaching cells were observed. The cell-cell junctions appear morphologically more intact and comparable to nfc. Furthermore, proliferation and viability were not reduced after vitrification compared to nfc (Fig. 36 B and C). Another striking aspect is that there was no gene expression change of *CDH1* and *OCT3/4* marker 24 h a.w. compared to 24 a.t. of slow-rate frozen samples (Fig. 37). Due to the reduction of the cryo-induced stress, the E-Cadherin connections were preserved, and de-differentiation pathways were not up-regulated. All these investigations indicate improved preservation of the cellular structure and viability after vitrification. The formation of inter-and intracellular ice and osmotic dehydration of the outer cells, as in the slow-frozen spheroids, could be avoided by vitrification. These analyses confirmed that the cryo injury mechanisms induced by slow-rate freezing and thawing affect cellular structure and viability loss. However, after warming of vitrified samples, single cells in the outer layer become apoptotic, which can be caused by devitrification during non-uniform cooling and warming or by high CPA cytotoxicity (Fig. 46). Devitrification is a significant problem in biological samples with larger volumes (Finger and Bischof 2018). The vitrification of vascularised tissues and entire organs is possible, but a full recovery of the viability is still not accomplished due to devitrification (Fahy et al. 2009). Warming rates are much lower than cooling rates, and in the warming phase above the glass transition temperature up to the melting temperature, ice nucleation and ice growth are very likely. Another limiting factor during the warming of vitrified 3D cell systems is the formation of cracks under mechanical stress, shown in elastic arteries (Pegg et al. 1997). This can be caused by the application of slow and non-uniform warming rates. To avoid these effects and maintain cellular architectures, CPA concentration must be increased, and the warming rate must be fast and homogeneous. However, applying controllable, very fast cooling and heating rates is complex and not standardised. In addition, CPAs become more cytotoxic with increasing concentration and cause oxidative stress, DNA fragmentation or reduction of protein and mitochondrial functions up to apoptosis (Best 2015). So far, only small tissues, such as ovarian tissue slices, can be vitrified and warmed rapidly and reliably enough to avoid harmful devitrification (Kometas et al. 2021). Improved viability values compared to slow-rate freezing have also been published for mesenchymal stem cell spheroids (Jeong et al. 2020), lung cancer organoids (Q. Liu et al. 2021) or mouse and human embryos in blastomer stage (Rall and Fahy 1985, Rezazadeh Valojerdi

et al. 2009). Currently, new warming approaches are being developed to effectively warm vitrified tissues and organs, like nanowarming or laser warming (Khosla et al. 2017, Daly et al. 2018). Nanowarming is based on inductive heating of magnetic nanoparticles, e.g. resulting in warming rates of 130 °C/min in porcine arteries in 1 ml vials with a radius of  $\geq 0.5$  cm (Manuchehrabadi et al. 2017). Only rates below 50 °C/min were detected in the same sample volumes with standard convective warming. By nanowarming, successful warming was reported up to a volume of 80 ml (Manuchehrabadi et al. 2017). However, ensuring both the biocompatibility and safe removal of nanoparticles, as well as achieving efficient and uniform heating, remains challenging (Ye et al. 2023).

In principle, the vitrification and warming process for a large batch of 3D cell systems are not standardised, and to date, no commercial vitrification device is available on the market. In this work, the Twist vitrification proved to be advantageous over direct application in LN<sub>2</sub> or vitrification straws (data not shown). The Twist approach ensures sterility and ultra-fast cooling rates while avoiding the harmful Leidenfrost effect (Beier et al. 2013, Amini and Benson 2023). However, the vessel design and handling protocol are not standardised yet for higher batches of 3D cell systems.

To summarise, these comparative analyses of both cryopreservation methods with spheroids are valuable for further understanding cryo injury mechanisms of 3D cell models. In principle, both cryopreservation regimes showed advantages and limitations. Although the vitrification approaches demonstrated an improvement in structural and viability analyses of spheroids up to a diameter of 600  $\mu\text{m}$ , the sufficient application of ultra-fast cooling rates and high CPA concentrations has not yet been achieved in larger tissues. Additionally, only a small number of spheroids from one batch can be vitrified simultaneously. In contrast, slow-rate freezing enables the preservation of large batches with easier handling. The process and cooling rates are more standardised to avoid high batch-to-batch variability. However, non-uniform dehydration and intracellular ice formation cause extensive intracellular changes to the cytoskeleton and membranes, leading to disrupted peripheral cell connections and triggering apoptosis (Fig. 46). The development of different cryopreservation methods may, therefore, be suitable depending on the subsequent application.

### **Different cryopreservation media induce osmotic changes of precursor organoids before slow-rate freezing**

The use of CPAs is essential to protect cells which are exposed to cryogenic temperatures. However, the impact of CPA cytotoxicity on cryo injury mechanisms must be considered in both cryopreservation regimes. Fahy et al. 1990 reported on a broad spectrum of cytotoxic effects caused by CPA incubation. They defined CPA cytotoxicity as an effect that must be significant, irreversible, analysed during an appropriate incubation period, and not caused by introduction or washout techniques. Cytotoxicity may be specific to a particular CPA or non-

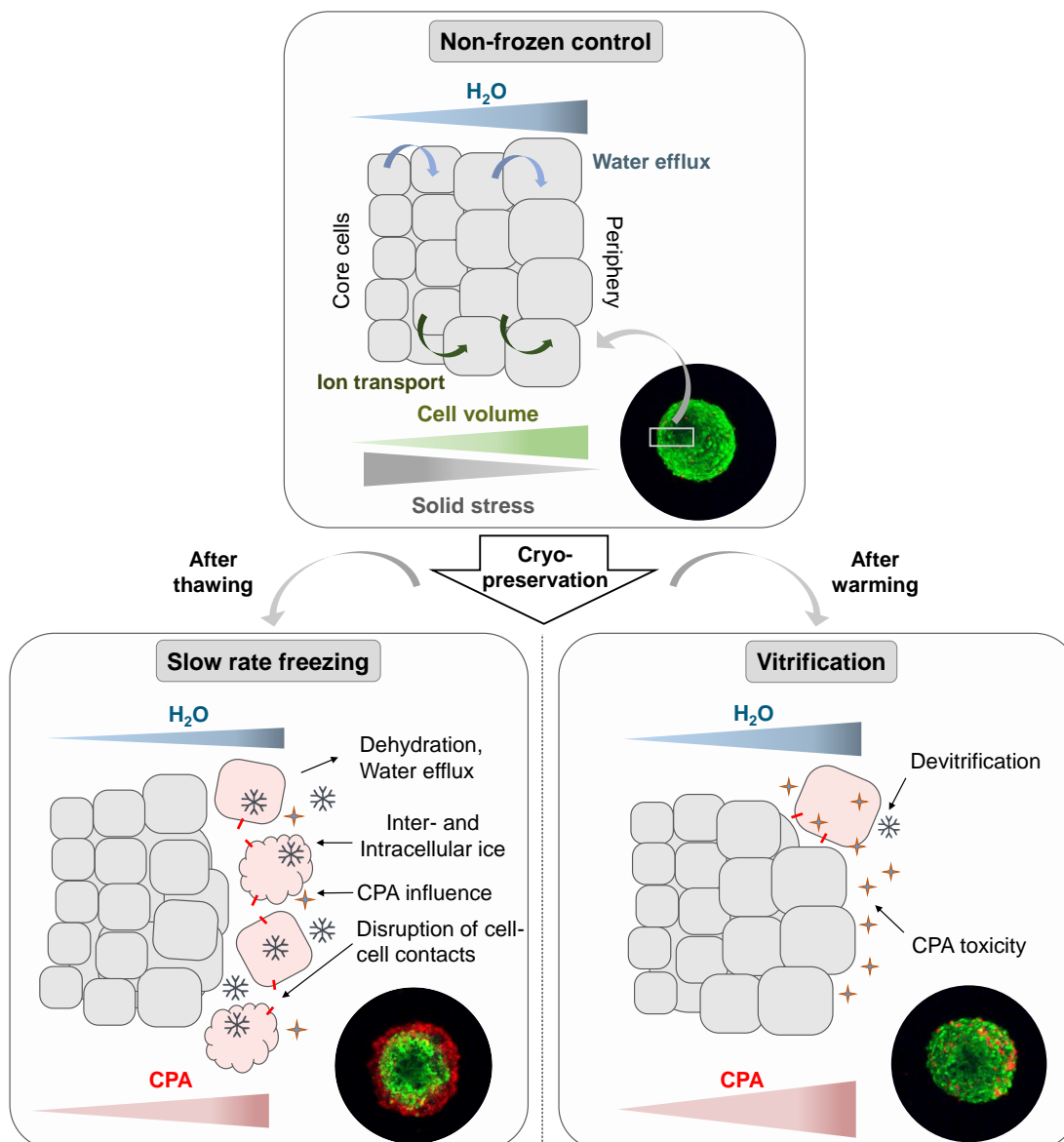


Figure 46: **Schematic overview of cellular effects in different spheroid zones in nfc and after cryopreservation.** Proliferation-induced solid stress drives ion transport and water efflux from the core to the periphery of nfc and leads to swelling of the outer cells. (A) Cryo-induced stress factors during slow-rate freezing and thawing trigger a deformation of the cells, which is more damaging to outer cells and causes the cells to detach. (B) Ultra-fast cooling rates avoided severe deformations of the cell during vitrification. Devitrification during warming and high CPA cytotoxicity are potentially harmful to the cells. Created with biorender.

specific, ranging from structural cell damage to metabolic impairment. The different effects depend on the cell system and the experimental conditions, such as the CPA concentration and exposure time, temperature and type of toxicity test.

When single cells are exposed to a hypertonic cryopreservation solution, an osmotic imbalance

arises across the cell membrane. Due to the osmotic pressure, intracellular water outflow occurs, which results in the activation of a regulatory volume response reduction. The cell volume decreases, and depending on the cell type, cells shrink until osmotic equilibrium is achieved (Levin and Miller 1981, Finan and Guilak 2010). This mainly occurs during the incubation with media containing impermeable CPAs, such as trehalose and sucrose. During the incubation in cryopreservation media with permeable CPAs, as DMSO, EG or glycerol cell volumes change in two different ways: a) If the membrane permeability and diffusion rate for water is much greater than that of respective CPA molecules, the cells initially shrink due to osmotic imbalances across the cell membrane. Then the cells gain volume again when equilibrium is reached, depending on membrane permeability of the CPA; b) with higher membrane permeability and diffusion rates of CPA molecules, there is a more simultaneous influx of both water and CPA molecules and the cell volume increases accordingly with the CPA concentration until equilibrium is reached (Levin and Miller 1981). So far, the impact of these effects has only been investigated in detail for individual cells in suspension. This work focuses on CPA cytotoxicity mechanisms in 3D cell structures regarding their volumes, viability, and gene and protein expressions. In this context, the effects of different permeable and non-permeable cryopreservation media with varying times of incubation and concentrations were investigated in NSC spheroids with three diameters. Permeable CPAs, such as DMSO or EG, are known as potent CPAs due to their unspecific, collective effects leading to the replacement of water molecules. This lowers the freezing temperature of aqueous solutions and reduces the formation of intracellular ice crystals (Lovellock and Bishop 1959). However, penetrating CPAs show a diverse range of specific and non-specific cytotoxic effects on cells (Best 2015). Besides cytotoxic effects, the introduction of CPAs additionally causes indirect damaging effects such as osmotic cell stress, which induces cell volume changes. The level of osmotic stress depends on the membrane permeability, which depends on the cell-specific membrane composition. Permeability is increased with higher lipid solubility of the substance and decreased with an increased hydrogen bonding. In general, molecules with reduced sizes have a higher membrane permeability. These single-cell effects are transferable to interconnected cells with separate membranes in NSC spheroids, but also to spheroids of other cell types. After the incubation in cryopreservation media with higher concentrated DMSO, CryoStor CS10, EG or CPA mixtures VS1/ VS2, the spheroid volume initially decreases ( $t = 5$  min) because of the osmotic imbalances (Fig. 12). Due to the lower permeability of CPAs compared to water molecules, water flows out of the cells, and the complete 3D system shrinks. The new equilibrium slowly emerges over time (Fig. 12,  $t = 30$  min). The hypothesis based on these results is illustrated schematically in Fig. 47 A. A similar effect was observed over time after the incubation in glycerol. The volume of the spheroids decreased even more at  $t = 5$  min and then only slowly increased again (Fig. 47 C). This can be explained by the lower membrane permeability of glycerol compared to DMSO, which has also been reported in red blood cells, where DMSO is twice as permeable as glycerol at 4 °C ( $1.3 \cdot 10^{-5}$  cm/s for DMSO and  $0.58 \cdot 10^{-5}$  cm/s for glycerol) (Naccache and Sha'afi 1973). In comparison, the membrane permeability of water for red blood cells is increased 700-fold ( $915 \cdot 10^{-5}$  cm/s) (Naccache and

Sha'afi 1973), which explains the rapid decrease in volume associated with water efflux after 5 min. However, the membrane permeability of different molecules can vary significantly in other cell types. Additionally, it depends on the molecule concentration. At lower DMSO or EG concentrations, the osmotic imbalance was decreased, so fewer water molecules diffused out of the cells, and the volume changes were more minor (Fig. 47 B). In contrast to permeable CPAs, non-penetrating CPAs, such as trehalose or sucrose, stabilise the polar groups of phospholipids on the extracellular side of the cell membrane during ice crystallisation (Clegg et al. 1982). The advantage of impermeable CPAs is that they do not show specific cytotoxic effects but can cause indirect damages such as excessive dehydration due to high osmolarity (Fig. 47 D).

### **Cryopreservation media cause osmotically-induced changes in the cytoskeleton and cell membranes**

The regulation of osmotically-induced volume changes (Fig. 47) strongly depends on the reorganisation of the actin-based cytoskeleton. As a result of the water and CPA molecules crossing the membrane, various proteins or protein clusters, such as mechanosensitive ion transporters, can be activated and influence the organisation of the cytoskeleton. This, in turn, triggers F-actin-associated proteins such as Rho-GTPase or membrane transport proteins to improve cell volume regulation. Pedersen et al. 2001 and Roffay et al. 2021 published comprehensive overviews about the mechanisms of volume regulations in cells. Actin changes can occur relatively fast, depending on extracellular osmolarity and the level of protein activation. Falzone et al. 2012 reported that little actin polymerisation was observed only 60 s after initiating isolated monomeric actin. After 135 s, short F-actin bundles appear, and after 600 s, an interconnected network of bundles can be formed. This assembly kinetic of actin may explain the significant increase in the relative cellular F-actin content in Ehrlich ascites tumour cells after 1 min incubation in a hypertonic solution and a similar fast decrease in a hypotonic solution (Pedersen et al. 1999). Besides this, other factors, such as the activation of volume-associated proteins and the plasma membrane rearrangement, also affect the regulation processes and can delay the response time. Additionally, genes involved in the synthesis of osmoprotectant molecules can be up-regulated by osmotic stress, but the timescale on the order of a few tens of minutes cannot explain the immediate cell response (Hoffmann et al. 2009). However, if the osmotic pressure is too high and the volume compensation of the osmotically active water by F-actin and membrane reorganisation is not sufficient, irreversible membrane ruptures, cytoplasmic protein aggregation and DNA damage can lead to apoptotic cell death (Galluzzi et al. 2018). To understand the osmotically-induced volume changes in organoids in response to hyper- or hypotonic solutions, it is important to study the F-actin kinetics in an interconnected 3D cellular network and not only in single cells. Transferring the assembly kinetics of F-actin to the volume analyses of precursor organoids after incubation in cryopreservation media, the relatively fast, significant changes after 5 min are reasonable. Volume-regulating mechanisms occur in every individual

cell of the 3D cell system. However, additional factors like cellular connections and interactions and different cell type properties influence the processes in every cell layer. Thus, in spheroids, the speed of volume changes in the inner cells depends not only on the membrane permeability but also on the intra- and intercellular diffusion kinetics of the solutes, which is influenced by the entire cell network. This effect was shown by different relative percentages of volumes in larger spheroids compared to small spheroids with the same CPA concentrations. For instance, the volume decrease was 6% higher in large spheroids after a 5 min incubation in 20% DMSO compared to small spheroids. This can be explained by the limited mass transfer of DMSO in larger spheroids to balance the water efflux. Densely packed inner cells were not supplied with DMSO after 5 min, so the return inflow of water was delayed. Nonetheless, the progressions of the volume changes over the incubation time within the respective spheroid diameters were similar (Fig. 13).

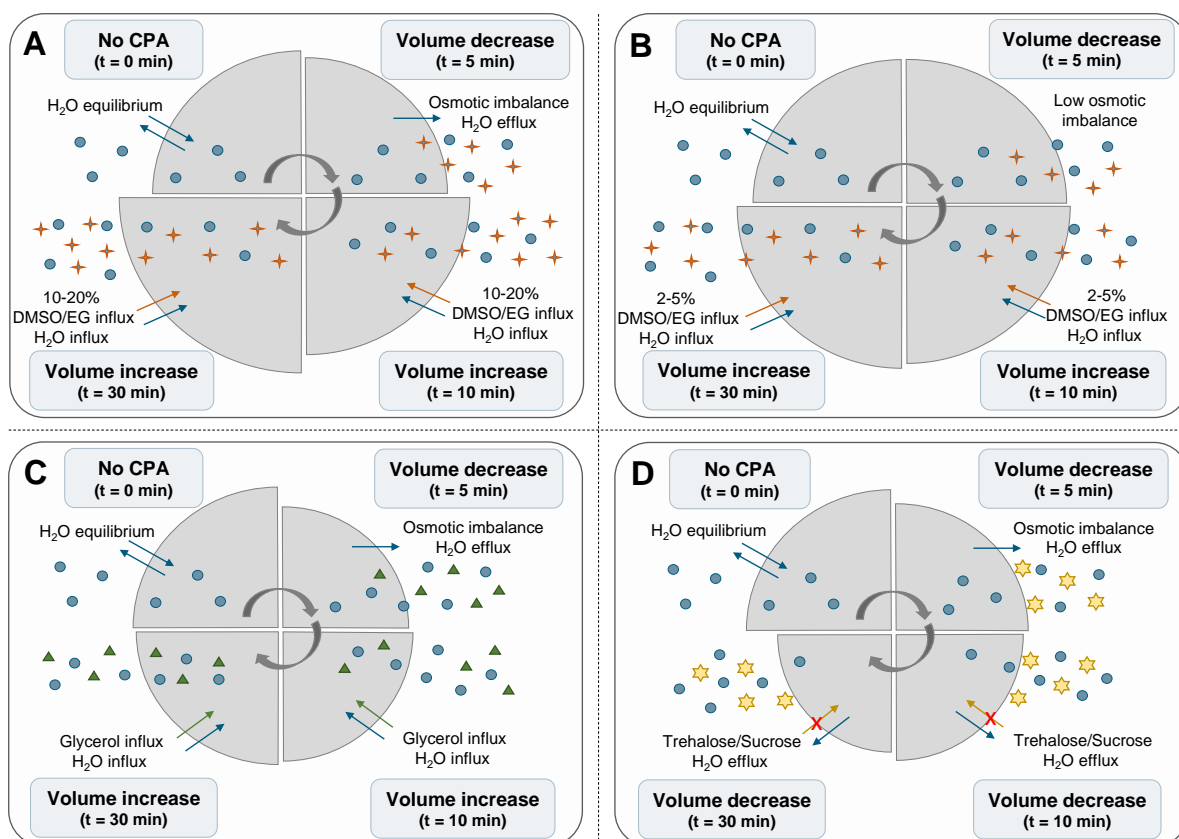


Figure 47: **Schematic overview on the volume regulation of spheroids after treatment with different CPAs over time.** Volume changes after treatment with (A) highly concentrated, permeable CPAs (10-20% DMSO and EG), (B) low-concentrated, permeable CPA (2-5% DMSO and EG), (C) permeable glycerol and (D) impermeable CPAs (0.3 M trehalose and sucrose) at  $t = 0$ -30 min.

### Different cryopreservation media influence the metabolism of precursor organoids

In addition to the indirect CPA damaging effects based on osmotic stress, specific CPA toxicities can be induced by permeable CPAs. This increases the impairment of viability, gene and protein expression and the functionality of the cells (Best 2015). A reduction in ATP-based relative cell viability was observed in all spheroids during incubation with all cryopreservation media (Fig. 14 A). The lowest viability was measured after the incubation with impermeable trehalose, sucrose and HypoThermosol FRS, which can be attributed to osmotic stress. But also after incubating in the cryopreservation media with all DMSO, EG and glycerol concentrations, the viability was reduced for all spheroid diameters. This can be associated with osmotic stress and specific CPA toxicities like plasma membrane damage and oxidative stress. For instance, DMSO binds via hydrogen bonds to the plasma membrane. The sulfinyl oxygen of DMSO forms a stronger hydrogen bond with water (approx. 30 kJ/mole) than water molecules do with each other (approx. 20 kJ/mole). Thus, DMSO dehydrates the membrane by displacing water molecules. On one side, this protects cells from intracellular ice crystallisation; on the other side, water replacement causes dehydration stress in the membranes (Westh 2004). The resulting effects range from the decrease of the membrane thickness at low DMSO concentrations to the formation of transient water pores at medium DMSO concentrations up to the destruction of the bilayer structure at higher DMSO concentrations (Wang et al. 2007). Moreover, the addition and removal of CPAs cause fast osmotic fluctuation, which enhances the tension on the membrane and cytoskeleton (Baust et al. 2017). Additionally, DMSO can promote oxidative stress by oxidising free thiol groups on proteins, leading to protein unfolding and loss of functionality (Snow et al. 1975). It is assumed that oxidative stress, together with the blocking of membrane channel proteins by DMSO, causes irreversible ultrastructure alterations in mammalian myocardium (Shlafer and Karow 1975, Ogura et al. 1995). Furthermore, DMSO shows pro-apoptotic properties at higher concentrations, which has also been demonstrated for ethylene glycol and glycerol (Best 2015). The combination of indirect and specific CPA toxic effects results in the reduction of cell viability. A striking aspect of the viability analyses of NSC spheroids is that the viability staining with FDA/EtB (Fig. 14 B) did not coincide with the ATP-based viability measurement (Fig. 14 A). The staining showed high viability for 10% DMSO, 0.3 M sucrose and CryoStor CS10. In particular, the viability after incubation in cryopreservation media containing impermeable sucrose is very different, as only 40-60% relative viability was determined based on the ATP measurement. This can be explained by the repression of cellular respiration by hypertonic medium. Hyperosmotic conditions can alter cellular energy metabolism due to the reduction of mitochondrial oxidative phosphorylation. Glycolysis is increased and respiration repressed, which is known as the Warburg or Crabtree effect (Warburg 1956, Eales et al. 2016). This happens in the order of a few seconds or a few minutes. In this context, the hypothesis is that the spheroids are exposed to a hyperosmotic cryopreservation medium, which induces glycolysis and reduces the production of ATP. The exact molecular mechanisms in mammalian cells are still under debate. It is hypothesised that the metabolic

shift towards glycolysis is triggered by a specific inflammatory pathway in response to osmotic pressure (Hamraz et al. 2020). Hence, ATP reduction was not detected by FDA staining as it determines esterase activities. To summarise, CPAs significantly affect the metabolism and reduce the ATP production in NSC spheroids. However, after 30 min incubation, active esterases were still detectable, indicating NSC spheroids' high CPA resistance. Further investigations of the gene expression of NSC spheroids after CPA treatment also revealed a CPA resistance (Fig. 15). In general, the speed of stress response is important to ensure cell survival. Over 500 genes can be transcribed relatively quickly in response to osmotic stress within 10-30 min of the stimulus (Nadal et al. 2011). For instance, it has been shown that gene expression and intracellular localisation of  $\beta$ -actin mRNA takes about 20-30 min after serum induction (Ben-Ari et al. 2010). Thus, if the time frame for induction and transcription of mRNA of stress or neuronal genes is of the same order of magnitude, a cytotoxicity-induced change in gene expression should be detectable after a 30 min incubation in different cryopreservation media. In contrast, stress and neural markers were not significantly altered after 30 min, which indicates only low cytotoxic stress induction of CPAs during this time. A slight significant expression increase was only observed for *CDH1* for several cryopreservation media in all spheroid diameters. This indicates that CPAs may cause cell detachment that affects the expression of the adhesion protein E-cadherin. The investigation on the E-cadherin protein expression supports these results (Fig. 16). Compared to non-treated spheroids, a decrease in E-cadherin of about 30-70% was measured for all cryopreservation media and spheroid diameters. This can be attributed to damage to the plasma membrane, followed by impairments of the associated adhesion proteins, like E-cadherin. Cell detachment was also observed in the 2D NSC culture after CPA treatment, accompanied by a reduction in cell viability (Fig. 48). It is hypothesised that the outer cell layer of NSC spheroids is mainly influenced by CPA-induced cell detachment due to longer exposure times. This means that only a small number of cells would be affected by apoptotic effects, which would also explain the small changes in gene expression. However, it has been reported that the addition and removal of CPAs can delay the formation of junctions in epithelial cells but does not fundamentally inhibit the cellular repair mechanisms for the formation of intercellular junctions (Armitage and Juss 2000). Therefore, recovery of E-cadherin may be likely.

In conclusion, the incubation of NSC spheroids in different cryopreservation media causes metabolic changes with associated lower ATP content and affects the expression of cell adhesion proteins. However, it is important to declare that the incubation time of 30 min in cryopreservation media is not common in standard cryopreservation protocols. Shorter incubation times may reduce cytotoxicity. At the same time, it is important to ensure that the CPA completely penetrates the viable cell layers of the 3D cell models to have a cryoprotective effect. Since it is assumed that the penetration of CPAs in 3D cell models takes longer and the incubation time must be extended, the prolonged incubation of up to 30 min was intentional to detect possible significant effects.

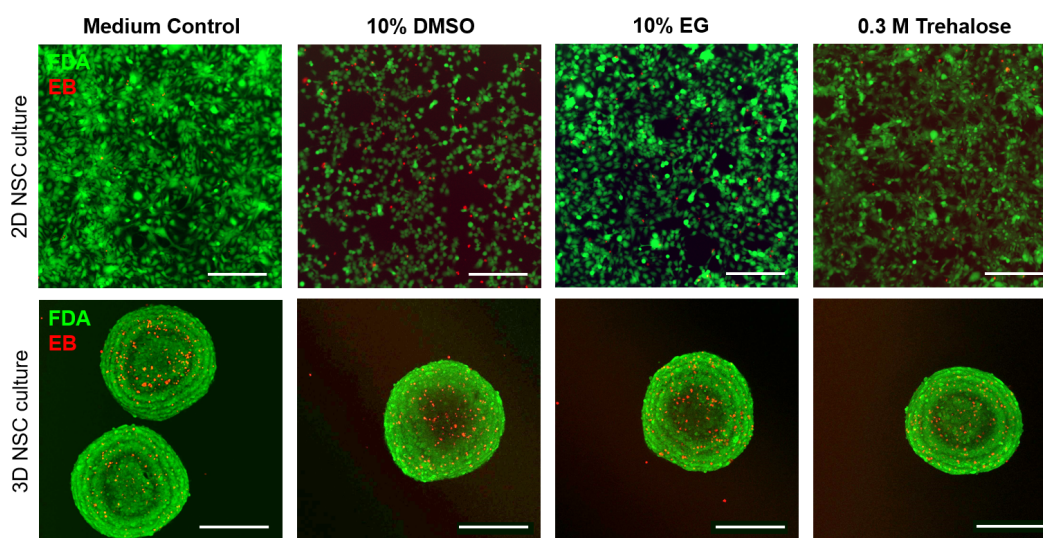


Figure 48: **Comparative analyses of CPA effects in terms of viability and adhesion on 2D NSC monolayers or 3D NSC spheroids.** Incubation for 30 min in a cryopreservation medium with 10% DMSO, 10% EG and 0.3 M trehalose leads to detachment of the cells and a reduction in cell viability; scale bars represent 200  $\mu\text{m}$  (top row) and 50  $\mu\text{m}$  (bottom row).

### CPA diffusion kinetics in precursor organoids can be analysed using bioorthogonal Raman micro-spectroscopy

To maximise the proliferation of viable cells in spheroids, the 3D cell cultivation methods must ensure a sufficient supply of necessary small molecules throughout the cellular network by diffusion. This depends on the diffusion properties of the compounds and the properties of the cell model, such as the cell type, the density or the number of cell compounds, but also on the temperature and the distribution dynamics of the molecules during the 3D cell culture (Volkmer et al. 2008, McMurtrey 2016). Thus, to optimise the 3D cell culture, it is essential to understand the diffusion properties of important small molecules. In general, diffusion kinetics of various molecules have been researched in different fields, such as pharmacology (Hicks et al. 2006, Chiu et al. 2015), medical diagnostics (Nederman et al. 1983, Pauleit et al. 2004, Alexandrovskaya et al. 2023) cell metabolism and signalling studies (MacDougall and McCabe 1967, Bertram and Pernarowski 1998) and food science (Shi et al. 2023) but also cryopreservation (Han et al. 2019). In general, magnetic resonance imaging and attenuated total reflection (ATR) spectroscopy are the predominant analytic methods for diffusion in macroscopic samples (Huck 2014, Tang and Zhou 2019, Carneiro et al. 2019). Optical analyses based on the tracking of fluorescent (labelled) compounds are mainly used for diffusion studies in the microscopic range (McGowan et al. 1988, Sniekers and van Donkelaar 2005). However, transferring diffusion kinetics to non-fluorescent compounds is complex, and fluorescence labelling can alter the size and structure of the molecule, changing its penetration properties. This also complicates diffusion studies of non-fluorescent CPAs before cryopreservation. As discussed in the previous section, a prerequisite

for successful cryopreservation is a sufficient supply of CPAs to achieve a cryoprotective effect while reducing cytotoxic effects due to excessive incubation times (Karlsson and Toner 1996). However, the penetration and membrane permeability of CPAs are mainly investigated in single cells, which is not comparable to cellular 3D structures (Naccache and Sha'afi 1973). The main reason, therefore, is the lack of knowledge about the perfusion properties of water and CPAs in cell networks. Hence, analysing specific CPA diffusion kinetics in 3D cell systems would provide advanced pre-incubation conditions for cryopreservation media to reduce cytotoxicity.

To overcome these challenges, this work introduces bioorthogonal Raman micro-spectroscopy as a contactless technique for analysing the penetration of different molecules in 3D cell systems (Altmaier et al. 2024). In general, Raman spectroscopy has already been used to measure diffusion coefficients of various molecules in multi-component liquid mixtures (Bardow et al. 2003). Compounds that exhibit clear vibration bands without interference from the spectral background can be analysed directly. Molecules with no distinct vibrational feature have to be slightly chemically modified by isotope exchange or the introduction of nitrile groups. This enables a spectroscopic separation from the considerable unspecific background while diffusion properties remain almost unchanged, which is an advantage of this method over fluorescence labelling. These experimental approaches are called bioorthogonal labelling (Azemtsop Matanfack et al. 2020). Bioorthogonal Raman micro-spectroscopy has already been implemented for various studies, e.g. to analyse the penetration of drugs into human nails (Chiu et al. 2015). The present thesis focuses on bioorthogonal Raman micro-spectroscopy as a non-invasive method to investigate the radial perfusion of deuterated DMSO-d6 in NSC and HP spheroids and HLC organoids. The fit model developed in this study can be used to analyse the penetration of DMSO-d6 into spherical 3D cell systems to derive the diffusion coefficients and perfusion times based on model-specific properties. Although HLC organoids do not represent a homogeneous spherical model, a spherical geometry was nevertheless assumed to simplify the diffusion model. Diffusion analyses with other sample geometries, such as cylinders, could also be carried out using an adapted fit model based on Fick's law of diffusion.

It was assumed that the diffusion coefficient  $D$  of DMSO-d6 is constant in all spheroid diameters. However,  $D$  remains constant up to a diameter of about 500-600  $\mu\text{m}$  ( $D = 88.8 \pm 14.4 \mu\text{m}^2\text{s}^{-1}$ ) but increases as the diameter becomes larger ( $D = 178.6 \pm 38.5 \mu\text{m}^2\text{s}^{-1}$ ) (Fig. 39 E). Fig. 49 illustrate the increase of the diameters and thus the increase of  $D$  that is directly correlated to the seeding cell number and cultivation days. This effect was observed in NSC and HP spheroids and HLC organoids. However, since the experiment only investigates the DMSO-d6 concentration in the centre of the spheroid, it is not clear whether the increase in  $D$  is uniform across the entire spheroid or occurs only in specific layers or in the core of the spheroid.  $D$  is averaged over the radius of the spheroids. The increase of DMSO permeability in 3D cell models with increasing diameters has not been described so far. The hypothesis to explain this effect consists of the possibly altered permeability properties of the cell layers within the spheroids. In a previous part of the discussion, it was already described that spheroids with diameters greater than 300  $\mu\text{m}$  probably have hypoxic areas, while those greater than 500  $\mu\text{m}$  have necrotic cores

(Glicklis et al. 2004, Schmitz et al. 2021). The limited diffusion of oxygen and nutrients and the accumulation of cellular waste in the core of the spheroids lead to reduced metabolism and a deficiency of ATP production (Fig. 33). This may cause eventual failures of ion pumps in the plasma membrane, resulting in structural impairments of the bilayer structure (D'Arcy 2019). Additionally, oligomerised mixed lineage kinase domain-like pseudokinase (MLKL), which is an essential factor in tumour necrosis factor (TNF)-induced regulated cell death, can migrate and bind to the phosphatidylinositol lipids and cardiolipin of the plasma membrane that increases membrane permeabilisation and induces cell death (D'Arcy 2019). Hence, altered membrane permeability in under-supplied or necrotic cells may accelerate the diffusion of DMSO in the inner layers of avascular spheroids with diameters greater than 500  $\mu\text{m}$ . This may lead to an increase in the average diffusion coefficient. Further investigations on the diffusion rates in the respective cell layers could support this hypothesis. Nevertheless, the order of magnitude of the diffusion coefficients of DMSO is comparable to the values described in the literature, which were determined by osmolarity or ATR-FTIR measurement (Tapia Lishner et al. 2023, Vásquez-Rivera et al. 2018). So far, there are only a few recently published reports on the diffusion kinetics of cryoprotectants in 3D cell models. Most publications deal with the diffusion of DMSO as an effective and most commonly used substance for many cryopreservation protocols. For instance, Dolezalova et al. 2021 developed a method to investigate the diffusion kinetics of small molecules in pancreatic islets using Hoechst 33342 dye. Based on this, they estimated the diffusion of DMSO and trehalose into the core of the pancreatic islets. However, these results only provide an approximation of DMSO diffusion. Every molecule follows different diffusion rates based on size, charge, concentration and penetration route. This has also been shown with different dye molecules in Fig. 40. Thus, it is only limited possible to deduce diffusion kinetics from one substance to another. In another publication, Tapia Lishner et al. 2023 determined the permeation kinetics of DMSO into porcine corneal discs by fitting weight and osmolarity measurements over time to Fick's law of diffusion. They calculated an effective diffusion coefficient of DMSO in porcine corneal discs of  $53.06 \mu\text{m}^2\text{s}^{-1}$  at  $0^\circ\text{C}$ . The advantage of this method is that the diffusion coefficient can be derived indirectly from the penetration and efflux of DMSO and not from another molecule. However, the mass of smaller 3D cell models such as spheroids, which contain about  $1 \cdot 10^4$  to  $5 \cdot 10^5$  cells, is in the order of nanograms (Phillips et al. 2012). The measurement of very low spheroid masses and only slight changes in osmolarity after removing DMSO is challenging. In the publication of Vásquez-Rivera et al. 2018, the diffusion kinetics of DMSO were also assessed via osmolarity measurements in decellularized heart valve tissues. They determined a diffusion coefficient of DMSO of  $514 \mu\text{m}^2\text{s}^{-1}$  at  $22^\circ\text{C}$ . They also established an ATR-Fourier transform infrared (FTIR) spectroscopy setup to confirm these studies. Using the ATR-FTIR spectroscopy, a diffusion coefficient of DMSO of  $302 \mu\text{m}^2\text{s}^{-1}$  was determined at  $22^\circ\text{C}$ . The limitation of ATR-FTIR is that this method is based on the surface reflectance technique, i.e. it is impossible to detect DMSO diffusion inside of the tissue directly, but only after the penetration through the cylindrical-shaped tissue. This complicates the use of ATR-FTIR in tissue with other

geometries, like spheroids.

In general, the diffusion of DMSO-d6 in NSC spheroids is about seven times slower in the peripheral, viable cell layers and three times slower in the under-supplied, hypoxic inner cells (Fig. 39) than the diffusion of pure DMSO-d6 in heavy water with self-diffusion coefficient of about  $650 \mu\text{m}^2\text{s}^{-1}$  (Holz et al. 1996, Valente and Söderman 2019). However, compared to impermeable CPAs, such as the tested disaccharides sucrose and trehalose, DMSO generally penetrates the cell membrane faster due to its high permeability. The diffusion coefficients of impermeable CPA molecules can range from  $48 \mu\text{m}^2\text{s}^{-1}$  in skeletal muscle of rabbits for sucrose (Pineiro et al. 2023) to  $0.1 \mu\text{m}^2\text{s}^{-1}$  for trehalose oxygen atoms in T-cells (Weng et al. 2016). However, also higher diffusion coefficients of sucrose were reported in different tissues, like  $350 \mu\text{m}^2\text{s}^{-1}$  in pulmonary artery ECM (S. Wang et al. 2015). In principle, disaccharides cannot diffuse passively across the bilayer structure of the plasma membrane due to their high polarity and molecule size (Meyer et al. 2011). However, disaccharides can penetrate intercellularly depending on their molecule size and the density of the cell network in the tissue. Protein-mediated sugar transport, as with the glucose transporter (GLUT) for glucose, is restricted to monosaccharides (Meyer et al. 2011, Yang and Hinner 2015). Small staining molecules, such as Hoechst 33342 and rhodamine B, also penetrate much more slowly than DMSO. Their perfusion times into the core of the spheroids are several hours (Fig. 40). Compared to the diffusion of metabolically essential, very small molecules, such as oxygen, with a diffusion coefficient of  $1000 \mu\text{m}^2\text{s}^{-1}$  in human brain tissue (McMurtrey 2016), DMSO molecules diffuse around 10 times slower.

The size-dependent diffusion coefficients also influence the respective perfusion time, which is inversely proportional to the diffusion coefficient and directly proportional to the square of the spheroid radius. It has been shown that the perfusion time  $t_{90\%}$  is highly dependent on the diameter of the spheroid and varies significantly for diameters ranging from  $300 \mu\text{m}$  to  $1100 \mu\text{m}$ . The observation of longer perfusion times for larger spheroids was expected. However, the significant size dependence demonstrates the practical importance of measuring  $t_{90\%}$ . In general, the time  $t_{90\%}$  for the perfusion of DMSO-d6 into sub-millimetre spheroids is several minutes at room temperature, as shown in Fig. 39 F. This highlights the significance of understanding the uptake kinetics of CPA into 3D cell models for cryopreservation protocols. Knowing the perfusion times enables the implementation of proper CPA incubation protocols, preventing insufficient penetration of the spheroids and overexposure of DMSO to the peripheral cells. Hence, before cryopreservation of spheroids and other 3D tissue models, it may be necessary to adjust the DMSO pre-incubation times according to cell type, diameter and age.

### **Model specific predictions of CPA diffusion kinetics improve the recovery of precursor organoids after vitrification**

To confirm the assumption that an optimised perfusion time improves cryopreservation success, NSC spheroids with different diameters were slow-rate frozen after DMSO pre-incubation with corresponding perfusion times  $t_{90\%}$  based on Raman micro-spectroscopy data (Fig. 41, 42 and

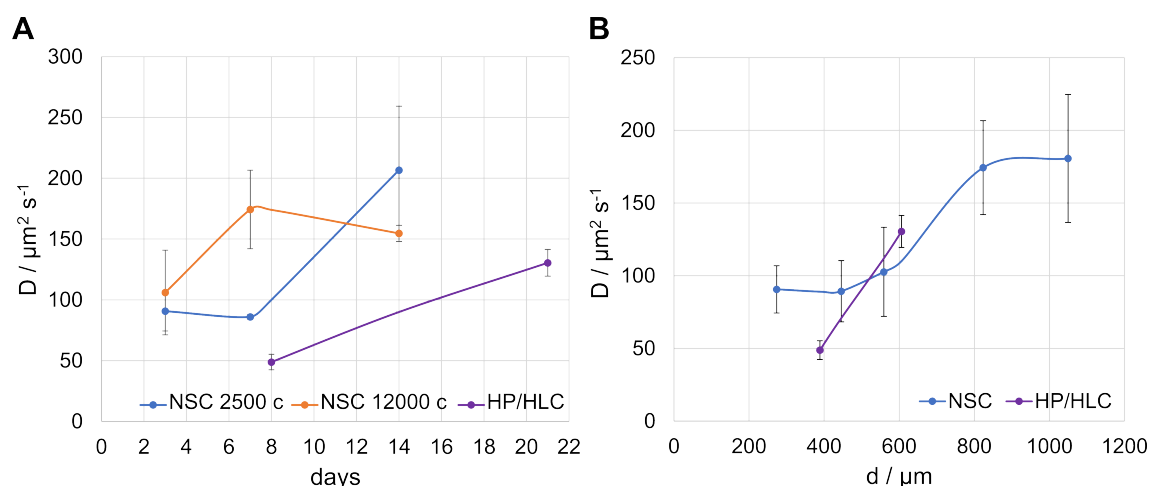


Figure 49: **Diffusion coefficient progression in avascular spheroids and organoids based on Raman micro-spectroscopy.** Plot of diffusion coefficient  $D$  of NSC and HP spheroids and HLC organoids against (A) the cultivation days and (B) the diameters  $d$  [ $\mu\text{m}$ ]. The number of seeded cells and the cultivation time directly determine the diameter of the spheroids and indirectly influence the correlated diffusion coefficients.

43). Studies on the viability of NSC spheroids after thawing showed no significant differences between 0 min of DMSO pre-incubation and after incubation with corresponding  $t_{90\%}$  (Fig. 42). These results indicate that Raman micro-spectroscopy-derived DMSO incubation times do not alter cryopreservation outcomes. However, all spheroids were slowly frozen with a cooling rate of  $-1$   $^{\circ}\text{C}/\text{min}$  from  $4$   $^{\circ}\text{C}$ , i.e. if the seeding temperature of water is between  $-4$   $^{\circ}\text{C}$  and  $-8$   $^{\circ}\text{C}$  (Trad et al. 1999, Li et al. 2018), the respective DMSO diffusion is extended to at least 8 min until ice crystallisation occurs. Thus, all samples were incubated for at least 8 min in a liquid state, which is even higher than the calculated perfusion time  $t_{90\%}$  of large spheroids. This indicates that probably all samples were sufficiently supplied with DMSO due to process-related prolonged incubation. Additional Raman micro-spectroscopy analyses to study diffusion kinetics of DMSO at sub-zero temperatures would enable the adaptation of the diffusion model fit to the actual slow-rate freezing conditions by including the Arrhenius coefficients.

To confirm this hypothesis, NSC spheroids were additionally cryopreserved by vitrification after DMSO incubation with the derived times  $t_{90\%}$  and  $t_{50\%}$ . When ultra-fast cooling rates were applied by  $\text{LN}_2$ , the spheroids were immediately converted into a glass-like state, and no additional DMSO diffusion should occur. After vitrification, the relative cell viability was significantly increased with the corresponding Raman micro-spectroscopy-derived DMSO incubation time  $t_{90\%}$  (Fig. 43). These results support the hypothesis that prolonged incubation during slow-rate freezing leads to a complete supply of DMSO in all spheroid diameters, which causes comparable cell viability after cryopreservation. With adapted incubation times, the cells can be adequately supplied, and cytotoxicity reduced simultaneously. However, a contradictory aspect is that even after a 15 min incubation with DMSO, no significant changes in cell viability were observed compared to a 0 min incubation, although cytotoxic effects were expected after

prolonged DMSO exposure (Awan et al. 2020). However, the presentation of 10% DMSO has only a marginal effect on the cell viability in NSC spheroids (Fig. 14) but can affect the expression of genes and proteins, as shown in Fig. 15 and 16. Thus, the minimal incubation times required could be beneficial, and additional studies on functionality could further substantiate these results.

### **Challenges in measuring diffusion kinetics with Raman micro-spectroscopy**

Despite these promising results, the current Raman micro-spectroscopy technique is still limited by sample handling. To perform Raman micro-spectroscopy, the spheroid must be immobilised for a long time, even during fast medium exchange. The challenge here is to meet the requirements of the diffusion fitting model for symmetric geometries, which excludes immobilisation approaches that significantly deform the samples or hinder penetration by covering part of the surface. Attempts to mechanically fix spheroids in a medium perfusion channel have led to excessive deformation and detachments during the medium exchange. Alternatively, non-contact immobilisation methods using ultrasound (Kvåle Løvmo et al. 2023) and digital acoustofluidics (Cai et al. 2020) are currently being investigated to overcome these hurdles. In the present proof-of-concept method, DMSO-d6 is only manually added to a slightly attached spheroid in a small droplet of medium. As a result, the start of the detection of Raman spectra is delayed by about 20-30 s since considerable time is required for homogenising the medium and checking the focus after applying DMSO-d6. Hence, the development of innovative 3D model handling techniques that enable reliable immobilisation with controlled, fast liquid medium changes while maintaining the geometries would reduce most interfering processes and enable a defined start time for Raman micro-spectroscopy measurement. In addition, the diffusion processes in spheroids incubated in larger volumes of cryopreservation media, as in cryovials, could be better simulated. Nevertheless, the present technique is valuable for determining the perfusion times of various compounds in differently shaped 3D cell models to derive appropriate model-specific diffusion kinetics. The technique provides an easy way to assess CPA perfusion times into tissue, which will significantly impact the cryopreservation of specimens beyond isolated cells.

## 6 Conclusion and Outlook

This work focuses on investigating the cryo injury effects in hiPSCs-derived 3D cell models. These analyses provide new insights into cryo-induced mechanisms in single-cell-type precursor organoids and organoids to improve the understanding and unravel cryo processes in 3D cell models with increasing interest in biomedical research. On this basis, innovative cryopreservation concepts and procedures for 3D cell models can be derived and established. So far, the main hurdles to successful cryopreservation of 3D cell systems are the inhomogeneous cooling and heat transfer and the retarded penetration of CPAs. Hence, different parameters, such as the spheroid volume and maturity level concerning cell junctions, significantly influence the cryopreservation outcome. In these studies, similar cryo-damaging effects were reported in different spheroid and organoid volumes, such as the detachment of the three peripheral cell layers with similar thicknesses. Structural cell analyses and vitrification contributed to a better understanding of the rupture of cell-cell junctions in the periphery due to high osmotic stress and IFF. Additional integration of monitoring microsensors into the spheroids to measure osmotic-induced tension on the plasma membrane (Charras and Yap 2018) of cells in different layers would be beneficial to get further insights into the structural changes in the peripheral cells before and after cryopreservation. The aim is to reduce the cell detachment after thawing, e.g. by adding specific growth factors to stabilise the interactions of the cell junction (Angulo-Urarte et al. 2020). In the scope of this work, it has been demonstrated that the loss of viable cells is not proportional to the spheroid volume due to radial avascular growth kinetics with a power of three. Thus, the selection of suitable spheroid volumes for cryopreservation protocols depends on the required applications. Large spheroids provide a percentage larger volume of viable cells, while small spheroids have higher proliferation rates after thawing. After the detachment of the peripheral cells, it could be demonstrated that the former intermediate cells were able to regain high viability values, proliferation capacities and genetic state within a short recovery time after thawing. In particular, hepatic spheroids have also been shown to maintain their differentiation potential even after being thawed. However, it could also be shown that the recovery potential must always be examined for the respective model-specific characteristics and functions. Successful recovery in precursor organoids was achieved by an adequate supply of CPAs in the outer cell layers of viable cells, which was confirmed by DMSO diffusion kinetics in spheroids using bioorthogonal Raman micro-spectroscopy. This technique was introduced to determine the perfusion times of CPAs in the inner cells of 3D cell models. Understanding the perfusion times of CPAs is essential for appropriate application and pre-incubation before cryopreservation while avoiding cytotoxicity. The method is versatile and can be easily applied to other 3D model geometries and compounds, such as drug screening studies. Compared to other diffusion analyses, the advantage of this method is the ability to measure compound perfusion without contact and to set the focus directly inside the tissue. Further research into the immobilisation of spheroids and organoids would improve focusing during measurement, e.g. with ultrasound (Kvåle Løvmo et al. 2023) or digital acoustofluidics (Cai et al. 2020).

In the next step, the technique and the diffusion fit model could be extended to an inline Raman micro-spectroscopy monitoring before cryopreservation of 3D cell models. This would provide the opportunity to combine the determination of model-specific CPA penetration with subsequently adapted cryopreservation protocols (Fig. 50). Accordingly, CPA concentrations, incubation times, and sample volumes could be immediately adjusted in line with the integration of the simultaneously analysed Raman micro-spectroscopy data. An additional upstream selection of 3D cell models according to various parameters, such as volume or cell density, would enable a corresponding model- and parameter-specific CPA supply to develop innovative and standardised cryopreservation procedures for large, heterogeneous spheroid and organoid batches.

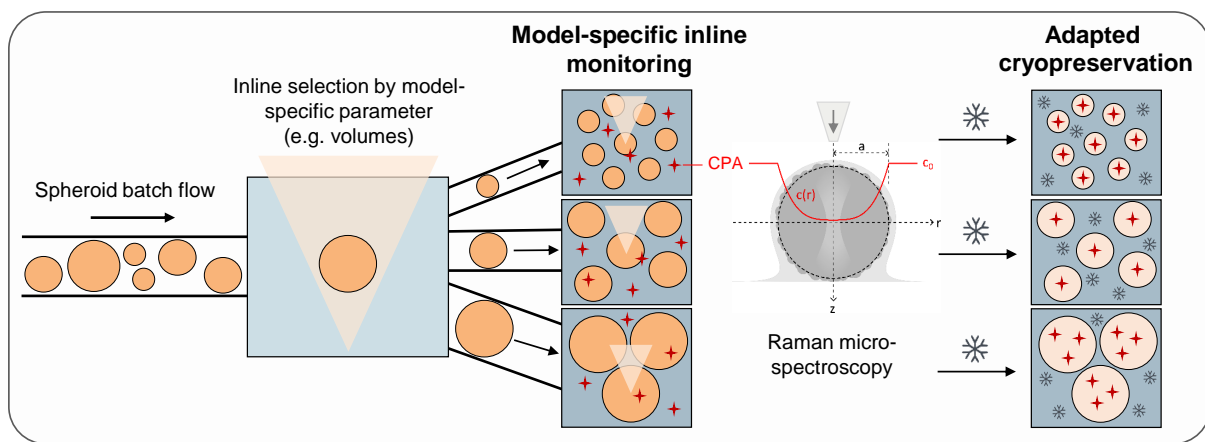


Figure 50: **Schematic overview of model-specific inline monitoring using Raman micro-spectroscopy.** The integration of non-contact Raman technology for the inline determination of CPA penetration would standardise the cryopreservation of large, heterogeneous spheroid and organoid batches. An upstream selection according to model-specific parameters would enable parameter-related adaptation for cryopreservation. Based on this, new, innovative cryopreservation protocols could be established.

---

## 7 References

- [1] J. Aach, J. Lunshof, E. Iyer, and G. M. Church (2017). “Addressing the ethical issues raised by synthetic human entities with embryo-like features”. *eLife* 6, e20674. DOI: 10.7554/eLife.20674.
- [2] J. P. Acker, J. A. Elliott, and L. E. McGann (2001). “Intercellular ice propagation: experimental evidence for ice growth through membrane pores”. *Biophysical journal* 81(3), 1389–1397. DOI: 10.1016/S0006-3495(01)75794-3.
- [3] J. P. Acker, A. Larese, H. Yang, A. Petrenko, and L. E. McGann (1999). “Intracellular ice formation is affected by cell interactions”. *Cryobiology* 38(4), 363–371. DOI: 10.1006/cryo.1999.2179.
- [4] J. P. Acker (2007). “Biopreservation of cells and engineered tissues”. *Advances in biochemical engineering/biotechnology* 103, 157–187. DOI: 10.1007/b137204.
- [5] Y. Agca (2000). “Cryopreservation of oocyte and ovarian tissue”. *ILAR journal* 41(4), 207–220. DOI: 10.1093/ilar.41.4.207.
- [6] Y. M. Alexandrovskaya, E. M. Kasianenko, A. A. Sovetsky, A. L. Matveyev, and V. Y. Zaitsev (2023). “Spatio-Temporal Dynamics of Diffusion-Associated Deformations of Biological Tissues and Polyacrylamide Gels Observed with Optical Coherence Elastography”. *Materials (Basel, Switzerland)* 16(5), 2036. DOI: 10.3390/ma16052036.
- [7] A. Ali, A. I. Nykanen, E. Beroncal, E. Brambate, A. Mariscal, V. Michaelsen, A. Wang, M. Kawashima, R. V. P. Ribeiro, Y. Zhang, E. Fan, L. Brochard, J. Yeung, T. Waddell, M. Liu, A. C. Andreatza, S. Keshavjee, and M. Cypel (2022). “Successful 3-day lung preservation using a cyclic normothermic ex vivo lung perfusion strategy”. *EBioMedicine* 83, 104210. DOI: 10.1016/j.ebiom.2022.104210.
- [8] R. B. Alley, J. H. Pehrepecko, and C. R. Bentley (1986). “Grain Growth in Polar Ice: I. Theory”. *Journal of Glaciology* 32(112), 415–424. DOI: 10.3189/S0022143000012120.
- [9] P. E. de Almeida, J. D. Ransohoff, A. Nahid, and J. C. Wu (2013). “Immunogenicity of pluripotent stem cells and their derivatives”. *Circulation research* 112(3), 549–561. DOI: 10.1161/CIRCRESAHA.111.249243.
- [10] S. Altmaier, I. Meiser, E. Lemesre, B. Chanrion, R. Steeg, L. E. Leonte, B. Holst, B. S. Nielsen, C. Clausen, K. Schmidt, A. M. Vinggaard, H. Zimmermann, J. C. Neubauer, and M. A. Rasmussen (2022). “Human iPSC-derived hepatocytes in 2D and 3D suspension culture for cryopreservation and in vitro toxicity studies”. *Reproductive toxicology (Elmsford, N.Y.)* 111, 68–80. DOI: 10.1016/j.reprotox.2022.05.005.
- [11] S. Altmaier, I. Meiser, F. Stracke, and H. Zimmermann (2024). “Diffusion kinetics & perfusion times in tissue models obtained by bioorthogonal Raman  $\mu$ -spectroscopy”. *Biophysical Reports* 4(2), 100150. DOI: 10.1016/j.bpr.2024.100150.
- [12] M. Amini and J. D. Benson (2023). “Technologies for Vitrification Based Cryopreservation”. *Bioengineering (Basel, Switzerland)* 10(5), 508. DOI: 10.3390/bioengineering10050508.

- 
- [13] A. A. Ampaw, A. Sibthorpe, and R. N. Ben (2021). “Use of Ice Recrystallization Inhibition Assays to Screen for Compounds That Inhibit Ice Recrystallization”. In: *Cryopreservation and Freeze-Drying Protocols*. Ed. by W. F. Wolkers and H. Oldenhof. New York, NY: Springer US, pp. 271–283. ISBN: 978-1-0716-0782-4.
- [14] A. Angulo-Urarte, T. van der Wal, and S. Huveneers (2020). “Cell-cell junctions as sensors and transducers of mechanical forces”. *Biochimica et biophysica acta. Biomembranes* 1862(9), 183316. DOI: 10.1016/j.bbamem.2020.183316.
- [15] P. A. Apostolidis, A. Tseng, M.-E. Koziol, M. J. Betenbaugh, and B. Chiang (2015). “Investigation of low viability in sparged bioreactor CHO cell cultures points to variability in the Pluronic F-68 shear protecting component of cell culture media”. *Biochemical Engineering Journal* 98, 10–17. DOI: 10.1016/j.bej.2015.01.013.
- [16] A. Arav and D. Natan (2012). “Directional freezing of reproductive cells and organs”. *Reproduction in domestic animals* 47, 193–196. DOI: 10.1111/j.1439-0531.2012.02075.x.
- [17] A. Arav (2022). “Cryopreservation by Directional Freezing and Vitrification Focusing on Large Tissues and Organs”. *Cells* 11(7), 1072. DOI: 10.3390/cells11071072.
- [18] W. J. Armitage and B. K. Juss (2000). “Assembly of intercellular junctions in epithelial cell monolayers following exposure to cryoprotectants”. *Cryobiology* 41(1), 58–65. DOI: 10.1006/cryo.2000.2266.
- [19] W. J. Armitage and B. K. Juss (2003). “Freezing monolayers of cells without gap junctions”. *Cryobiology* 46(2), 194–196. DOI: 10.1016/s0011-2240(03)00017-8.
- [20] S. K. Asrani, J. J. Larson, B. Yawn, T. M. Therneau, and W. R. Kim (2013). “Underestimation of liver-related mortality in the United States”. *Gastroenterology* 145(2), 375-82.e1–2. DOI: 10.1053/j.gastro.2013.04.005.
- [21] M. Awan, I. Buriak, R. Fleck, B. Fuller, A. Goltsev, J. Kerby, M. Lowdell, P. Mericka, A. Petrenko, Y. Petrenko, O. Rogulska, A. Stolzing, and G. N. Stacey (2020). “Dimethyl sulfoxide: a central player since the dawn of cryobiology, is efficacy balanced by toxicity?” *Regenerative medicine* 15(3), 1463–1491. DOI: 10.2217/rme-2019-0145.
- [22] G. Azemtso Matanfack, J. Rüger, C. Stiebing, M. Schmitt, and J. Popp (2020). “Imaging the invisible-Bioorthogonal Raman probes for imaging of cells and tissues”. *Journal of biophotonics* 13(9), e202000129. DOI: 10.1002/jbio.202000129.
- [23] F. Baino, G. Novajra, and C. Vitale-Brovarone (2015). “Bioceramics and Scaffolds: A Winning Combination for Tissue Engineering”. *Frontiers in bioengineering and biotechnology* 3, 202. DOI: 10.3389/fbioe.2015.00202.
- [24] A. Bandzerewicz and A. Gadowska-Gajadhur (2022). “Into the Tissues: Extracellular Matrix and Its Artificial Substitutes: Cell Signalling Mechanisms”. *Cells* 11(5), 914. DOI: 10.3390/cells11050914.
- [25] M. H. Barcellos-Hoff, J. Aggeler, T. G. Ram, and M. J. Bissell (1989). “Functional differentiation and alveolar morphogenesis of primary mammary cultures on reconstituted basement membrane”. *Development (Cambridge, England)* 105(2), 223–235. DOI: 10.1242/dev.105.2.223.

- 
- [26] A. Bardow, W. Marquardt, V. Göke, H.-J. Koss, and K. Lucas (2003). “Model-based measurement of diffusion using Raman spectroscopy”. *AIChE Journal* 49(2), 323–334. DOI: 10.1002/aic.690490205.
- [27] D. W. Barnes and J. F. Loutit (1967). “Haemopoietic stem cells in the peripheral blood”. *The Lancet* 2(7526), 1138–1141. DOI: 10.1016/S0140-6736(67)90636-8.
- [28] R. C. Bates, N. S. Edwards, and J. D. Yates (2000). “Spheroids and cell survival”. *Critical reviews in oncology/hematology* 36(2-3), 61–74. DOI: 10.1016/S1040-8428(00)00077-9.
- [29] J. G. Baust and J. M. Baust (2007). “Biology of Cell Survival in the Cold: The Basis for Biopreservation of Tissues and Organs”. In: *Advances in biopreservation*. Ed. by J. G. Baust and J. M. Baust. Boca Raton, FL: CRC/Taylor & Francis. ISBN: 978-0-4291-2989-6.
- [30] J. M. Baust, L. H. Campbell, and J. W. Harbell (2017). “Best practices for cryopreserving, thawing, recovering, and assessing cells”. *In vitro cellular & developmental biology. Animal* 53(10), 855–871. DOI: 10.1007/s11626-017-0201-y.
- [31] T. G. Beach, S. E. Monsell, L. E. Phillips, and W. Kukull (2012). “Accuracy of the clinical diagnosis of Alzheimer disease at National Institute on Aging Alzheimer Disease Centers, 2005-2010”. *Journal of neuropathology and experimental neurology* 71(4), 266–273. DOI: 10.1097/NEN.0b013e31824b211b.
- [32] M. Beaumont, F. Blanc, C. Cherbuy, G. Egidy, E. Giuffra, S. Lacroix-Lamandé, and A. Wiedemann (2021). “Intestinal organoids in farm animals”. *Veterinary research* 52(1), 33. DOI: 10.1186/s13567-021-00909-x.
- [33] S. Behl, V. B. Joshi, N. B. Larson, M. C. Young, M. Bilal, D. L. Walker, Z. Khan, C. F. Granberg, A. Chattha, and Y. Zhao (2023). “Vitrification versus slow freezing of human ovarian tissue: a systematic review and meta-analysis of histological outcomes”. *Journal of assisted reproduction and genetics* 40(3), 455–464. DOI: 10.1007/s10815-022-02692-w.
- [34] A. Beier, J. Schulz, D. Dörr, A. Katsen-Globa, A. Sachinidis, J. Hescheler, and H. Zimmermann (2011). “Effective surface-based cryopreservation of human embryonic stem cells by vitrification”. *Cryobiology* 63(3), 175–185. DOI: 10.1016/j.cryobiol.2011.06.003..
- [35] A. Beier, J. Schulz, and H. Zimmermann (2013). “Cryopreservation with a twist - towards a sterile, serum-free surface-based vitrification of hESCs”. *Cryobiology* 66(1), 8–16. DOI: 10.1016/j.cryobiol.2012.10.001.
- [36] S. Bell, N. C. Hettige, H. Silveira, H. Peng, H. Wu, M. Jefri, L. Antonyan, Y. Zhang, X. Zhang, and C. Ernst (2019). “Differentiation of Human Induced Pluripotent Stem Cells (iPSCs) into an Effective Model of Forebrain Neural Progenitor Cells and Mature Neurons”. *Bio-protocol* 9(5), e3188. DOI: 10.21769/BioProtoc.3188.
- [37] Y. Ben-Ari, Y. Brody, N. Kinor, A. Mor, T. Tsukamoto, D. L. Spector, R. H. Singer, and Y. Shav-Tal (2010). “The life of an mRNA in space and time”. *Journal of cell science* 123(10), 1761–1774. DOI: 10.1242/jcs.062638.

- [38] W. K. Berger and B. Uhrík (1996). “Freeze-induced shrinkage of individual cells and cell-to-cell propagation of intracellular ice in cell chains from salivary glands”. *Experientia* 52(9), 843–850. DOI: 10.1007/BF01938868.
- [39] R. Bertram and M. Pernarowski (1998). “Glucose diffusion in pancreatic islets of Langerhans”. *Biophysical journal* 74(4), 1722–1731. DOI: 10.1016/S0006-3495(98)77883-X.
- [40] B. P. Best (2015). “Cryoprotectant Toxicity: Facts, Issues, and Questions”. *Rejuvenation research* 18(5), 422–436. DOI: 10.1089/rej.2014.1656.
- [41] A. Bhaduri, M. G. Andrews, W. Mancina Leon, D. Jung, D. Shin, D. Allen, D. Jung, G. Schmunk, M. Haeussler, J. Salma, A. A. Pollen, T. J. Nowakowski, and A. R. Kriegstein (2020). “Cell stress in cortical organoids impairs molecular subtype specification”. *Nature* 578(7793), 142–148. DOI: 10.1038/s41586-020-1962-0.
- [42] A. L. Bishop and A. Hall (2000). “Rho GTPases and their effector proteins”. *The Biochemical journal* 348(2), 241–255. DOI: 10.1042/bj3480241.
- [43] A. Bissoyi, R. M. F. Tomás, Y. Gao, Q. Guo, and M. I. Gibson (2023). “Cryopreservation of Liver-Cell Spheroids with Macromolecular Cryoprotectants”. *ACS applied materials & interfaces* 15(2), 2630–2638. DOI: 10.1021/acsami.2c18288.
- [44] O. W. Blaschuk (2022). “Potential Therapeutic Applications of N-Cadherin Antagonists and Agonists”. *Frontiers in cell and developmental biology* 10, 866200. DOI: 10.3389/fcell.2022.866200.
- [45] J. Blaszkiewicz and S. A. Duncan (2022). “Advancements in Disease Modeling and Drug Discovery Using iPSC-Derived Hepatocyte-like Cells”. *Genes* 13(4), 573. DOI: 10.3390/genes13040573.
- [46] BMBF (2023). *Richtlinie zur Förderung von Analysen zu OMICS-Studien zur Identifizierung neuer Wirkstoffkandidaten im Rahmen des European Joint Programme – Neurodegenerative Disease Research (JPND)*. URL: <https://www.bmbf.de/bmbf/shareddocs/bekanntmachungen/de/2023/03/2023-03-17-Bekanntmachung-JPND.html>(26.02.24).
- [47] S. Bojic, A. Murray, B. L. Bentley, R. Spindler, P. Pawlik, J. L. Cordeiro, R. Bauer, and J. P. de Magalhães (2021). “Winter is coming: the future of cryopreservation”. *BMC biology* 19(1), 56. DOI: 10.1186/s12915-021-00976-8.
- [48] R. Boyle (1683). “New Experiments and Observations Touching Cold, or, An Experimental History of Cold, Begun”. *London : Printed for Richard Davis*. URL: <https://books.google.com/books?id=2p1kAAAACAAJ&printsec=frontcover>.
- [49] A. Bradford, M. E. Kunik, P. Schulz, S. P. Williams, and H. Singh (2009). “Missed and delayed diagnosis of dementia in primary care: prevalence and contributing factors”. *Alzheimer disease and associated disorders* 23(4), 306–314. DOI: 10.1097/WAD.0b013e3181a6bebc.
- [50] J. A. Brassard and M. P. Lutolf (2019). “Engineering Stem Cell Self-organization to Build Better Organoids”. *Cell stem cell* 24(6), 860–876. DOI: 10.1016/j.stem.2019.05.005.
- [51] A. Bubnys and L.-H. Tsai (2022). “Harnessing cerebral organoids for Alzheimer’s disease research”. *Current opinion in neurobiology* 72, 120–130. DOI: 10.1016/j.conb.2021.10.003.

- 
- [52] C. Budke, C. Heggemann, M. Koch, N. Sewald, and T. Koop (2009). “Ice recrystallization kinetics in the presence of synthetic antifreeze glycoprotein analogues using the framework of LSW theory”. *The journal of physical chemistry. B* 113(9), 2865–2873. DOI: 10.1021/jp805726e.
- [53] K. Bujko, M. Kucia, J. Ratajczak, and M. Z. Ratajczak (2019). “Hematopoietic Stem and Progenitor Cells (HSPCs)”. *Advances in experimental medicine and biology* 1201, 49–77. DOI: 10.1007/978-3-030-31206-0\_3.
- [54] W. B. Busa (1986). “Mechanisms and consequences of pH-mediated cell regulation”. *Annual review of physiology* 48, 389–402. DOI: 10.1146/annurev.ph.48.030186.002133.
- [55] H. Cai, Z. Wu, Z. Ao, A. Nunez, B. Chen, L. Jiang, M. Bondesson, and F. Guo (2020). “Trapping cell spheroids and organoids using digital acoustofluidics”. *Biofabrication* 12(3), 035025. DOI: 10.1088/1758-5090/ab9582.
- [56] S. Capaccioli and K. L. Ngai (2011). “Resolving the controversy on the glass transition temperature of water?” *The Journal of Chemical Physics* 135(10), 104504. DOI: 10.1063/1.3633242.
- [57] I. Carneiro, S. Carvalho, R. Henrique, L. M. Oliveira, and V. V. Tuchin (2019). “A robust ex vivo method to evaluate the diffusion properties of agents in biological tissues”. *Journal of biophotonics* 12(4), e201800333. DOI: 10.1002/jbio.201800333.
- [58] A. Carpentier, I. Nimgaonkar, V. Chu, Y. Xia, Z. Hu, and T. J. Liang (2016). “Hepatic differentiation of human pluripotent stem cells in miniaturized format suitable for high-throughput screen”. *Stem cell research* 16(3), 640–650. DOI: 10.1016/j.scr.2016.03.009.
- [59] A. Casado-Díaz (2022). “Stem Cells in Regenerative Medicine”. *Journal of clinical medicine* 11(18), 5460. DOI: 10.3390/jcm11185460.
- [60] J. Cerneckis, G. Bu, and Y. Shi (2023). “Pushing the boundaries of brain organoids to study Alzheimer’s disease”. *Trends in molecular medicine* 29(8), 659–672. DOI: 10.1016/j.molmed.2023.05.007.
- [61] N. Chaicharoenaudomrung, P. Kunhorm, and P. Noisa (2019). “Three-dimensional cell culture systems as an in vitro platform for cancer and stem cell modeling”. *World journal of stem cells* 11(12), 1065–1083. DOI: 10.4252/wjsc.v11.i12.1065.
- [62] A. Chandrasekaran, H. X. Avci, A. Ochalek, L. N. Rösingh, K. Molnár, L. László, T. Bellák, A. Téglási, K. Pesti, A. Mike, P. Phanthong, O. Bíró, V. Hall, N. Kitiyanant, K.-H. Krause, J. Kobilák, and A. Dinnyés (2017). “Comparison of 2D and 3D neural induction methods for the generation of neural progenitor cells from human induced pluripotent stem cells”. *Stem cell research* 25, 139–151. DOI: 10.1016/j.scr.2017.10.010.
- [63] D. Chang, R. Fox, E. Hicks, R. Ferguson, K. Chang, D. Osborne, W. Hu, and O. D. Velev (2017). “Investigation of interfacial properties of pure and mixed poloxamers for surfactant-mediated shear protection of mammalian cells”. *Colloids and surfaces. B, Biointerfaces* 156, 358–365. DOI: 10.1016/j.colsurfb.2017.05.040.
- [64] G. T. Charras and A. S. Yap (2018). “Tensile Forces and Mechanotransduction at Cell-Cell Junctions”. *Current biology : CB* 28(8), R445–R457. DOI: 10.1016/j.cub.2018.02.003.

- 
- [65] G. T. Charras, C.-K. Hu, M. Coughlin, and T. J. Mitchison (2006). “Reassembly of contractile actin cortex in cell blebs”. *The Journal of cell biology* 175(3), 477–490. DOI: 10.1083/jcb.200602085.
- [66] A. Chatterjee, D. Saha, H. Niemann, O. Gryshkov, B. Glasmacher, and N. Hofmann (2017). “Effects of cryopreservation on the epigenetic profile of cells”. *Cryobiology* 74, 1–7. DOI: 10.1016/j.cryobiol.2016.12.002.
- [67] C. Chesné and A. Guillouzo (1988). “Cryopreservation of isolated rat hepatocytes: a critical evaluation of freezing and thawing conditions”. *Cryobiology* 25(4), 323–330. DOI: 10.1016/0011-2240(88)90040-5..
- [68] K. Chitcholtan, E. Asselin, S. Parent, P. H. Sykes, and J. J. Evans (2013). “Differences in growth properties of endometrial cancer in three dimensional (3D) culture and 2D cell monolayer”. *Experimental Cell Research* 319(1), 75–87. DOI: 10.1016/j.yexcr.2012.09.012.
- [69] W. S. Chiu, N. A. Belsey, N. L. Garrett, J. Moger, M. B. Delgado-Charro, and R. H. Guy (2015). “Molecular diffusion in the human nail measured by stimulated Raman scattering microscopy”. *Proceedings of the National Academy of Sciences of the United States of America* 112(25), 7725–7730. DOI: 10.1073/pnas.1503791112.
- [70] J. Choi, B. Lee, E. Lee, B.-K. Yoon, D. Bae, and D. Choi (2008). “Cryopreservation of ovarian tissues temporarily suppresses the proliferation of granulosa cells in mouse preantral follicles”. *Cryobiology* 56(1), 36–42. DOI: 10.1016/j.cryobiol.2007.10.174.
- [71] D. A. Claassen, M. M. Desler, and A. Rizzino (2009). “ROCK inhibition enhances the recovery and growth of cryopreserved human embryonic stem cells and human induced pluripotent stem cells”. *Molecular reproduction and development* 76(8), 722–732. DOI: 10.1002/mrd.21021.
- [72] J. S. Clegg, P. Seitz, W. Seitz, and C. F. Hazlewood (1982). “Cellular responses to extreme water loss: the water-replacement hypothesis”. *Cryobiology* 19(3), 306–316. DOI: 10.1016/0011-2240(82)90159-6..
- [73] H. Clevers (2016). “Modeling Development and Disease with Organoids”. *Cell* 165(7), 1586–1597. DOI: 10.1016/j.cell.2016.05.082.
- [74] M. L. Condic (2014). “Totipotency: what it is and what it is not”. *Stem cells and development* 23(8), 796–812. DOI: 10.1089/scd.2013.0364.
- [75] A. Corral, M. Clavero, M. Gallardo, M. Balcerzyk, C. A. Amorim, Á. Parrado-Gallego, M.-M. Dolmans, F. Paulini, J. Morris, and R. Risco (2018). “Ovarian tissue cryopreservation by stepped vitrification and monitored by X-ray computed tomography”. *Cryobiology* 81, 17–26. DOI: 10.1016/j.cryobiol.2018.03.001.
- [76] E. C. Costa, A. F. Moreira, D. de Melo-Diogo, V. M. Gaspar, M. P. Carvalho, and I. J. Correia (2016). “3D tumor spheroids: an overview on the tools and techniques used for their analysis”. *Biotechnology advances* 34(8), 1427–1441. DOI: 10.1016/j.biotechadv.2016.11.002.
- [77] J. Crank (2009). *The mathematics of diffusion*. 2. ed., reprinted. Oxford science publications. Oxford: Oxford Univ. Press. ISBN: 978-0-1985-3411-2.

- [78] D. Cyranoski (2018). “How human embryonic stem cells sparked a revolution”. *Nature* 555(7697), 428–430. DOI: 10.1038/d41586-018-03268-4.
- [79] M. S. D’Arcy (2019). “Cell death: a review of the major forms of apoptosis, necrosis and autophagy”. *Cell biology international* 43(6), 582–592. DOI: 10.1002/cbin.11137.
- [80] J. Daly, N. Zuchowicz, C. I. Nuñez Lendo, K. Khosla, C. Lager, E. M. Henley, J. Bischof, F. W. Kleinhaus, C. Lin, E. C. Peters, and M. Hagedorn (2018). “Successful cryopreservation of coral larvae using vitrification and laser warming”. *Scientific reports* 8(1), 15714. DOI: 10.1038/s41598-018-34035-0.
- [81] A. A. Dayem, S. B. Lee, K. Kim, K. M. Lim, T.-I. Jeon, and S.-G. Cho (2019). “Recent advances in organoid culture for insulin production and diabetes therapy: methods and challenges”. *BMB reports* 52(5), 295–303. DOI: 10.5483/BMBRep.2019.52.5.089.
- [82] M. Desouza, P. W. Gunning, and J. R. Stehn (2012). “The actin cytoskeleton as a sensor and mediator of apoptosis”. *Bioarchitecture* 2(3), 75–87. DOI: 10.4161/bioa.20975.
- [83] H. Devarbhavi, S. K. Asrani, J. P. Arab, Y. A. Nartey, E. Pose, and P. S. Kamath (2023). “Global burden of liver disease: 2023 update”. *Journal of hepatology* 79(2), 516–537. DOI: 10.1016/j.jhep.2023.03.017.
- [84] A. L. DeVries (1983). “Antifreeze peptides and glycopeptides in cold-water fishes”. *Annual review of physiology* 45, 245–260. DOI: 10.1146/annurev.ph.45.030183.001333.
- [85] A. A. Diaz, H. Kubo, N. Handa, M. Hanna, and M. M. Laronda (2022). “A Systematic Review of Ovarian Tissue Transplantation Outcomes by Ovarian Tissue Processing Size for Cryopreservation”. *Frontiers in endocrinology* 13, 918899. DOI: 10.3389/fendo.2022.918899.
- [86] N. Dolezalova, A. Gruszczuk, K. Barkan, J. A. Gamble, S. Galvin, T. Moreth, K. O’Holleran, K. T. Mahbubani, J. A. Higgins, F. M. Gribble, F. Reimann, J. Surmacki, S. Andrews, J. J. Casey, F. Pampaloni, M. P. Murphy, G. Ladds, N. K. H. Slater, and K. Saeb-Parsy (2021). “Accelerating cryoprotectant diffusion kinetics improves cryopreservation of pancreatic islets”. *Scientific reports* 11(1), 10418. DOI: 10.1038/s41598-021-89853-6.
- [87] J. Dornhof, V. Zieger, J. Kieninger, D. Frejek, R. Zengerle, G. A. Urban, S. Kartmann, and A. Weltin (2022). “Bioprinting-based automated deposition of single cancer cell spheroids into oxygen sensor microelectrode wells”. *Lab on a chip* 22(22), 4369–4381. DOI: 10.1039/D2LC00705C.
- [88] M. X. Doss, C. I. Koehler, C. Gissel, J. Hescheler, and A. Sachinidis (2004). “Embryonic stem cells: a promising tool for cell replacement therapy”. *Journal of cellular and molecular medicine* 8(4), 465–473. DOI: 10.1111/j.1582-4934.2004.tb00471.x.
- [89] M. X. Doss and A. Sachinidis (2019). “Current Challenges of iPSC-Based Disease Modeling and Therapeutic Implications”. *Cells* 8(5), 403. DOI: 10.3390/cells8050403.
- [90] C. Du, Y. Feng, D. Qiu, Y. Xu, M. Pang, N. Cai, A. P. Xiang, and Q. Zhang (2018). “Highly efficient and expedited hepatic differentiation from human pluripotent stem cells

- by pure small-molecule cocktails”. *Stem cell research & therapy* 9(1), 58. DOI: 10.1186/s13287-018-0794-4.
- [91] K. Duval, H. Grover, L.-H. Han, Y. Mou, A. F. Pegoraro, J. Fredberg, and Z. Chen (2017). “Modeling Physiological Events in 2D vs. 3D Cell Culture”. *Physiology (Bethesda, Md.)* 32(4), 266–277. DOI: 10.1152/physiol.00036.2016.
- [92] K. L. Eales, K. E. R. Hollinshead, and D. A. Tennant (2016). “Hypoxia and metabolic adaptation of cancer cells”. *Oncogenesis* 5(1), e190. DOI: 10.1038/oncsis.2015.50.
- [93] A. K. Ekaputra, G. D. Prestwich, S. M. Cool, and D. W. Hutmacher (2011). “The three-dimensional vascularization of growth factor-releasing hybrid scaffold of poly (epsilon-caprolactone)/collagen fibers and hyaluronic acid hydrogel”. *Biomaterials* 32(32), 8108–8117. DOI: 10.1016/j.biomaterials.2011.07.022.
- [94] T. El Cury-Silva, M. E. G. Nunes, M. Casalechi, F. V. Comim, J. K. Rodrigues, and F. M. Reis (2021). “Cryoprotectant agents for ovarian tissue vitrification: Systematic review”. *Cryobiology* 103, 7–14. DOI: 10.1016/j.cryobiol.2021.08.001.
- [95] G. D. Elliott, S. Wang, and B. J. Fuller (2017). “Cryoprotectants: A review of the actions and applications of cryoprotective solutes that modulate cell recovery from ultra-low temperatures”. *Cryobiology* 76, 74–91. DOI: 10.1016/j.cryobiol.2017.04.004.
- [96] M. L. Etheridge and J. C. Bischof (2013). “Optimizing magnetic nanoparticle based thermal therapies within the physical limits of heating”. *Annals of biomedical engineering* 41(1), 78–88. DOI: 10.1007/s10439-012-0633-1.
- [97] S. Etienne-Manneville and A. Hall (2002). “Rho GTPases in cell biology”. *Nature* 420(6916), 629–635. DOI: 10.1038/nature01148.
- [98] G. M. Fahy, T. H. Lilley, H. Linsdell, M. S. Douglas, and H. T. Meryman (1990). “Cryoprotectant toxicity and cryoprotectant toxicity reduction: in search of molecular mechanisms”. *Cryobiology* 27(3), 247–268. DOI: 10.1016/0011-2240(90)90025-Y.
- [99] G. M. Fahy, D. R. MacFarlane, C. A. Angell, and H. T. Meryman (1984). “Vitrification as an approach to cryopreservation”. *Cryobiology* 21(4), 407–426. DOI: 10.1016/0011-2240(84)90079-8..
- [100] G. M. Fahy and W. F. Rall (2007). “Vitrification: an overview”. In: *Vitrification in Assisted Reproduction*. Ed. by M. J. Tucker and J. Liebermann. Reproductive Medicine and Assisted Reproductive Techniques. Informa Healthcare, pp. 1–20. ISBN: 0-203-09002-0. DOI: 10.3109/9780203090022.001.
- [101] G. M. Fahy and B. Wowk (2021). “Principles of Ice-Free Cryopreservation by Vitrification”. In: *Cryopreservation and Freeze-Drying Protocols*. Ed. by W. F. Wolkers and H. Oldenhof. New York, NY: Springer US, pp. 27–97. ISBN: 978-1-0716-0782-4.
- [102] G. M. Fahy, B. Wowk, R. Pagotan, A. Chang, J. Phan, B. Thomson, and L. Phan (2009). “Physical and biological aspects of renal vitrification”. *Organogenesis* 5(3), 167–175. DOI: 10.4161/org.5.3.9974.
- [103] E. Falcieri, P. Gobbi, L. Zamai, and M. Vitale (1994). “Ultrastructural features of apoptosis”. *Scanning microscopy* 8(3), 653–655. DOI: -.

- 
- [104] T. T. Falzone, M. Lenz, D. R. Kovar, and M. L. Gardel (2012). “Assembly kinetics determine the architecture of  $\alpha$ -actinin crosslinked F-actin networks”. *Nature communications* 3, 861. DOI: 10.1038/ncomms1862.
- [105] M. Ferreira, A. Bos-Mikich, N. Frantz, J. L. Rodrigues, A. L. Brunetto, and G. Schwartsmann (2010). “The effects of sample size on the outcome of ovarian tissue cryopreservation”. *Reproduction in domestic animals* 45(1), 99–102. DOI: 10.1111/j.1439-0531.2008.01261.x.
- [106] J. E. Ferrell (2012). “Bistability, bifurcations, and Waddington’s epigenetic landscape”. *Current biology : CB* 22(11), R458–66. DOI: 10.1016/j.cub.2012.03.045.
- [107] J. D. Finan and F. Guilak (2010). “The effects of osmotic stress on the structure and function of the cell nucleus”. *Journal of cellular biochemistry* 109(3), 460–467. DOI: 10.1002/jcb.22437.
- [108] E. B. Finger and J. C. Bischof (2018). “Cryopreservation by vitrification: a promising approach for transplant organ banking”. *Current opinion in organ transplantation* 23(3), 353–360. DOI: 10.1097/MOT.0000000000000534.
- [109] A. A. Friedman, A. Letai, D. E. Fisher, and K. T. Flaherty (2015). “Precision medicine for cancer with next-generation functional diagnostics”. *Nature reviews. Cancer* 15(12), 747–756. DOI: 10.1038/nrc4015.
- [110] B. J. Fuller and C. Y. Lee (2007). “Hypothermic perfusion preservation: the future of organ preservation revisited?” *Cryobiology* 54(2), 129–145. DOI: 10.1016/j.cryobiol.2007.01.003.
- [111] M. Gallardo-Villagrán, L. Paulus, D. Y. Leger, B. Therrien, and B. Liagre (2022). “Dimethyl Sulfoxide: A Bio-Friendly or Bio-Hazard Chemical? The Effect of DMSO in Human Fibroblast-like Synoviocytes”. *Molecules (Basel, Switzerland)* 27(14), 4472. DOI: 10.3390/molecules27144472.
- [112] L. Galluzzi, T. Yamazaki, and G. Kroemer (2018). “Linking cellular stress responses to systemic homeostasis”. *Nature reviews. Molecular cell biology* 19(11), 731–745. DOI: 10.1038/s41580-018-0068-0.
- [113] Z. Gao, B. Namsrai, Z. Han, P. Joshi, J. S. Rao, V. Ravikumar, A. Sharma, H. L. Ring, D. Idiyatullin, E. C. Magnuson, P. A. Iaizzo, E. G. Tolkacheva, M. Garwood, Y. Rabin, M. Etheridge, E. B. Finger, and J. C. Bischof (2022). “Vitrification and Rewarming of Magnetic Nanoparticle-Loaded Rat Hearts”. *Advanced materials technologies* 7(3), 2100873. DOI: 10.1002/admt.202100873.
- [114] S. E. Gellert, S. E. Pors, S. G. Kristensen, A. M. Bay-Bjørn, E. Ernst, and C. Yding Andersen (2018). “Transplantation of frozen-thawed ovarian tissue: an update on worldwide activity published in peer-reviewed papers and on the Danish cohort”. *Journal of assisted reproduction and genetics* 35(4), 561–570. DOI: 10.1007/s10815-018-1144-2.
- [115] S. Giallongo, D. Rehakova, M. Raffaele, O. Lo Re, I. Koutna, and M. Vinciguerra (2021). “Redox and Epigenetics in Human Pluripotent Stem Cells Differentiation”. *Antioxidants & redox signaling* 34(4), 335–349. DOI: 10.1089/ars.2019.7983..

- 
- [116] R. Glicklis, J. C. Merchuk, and S. Cohen (2004). “Modeling mass transfer in hepatocyte spheroids via cell viability, spheroid size, and hepatocellular functions”. *Biotechnology and bioengineering* 86(6), 672–680. DOI: 10.1002/bit.20086.
- [117] Y. González Hernández and R. W. Fischer (2007). “Serum-free culturing of mammalian cells—adaptation to and cryopreservation in fully defined media”. *ALTEX* 24(2), 110–116. DOI: 10.14573/altex.2007.2.110.
- [118] M. Griffith, C. Lumb, S. B. Wiseman, M. Wisniewski, R. W. Johnson, and A. G. Marangoni (2005). “Antifreeze proteins modify the freezing process in planta”. *Plant physiology* 138(1), 330–340. DOI: 10.1104/pp.104.058628.
- [119] E. E. Guibert, A. Y. Petrenko, C. L. Balaban, A. Y. Somov, J. V. Rodriguez, and B. J. Fuller (2011). “Organ Preservation: Current Concepts and New Strategies for the Next Decade”. *Transfusion medicine and hemotherapy : offizielles Organ der Deutschen Gesellschaft fur Transfusionsmedizin und Immunhamatologie* 38(2), 125–142. DOI: 10.1159/000327033.
- [120] S. Gunti, A. T. K. Hoke, K. P. Vu, and N. R. London (2021). “Organoid and Spheroid Tumor Models: Techniques and Applications”. *Cancers* 13(4), 874. DOI: 10.3390/cancer13040874.
- [121] S. Y. Ha, B. C. Jee, C. S. Suh, H. S. Kim, S. K. Oh, S. H. Kim, and S. Y. Moon (2005). “Cryopreservation of human embryonic stem cells without the use of a programmable freezer”. *Human reproduction (Oxford, England)* 20(7), 1779–1785. DOI: 10.1093/humrep/deh854..
- [122] M. Hamraz, R. Abolhassani, M. Andriamihaja, C. Ransy, V. Lenoir, L. Schwartz, and F. Bouillaud (2020). “Hypertonic external medium represses cellular respiration and promotes Warburg/Crabtree effect”. *FASEB journal : official publication of the Federation of American Societies for Experimental Biology* 34(1), 222–236. DOI: 10.1096/fj.201900706RR.
- [123] J. Han, B. Sydykov, H. Yang, H. Sieme, H. Oldenhof, and W. F. Wolkers (2019). “Spectroscopic monitoring of transport processes during loading of ovarian tissue with cryoprotective solutions”. *Scientific reports* 9(1), 15577. DOI: 10.1038/s41598-019-51903-5.
- [124] S.-H. Han, S. Shim, M.-J. Kim, H.-Y. Shin, W.-S. Jang, S.-J. Lee, Y.-W. Jin, S.-S. Lee, S. B. Lee, and S. Park (2017). “Long-term culture-induced phenotypic difference and efficient cryopreservation of small intestinal organoids by treatment timing of Rho kinase inhibitor”. *World journal of gastroenterology* 23(6), 964–975. DOI: 10.3748/wjg.v23.i6.964.
- [125] O. Hansson (2021). “Biomarkers for neurodegenerative diseases”. *Nature medicine* 27(6), 954–963. DOI: 10.1038/s41591-021-01382-x.
- [126] J. P. Hartnett and M. Kostic (1989). “Heat Transfer to Newtonian and Non-Newtonian Fluids in Rectangular Ducts”. *Advances in Heat Transfer* 19, 247–356. DOI: 10.1016/S0065-2717(08)70214-4.

- 
- [127] S. Al-Hasani, K. Diedrich, H. van der Ven, A. Reinecke, M. Hartje, and D. Krebs (1987). “Cryopreservation of human oocytes”. *Human reproduction (Oxford, England)* 2(8), 695–700. DOI: 10.1093/oxfordjournals.humrep.a136616..
- [128] S. Herculano-Houzel (2011). “Scaling of brain metabolism with a fixed energy budget per neuron: implications for neuronal activity, plasticity and evolution”. *PLoS one* 6(3), e17514. DOI: 10.1371/journal.pone.0017514.
- [129] K. O. Hicks, F. B. Pruijn, T. W. Secomb, M. P. Hay, R. Hsu, J. M. Brown, W. A. Denny, M. W. Dewhirst, and W. R. Wilson (2006). “Use of three-dimensional tissue cultures to model extravascular transport and predict in vivo activity of hypoxia-targeted anticancer drugs”. *Journal of the National Cancer Institute* 98(16), 1118–1128. DOI: 10.1093/jnci/djj306.
- [130] A. Z. Higgins and J. O. M. Karlsson (2013). “Effects of intercellular junction protein expression on intracellular ice formation in mouse insulinoma cells”. *Biophysical journal* 105(9), 2006–2015. DOI: 10.1016/j.bpj.2013.09.028.
- [131] G. Hirode, S. Saab, and R. J. Wong (2020). “Trends in the Burden of Chronic Liver Disease Among Hospitalized US Adults”. *JAMA network open* 3(4), e201997. DOI: 10.1001/jamanetworkopen.2020.1997.
- [132] E. K. Hoffmann, I. H. Lambert, and S. F. Pedersen (2009). “Physiology of cell volume regulation in vertebrates”. *Physiological reviews* 89(1), 193–277. DOI: 10.1152/physrev.00037.2007.
- [133] M. Holz, X.-a. Mao, D. Seiferling, and A. Sacco (1996). “Experimental study of dynamic isotope effects in molecular liquids: Detection of translation-rotation coupling”. *The Journal of Chemical Physics* 104(2), 669–679. DOI: 10.1063/1.470863.
- [134] C. Hu and L. Li (2015). “In vitro culture of isolated primary hepatocytes and stem cell-derived hepatocyte-like cells for liver regeneration”. *Protein & cell* 6(8), 562–574. DOI: 10.1007/s13238-015-0180-2.
- [135] C.-Y. Huang, C.-L. Liu, C.-Y. Ting, Y.-T. Chiu, Y.-C. Cheng, M. W. Nicholson, and P. C. H. Hsieh (2019). “Human iPSC banking: barriers and opportunities”. *Journal of biomedical science* 26(1), 87. DOI: 10.1186/s12929-019-0578-x.
- [136] X. Huang, Z. Huang, W. Gao, W. Gao, R. He, Y. Li, R. Crawford, Y. Zhou, L. Xiao, and Y. Xiao (2022). “Current Advances in 3D Dynamic Cell Culture Systems”. *Gels (Basel, Switzerland)* 8(12), 829. DOI: 10.3390/gels8120829.
- [137] M. Huch, J. A. Knoblich, M. P. Lutolf, and A. Martinez-Arias (2017). “The hope and the hype of organoid research”. *Development (Cambridge, England)* 144(6), 938–941. DOI: 10.1242/dev.150201.
- [138] C. W. Huck (2014). “Advances of vibrational spectroscopic methods in phytomics and bioanalysis”. *Journal of pharmaceutical and biomedical analysis* 87, 26–35. DOI: 10.1016/j.jpba.2013.05.010.

- [139] T. Ihara, T. Yamamoto, M. Sugamata, H. Okumura, and Y. Ueno (1998). “The process of ultrastructural changes from nuclei to apoptotic body”. *Virchows Archiv : an international journal of pathology* 433(5), 443–447. DOI: 10.1007/s004280050272.
- [140] J. Inui, Y. Ueyama-Toba, S. Mitani, and H. Mizuguchi (2023). “Development of a method of passaging and freezing human iPS cell-derived hepatocytes to improve their functions”. *PloS one* 18(5), e0285783. DOI: 10.1371/journal.pone.0285783.
- [141] D. Irimia and J. O. M. Karlsson (2002). “Kinetics and mechanism of intercellular ice propagation in a micropatterned tissue construct”. *Biophysical journal* 82(4), 1858–1868. DOI: 10.1016/S0006-3495(02)75536-7.
- [142] R. K. Jain, P. Au, J. Tam, D. G. Duda, and D. Fukumura (2005). “Engineering vascularized tissue”. *Nature biotechnology* 23(7), 821–823. DOI: 10.1038/nbt0705-821.
- [143] S. Jalil, T. Keskinen, R. Maldonado, J. Sokka, R. Trokovic, T. Otonkoski, and K. Wartiovaara (2021). “Simultaneous high-efficiency base editing and reprogramming of patient fibroblasts”. *Stem cell reports* 16(12), 3064–3075. DOI: 10.1016/j.stemcr.2021.10.017.
- [144] C. Jensen and Y. Teng (2020). “Is It Time to Start Transitioning From 2D to 3D Cell Culture?” *Frontiers in molecular biosciences* 7, 33. DOI: 10.3389/fmolb.2020.00033.
- [145] Y.-H. Jeong, U. Kim, S.-G. Lee, B. Ryu, J. Kim, A. Igor, J. S. Kim, C.-R. Jung, J.-H. Park, and C.-Y. Kim (2020). “Vitrification for cryopreservation of 2D and 3D stem cells culture using high concentration of cryoprotective agents”. *BMC biotechnology* 20(1), 45. DOI: 10.1186/s12896-020-00636-9.
- [146] P. V. Jeurink, Y. M. Vissers, B. Rappard, and H. F. J. Savelkoul (2008). “T cell responses in fresh and cryopreserved peripheral blood mononuclear cells: kinetics of cell viability, cellular subsets, proliferation, and cytokine production”. *Cryobiology* 57(2), 91–103. DOI: 10.1016/j.cryobiol.2008.06.002.
- [147] R. S. Kadzik, K. E. Homa, and D. R. Kovar (2020). “F-Actin Cytoskeleton Network Self-Organization Through Competition and Cooperation”. *Annual review of cell and developmental biology* 36, 35–60. DOI: 10.1146/annurev-cellbio-032320-094706.
- [148] J. O. M. Karlsson and M. Toner (1996). “Long-term storage of tissues by cryopreservation: critical issues”. *Biomaterials* 17(3), 243–256. DOI: 10.1016/0142-9612(96)85562-1.
- [149] J. O. M. Karlsson (2010). “Effects of solution composition on the theoretical prediction of ice nucleation kinetics and thermodynamics”. *Cryobiology* 60(1), 43–51. DOI: 10.1016/j.cryobiol.2009.07.004.
- [150] A. M. Karow (1969). “Cryoprotectants—a new class of drugs”. *The Journal of pharmacy and pharmacology* 21(4), 209–223. DOI: 10.1111/j.2042-7158.1969.tb08235.x..
- [151] A. D. Katsen, B. Vollmar, P. Mestres-Ventura, and M. D. Menger (1998). “Cell surface and nuclear changes during TNF-alpha-induced apoptosis in WEHI 164 murine fibrosarcoma cells. A correlative light, scanning, and transmission electron microscopical study”. *Virchows Archiv : an international journal of pathology* 433(1), 75–83. DOI: 10.1007/s004280050219.

- [152] V. Kerleta (2010). “Poloxamer 188 supplemented culture medium increases the vitality of Caco-2 cells after subcultivation and freeze/thaw cycles”. *ALTEX* 27(3), 191–197. DOI: 10.14573/altex.2010.3.191.
- [153] K. Khosla, Y. Wang, M. Hagedorn, Z. Qin, and J. Bischof (2017). “Gold Nanorod Induced Warming of Embryos from the Cryogenic State Enhances Viability”. *ACS nano* 11(8), 7869–7878. DOI: 10.1021/acsnano.7b02216.
- [154] H. J. Kim, G. Kim, K. Y. Chi, and J.-H. Kim (2023). “In Vitro Generation of Luminal Vasculature in Liver Organoids: From Basic Vascular Biology to Vascularized Hepatic Organoids”. *International journal of stem cells* 16(1), 1–15. DOI: 10.15283/ijsc22154.
- [155] J. Kim, B.-K. Koo, and J. A. Knoblich (2020). “Human organoids: model systems for human biology and medicine”. *Nature reviews. Molecular cell biology* 21(10), 571–584. DOI: 10.1038/s41580-020-0259-3.
- [156] S. Kobold, N. Bultjer, G. Stacey, S. C. Mueller, A. Kurtz, and N. Mah (2023). “History and current status of clinical studies using human pluripotent stem cells”. *Stem cell reports* 18(8), 1592–1598. DOI: 10.1016/j.stemcr.2023.03.005.
- [157] M. Kometas, G. M. Christman, J. Kramer, and A. Rhoton-Vlasak (2021). “Methods of Ovarian Tissue Cryopreservation: Is Vitrification Superior to Slow Freezing?-Ovarian Tissue Freezing Methods”. *Reproductive sciences (Thousand Oaks, Calif.)* 28(12), 3291–3302. DOI: 10.1007/s43032-021-00591-6.
- [158] B. Koo, B. Choi, H. Park, and K.-J. Yoon (2019). “Past, Present, and Future of Brain Organoid Technology”. *Molecules and cells* 42(9), 617–627. DOI: 10.14348/molcells.2019.0162.
- [159] E. Kristiansen and K. E. Zachariassen (2005). “The mechanism by which fish antifreeze proteins cause thermal hysteresis”. *Cryobiology* 51(3), 262–280. DOI: 10.1016/j.cryobiol.2005.07.007.
- [160] M. J. Kuiper, C. J. Morton, S. E. Abraham, and A. Gray-Weale (2015). “The biological function of an insect antifreeze protein simulated by molecular dynamics”. *eLife* 4, e05142. DOI: 10.7554/eLife.05142.
- [161] L. L. Kuleshova and A. Lopata (2002). “Vitrification can be more favorable than slow cooling”. *Fertility and sterility* 78(3), 449–454. DOI: 10.1016/s0015-0282(02)03305-8.
- [162] T. Kurokawa, T. Kinoshita, T. Ito, H. Saito, and T. Hotta (1996). “Detection of minimal residual disease B cell lymphoma by a PCR-mediated RNase protection assay”. *Leukemia* 10(7), 1222–1231. DOI: -.
- [163] M. Kvåle Løvmo, S. Deng, S. Moser, R. Leitgeb, W. Drexler, and M. Ritsch-Marte (2023). “Ultrasound-Induced Reorientation for Multi-Angle Optical Coherence Tomography”. *Nature Communications* 15, 2391. DOI: 10.1038/s41467-024-46506-2.
- [164] M. Kvarnström, M. C. Jenmalm, and C. Ekerfelt (2004). “Effect of cryopreservation on expression of Th1 and Th2 cytokines in blood mononuclear cells from patients with different cytokine profiles, analysed with three common assays: an overall decrease of interleukin-4”. *Cryobiology* 49(2), 157–168. DOI: 10.1016/j.cryobiol.2004.06.003.

- 
- [165] C. K. Kwok, I. Sébastien, K. Hariharan, I. Meiser, J. Wihan, S. Altmaier, I. Karnatz, D. Bauer, B. Fischer, A. Feile, A. Cabrera-Socorro, M. Rasmussen, B. Holst, J. C. Neubauer, C. Clausen, C. Verfaillie, A. Ebneith, M. Hansson, R. Steeg, and H. Zimmermann (2022). “Scalable expansion of iPSC and their derivatives across multiple lineages”. *Reproductive toxicology (Elmsford, N.Y.)* 112, 23–35. DOI: 10.1016/j.reprotox.2022.05.007.
- [166] E. LaMontagne, A. R. Muotri, and A. J. Engler (2022). “Recent advancements and future requirements in vascularization of cortical organoids”. *Frontiers in bioengineering and biotechnology* 10, 1048731. DOI: 10.3389/fbioe.2022.1048731.
- [167] M. A. Lancaster and J. A. Knoblich (2014). “Organogenesis in a dish: modeling development and disease using organoid technologies”. *Science (New York, N.Y.)* 345(6194), 1247125. DOI: 10.1126/science.1247125.
- [168] E. Lau, D. T. Paik, and J. C. Wu (2019). “Systems-Wide Approaches in Induced Pluripotent Stem Cell Models”. *Annual review of pathology* 14, 395–419. DOI: 10.1146/annurev-pathmechdis-012418-013046.
- [169] B. E. Lee, B. J. Lee, K. J. Lee, M. Lee, Y. J. Lim, J. K. Choi, and B. Keum (2022). “A simple and efficient cryopreservation method for mouse small intestinal and colon organoids for regenerative medicine”. *Biochemical and biophysical research communications* 595, 14–21. DOI: 10.1016/j.bbrc.2021.12.021.
- [170] X. Lei, Z. Deng, H. Zhang, H. Zhao, J. Zhou, S. Liu, Q. Chen, L. Ning, Y. Cao, X. Wang, X. Zhang, and E. Duan (2014). “Rotary suspension culture enhances mesendoderm differentiation of embryonic stem cells through modulation of Wnt/ $\beta$ -catenin pathway”. *Stem cell reviews and reports* 10(4), 526–538. DOI: 10.1007/s12015-014-9511-6.
- [171] B. L. LeSavage, R. A. Suhar, N. Broguiere, M. P. Lutolf, and S. C. Heilshorn (2022). “Next-generation cancer organoids”. *Nature materials* 21(2), 143–159. DOI: 10.1038/s41563-021-01057-5.
- [172] R. L. Levin and T. W. Miller (1981). “An optimum method for the introduction or removal of permeable cryoprotectants: isolated cells”. *Cryobiology* 18(1), 32–48. DOI: 10.1016/0011-2240(81)90004-3.
- [173] M. Li, L. Gao, L. Zhao, T. Zou, and H. Xu (2023). “Toward the next generation of vascularized human neural organoids”. *Medicinal research reviews* 43(1), 31–54. DOI: 10.1002/med.21922.
- [174] R. Li, G. Yu, S. M. Azarin, and A. Hubel (2018). “Freezing Responses in DMSO-Based Cryopreservation of Human iPSCs: Aggregates Versus Single Cells”. *Tissue engineering. Part C, Methods* 24(5), 289–299. DOI: 10.1089/ten.tec.2017.0531.
- [175] X. Li, G. Meng, R. Krawetz, S. Liu, and D. E. Rancourt (2008). “The ROCK inhibitor Y-27632 enhances the survival rate of human embryonic stem cells following cryopreservation”. *Stem cells and development* 17(6), 1079–1085. DOI: 10.1089/scd.2007.0247.
- [176] Li, Y. and Ma, T. (2012). “Bioprocessing of cryopreservation for large-scale banking of human pluripotent stem cells”. *BioResearch open access* 1(5), 205–214. DOI: 10.1089/biores.2012.0224.

- [177] J. K. Liao, M. Seto, and K. Noma (2007). “Rho kinase (ROCK) inhibitors”. *Journal of cardiovascular pharmacology* 50(1), 17–24. DOI: 10.1097/FJC.0b013e318070d1bd.
- [178] J. Liao, Z. Wu, Y. Wang, L. Cheng, C. Cui, Y. Gao, T. Chen, L. Rao, S. Chen, N. Jia, H. Dai, S. Xin, J. Kang, G. Pei, and L. Xiao (2008). “Enhanced efficiency of generating induced pluripotent stem (iPS) cells from human somatic cells by a combination of six transcription factors”. *Cell research* 18(5), 600–603. DOI: 10.1038/cr.2008.51.
- [179] J. Liebermann, M. J. Tucker, J. R. Graham, T. Han, A. Davis, and M. J. Levy (2002). “Blastocyst development after vitrification of multipronuclear zygotes using the Flexipet denuding pipette”. *Reproductive biomedicine online* 4(2), 146–150. DOI: 10.1016/S1472-6483(10)61932-3.
- [180] M. Lin, H. Cao, and J. Li (2023). “Control strategies of ice nucleation, growth, and recrystallization for cryopreservation”. *Acta biomaterialia* 155, 35–56. DOI: 10.1016/j.actbio.2022.10.056.
- [181] R.-Z. Lin, L.-F. Chou, C.-C. M. Chien, and H.-Y. Chang (2006). “Dynamic analysis of hepatoma spheroid formation: roles of E-cadherin and beta1-integrin”. *Cell and tissue research* 324(3), 411–422. DOI: 10.1007/s00441-005-0148-2.
- [182] Y.-T. Lin, J. Seo, F. Gao, H. M. Feldman, H.-L. Wen, J. Penney, H. P. Cam, E. GJoneska, W. K. Raja, J. Cheng, R. Rueda, O. Kritskiy, F. Abdurrob, Z. Peng, B. Milo, C. J. Yu, S. Elmsaouri, D. Dey, T. Ko, B. A. Yankner, and L.-H. Tsai (2018). “APOE4 Causes Widespread Molecular and Cellular Alterations Associated with Alzheimer’s Disease Phenotypes in Human iPSC-Derived Brain Cell Types”. *Neuron* 98(6), 1141–1154.e7. DOI: 10.1016/j.neuron.2018.05.008.
- [183] Lin, C. and Tsai, S. (2012). “The effect of cryopreservation on DNA damage, gene expression and protein abundance in vertebrate”. *Italian Journal of Animal Science* 11(1), e21. DOI: 10.4081/ijas.2012.e21.
- [184] D. Liu, S. Chen, and M. Win Naing (2021). “A review of manufacturing capabilities of cell spheroid generation technologies and future development”. *Biotechnology and bioengineering* 118(2), 542–554. DOI: 10.1002/bit.27620.
- [185] Q. Liu, T. Zhao, X. Wang, Z. Chen, Y. Hu, and X. Chen (2021). “In Situ Vitrification of Lung Cancer Organoids on a Microwell Array”. *Micromachines* 12(6), 624. DOI: 10.3390/mi12060624.
- [186] Y. Liu, C. Meyer, C. Xu, H. Weng, C. Hellerbrand, P. ten Dijke, and S. Dooley (2013). “Animal models of chronic liver diseases”. *American journal of physiology. Gastrointestinal and liver physiology* 304(5), G449–68. DOI: 10.1152/ajpgi.00199.2012.
- [187] A. Louey, D. Hernández, A. Pébay, and M. Daniszewski (2021). “Automation of Organoid Cultures: Current Protocols and Applications”. *SLAS discovery : advancing life sciences R & D* 26(9), 1138–1147. DOI: 10.1177/24725552211024547.
- [188] J. E. Lovelock (1954). “The protective action of neutral solutes against haemolysis by freezing and thawing”. *The Biochemical journal* 56(2), 265–270. DOI: 10.1042/bj0560265.

- 
- [189] J. E. Lovelock and M. W. Bishop (1959). “Prevention of freezing damage to living cells by dimethyl sulphoxide”. *Nature* 183(4672), 1394–1395. DOI: 10.1038/1831394a0.
- [190] J. E. Lovelock (1953). “Het mechanism of the protective action of glycerol against haemolysis by freezing and thawing”. *Biochimica et biophysica acta* 11, 28–36. DOI: 10.1016/006-3002(53)90005-5.
- [191] J. E. Lovelock (1953b). “The haemolysis of human red blood-cells by freezing and thawing”. *Biochimica et biophysica acta* 10(3), 414–426. DOI: 10.1016/0006-3002(53)90273-x.
- [192] C. M. Lucci, M. A. Kacinskis, L. H. R. Lopes, R. Rumpf, and S. N. B ao (2004). “Effect of different cryoprotectants on the structural preservation of follicles in frozen zebu bovine (*Bos indicus*) ovarian tissue”. *Theriogenology* 61(6), 1101–1114. DOI: 10.1016/j.theriogenology.2003.06.004.
- [193] Z. Luo, B. Xian, K. Li, K. Li, R. Yang, M. Chen, C. Xu, M. Tang, H. Rong, D. Hu, M. Ye, S. Yang, S. Lu, H. Zhang, and J. Ge (2021). “Biodegradable scaffolds facilitate epiretinal transplantation of hiPSC-Derived retinal neurons in nonhuman primates”. *Acta biomaterialia* 134, 289–301. DOI: 10.1016/j.actbio.2021.07.040.
- [194] C. Lyu, G. Nastase, G. Ukpai, A. Serban, and B. Rubinsky (2017). “A comparison of freezing-damage during isochoric and isobaric freezing of the potato”. *PeerJ* 5, e3322. DOI: 10.7717/peerj.3322.
- [195] X.-H. Ma, Y. Shi, Y. Hou, Y. Liu, L. Zhang, W.-X. Fan, D. Ge, T.-Q. Liu, and Z.-F. Cui (2010). “Slow-freezing cryopreservation of neural stem cell spheres with different diameters”. *Cryobiology* 60(2), 184–191. DOI: 10.1016/j.cryobiol.2009.10.013.
- [196] K. M. Mabry, S. Z. Payne, and K. S. Anseth (2016). “Microarray analyses to quantify advantages of 2D and 3D hydrogel culture systems in maintaining the native valvular interstitial cell phenotype”. *Biomaterials* 74, 31–41. DOI: 10.1016/j.biomaterials.2015.09.035.
- [197] J. D. MacDougall and M. McCabe (1967). “Diffusion coefficient of oxygen through tissues”. *Nature* 215(5106), 1173–1174. DOI: 10.1038/2151173a0.
- [198] S. Maffei, G. Pennarossa, T. A. L. Brevini, A. Arav, and F. Gandolfi (2014). “Beneficial effect of directional freezing on in vitro viability of cryopreserved sheep whole ovaries and ovarian cortical slices”. *Human reproduction (Oxford, England)* 29(1), 114–124. DOI: 10.1093/humrep/det377.
- [199] R. H. Maffly and A. Leaf (1959). “The potential of water in mammalian tissues”. *The Journal of general physiology* 42(6), 1257–1275. DOI: 10.1085/jgp.42.6.1257.
- [200] R. Magalh aes, B. Nugraha, S. Pervaiz, H. Yu, and L. L. Kuleshova (2012). “Influence of cell culture configuration on the post-cryopreservation viability of primary rat hepatocytes”. *Biomaterials* 33(3), 829–836. DOI: 10.1016/j.biomaterials.2011.10.015.
- [201] S. Maharjan, C. Ma, B. Singh, H. Kang, G. Orive, J. Yao, and Y. Shrike Zhang (2024). “Advanced 3D imaging and organoid bioprinting for biomedical research and therapeutic applications”. *Advanced drug delivery reviews* 208, 115237. DOI: 10.1016/j.addr.2024.115237.

- [202] M. Mahmoudi Asl, R. Rahbarghazi, R. Beheshti, A. Alihemmati, M. R. Aliparasti, and A. Abedelahi (2021). “Effects of Different Vitrification Solutions and Protocol on Follicular Ultrastructure and Revascularization of Autografted Mouse Ovarian Tissue”. *Cell journal* 22(4), 491–501. DOI: 10.22074/cellj.2021.6877.
- [203] J. Malda, T. J. Klein, and Z. Upton (2007). “The roles of hypoxia in the in vitro engineering of tissues”. *Tissue engineering* 13(9), 2153–2162. DOI: 10.1089/ten.2006.0417.
- [204] A. A. Mansour, J. T. Gonçalves, C. W. Bloyd, H. Li, S. Fernandes, D. Quang, S. Johnston, S. L. Parylak, X. Jin, and F. H. Gage (2018). “An in vivo model of functional and vascularized human brain organoids”. *Nature biotechnology* 36(5), 432–441. DOI: 10.1038/nbt.4127.
- [205] N. Manuchehrabadi, Z. Gao, J. Zhang, H. L. Ring, Q. Shao, F. Liu, M. McDermott, A. Fok, Y. Rabin, K. G. M. Brockbank, M. Garwood, C. L. Haynes, and J. C. Bischof (2017). “Improved tissue cryopreservation using inductive heating of magnetic nanoparticles”. *Science translational medicine* 9(379), eaah4586. DOI: 10.1126/scitranslmed.aah4586.
- [206] A. Marchini and F. Gelain (2022). “Synthetic scaffolds for 3D cell cultures and organoids: applications in regenerative medicine”. *Critical reviews in biotechnology* 42(3), 468–486. DOI: 10.1080/07388551.2021.1932716.
- [207] M. Markou, D. Kouroupis, F. Badounas, A. Katsouras, A. Kyrkou, T. Fotsis, C. Murphy, and E. Bagli (2020). “Tissue Engineering Using Vascular Organoids From Human Pluripotent Stem Cell Derived Mural Cell Phenotypes”. *Frontiers in bioengineering and biotechnology* 8, 278. DOI: 10.3389/fbioe.2020.00278.
- [208] I. Martin, D. Wendt, and M. Heberer (2004). “The role of bioreactors in tissue engineering”. *Trends in biotechnology* 22(2), 80–86. DOI: 10.1016/j.tibtech.2003.12.001.
- [209] P. Martin, W. Anders, G. Maelenn, A. Gemma-Claire, W. Yu-Tzu, and P. Matthew (2015). *World Alzheimer Report 2015 - The Global Impact of Dementia: An analysis of prevalence, incidence, cost and trends*. URL: <https://www.alzint.org/resource/world-alzheimer-report-2015/>.
- [210] W. Masselink, D. Reumann, P. Murawala, P. Pasierbek, Y. Taniguchi, F. Bonnay, K. Meixner, J. A. Knoblich, and E. M. Tanaka (2019). “Broad applicability of a streamlined ethyl cinnamate-based clearing procedure”. *Development (Cambridge, England)* 146(3), dev166884. DOI: 10.1242/dev.166884.
- [211] H. Matsumoto, J. Y. Jiang, T. Tanaka, H. Sasada, and E. Sato (2001). “Vitrification of large quantities of immature bovine oocytes using nylon mesh”. *Cryobiology* 42(2), 139–144. DOI: 10.1006/cryo.2001.2309.
- [212] S. R. May and J. G. Baust (1988). “Cryobiology of tissues”. In: *Cardiac Valve Allografts 1962–1987*. Ed. by A. C. Yankah, R. Hetzer, D. C. Miller, D. Ross, J. Somerville, and M. H. Yacoub. Heidelberg: Steinkopff, pp. 27–34. ISBN: 978-3-642-72422-0. DOI: 10.1007/978-3-642-72420-6\_5.

- 
- [213] C. N. Mayhew and R. Singhanian (2022). “A review of protocols for brain organoids and applications for disease modeling”. *STAR protocols* 4(1), 101860. DOI: 10.1016/j.xpro.2022.101860.
- [214] P. Mazur (1963). “Kinetics of water loss from cells at subzero temperatures and the likelihood of intracellular freezing”. *The Journal of general physiology* 47(2), 347–369. DOI: 10.1085/jgp.47.2.347.
- [215] P. Mazur, S. P. Leibo, and E. Chu (1972). “A two-factor hypothesis of freezing injury”. *Experimental Cell Research* 71(2), 345–355. DOI: 10.1016/0014-4827(72)90303-5.
- [216] P. Mazur (1977). “The role of intracellular freezing in the death of cells cooled at supraoptimal rates”. *Cryobiology* 14(3), 251–272. DOI: 10.1016/0011-2240(77)90175-4.
- [217] P. Mazur (1984). “Freezing of living cells: mechanisms and implications”. *The American journal of physiology* 247(3), C125–42. DOI: 10.1152/ajpcell.1984.247.3.C125..
- [218] S. F. McComish, A. N. MacMahon Copas, and M. A. Caldwell (2022). “Human Brain-Based Models Provide a Powerful Tool for the Advancement of Parkinson’s Disease Research and Therapeutic Development”. *Frontiers in neuroscience* 16, 851058. DOI: 10.3389/fnins.2022.851058.
- [219] E. McEvoy, Y. L. Han, M. Guo, and V. B. Shenoy (2020). “Gap junctions amplify spatial variations in cell volume in proliferating tumor spheroids”. *Nature communications* 11(1), 6148. DOI: 10.1038/s41467-020-19904-5.
- [220] P. F. McGowan, R. E. Hurst, R. A. Bass, L. J. Wilcox, G. P. Hemstreet, and R. G. Postier (1988). “Equilibrium binding of Hoechst 33258 and Hoechst 33342 fluorochromes with rat colorectal cells”. *The journal of histochemistry and cytochemistry : official journal of the Histochemistry Society* 36(7), 757–762. DOI: 10.1177/36.7.2454985.
- [221] R. J. McMurtrey (2016). “Analytic Models of Oxygen and Nutrient Diffusion, Metabolism Dynamics, and Architecture Optimization in Three-Dimensional Tissue Constructs with Applications and Insights in Cerebral Organoids”. *Tissue engineering. Part C, Methods* 22(3), 221–249. DOI: 10.1089/ten.tec.2015.0375.
- [222] J. Meneghel, P. Kilbride, and G. J. Morris (2020). “Cryopreservation as a Key Element in the Successful Delivery of Cell-Based Therapies-A Review”. *Frontiers in medicine* 7, 592242. DOI: 10.3389/fmed.2020.592242.
- [223] H. T. Meryman (1970). “The Exceeding of a Minimum Tolerable Cell Volume in Hypertonic Suspension as a Cause of Freezing Injury”. In: *Ciba Foundation Symposium – The Frozen Cell*. Ed. by G. E. W. Wolstenholme and M. O’Connor. Novartis Foundation Symposia. Wiley, pp. 51–67. ISBN: 978-0-4706-6278-6. DOI: 10.1002/9780470719732.ch4.
- [224] H. Meyer, O. Vitavska, and H. Wiczorek (2011). “Identification of an animal sucrose transporter”. *Journal of cell science* 124(12), 1984–1991. DOI: 10.1242/jcs.082024.
- [225] E. L. Michalets (1998). “Update: Clinically Significant Cytochrome P–450 Drug Interactions”. *Pharmacotherapy: The Journal of Human Pharmacology and Drug Therapy* 18(1), 84–112. DOI: 10.1002/j.1875-9114.1998.tb03830.x.

- [226] A. Mongera, P. Rowghanian, H. J. Gustafson, E. Shelton, D. A. Kealhofer, E. K. Carn, F. Serwane, A. A. Lucio, J. Giammona, and O. Campàs (2018). “A fluid-to-solid jamming transition underlies vertebrate body axis elongation”. *Nature* 561(7723), 401–405. DOI: 10.1038/s41586-018-0479-2.
- [227] G. J. Morris and E. Acton (2013). “Controlled ice nucleation in cryopreservation—a review”. *Cryobiology* 66(2), 85–92. DOI: 10.1016/j.cryobiol.2012.11.007..
- [228] T. Mukaida, S. Wada, K. Takahashi, P. B. Pedro, T. Z. An, and M. Kasai (1998). “Vitrification of human embryos based on the assessment of suitable conditions for 8-cell mouse embryos”. *Human reproduction (Oxford, England)* 13(10), 2874–2879. DOI: 10.1093/humrep/13.10.2874.
- [229] S. F. Mullen and J. K. Critser, eds. (2007a). *Oncofertility Fertility Preservation for Cancer Survivors: The Science of Cryobiology*. Vol. 138. SpringerLink Bücher. Boston, MA: Springer US. ISBN: 978-0-387-72292-4. DOI: 10.1007/978-0-387-72293-1.
- [230] S. F. Mullen and J. K. Critser (2007b). “The science of cryobiology”. *Cancer treatment and research* 138, 83–109. DOI: 10.1007/978-0-387-72293-1\_7.
- [231] S. J. Mun (2019). “Generation of expandable human pluripotent stem cell-derived hepatocyte-like liver organoids”. *Journal of hepatology* 71, 970–985. DOI: 10.1016/j.jhep.2019.06.030.
- [232] K. A. Murray and M. I. Gibson (2022). “Chemical approaches to cryopreservation”. *Nature reviews. Chemistry* 6(8), 579–593. DOI: 10.1038/s41570-022-00407-4.
- [233] P. Naccache and R. I. Sha’afi (1973). “Patterns of nonelectrolyte permeability in human red blood cell membrane”. *The Journal of general physiology* 62(6), 714–736. DOI: 10.1085/jgp.62.6.714.
- [234] E. de Nadal, G. Ammerer, and F. Posas (2011). “Controlling gene expression in response to stress”. *Nature reviews. Genetics* 12(12), 833–845. DOI: 10.1038/nrg3055.
- [235] S. R. Nagarajan, M. Paul-Heng, J. R. Krycer, D. J. Fazakerley, A. F. Sharland, and A. J. Hoy (2019). “Lipid and glucose metabolism in hepatocyte cell lines and primary mouse hepatocytes: a comprehensive resource for in vitro studies of hepatic metabolism”. *American journal of physiology. Endocrinology and metabolism* 316(4), E578–E589. DOI: 10.1152/ajpendo.00365.2018.
- [236] Z. P. Nagy, D. Shapiro, and C.-C. Chang (2020). “Vitrification of the human embryo: a more efficient and safer in vitro fertilization treatment”. *Fertility and sterility* 113(2), 241–247. DOI: 10.1016/j.fertnstert.2019.12.009.
- [237] T. Nederman, H. Acker, and J. Carlsson (1983). “Penetration of substances into tumor tissue: a methodological study with microelectrodes and cellular spheroids”. *In vitro* 19(6), 479–488. DOI: 10.1007/BF02619595.
- [238] S. Ng, R. E. Schwartz, S. March, A. Galstian, N. Gural, J. Shan, M. Prabhu, M. M. Mota, and S. N. Bhatia (2015). “Human iPSC-derived hepatocyte-like cells support Plasmodium liver-stage infection in vitro”. *Stem cell reports* 4(3), 348–359. DOI: 10.1016/j.stemcr.2015.01.002.

- [239] S. T. Nguyen, H. T.-L. Nguyen, and K. D. Truong (2020). “Comparative cytotoxic effects of methanol, ethanol and DMSO on human cancer cell lines”. *Biomedical Research and Therapy* 7(7), 3855–3859. DOI: 10.15419/bmrat.v7i7.614.
- [240] Y.-Z. Nie, Y.-W. Zheng, K. Miyakawa, S. Murata, R.-R. Zhang, K. Sekine, Y. Ueno, T. Takebe, T. Wakita, A. Ryo, and H. Taniguchi (2018). “Recapitulation of hepatitis B virus-host interactions in liver organoids from human induced pluripotent stem cells”. *EBioMedicine* 35, 114–123. DOI: 10.1016/j.ebiom.2018.08.014.
- [241] B. Nießing, R. Kiesel, L. Herbst, and R. H. Schmitt (2021). “Techno-Economic Analysis of Automated iPSC Production”. *Processes* 9(2), 240. DOI: 10.3390/pr9020240.
- [242] N. Oberstein, M. K. O’Donovan, J. E. Bruemmer, G. E. Seidel, E. M. Carnevale, and E. L. Squires (2001). “Cryopreservation of equine embryos by open pulled straw, cryoloop, or conventional slow cooling methods”. *Theriogenology* 55(2), 607–613. DOI: 10.1016/S0093-691X(01)00429-0.
- [243] T. Ogura, L. M. Shuba, and T. F. McDonald (1995). “Action potentials, ionic currents and cell water in guinea pig ventricular preparations exposed to dimethyl sulfoxide”. *The Journal of pharmacology and experimental therapeutics* 273(3), 1273–1286. DOI: -.
- [244] K. Papis, M. Shimizu, and Y. Izaike (2000). “Factors affecting the survivability of bovine oocytes vitrified in droplets”. *Theriogenology* 54(5), 651–658. DOI: 10.1016/S0093-691X(00)00380-0.
- [245] J. Park, J. Kim, B. Shin, H. R. Schöler, J. Kim, and K.-P. Kim (2024). “Inducing Pluripotency in Somatic Cells: Historical Perspective and Recent Advances”. *International journal of stem cells*, Online ahead of print. DOI: 10.15283/ijsc23148.
- [246] A. S. Parkes (1964). “Cryobiology”. *Cryobiology* 1(1), 3. DOI: 10.1016/0011-2240(64)90014-8.
- [247] W. Paskal, A. M. Paskal, T. Dębski, M. Gryziak, and J. Jaworowski (2018). “Aspects of Modern Biobank Activity - Comprehensive Review”. *Pathology oncology research : POR* 24(4), 771–785. DOI: 10.1007/s12253-018-0418-4.
- [248] D. Pauleit, K.-J. Langen, F. Floeth, H. Hautzel, M. J. Riemenschneider, G. Reifenberger, N. J. Shah, and H.-W. Müller (2004). “Can the apparent diffusion coefficient be used as a noninvasive parameter to distinguish tumor tissue from peritumoral tissue in cerebral gliomas?” *Journal of magnetic resonance imaging : JMRI* 20(5), 758–764. DOI: 10.1002/jmri.20177.
- [249] S. F. Pedersen, E. K. Hoffmann, and J. W. Mills (2001). “The cytoskeleton and cell volume regulation”. *Comparative biochemistry and physiology. Part A, Molecular & integrative physiology* 130(3), 385–399. DOI: 10.1016/S1095-6433(01)00429-9.
- [250] S. F. Pedersen, J. W. Mills, and E. K. Hoffmann (1999). “Role of the F-actin cytoskeleton in the RVD and RVI processes in Ehrlich ascites tumor cells”. *Experimental Cell Research* 252(1), 63–74. DOI: 10.1006/excr.1999.4615.
- [251] D. E. Pegg, M. C. Wusteman, and S. Boylan (1997). “Fractures in cryopreserved elastic arteries”. *Cryobiology* 34(2), 183–192. DOI: 10.1006/cryo.1996.1997.

- [252] P. Penfornis, K. C. Vallabhaneni, A. V. Janorkar, and R. R. Pochampally (2017). “Three dimensional tumor models for cancer studies”. *Frontiers in bioscience (Elite edition)* 9(1), 162–173. DOI: 10.2741/e793.
- [253] O. W. Petersen, L. Rønnov-Jessen, A. R. Howlett, and M. J. Bissell (1992). “Interaction with basement membrane serves to rapidly distinguish growth and differentiation pattern of normal and malignant human breast epithelial cells”. *Proceedings of the National Academy of Sciences of the United States of America* 89(19), 9064–9068. DOI: 10.1073/pnas.89.19.9064.
- [254] Y. A. Petrenko, A. Y. Petrenko, I. Martin, and D. Wendt (2017). “Perfusion bioreactor-based cryopreservation of 3D human mesenchymal stromal cell tissue grafts”. *Cryobiology* 76, 150–153. DOI: 10.1016/j.cryobiol.2017.04.001.
- [255] G. Pettinato, R. Ramanathan, R. A. Fisher, M. J. Mangino, N. Zhang, and X. Wen (2016). “Scalable Differentiation of Human iPSCs in a Multicellular Spheroid-based 3D Culture into Hepatocyte-like Cells through Direct Wnt/ $\beta$ -catenin Pathway Inhibition”. *Scientific reports* 6, 32888. DOI: 10.1038/srep32888.
- [256] M. W. Pfaffl (2001). “A new mathematical model for relative quantification in real-time RT-PCR”. *Nucleic acids research* 29(9), e45. DOI: 10.1093/nar/29.9.e45.
- [257] M. T. Pham, K. M. Pollock, M. D. Rose, W. A. Cary, H. R. Stewart, P. Zhou, J. A. Nolte, and B. Waldau (2018). “Generation of human vascularized brain organoids”. *Neuroreport* 29(7), 588–593. DOI: 10.1097/WNR.0000000000001014.
- [258] K. G. Phillips, S. L. Jacques, and O. J. T. McCarty (2012). “Measurement of single cell refractive index, dry mass, volume, and density using a transillumination microscope”. *Physical review letters* 109(11), 118105. DOI: 10.1103/PhysRevLett.109.118105.
- [259] E. T. Pineda, R. M. Nerem, and T. Ahsan (2013). “Differentiation patterns of embryonic stem cells in two- versus three-dimensional culture”. *Cells, tissues, organs* 197(5), 399–410. DOI: 10.1159/000346166.
- [260] M. R. Pinheiro, V. V. Tuchin, and L. M. Oliveira (2023). “Invasive and Minimally Invasive Evaluation of Diffusion Properties of Sugar in Muscle”. *IEEE Journal of Selected Topics in Quantum Electronics* 29(4), 1–8. DOI: 10.1109/JSTQE.2023.3255801.
- [261] M. S. Poetsch, A. Strano, and K. Guan (2022). “Human Induced Pluripotent Stem Cells: From Cell Origin, Genomic Stability, and Epigenetic Memory to Translational Medicine”. *Stem cells (Dayton, Ohio)* 40(6), 546–555. DOI: 10.1093/stmcls/sxac020.
- [262] J. S. Poisson, J. P. Acker, J. G. Briard, J. E. Meyer, and R. N. Ben (2019). “Modulating Intracellular Ice Growth with Cell-Permeating Small-Molecule Ice Recrystallization Inhibitors”. *Langmuir : the ACS journal of surfaces and colloids* 35(23), 7452–7458. DOI: 10.1021/acs.langmuir.8b02126.
- [263] Polge C., Smith A. U., and A. S. Parkes (1949). “Revival of spermatozoa after vitrification and dehydration at low temperatures”. *Nature* 164(4172), 666. DOI: 10.1038/164666a0..

- [264] E. Puschmann, C. Selden, S. Butler, and B. Fuller (2014). “Liquidus tracking: controlled rate vitrification for the cryopreservation of larger volumes and tissues”. *Cryo Letters* 35(4), 345–355. DOI: -.
- [265] W. K. Raja, A. E. Mungenast, Y.-T. Lin, T. Ko, F. Abdurrob, J. Seo, and L.-H. Tsai (2016). “Self-Organizing 3D Human Neural Tissue Derived from Induced Pluripotent Stem Cells Recapitulate Alzheimer’s Disease Phenotypes”. *PloS one* 11(9), e0161969. DOI: 10.1371/journal.pone.0161969.
- [266] W. F. Rall and G. M. Fahy (1985). “Ice-free cryopreservation of mouse embryos at -196 degrees C by vitrification”. *Nature* 313(6003), 573–575. DOI: 10.1038/313573a0.
- [267] M. N. B. Ramli, Y. S. Lim, C. T. Koe, D. Demircioglu, W. Tng, K. A. U. Gonzales, C. P. Tan, I. Szczerbinska, H. Liang, E. L. Soe, Z. Lu, C. Ariyachet, K. M. Yu, S. H. Koh, L. P. Yaw, N. H. B. Jumat, J. S. Y. Lim, G. Wright, A. Shabbir, Y. Y. Dan, H.-H. Ng, and Y.-S. Chan (2020). “Human Pluripotent Stem Cell-Derived Organoids as Models of Liver Disease”. *Gastroenterology* 159(4), 1471–1486.e12. DOI: 10.1053/j.gastro.2020.06.010.
- [268] A. A. Raslan and Y. Kee (2013). “Tackling neurodegenerative diseases: animal models of Alzheimer’s disease and Parkinson’s disease”. *Genes & Genomics* 35(4), 425–440. DOI: 10.1007/s13258-013-0116-2.
- [269] A. Regev, S. A. Teichmann, E. S. Lander, I. Amit, C. Benoist, E. Birney, B. Bodenmiller, P. Campbell, P. Carninci, M. Clatworthy, H. Clevers, B. Deplancke, I. Dunham, J. Eberwine, R. Eils, W. Enard, A. Farmer, L. Fugger, B. Göttgens, N. Hacohen, M. Haniffa, M. Hemberg, S. Kim, P. Klenerman, A. Kriegstein, E. Lein, S. Linnarsson, E. Lundberg, J. Lundeberg, P. Majumder, J. C. Marioni, M. Merad, M. Mhlanga, M. Nawijn, M. Netea, G. Nolan, D. Pe’er, A. Phillipakis, C. P. Ponting, S. Quake, W. Reik, O. Rozenblatt-Rosen, J. Sanes, R. Satija, T. N. Schumacher, A. Shalek, E. Shapiro, P. Sharma, J. W. Shin, O. Stegle, M. Stratton, M. J. T. Stubbington, F. J. Theis, M. Uhlen, A. van Oudenaarden, A. Wagner, F. Watt, J. Weissman, B. Wold, R. Xavier, and N. Yosef (2017). “The Human Cell Atlas”. *eLife* 6, e27041. DOI: 10.7554/eLife.27041.
- [270] S. Reichman, A. Slembrouck, G. Gagliardi, A. Chaffiol, A. Terray, C. Nanteau, A. Potey, M. Belle, O. Rabesandratana, J. Duebel, G. Orieux, E. F. Nandrot, J.-A. Sahel, and O. Goureau (2017). “Generation of Storable Retinal Organoids and Retinal Pigmented Epithelium from Adherent Human iPS Cells in Xeno-Free and Feeder-Free Conditions”. *Stem cells (Dayton, Ohio)* 35(5), 1176–1188. DOI: 10.1002/stem.2586.
- [271] P. Reinhardt, M. Glatza, K. Hemmer, Y. Tsytsyura, C. S. Thiel, S. Höing, S. Moritz, J. A. Parga, L. Wagner, J. M. Bruder, G. Wu, B. Schmid, A. Röpke, J. Klingauf, J. C. Schwamborn, T. Gasser, H. R. Schöler, and J. Sternecker (2013). “Derivation and expansion using only small molecules of human neural progenitors for neurodegenerative disease modeling”. *PloS one* 8(3), e59252. DOI: 10.1371/journal.pone.0059252.
- [272] J. G. Ren, R. L. Zheng, Y. M. Shi, B. Gong, and J. F. Li (1998). “Apoptosis, redifferentiation and arresting proliferation simultaneously triggered by oxidative stress in human hepatoma cells”. *Cell biology international* 22(1), 41–49. DOI: 10.1006/cbir.1998.0226.

- [273] B. E. Reubinoff, M. F. Pera, C. Y. Fong, A. Trounson, and A. Bongso (2000). “Embryonic stem cell lines from human blastocysts: somatic differentiation in vitro”. *Nature biotechnology* 18(4), 399–404. DOI: 10.1038/74447..
- [274] B. E. Reubinoff, M. F. Pera, G. Vajta, and A. O. Trounson (2001). “Effective cryopreservation of human embryonic stem cells by the open pulled straw vitrification method”. *Human reproduction (Oxford, England)* 16(10), 2187–2194. DOI: 10.1093/humrep/16.10.2187.
- [275] A. Rezania, J. E. Bruin, P. Arora, A. Rubin, I. Batushansky, A. Asadi, S. O’Dwyer, N. Quiskamp, M. Mojibian, T. Albrecht, Y. H. C. Yang, J. D. Johnson, and T. J. Kieffer (2014). “Reversal of diabetes with insulin-producing cells derived in vitro from human pluripotent stem cells”. *Nature biotechnology* 32(11), 1121–1133. DOI: 10.1038/nbt.3033.
- [276] M. Rezazadeh Valojerdi, P. Eftekhari-Yazdi, L. Karimian, F. Hassani, and B. Movaghar (2009). “Vitrification versus slow freezing gives excellent survival, post warming embryo morphology and pregnancy outcomes for human cleaved embryos”. *Journal of assisted reproduction and genetics* 26(6), 347–354. DOI: 10.1007/s10815-009-9318-6.
- [277] C. de Rham and J. Villard (2014). “Potential and limitation of HLA-based banking of human pluripotent stem cells for cell therapy”. *Journal of immunology research* 2014, 518135. DOI: 10.1155/2014/518135.
- [278] E. C. Rivas Leonel, C. M. Lucci, and C. A. Amorim (2019). “Cryopreservation of Human Ovarian Tissue: A Review”. *Transfusion medicine and hemotherapy : offzielles Organ der Deutschen Gesellschaft fur Transfusionsmedizin und Immunhamatologie* 46(3), 173–181. DOI: 10.1159/000499054.
- [279] R. Rizzo, V. Onesto, S. Forciniti, A. Chandra, S. Prasad, H. Iuele, F. Colella, G. Gigli, and L. L. Del Mercato (2022). “A pH-sensor scaffold for mapping spatiotemporal gradients in three-dimensional in vitro tumour models”. *Biosensors & bioelectronics* 212, 114401. DOI: 10.1016/j.bios.2022.114401.
- [280] C. Roffay, G. Molinard, K. Kim, M. Urbanska, V. Andrade, V. Barbarasa, P. Nowak, V. Mercier, J. García-Calvo, S. Matile, R. Loewith, A. Echard, J. Guck, M. Lenz, and A. Roux (2021). “Passive coupling of membrane tension and cell volume during active response of cells to osmosis”. *Proceedings of the National Academy of Sciences of the United States of America* 118(47), e2103228118. DOI: 10.1073/pnas.2103228118.
- [281] O. Rogulska, J. Havelkova, and Y. Petrenko (2023). “Cryopreservation of Organoids”. *Cryo Letters* 44(2), 65–75. DOI: 10.54680/fr23210110112.
- [282] G. Rossi, A. Manfrin, and M. P. Lutolf (2018). “Progress and potential in organoid research”. *Nature reviews. Genetics* 19(11), 671–687. DOI: 10.1038/s41576-018-0051-9.
- [283] N. Rousset, R. L. Sandoval, M. M. Modena, A. Hierlemann, and P. M. Misun (2022). “Modeling and measuring glucose diffusion and consumption by colorectal cancer spheroids in hanging drops using integrated biosensors”. *Microsystems & nanoengineering* 8, 14. DOI: 10.1038/s41378-021-00348-w.

- [284] B. Rubinsky (2015). “27. Biological matter in isochoric systems”. *Cryobiology* 71(1), 172. DOI: 10.1016/j.cryobiol.2015.05.033.
- [285] A. S. Rudolph and J. H. Crowe (1985). “Membrane stabilization during freezing: the role of two natural cryoprotectants, trehalose and proline”. *Cryobiology* 22(4), 367–377. DOI: 10.1016/0011-2240(85)90184-1..
- [286] R. Rungsiwiwut, C. Manolertthewan, P. Numchaisrika, V. Ahnonkitpanit, P. Virutamasen, M. Techakumphu, and K. Pruksananonda (2013). “The ROCK inhibitor Y-26732 enhances the survival and proliferation of human embryonic stem cell-derived neural progenitor cells upon dissociation”. *Cells, tissues, organs* 198(2), 127–138. DOI: 10.1159/000354031.
- [287] J. Safta, K. Z. Case, L. Brandt, A. M. Matathia, M.-C. Hsieh, T. Blanc, L. Huang, V. Goetz, and D. T. Dorundo (2024). “Uncovering new poloxamer attributes which significantly impact mammalian cell growth performance”. *Biochemical Engineering Journal* 202, 109146. DOI: 10.1016/j.bej.2023.109146.
- [288] A. C. Saito, T. Higashi, and H. Chiba (2023). “Tight-junction strand networks and tightness of the epithelial barrier”. *Microscopy (Oxford, England)* 72(3), 213–225. DOI: 10.1093/jmicro/dfad008.
- [289] Y. Sasai (2013). “Cytosystems dynamics in self-organization of tissue architecture”. *Nature* 493(7432), 318–326. DOI: 10.1038/nature11859.
- [290] G. Scesa, R. Adami, and D. Bottai (2021). “iPSC Preparation and Epigenetic Memory: Does the Tissue Origin Matter?” *Cells* 10(6), 1470. DOI: 10.3390/cells10061470..
- [291] A. Schmitz, S. C. Fischer, C. Mattheyer, F. Pampaloni, and E. H. K. Stelzer (2017). “Multiscale image analysis reveals structural heterogeneity of the cell microenvironment in homotypic spheroids”. *Scientific reports* 7, 43693. DOI: 10.1038/srep43693.
- [292] C. Schmitz, E. Potekhina, V. V. Belousov, and A. Lavrentieva (2021). “Hypoxia Onset in Mesenchymal Stem Cell Spheroids: Monitoring With Hypoxia Reporter Cells”. *Frontiers in bioengineering and biotechnology* 9, 611837. DOI: 10.3389/fbioe.2021.611837.
- [293] A. Sharma, S. Sances, M. J. Workman, and C. N. Svendsen (2020). “Multi-lineage Human iPSC-Derived Platforms for Disease Modeling and Drug Discovery”. *Cell stem cell* 26(3), 309–329. DOI: 10.1016/j.stem.2020.02.011.
- [294] M. Shi, S. Feng, X. Zhang, C. Ji, F. Xu, and T. J. Lu (2018). “Droplet based vitrification for cell aggregates: Numerical analysis”. *Journal of the mechanical behavior of biomedical materials* 82, 383–393. DOI: 10.1016/j.jmbbm.2018.03.026.
- [295] Y. Shi, H. Inoue, J. C. Wu, and S. Yamanaka (2017). “Induced pluripotent stem cell technology: a decade of progress”. *Nature reviews. Drug discovery* 16(2), 115–130. DOI: 10.1038/nrd.2016.245.
- [296] Y. Shi, P. Kirwan, and F. J. Livesey (2012). “Directed differentiation of human pluripotent stem cells to cerebral cortex neurons and neural networks”. *Nature protocols* 7(10), 1836–1846. DOI: 10.1038/nprot.2012.116.

- [297] Y. Shi, Y. Wang, J. Shi, Z. Li, X. Huang, J. Liang, X. Zhang, Di Zhang, X. Zou, and X. Hu (2023). “Simulation of diffusion behavior of NaCl in multi-tissue beef marination process”. *Food chemistry* 402, 134164. DOI: 10.1016/j.foodchem.2022.134164.
- [298] M. Schlafer and A. M. Karow (1975). “Pharmacological effects of dimethyl sulfoxide on the mammalian myocardium”. *Annals of the New York Academy of Sciences* 243, 110–121. DOI: 10.1111/j.1749-6632.1975.tb25350.x.
- [299] O. Shoshani and D. Zipori (2011). “Mammalian cell dedifferentiation as a possible outcome of stress”. *Stem cell reviews and reports* 7(3), 488–493. DOI: 10.1007/s12015-011-9231-0.
- [300] R. Silva-Pedrosa, A. J. Salgado, and P. E. Ferreira (2023). “Revolutionizing Disease Modeling: The Emergence of Organoids in Cellular Systems”. *Cells* 12(6), 930. DOI: 10.3390/cells12060930.
- [301] M. Simian and M. J. Bissell (2017). “Organoids: A historical perspective of thinking in three dimensions”. *The Journal of cell biology* 216(1), 31–40. DOI: 10.1083/jcb.201610056.
- [302] L. M. Smits and J. C. Schwamborn (2020). “Midbrain Organoids: A New Tool to Investigate Parkinson’s Disease”. *Frontiers in cell and developmental biology* 8, 359. DOI: 10.3389/fcell.2020.00359.
- [303] Y. H. Sniekers and C. C. van Donkelaar (2005). “Determining diffusion coefficients in inhomogeneous tissues using fluorescence recovery after photobleaching”. *Biophysical journal* 89(2), 1302–1307. DOI: 10.1529/biophysj.104.053652.
- [304] J. T. Snow, J. W. Finley, and M. Friedman (1975). “Oxidation of sulfhydryl groups to disulfides by sulfoxides”. *Biochemical and biophysical research communications* 64(1), 441–447. DOI: 10.1016/0006-291X(75)90272-7.
- [305] L. Sokoloff (1977). “Relation between physiological function and energy metabolism in the central nervous system”. *Journal of neurochemistry* 29(1), 13–26. DOI: 10.1111/j.1471-4159.1977.tb03919.x.
- [306] Z. Song, J. Cai, Y. Liu, D. Zhao, J. Yong, S. Duo, X. Song, Y. Guo, Y. Zhao, H. Qin, X. Yin, C. Wu, J. Che, S. Lu, M. Ding, and H. Deng (2009). “Efficient generation of hepatocyte-like cells from human induced pluripotent stem cells”. *Cell research* 19(11), 1233–1242. DOI: 10.1038/cr.2009.107.
- [307] J. R. Spence, C. N. Mayhew, S. A. Rankin, M. F. Kuhar, J. E. Vallance, K. Tolle, E. E. Hoskins, V. V. Kalinichenko, S. I. Wells, A. M. Zorn, N. F. Shroyer, and J. M. Wells (2011). “Directed differentiation of human pluripotent stem cells into intestinal tissue in vitro”. *Nature* 470(7332), 105–109. DOI: 10.1038/nature09691.
- [308] B. Stokich, Q. Osgood, D. Grimm, S. Moorthy, N. Chakraborty, and M. A. Menze (2014). “Cryopreservation of hepatocyte (HepG2) cell monolayers: impact of trehalose”. *Cryobiology* 69(2), 281–290. DOI: 10.1016/j.cryobiol.2014.08.001.
- [309] K. B. Storey and J. M. Storey (2013). “Molecular biology of freezing tolerance”. *Comprehensive Physiology* 3(3), 1283–1308. DOI: 10.1002/cphy.c130007.

- [310] H. A. Strobel, S. M. Moss, and J. B. Hoying (2022). “Methods for vascularization and perfusion of tissue organoids”. *Mammalian genome : official journal of the International Mammalian Genome Society* 33(3), 437–450. DOI: 10.1007/s00335-022-09951-2.
- [311] M. Sudo, M. Nishihara, J. Takahashi, and S. Asahi (2017). “Long-Term Stability of Cryopreserved Human Hepatocytes: Evaluation of Phase I and II Drug-Metabolizing Enzyme Activities and CYP3A4/5 Induction for More than a Decade”. *Drug metabolism and disposition: the biological fate of chemicals* 45(7), 734–736. DOI: 10.1124/dmd.117.075234.
- [312] S. Sullivan, P. J. Fairchild, S. G. E. Marsh, C. R. Müller, M. L. Turner, J. Song, and D. Turner (2020). “Haplobanking induced pluripotent stem cells for clinical use”. *Stem cell research* 49, 102035. DOI: 10.1016/j.scr.2020.102035.
- [313] S. A. Szobota and B. Rubinsky (2006). “Analysis of isochoric subcooling”. *Cryobiology* 53(1), 139–142. DOI: 10.1016/j.cryobiol.2006.04.001.
- [314] J. Takahashi (2019). “Preparing for first human trial of induced pluripotent stem cell-derived cells for Parkinson’s disease: an interview with Jun Takahashi”. *Regenerative medicine* 14(2), 93–95. DOI: 10.2217/rme-2018-0158.
- [315] K. Takahashi, K. Tanabe, M. Ohnuki, M. Narita, T. Ichisaka, K. Tomoda, and S. Yamanaka (2007). “Induction of pluripotent stem cells from adult human fibroblasts by defined factors”. *Cell* 131(5), 861–872. DOI: 10.1016/j.cell.2007.11.019.
- [316] K. Takahashi and S. Yamanaka (2006). “Induction of pluripotent stem cells from mouse embryonic and adult fibroblast cultures by defined factors”. *Cell* 126(4), 663–676. DOI: 10.1016/j.cell.2006.07.024.
- [317] T. Takebe and J. M. Wells (2019). “Organoids by design”. *Science (New York, N.Y.)* 364(6444), 956–959. DOI: 10.1126/science.aaw7567.
- [318] L. Tang and X. J. Zhou (2019). “Diffusion MRI of cancer: From low to high b-values”. *Journal of magnetic resonance imaging : JMRI* 49(1), 23–40. DOI: 10.1002/jmri.26293.
- [319] S. E. Tapia Lishner, L. A. Marquez-Curtis, and J. A. W. Elliott (2023). “Permeation kinetics of dimethyl sulfoxide in porcine corneal discs”. *Cryobiology* 113, 104566. DOI: 10.1016/j.cryobiol.2023.104566.
- [320] M. J. Taylor and D. E. Pegg (1983). “The effect of ice formation on the function of smooth muscle tissue stored at -21 or -60 degrees C”. *Cryobiology* 20(1), 36–40. DOI: 10.1016/0011-2240(83)90057-3.
- [321] M. J. Taylor, B. P. Weegman, S. C. Baicu, and S. E. Giwa (2019). “New Approaches to Cryopreservation of Cells, Tissues, and Organs”. *Transfusion medicine and hemotherapy : offizielles Organ der Deutschen Gesellschaft für Transfusionsmedizin und Immunhamatologie* 46(3), 197–215. DOI: 10.1159/000499453.
- [322] M. J. Taylor, Y. C. Song, and K. G. M. Brockbank (2004). “Vitrification in Tissue Preservation: New Developments”. In: *Life in the frozen state*. Ed. by B. J. Fuller, N. Lane, and E. E. Benson. Boca Raton, Fla.: CRC Press, pp. 603–641. ISBN: 978-0-4292-1248-2.

- [323] J. A. TerWee, C. L. Chin, S. Watrin, R. F. Tello, N. J. Rieder, J. D. Lowell, and D. Latham-Timmons (2011). “Increased consistency and efficiency in routine potency testing by bioassay with direct use of cryopreserved (ready-to-plate) cells”. *Journal of immunological methods* 370(1-2), 65–74. DOI: 10.1016/j.jim.2011.05.009.
- [324] J. A. Thomson, J. Itskovitz-Eldor, S. S. Shapiro, M. A. Waknitz, J. J. Swiergiel, V. S. Marshall, and J. M. Jones (1998). “Embryonic stem cell lines derived from human blastocysts”. *Science (New York, N.Y.)* 282(5391), 1145–1147. DOI: 10.1126/science.282.5391.1145.
- [325] K. E. Thorpe, A. I. Levey, and J. Thomas (2021). “U.S. Burden of neurodegenerative disease”. URL: [https://www.fightchronicdisease.org/resources/us-burden-neurodegenerative-disease\(23.08.24\)](https://www.fightchronicdisease.org/resources/us-burden-neurodegenerative-disease(23.08.24)).
- [326] R. M. F. Tomás, A. Bissoyi, T. R. Congdon, and M. I. Gibson (2022). “Assay-ready Cryopreserved Cell Monolayers Enabled by Macromolecular Cryoprotectants”. *Biomacromolecules* 23(9), 3948–3959. DOI: 10.1021/acs.biomac.2c00791.
- [327] M. Toner, E. G. Cravalho, and M. Karel (1990). “Thermodynamics and kinetics of intracellular ice formation during freezing of biological cells”. *Journal of Applied Physics* 67(3), 1582–1593. DOI: 10.1063/1.345670.
- [328] F. S. Trad, M. Toner, and J. D. Biggers (1999). “Effects of cryoprotectants and ice-seeding temperature on intracellular freezing and survival of human oocytes”. *Human reproduction (Oxford, England)* 14(6), 1569–1577. DOI: 10.1093/humrep/14.6.1569.
- [329] T. Tricot, C. M. Verfaillie, and M. Kumar (2022). “Current Status and Challenges of Human Induced Pluripotent Stem Cell-Derived Liver Models in Drug Discovery”. *Cells* 11(3), 442. DOI: 10.3390/cells11030442.
- [330] Y.-H. Tsai, M. Czerwinski, A. Wu, M. K. Dame, D. Attili, E. Hill, J. A. Colacino, L. M. Nowacki, N. F. Shroyer, P. D. R. Higgins, J. Y. Kao, and J. R. Spence (2018). “A Method for Cryogenic Preservation of Human Biopsy Specimens and Subsequent Organoid Culture”. *Cellular and molecular gastroenterology and hepatology* 6(2), 218–222.e7. DOI: 10.1016/j.jcmgh.2018.04.008.
- [331] Y.-C. Tung, A. Y. Hsiao, S. G. Allen, Y.-s. Torisawa, M. Ho, and S. Takayama (2011). “High-throughput 3D spheroid culture and drug testing using a 384 hanging drop array”. *The Analyst* 136(3), 473–478. DOI: 10.1039/c0an00609b.
- [332] G. Vajta, P. Holm, M. Kuwayama, P. J. Booth, H. Jacobsen, T. Greve, and H. Callesen (1998). “Open pulled straw (OPS) vitrification: A new way to reduce cryoinjuries of bovine ova and embryos”. *Molecular Reproduction and Development* 51(1), 53–58. DOI: 10.1002/(SICI)1098-2795(199809)51:1<53::AID-MRD6>3.0.CO;2-V.
- [333] A. J. Valente and O. Söderman (2019). “Do the solvent properties affect the propensity for self-association of  $\alpha$ -cyclodextrin? Insights from NMR self-diffusion”. *Journal of Molecular Liquids* 295, 111869. DOI: 10.1016/j.molliq.2019.111869.
- [334] B. H. Várkuti, M. Képiró, I. Á. Horváth, L. Végner, S. Ráti, Á. Zsigmond, G. Hegyi, Z. Lenkei, M. Varga, and A. Málnási-Csizmadia (2016). “A highly soluble, non-phototoxic,

- non-fluorescent blebbistatin derivative”. *Scientific reports* 6, 26141. DOI: 10.1038/srep26141.
- [335] A. Vásquez-Rivera, K. K. Sommer, H. Oldenhof, A. Z. Higgins, K. G. M. Brockbank, A. Hilfiker, and W. F. Wolkers (2018). “Simultaneous monitoring of different vitrification solution components permeating into tissues”. *The Analyst* 143(2), 420–428. DOI: 10.1039/c7an01576c.
- [336] M. Verheijen, M. Lienhard, Y. Schrooders, O. Clayton, R. Nudischer, S. Boerno, B. Timmermann, N. Selevsek, R. Schlapbach, H. Gmuender, S. Gotta, J. Geraedts, R. Herwig, J. Kleinjans, and F. Caiment (2019). “DMSO induces drastic changes in human cellular processes and epigenetic landscape in vitro”. *Scientific reports* 9(1), 4641. DOI: 10.1038/s41598-019-40660-0.
- [337] L. M. Vining, L. J. Zak, S. C. Harvey, and K. E. Harvey (2021). “The role of apoptosis in cryopreserved animal oocytes and embryos”. *Theriogenology* 173, 93–101. DOI: 10.1016/j.theriogenology.2021.07.017.
- [338] A. D. Vogel, R. Suk, C. Haran, P. G. Dickinson, K. L. Helke, M. Hassid, D. C. Fitzgerald, J. W. Turek, K. G. M. Brockbank, and T. K. Rajab (2024). “The impact of heart valve and partial heart transplant models on the development of banking methods for tissues and organs: A concise review”. *Cryobiology* 115, 104880. DOI: 10.1016/j.cryobiol.2024.104880.
- [339] E. Volkmer, I. Drosse, S. Otto, A. Stangelmayer, M. Stengele, B. C. Kallukalam, W. Mutschler, and M. Schieker (2008). “Hypoxia in static and dynamic 3D culture systems for tissue engineering of bone”. *Tissue engineering. Part A* 14(8), 1331–1340. DOI: 10.1089/ten.tea.2007.0231.
- [340] B. D. Walters and J. P. Stegemann (2014). “Strategies for directing the structure and function of three-dimensional collagen biomaterials across length scales”. *Acta biomaterialia* 10(4), 1488–1501. DOI: 10.1016/j.actbio.2013.08.038.
- [341] S. Wang, H. Oldenhof, T. Goecke, R. Ramm, M. Harder, A. Haverich, A. Hilfiker, and W. F. Wolkers (2015). “Sucrose Diffusion in Decellularized Heart Valves for Freeze-Drying”. *Tissue engineering. Part C, Methods* 21(9), 922–931. DOI: 10.1089/ten.TEC.2014.0681.
- [342] X. Wang, T.-C. Hua, D.-W. Sun, B. Liu, G. Yang, and Y. Cao (2007). “Cryopreservation of tissue-engineered dermal replacement in Me2SO: Toxicity study and effects of concentration and cooling rates on cell viability”. *Cryobiology* 55(1), 60–65. DOI: 10.1016/j.cryobiol.2007.05.006.
- [343] X.-Y. Wang, Z.-H. Jin, B.-W. Gan, S.-W. Lv, M. Xie, and W.-H. Huang (2014). “Engineering interconnected 3D vascular networks in hydrogels using molded sodium alginate lattice as the sacrificial template”. *Lab on a chip* 14(15), 2709–2716. DOI: 10.1039/c4lc00069b.

- [344] Z. Wang, S.-N. Wang, T.-Y. Xu, Z.-W. Miao, D.-F. Su, and C.-Y. Miao (2017). “Organoid technology for brain and therapeutics research”. *CNS neuroscience & therapeutics* 23(10), 771–778. DOI: 10.1111/cns.12754.
- [345] J. Wanigasekara, L. J. Carroll, P. J. Cullen, B. Tiwari, and J. F. Curtin (2023). “Three-Dimensional (3D) in vitro cell culture protocols to enhance glioblastoma research”. *PLoS one* 18(2), e0276248. DOI: 10.1371/journal.pone.0276248.
- [346] O. Warburg (1956). “On the origin of cancer cells”. *Science (New York, N.Y.)* 123(3191), 309–314. DOI: 10.1126/science.123.3191.309.
- [347] F. M. Watt and B. L. Hogan (2000). “Out of Eden: stem cells and their niches”. *Science (New York, N.Y.)* 287(5457), 1427–1430. DOI: 10.1126/science.287.5457.1427.
- [348] L.-B. Weiswald, D. Bellet, and V. Dangles-Marie (2015). “Spherical cancer models in tumor biology”. *Neoplasia (New York, N.Y.)* 17(1), 1–15. DOI: 10.1016/j.neo.2014.12.004.
- [349] D. Wendt, A. Marsano, M. Jakob, M. Heberer, and I. Martin (2003). “Oscillating perfusion of cell suspensions through three-dimensional scaffolds enhances cell seeding efficiency and uniformity”. *Biotechnology and bioengineering* 84(2), 205–214. DOI: 10.1002/bit.10759.
- [350] L. Weng, S. Ziaei, and G. D. Elliott (2016). “Effects of Water on Structure and Dynamics of Trehalose Glasses at Low Water Contents and its Relationship to Preservation Outcomes”. *Scientific reports* 6, 28795. DOI: 10.1038/srep28795.
- [351] P. Westh (2004). “Preferential interaction of dimethyl sulfoxide and phosphatidyl choline membranes”. *Biochimica et biophysica acta* 1664(2), 217–223. DOI: 10.1016/j.bbame.2004.06.001.
- [352] D. Whaley, K. Damyar, R. P. Witek, A. Mendoza, M. Alexander, and J. R. Lakey (2021). “Cryopreservation: An Overview of Principles and Cell-Specific Considerations”. *Cell transplantation* 30, 963689721999617. DOI: 10.1177/0963689721999617.
- [353] N. William and J. P. Acker (2020). “Control of ice recrystallization in liver tissues using small molecule carbohydrate derivatives”. *Cryobiology* 97, 250–253. DOI: 10.1016/j.cryobiol.2020.09.006.
- [354] L. Y. Wu, D. Di Carlo, and L. P. Lee (2008). “Microfluidic self-assembly of tumor spheroids for anticancer drug discovery”. *Biomedical microdevices* 10(2), 197–202. DOI: 10.1007/s10544-007-9125-8.
- [355] G. Wypych (2021). *Handbook of Nucleating Agents*. 2nd ed. San Diego: ChemTec Publishing. ISBN: 978-1-927885-81-9. DOI: 10.1016/C2020-0-00369-5.
- [356] X. Xie, X. Li, and W. Song (2023). “Tumor organoid biobank-new platform for medical research”. *Scientific reports* 13(1), 1819. DOI: 10.1038/s41598-023-29065-2.
- [357] X. Xu, S. Cowley, C. J. Flaim, W. James, L. Seymour, and Z. Cui (2010). “The roles of apoptotic pathways in the low recovery rate after cryopreservation of dissociated human embryonic stem cells”. *Biotechnology progress* 26(3), 827–837. DOI: 10.1002/btpr.368.

- 
- [358] K. Yajima, Y. Uno, N. Murayama, S. Uehara, M. Shimizu, C. Nakamura, K. Iwasaki, M. Utoh, and H. Yamazaki (2014). “Evaluation of 23 lots of commercially available cryopreserved hepatocytes for induction assays of human cytochromes P450”. *Drug metabolism and disposition: the biological fate of chemicals* 42(5), 867–871. DOI: 10.1124/dmd.113.056804.
- [359] N. J. Yang and M. J. Hinner (2015). “Getting across the cell membrane: an overview for small molecules, peptides, and proteins”. *Methods in molecular biology (Clifton, N.J.)* 1266, 29–53. DOI: 10.1007/978-1-4939-2272-7\_3.
- [360] Z. Ye, S. Liu, and Y. Yin (2023). “Magnetic nanoparticles for nanowarming: seeking a fine balance between heating performance and biocompatibility”. *Materials Chemistry Frontiers* 7(17), 3427–3433. DOI: 10.1039/D3QM00248A.
- [361] F. Yi, G.-H. Liu, and J. C. Izipisua Belmonte (2012). “Human induced pluripotent stem cells derived hepatocytes: rising promise for disease modeling, drug development and cell therapy”. *Protein & cell* 3(4), 246–250. DOI: 10.1007/s13238-012-2918-4.
- [362] K. E. Zachariassen and E. Kristiansen (2000). “Ice nucleation and antinucleation in nature”. *Cryobiology* 41(4), 257–279. DOI: 10.1006/cryo.2000.2289.
- [363] J. Zhao, M. Griffin, J. Cai, S. Li, P. E. Bulter, and D. M. Kalaskar (2016). “Bioreactors for tissue engineering: An update”. *Biochemical Engineering Journal* 109, 268–281. DOI: 10.1016/j.bej.2016.01.018.
- [364] W. Zhu, X. Qu, J. Zhu, X. Ma, S. Patel, J. Liu, P. Wang, C. S. E. Lai, M. Gou, Y. Xu, K. Zhang, and S. Chen (2017). “Direct 3D bioprinting of prevascularized tissue constructs with complex microarchitecture”. *Biomaterials* 124, 106–115. DOI: 10.1016/j.biomaterials.2017.01.042.

## 8 Appendix

## List of Figures

1	Concept and objective of present thesis. . . . .	6
2	Schematic overview of main characteristics of 3D cell cultures. . . . .	12
3	Overview of potential applications of stem cell-derived organoids. . . . .	14
4	Cryo injury mechanisms during cryopreservation. . . . .	17
5	Cryovariables influence cellular effects after cryopreservation. . . . .	18
6	Phase diagram of an aqueous solution at cryogenic temperatures. . . . .	19
7	Inhomogeneous thermal and mass transfer during cryopreservation of 3D cell systems. . . . .	23
8	Differentiation from hiPSCs to HLCs. . . . .	27
9	Overview of the workflow of (A) the generation and cultivation, (B) cryopreservation and (C) thawing or warming of 3D cell systems. . . . .	32
10	Diffusion analysis in NSC spheroids. . . . .	33
11	Differentiation of UKKi011-A into NSCs and proliferation of NSC spheroids. . . . .	45
12	Representative morphological characterisation of small, medium and large NSC spheroids without and with incubation in CryoStor CS10. . . . .	46
13	Relative mean diameters of NSC spheroids after incubating for 5 min, 15 min and 30 min in different cryopreservation media. . . . .	47
14	Relative mean cell viability of NSC spheroids after 30 min incubation in different cryopreservation media. . . . .	48
15	Gene expression analysis of NSC spheroids after 30 min incubation in cryopreservation media. . . . .	49
16	Quantitative protein expression analysis of NSC spheroids after 30 min incubation in cryopreservation media. . . . .	50
17	Morphological characterisation of small, medium and large NSC spheroids nfc and a.t., cultured and recovered in ULA plates. . . . .	51
18	Morphological characterisation of NSC spheroids nfc and a.t., cultured and recovered in the CERO 3D bioreactor. . . . .	52
19	Relative volumes of NSC spheroids nfc and a.t., cultured and recovered in ULA plates and the CERO 3D bioreactor. . . . .	53
20	Relative cell viability of NSC spheroids nfc and a.t. analysed by ATP measurement, cultured in ULA plates. . . . .	54
21	Relative cell viability measured by membrane integrity of NSC spheroids nfc and a.t., cultured in ULA plates. . . . .	55
22	Relative cell viability of NSC spheroids nfc and a.t., cultured in the CERO 3D bioreactor. . . . .	56
23	Representative viability stainings of NSC spheroids nfc and a.t. . . . .	57

---

24	Gene expression analysis of cells from NSC spheroids nfc and a.t. . . . . .	58
25	Relative cell viability and apoptosis of NSC spheroids nfc and a.t. after treatment with Chroman 1 (C), Y-27632 (Y) and without additive. . . . . .	59
26	Characterisation of HLC organoids differentiated via DE- and HP spheroids. . .	60
27	Morphological and metabolic characterisation of HP spheroids and HLC organoids nfc and a.t. . . . . .	61
28	Gene and protein expression of HP spheroids nfc and a.t. . . . . .	62
29	Gene and protein expression of HLC organoids nfc and a.t. . . . . .	63
30	Characterisation of the peripheral ultrastructure of NSC spheroids nfc and a.t.	65
31	Characterisation of cytoskeleton and adhesion proteins of NSC spheroids nfc and a.t. . . . . .	66
32	Morphological assessment of fusion properties of NSC spheroids nfc and a.t. . .	67
33	Viability and proliferation analysis of inner cell layers of NSC spheroids nfc and a.t. . . . . .	68
34	Relative cell viability of NSC spheroids nfc and a.t. with and without treatment of PO, cultured in the CERO 3D bioreactor. . . . . .	69
35	Relative cell viability of NSC spheroids nfc and a.t. after treatment with Blebb, with PO and without additives. . . . . .	70
36	Morphology and viability analysis of vitrified NSC spheroids a.w. . . . . .	71
37	Gene expression of nfc and vitrified NSC spheroids a.w. . . . . .	72
38	Characterisation of the peripheral ultrastructure of nfc and vitrified NSC spheroids a.w. . . . . .	73
39	Bioorthogonal Raman micro-spectroscopy to analyse DMSO-d6 perfusion in diverse organoids. . . . . .	76
40	Two representative multichannel images of NSC spheroids acquired by two-photon excitation microscopy. . . . . .	77
41	Relative cell viability and fusion properties of NSC spheroids incubated in DMSO and DMSO-d6 before slow-rate freezing. . . . . .	78
42	Viability analyses of NSC spheroids a.t., incubated in 10% DMSO for different times before slow-rate freezing. . . . . .	79
43	Viability analyses of NSC spheroids a.w., which were incubated in 10% DMSO for different times before vitrification. . . . . .	80
44	Workflow to enable a constant supply of complex 3D cell models for biomedical and pharmaceutical research and diagnostics using living biobanking. . . . . .	82
45	Percentage volume decrease of spheroids with different diameters due to the detachment of peripheral cells in the proliferating zone after cryopreservation ( $V_{cryo}$ ). . . . . .	88
46	Schematic overview of cellular effects in different spheroid zones in nfc and after cryopreservation. . . . . .	99

47	Schematic overview on the volume regulation of spheroids after treatment with different CPAs over time. . . . .	102
48	Comparative analyses of CPA effects in terms of viability and adhesion on 2D NSC monolayers or 3D NSC spheroids. . . . .	105
49	Diffusion coefficient progression in avascular spheroids and organoids based on Raman micro-spectroscopy. . . . .	109
50	Schematic overview of model-specific inline monitoring using bioorthogonal Raman micro-spectroscopy. . . . .	112

## List of Tables

1	List of hiPSC lines used. . . . .	25
2	Neural differentiation media for generating hiPSCs-derived NSCs. . . . .	27
3	Hepatocyte differentiation media for generating hiPSCs-derived HLCs. . . . .	28
4	List of cryopreservation media used for cryopreservation of NSC spheroids. . . . .	33
5	Staining reagents of Apoptosis/Necrosis Assay Kit. . . . .	35
6	Primary antibodies for ICC. . . . .	37
7	Secondary antibodies for ICC. . . . .	38
8	List of TaqMan assays for RT-qPCR of NSCs. . . . .	40
9	List of TaqMan assays for RT-qPCR of hepatocytes. . . . .	41
10	Antibodies and isotype controls for FC. . . . .	42

## Published work

**Peer-reviewed publications**

- S. Altmaier, I. Meiser, E. Lemesre, B. Chanrion, R. Steeg, L. E. Leonte, B. Holst, B. Schnack Nielsen, C. Clausen, K. Schmidt, A. M. Vinggaard, H. Zimmermann, J. C. Neubauer, M. A. Rasmussen (2022). "Human iPSC-derived hepatocytes in 2D and 3D suspension culture for cryopreservation and in vitro toxicity studies", *Reproductive Toxicology*. DOI: 10.1016/j.reprotox.2022.05.005.
- C. K. Kwok, I. Sébastien, K. Hariharan, I. Meiser, J. Wihan, S. Altmaier, I. Karnatz, D. Bauer, B. Fischer, A. Feile, A. Cabrera Socorro, M. A. Rasmussen, B. Holst, J. C. Neubauer, C. Clausen, C. Verfaillie, A. Ebnet, M. Hansson, R. Steeg, H. Zimmermann (2022). "Scalable expansion of iPSC and their derivatives across multiple lineages", *Reproductive Toxicology*. DOI: 10.1016/j.reprotox.2022.05.007.
- S. Altmaier, I. Meiser, F. Stracke, H. Zimmermann (2024). "Diffusion kinetics & perfusion times in tissue models obtained by bioorthogonal Raman  $\mu$ -spectroscopy", *Biophysical Reports*. DOI: 10.1016/j.bpr.2024.100150.
- S. Altmaier, R. Le Harzic, F. Stracke, A. M. Speicher, D. Uhl, J. Ehrlich, T. Gerlach, K. Schmidt, K. Lemmer, F. Lautenschläger, H. Böse, J. C. Neubauer, H. Zimmermann, I. Meiser (2024). "Cytoskeleton adaptation to stretchable surface relaxation improves adherent cryopreservation of human mesenchymal stem cells", *Cryobiology*. DOI: 10.1016/j.cryobiol. 2024.104958.

**Conference Contributions**

- S. Altmaier, J. Majer, K. Schmidt, T. Maarefvand, A. Samoylenko, A. Zhyvolozhnyi, S. Vainio, J. C. Neubauer, I. Meiser, H. Zimmermann (2021). "Cryopreservation as a key technology for neural 3D cell models in next-generation theranostics of brain pathologies" (Poster presentation at International Society for Stem Cell Research (ISSCR), only virtual).
- K. Schmidt, S. Altmaier, M. A. Rasmussen, I. Meiser, B. Holst, S. Bur, C. Clausen, B. S. Nielsen, J. C. Neubauer, H. Zimmermann (2021). "Large-scale expansion and cryopreservation of human iPSC-based hepatic organoids" (Poster presentation at International Society for Stem Cell Research (ISSCR), only virtual).
- S. Altmaier, I. Meiser, J. Majer, J. C. Neubauer, H. Zimmermann (2022). "Cryopreservation of iPSC-derived neural 3D cell models as a fundamental key technology in biotechnology and biomedicine" (Lecture at CRYO, 59th Annual Meeting of the Society for Cryobiology in Dublin (Ireland), *Cryobiology*. DOI: 10.1016/j.cryobiol.2022.11.079).

- I. Meiser, B. Stephan, J. Majer, S. Altmaier, D. Van De Sande, M. Kreir, A. Cabrera Socorro, J. D. Pita Almenar, J. C. Neubauer, A. Ebneith, H. Zimmermann (2022). "Ready-to-use adherent hiPSC-derived neural co-cultures by vitrification" (Poster presentation at CRYO, 59th Annual Meeting of the Society for Cryobiology in Dublin (Ireland), Cryobiology. DOI: 10.1016/j.cryobiol.2022.11.157).
- S. Altmaier, I. Meiser, F. Stracke, R. Le Harzic, J. C. Neubauer, H. Zimmermann (2023). "Cryopreservation of iPS-derived early neural organoids as an enabling technology for standardization of 3D cell culture models" (Lecture at DECHEMA 3D conference in Freiburg).
- S. Altmaier, I. Meiser, F. Stracke, R. Le Harzic, J. C. Neubauer, H. Zimmermann (2023). "Enhanced cryopreservation efficiency of hiPSC-derived neural organoids based on raman studies" (Poster presentation at CRYO, 60th Annual Meeting of the Society for Cryobiology in Minneapolis (USA) & virtual, Cryobiology. DOI: 10.1016/j.cryobiol.2023.104750).
- R. Kettenhofen, C. K. Kwok, I. Sébastien, K. Hariharan, I. Meiser, J. Wihan, S. Altmaier, I. Karnatz, A. Feile, A. Cabrera Socorro, J. Meidahl Petersen, K. Schachter, M. Rasmussen, B. Holst, C. Clausen, C. Verfaillie, A. Ebneith, M. Hansson, R. Steeg, J. C. Neubauer, H. Zimmermann (2023). "Standardization, scalable expansion and differentiation of human iPS cells cultures in 3D bioreactors" (Poster contribution at GSCN, The German Stem Cell Network in Ulm).
- S. Altmaier, I. Meiser, F. Stracke, R. Le Harzic, J. C. Neubauer, H. Zimmermann (2023). "Cryopreservation of hiPSCs-derived neural organoids as a basis for the development of cryopreservation routines for 3D cell systems" (Lecture at SLTB, 59th meeting of Society for Low-Temperature Biology in Vigo (Spain)).
- D. Amelin, S. Ganz, T. Knoll, S. Altmaier, F. Musiol, M. Gepp, R. Ruff (2023). "AI-based analysis of the spheroid cultivation process in real time" (Poster contribution at International Society for Stem Cell Research (ISSCR) in Hamburg).
- M. Carrillo, S. Altmaier, I. Meiser, F. R. Ihmig (2024). "Non-invasive and continuous monitoring of 3D stem cell culture in a bioreactor - An embedded machine learning approach" (Conference paper, 58th Annual Conference of the German Society for Biomedical Engineering (BMT) in Stuttgart).

## Awards

- "MLP Scholarship in category Science" from MLP AG in Wiesloch, 2022
- "Add-on Fellowship for Interdisciplinary Life Science" from Joachim Herz Stiftung in Hamburg, 2023.

## Acknowledgement

I gratefully thank Prof. Dr. Heiko Zimmermann, head of Fraunhofer Institute for Biomedical Engineering and Professor of Molecular and Cellular Biotechnology/ Nanotechnology at Saarland University for the opportunity to work on this fascinating research subject at IBMT. I thank Prof. Dr. Heiko Zimmermann for providing the scientific subject and for providing the laboratory rooms and materials. I am deeply thankful for the advisory assistance and critical scientific discussions during this time that enabled this work.

I would like to thank Prof. Dr. Franziska Lautenschläger, head of the Division of Cytoskeletal Fibers, Saarland University, for accepting the responsibility of being my second supervisor. I am thankful for the advice on this project and the critical discussions during the group seminars.

I especially thank Dr. Ina Meiser, former head of the Group Cryosensor Technology at IBMT, for enabling this project in her department, her advisory support and all the scientific discussions.

I thank our cooperation partners from the EBiSC2 project, funded by the Innovative Medicines Initiative 2 Joint Undertaking (IMI2 JU) under grant agreement No 821362. I especially thank our project partner, Bioneer (Hørsholm, Denmark), for providing the cell line BIONi010-C-64, the protocols of hepatocyte differentiation and the assistance with the quality analyses of hepatocytes.

I thank Dr. Frank Stracke and Dr. Ronan le Harzic for the scientific discussions and the support regarding Raman micro-spectroscopy and two-photon excitation microscopy.

I thank Dr. Anna Speicher for all her discussions about neural stem cells and for her helpfulness in proofreading scientific subjects.

I would like to thank Julia Majer for the introduction to NSC differentiation and 3D cell culture, and Franziska Musiol for her support with the spheroid clearing and immunocytochemistry experiments.

I thank Susan Zöllner and Frank Bauerfeld for their introduction and support in the scanning electron microscopy experiments.

Furthermore, I thank the students who contributed to this work under my supervision. I thank Goma Adhikari for the toxicity screenings of cryopreservation media in NSC spheroids. I thank Katja Lemmer for her support in carrying out RT-qPCR analyses. I thank Yesica Fernanda Florez Villabona for her support in analysing the spheroid fusion.

I thank all my colleagues from the former Cryosensor Technology department and Bioprocesses and Bioanalytics department at IBMT for the good working atmosphere, friendly cooperation, and helpfulness.

Finally, I am grateful to my family for all the loving support and encouragement throughout these years. My special thanks go to Niklas Metzger, who always encourages and motivates me. Thank you for your constant support and patience.